Biosignatures, the Origin of Life, and the Early Earth Atmosphere

Nicholas F. Wogan

A dissertation
submitted in partial fulfillment of the
requirements for the degree of

Doctor of Philosophy

University of Washington

2023

Reading Committee:
David C. Catling, Chair
Kevin J. Zahnle
Roger Buick
Rory Barnes

Program Authorized to Offer Degree:
Department of Earth and Space Sciences

University of Washington

Abstract

Biosignatures, the Origin of Life, and the Early Earth Atmosphere

Nicholas F. Wogan

Chair of the Supervisory Committee:
David C. Catling
Department of Earth and Space Sciences

The ancient Earth atmosphere is our only example for how a microbial biosphere impacts planetary atmospheres and is therefore a critical asset to the spectroscopic search for life on exoplanets. Additionally, for a subaerial origin of life, the nature of the earliest Earth atmosphere determines the environmental conditions under which life began. However, our understanding of the early Earth is shrouded by deep time; very few clues to its composition, climate and biosphere have been preserved over billions of years. To complement the sparse geologic record, this thesis uses thermodynamic, photochemical, and climate models to better understand the atmospheres of early Earth to inform the search for life on exoplanets and improve our understanding of the origin of life.

In Part I of this dissertation, I investigate atmospheric chemical disequilibrium anti-biosignatures, as well as methane and oxygen biosignatures during the Archean (4.0 - 2.5 Ga) and Proterozoic (2.5 - 0.54 Ga) eons. By modeling the change in Earth's atmospheric composition when life first began, I argue that the disequilibrium coexistence of atmospheric H_2 and CO_2 or CO and water vapor is an anti-biosignature if observed on an exoplanet because these easily metabolized species should be consumed if life was present. Next, I estimate the likelihood of volcanism on an exoplanet mimicking the CH_4+CO_2 biosignature characteristic of the Archean Earth. I find that significant volcanic methane is unlikely, but, if possible, could be identified by observations of atmospheric CO because volcanoes

that produce CH_4 should also make CO. The final Chapter in Part I argues that atmospheric oxygen, Earth's most recognizable biosignature gas, was unstable during the Great Oxidation Event ($\sim$ 2.4 Ga). I also set a lower limit on O_2 levels during the Proterozoic eon, which improves potential detectability of O_2 on an exoplanet if it was like the ancient Earth.

Part II explores how Earth's Hadean (4.5 - 4.0 Ga) atmosphere may have influenced the origin of life. Specifically, I use atmospheric models to estimate the HCN and HCCCN produced in the Hadean atmosphere in the wake of large asteroid impacts. Both HCN and HCCCN are critical ingredients in "RNA world" origin of life hypotheses. Simulations show that asteroid impacts make transient H_2- and CH_4-rich atmospheres that persist for millions of years, until hydrogen escapes to space. I find that impacts larger than between 5×10^{20} to 4×10^{21} kg (570 to 1330 km diameter) produce sufficient atmospheric CH_4 to cause ample HCN and HCCCN photochemical production and rainout to the surface, while smaller impacts produce negligible amounts of origin-of-life molecules. The second chapter of Part II places these results in the context of Earth's impact history. I estimate when 5×10^{20} to 4×10^{21} kg impacts most likely occurred on the early Earth to shed light on when life began if it did so in an impact-driven scenario.

TABLE OF CONTENTS

LIST OF FIGURES

LIST OF TABLES

ACKNOWLEDGMENTS

This dissertation was made possible by a long list of mentors, graduate students, staff, friends and family.

First I would like to thank my advisor, David Catling. I have been very fortunate to benefit from David's vast knowledge of astrobiology and planetary science. I could not have asked for a better advisor. I also need to thank my mentor and committee member Kevin Zahnle. Almost all of my dissertation chapters were improved by Kevin's intuition for how planet work. Additionally, I thank the rest of my committee members, Rory Barnes and Roger Buick, for providing me with constructive feedback on my research over the last few years.

This thesis would not have been successful without Josh Krissansen-Totton. Thanks for being a great friend, collaborator, and mentor.

The Astrobiology Program has been an integral part of my experience at the University of Washington. Thanks to the director Victoria Meadows, and the many staff and students that kept the program thriving while I was a part of it.

I also need to thank the following friends, colleague or mentors for helping me at various stages of my PhD: Andrew Hoffman, Gemma O'Conner, Lucas Fifer, Trent Thomas, Zoe Todd, Zack Cohen, Ping-Chun Lin, Andrew Shumway, Maggie Thompson, Shintaro Kadoya, Eric Wolf, Shawn Domagal-Goldman, Sandra Bastelberger, Chris Stark, Dale Winebrenner, Jake Lustig-Yaeger, and Andrew Lincowski.

My family has always given me unconditional love and support. Thank you Mom, Dad and Ted. Finally, I need to thank Emily Honea for consistently being there for me.

DEDICATION

To my parents, Cam and Mary Lou, and my brother, Ted.

Chapter 1

INTRODUCTION

"It has been said that astronomy is a humbling and character-building experience. There is perhaps no better demonstration of the folly of human conceits than this distant image of our tiny world." - Carl Sagan, in the Pale Blue Dot

Past scientific exploration of the cosmos has delivered us repeated lessons in humility. Before Copernicus, humans perceived Earth to be at the center of the universe. Today, we know that rocky planets the size of Earth are common among the hundred-billion stars in our galaxy (Burke et al., 2015). But science has not yet fully addressed Earth's apparent remaining cosmic uniqueness: Earth gave rise to and harbors life. Astrobiology attempts to complete our lessons in humility by trying to determine life's prevalence or rarity in the universe.

Existing and future telescopes will allow for the search for life on planets orbiting other stars. The James Webb Space Telescope has begun to observe the atmospheres of small rocky planets and is sensitive enough to detect biogenic waste gases in some circumstances (Krissansen-Totton et al., 2018b). Additionally, the 2021 Decadal Survey on Astronomy and Astrophysics has recommended NASA construct the Habitable Worlds Observatory in the next few decades with a primary goal of characterizing exoplanet atmospheres and detecting biosignatures.

Even with precise observations of exoplanet atmospheres, confirming the presence or absence of life will be challenging. Gases that are typically associated with biology, like O_2, could potentially build-up in exoplanet atmospheres without life from geologic or photochemical processes (Krissansen-Totton et al., 2021a; Meadows et al., 2018). Additionally, given that exoplanets are many light-years away we will not have the opportunity to visit them with spacecraft to directly confirm or reject the hypothesis of life. Detecting life remotely will require a deep understanding of how life can influence an atmosphere, and the ways in which planetary evolution produces false-positive biosignatures.

To aid our understanding for how life might impact an exoplanet atmosphere, we can look to the co-evolution of Earth and its biosphere for the past 4 billion years. Earth's inhabited history has three main chapters with distinct atmospheres: The Archean (4.0 - 2.5 Ga), Proterozoic (2.5 - 0.54), and the modern Earth (0.54 - 0.0 Ga). Each era is an example atmosphere-biosphere interaction that might manifest on other worlds.

Furthermore, how life began on the early Earth informs the search for life elsewhere.

If the environmental conditions that led to life's origin on the early Earth were unique and uncommon on young exoplanets, then perhaps future telescopes are unlikely to detect spectral signatures of life. However, if instead life's emergence is an inevitable side effect of early planetary evolution, then future campaigns searching for life are much more likely to be successful.

1.1 Thesis outline

Part I of this thesis studies the interaction between the atmosphere and biosphere on the early Earth to inform the search for life on exoplanets. First, in Chapter 2, I investigate atmospheric chemical disequilibrium as a biosignature and anti-biosignature. The relationship between disequilibrium and life was first explored by Lovelock (1965) for the purposes of detecting microbes on the solar system planets. Since then, Sagan et al. (1993) observed that the disequilibrium coexistence of CH_4 and O_2 in Earth's modern atmosphere is a sign of life. CH_4 and O_2 rapidly annihilate each other through photochemical reactions, but the disequilibrium persists because of biological replenishment. More recently, Krissansen-Totton et al. (2016) rigorously quantified disequilibrium as the Gibbs free energy in the atmosphere-ocean system. They used multiphase thermodynamic calculations to show that modern Earth has an anomalously big biologically produced disequilibrium compared to other solar system planets.

Chapter 2 argues that disequilibrium is sometimes an anti-biosignature instead of a sign of life. Life is powered by chemical free energy. Therefore, in some circumstances, life should reduce the disequilibrium in its environment through its metabolism. I investigate this possibility by estimating how chemical disequilibrium changed when life first began on the early Earth. I demonstrate that Earth's atmosphere-ocean disequilibrium lowered when microbial life first appeared because such life likely consumed a pre-existing free energy in the atmosphere caused by volcanic outgassing. This chapter concludes by clarifying when atmospheric disequilibrium is a sign of life, and when it is instead an anti-biosignature.

In combination with previous research (Krissansen-Totton et al., 2018c), Chapter 2 also

established that the biogenic disequilibrium between atmospheric CH_4 and CO_2 was likely present through the entire Archean eon (4.0 - 2.4 Ga). Carbon dioxide was generated by volcanism and regulated by the geologic carbon cycle, while CH_4 concentrations resulted from methanogenic microbial life (Catling and Zahnle, 2020). Thus, the disequilibrium between methane and carbon dioxide might be a compelling biosignature if identified spectroscopically in an exoplanet atmosphere (Krissansen-Totton et al., 2018c). However, few studies have explored the possibility of non-biological CH_4 and CO_2 which might result in a false-positive detection of life.

Chapter 3 uses a model of volcanic outgassing to determine whether volcanoes on a terrestrial planet can produce atmospheric CH_4 and CO_2, thus mimicking Earth's Archean biosignature. In general, I find that significant volcanic methane is unlikely, but, if possible, could be identified by observations of atmospheric CO. Atmospheric CO is a false-positive diagnostic because volcanoes that produce CH_4 should also produce CO. Overall, when considering known mechanisms for generating abiotic CH_4 on rocky planets, I conclude that observations of atmospheric CH_4 with CO_2 are difficult to explain without the presence of biology when the CH_4 abundance implies a surface flux into the atmosphere comparable to modern Earth's biological CH_4 flux.

Chapters 2 and 3 investigate life's influence on the atmosphere in the late Hadean and early Archean atmosphere. However, arguably life's most profound impact on the atmosphere occurred much later, around 2.4 billion years ago, when oxygenic photosynthetic life (combined with several other factors) caused the Great Oxidation Event (GOE). The GOE marks the first appearance of the modern Earth's most identifiable biogenic gas: atmospheric oxygen.

In Chapter 4, I use a novel time-dependent one-dimensional photochemical model to simulate the Great Oxidation Event on Earth and find that the transition from an anoxic to an oxic atmosphere takes only 10^2 to 10^5 years. My model also suggests that O_2 between $\sim 10^{-8}$ and $\sim 10^{-4}$ mixing ratio is unstable, and prone to rapid change over geologic time. I suggest that this instability can explain geologic evidence for fluctuating O_2 levels during the

Great Oxidation Event (Poulton et al., 2021). This result is significant because it challenges an existing paradigm (Goldblatt et al., 2006) that the first rise of oxygen was a stable and irreversible event. I also argue that instability requires that the mid-Proterozoic (1.8 - 0.8 Ga) O_2 levels were bigger than 10^{-4} mixing ratio, because smaller O_2 levels would be unstable and ultimately incompatible with the geologic record of sulfur isotopes. Therefore, these results have implications for the detectability of Earth's O_2 biosignature during the Proterozoic.

Part II of this thesis addresses the broader question of which conditions lead to an origin of life on a planet. Understanding life's beginning on Earth, and whether it is likely to occur on an exoplanet is a pre-requisite to finding life elsewhere. A remote detection of a biosignature would be much less credible if the planet did not experience the conditions that are thought to be important for biopoiesis on the early Earth (Catling et al., 2018).

How life began on Earth is currently unknown, but one leading hypothesis suggests that strands of RNA were some of the first self-replicating molecules which perhaps ultimately evolved to become early life. In this scenario, RNA needs to be produced without life on the early Earth. Chemists have argued for several possible schemes, but all pathways require nitriles like HCN and HCCCN. Geochemical evidence suggests that volcanoes produced a CO_2- and N_2-rich Hadean atmosphere that would not generate essential prebiotic nitriles (Holland, 1984). Iron-rich asteroid impacts could have solved this problem because they may have transiently reduced the entire atmosphere, allowing HCN and HCCCN to form photochemically (Zahnle et al., 2020). Chapter 5 investigates this possibility by using novel coupled photochemical-climate models to simulate the Hadean atmosphere after massive impacts thereby quantify prebiotic nitrile production. Overall, I find that atmospheres after impacts are H_2-, CH_4- and NH_3-rich, and HCN and HCCCN are produced photochemically for impacts larger than between 5×10^{20} to 4×10^{21} kg (570 to 1330 km diameter). Smaller impacts chemically alter the Hadean atmosphere, but not by an amount that allows for the photochemical formation of both HCN and HCCCN.

The final chapter in this thesis (Chapter 6) combines the results from Chapter 5, with

Monte Carlo simulations of Earth's impact history to estimate the likelihood and timing of life's emergence in an impact-driven scenario. I use the lunar cratering record, and the abundance of highly siderophile elements in Earth's mantle to simulate the many possible impact histories that could have occurred on the early Earth. A fraction of the modeled impact histories experience impactors of sufficient mass to produce significant origin of life molecules, perhaps causing the emergence of life. However, in some cases life would not persist because the post-impact reducing atmosphere is subsequently followed by an ocean-vaporizing impact that would sterilize the planet. By considering the fraction of stochastic impact realizations that successfully initiate or fail to initiate life, I estimate the probability of life beginning if Earth history was rerun. Additionally, for impact histories where life is not destroyed by late ocean vaporization, I compute a probability distribution for when life began in an impact-driven scenario by considering the timing of the last post-impact reducing atmosphere.

Part I

ATMOSPHERIC BIOSIGNATURES, AND LIFE'S IMPACT ON THE EARLY EARTH

Chapter 2

ATMOSPHERIC CHEMICAL DISEQUILIBRIUM FROM DEAD TO LIVING WORLDS

"It may be some time before we can try these tests for life on the planets of other stars but in the meanwhile what started as an exercise in exobiology could become an expedition to discover the largest living creature on Earth, Gaia." - Lovelock (1975)

This chapter was originally published in collaboration with David C. Catling in the Astrophysical Journal (Wogan and Catling, 2020), and is reproduced below with the permission of the journal.

Summary

Chemical disequilibrium in exoplanetary atmospheres (detectable with remote spectroscopy) can indicate life. The modern Earth's atmosphere-ocean system has a much larger chemical disequilibrium than other solar system planets with atmospheres because of oxygenic photosynthesis. However, no analysis exists comparing disequilibrium on lifeless, prebiotic planets to disequilibrium on worlds with primitive chemotrophic biospheres that live off chemicals and not light. Here, we use a photochemical-microbial ecosystem model to calculate the atmosphere-ocean disequilibria of Earth with no life and with a chemotrophic biosphere. We show that the prebiotic Earth likely had a relatively large atmosphere-ocean disequilibrium due to the coexistence of water and volcanic H_2, CO_2, and CO. Subsequent chemotrophic life probably destroyed nearly all of the prebiotic disequilibrium through its metabolism, leaving a likely smaller disequilibrium between N_2, CO_2, CH_4, and liquid water. So, disequilibrium fell with the rise of chemotrophic life then later rose with atmospheric oxygenation due to oxygenic photosynthesis. We conclude that big prebiotic disequilibrium between H_2 and CO_2 or CO and water is an anti-biosignature because these easily metabolized species can be eaten due to redox reactions with low activation energy barriers. However, large chemical disequilibrium can also be a biosignature when the disequilibrium arises from a chemical mixture with biologically insurmountable activation energy barriers, and clearly identifiable biogenic gases. Earth's modern disequilibrium between O_2, N_2, and liquid water along with minor CH_4 is such a case. Thus, the interpretation of disequilibrium requires context. With context, disequilibrium can be used to infer dead or living worlds.

2.1 Introduction

It will soon be possible to look for biosignature gases in exoplanet atmospheres with telescopes. Within several years, the James Webb Space Telescope (JWST) will measure the composition of exoplanet atmospheres with transit spectroscopy (Fischer et al., 2019; Gaudi et al., 2019). Ground-based telescopes, such as the Extremely Large Telescope, will also play a role in the spectroscopic search for life by the mid 2020s (Lopez-Morales et al., 2019; Snellen et al., 2013).

Much biosignature research suggests that telescopes look for O_2 produced by oxygenic photosynthesis (Meadows, 2017; Meadows et al., 2018; Owen, 1980). Molecular oxygen can be a relatively easy biogenic gas to detect on an exoplanet (Meadows, 2017), and it is generated in large quantities by relatively few abiotic processes (Meadows et al., 2018).

However, Earth's O_2 biosignature has been strongly detectable for only the past $\sim 1/8$th of Earth's inhabited history. Fossil stromatolites show that the origin of life was before ~ 3.5 Ga (Walter et al., 1980), while geochemical data suggest that oxygenic photosynthesis could have arisen by ~ 3 Ga (Planavsky et al., 2014a). Despite the possible early rise of oxygenic photosynthesis, there was negligible atmospheric O_2 in the Archean eon (4.0 to 2.5 Ga) (Farquhar et al., 2000). Earth had O_2 in the Proterozoic Eon (2.5 to 0.541 Ga), but some atmospheric proxies (Planavsky et al., 2014b) indicate that O_2 may not have been plentiful enough to detect over interstellar distances with upcoming and future space-based telescopes (Krissansen-Totton et al., 2018b; Reinhard et al., 2017). Also, oxygenic photosynthesis is a complex metabolism that only evolved once on Earth (Fischer et al., 2016), and it is unknown whether its origin on an exoplanet is likely.

An alternative to looking for any single biogenic gas (e.g., O_2, CH_4, or N_2O), is to look for chemical disequilibrium, i.e., the long-term coexistence of two or more chemically incompatible species (Lovelock, 1965, 1975). On the modern Earth, different metabolisms produce different waste gases, which have a thermodynamic drive to react over long periods of time. Thus, incompatible waste gases, or disequilibria, are maintained in Earth's environment by

biogenic fluxes. The persistence of CH_4 and O_2 (which react through a series of intermediates) in Earth's modern atmosphere is an example and indicates continuous replenishment of these gases by biology.

Lovelock (1965) first proposed searching for life on other planets by looking for disequilibrium gases in planetary atmospheres, and subsequently Lovelock (1975) attempted to quantify the disequilibrium of Solar System planets. Unfortunately, knowledge of atmospheric composition of the Solar System planets, and computational methods for thermodynamic calculations were insufficient at the time for accurate calculations.

Using modern computational techniques and thermodynamics, Krissansen-Totton et al. (2016) calculated the atmosphere or atmosphere-ocean disequilibrium of several Solar System planets, Titan, and Earth. They found that Earth's atmosphere-ocean system has more than an order of magnitude disequilibrium (in joules per mole of atmosphere) than any other planet due to biogenic fluxes. They propose high atmosphere-ocean chemical disequilibrium as a biosignature for exoplanets similar to the modern Earth, with photosynthetic biospheres. Subsequently, Krissansen-Totton et al. (2018c) used atmospheric proxy and model-based estimates of Earth's Archean and Proterozoic atmosphere and ocean to calculate chemical disequilibrium over Earth history. They showed that disequilibrium rose to its present value because of atmospheric oxygen released from oxygenic photosynthesis, and N_2 put into the atmosphere from bacterial denitrification (conversion of NO_x to N_2) which uses organic carbon from photosynthesis (for further explanation see Section 4.1 in Krissansen-Totton et al. (2016)).

Despite this prior work, interpretation of disequilibrium as a sign of life is unclear. A planet without life might have a large disequilibrium of untapped free energy because life is not consuming it, so disequilibrium in that case is the very opposite of a sign of life: an anti-biosignature. If chemotrophic life evolves, its metabolism uses environmental free energy and tends to push environments toward thermodynamic equilibrium. Thus, we expect no big disequilibrium on a purely chemotrophic world. Finally, the modern state of high disequilibrium is a biosignature, but depends on the presence of a large, oxygenic photosynthetic

biosphere.

To elucidate these subtleties quantitatively, we use a photochemical model to calculate the plausible atmosphere-ocean disequilibrium of the prebiotic Earth and then couple the model to a simple microbial biosphere to investigate the Earth immediately after the origin of life. We demonstrate that atmosphere-ocean disequilibrium drops when chemotrophic life appears because such life destroys volcanically generated atmospheric free energy and can easily catalyze the reactions. However, the mixture of gases from phototrophs is not all consumed by chemotrophs because of insurmountable activation energy barriers, so this disequilibrium persists. Our results build upon previous studies (Krissansen-Totton et al., 2016, 2018c) to provide conservative estimates of chemical disequilibrium through Earth history by including the Hadean Earth. With our results, we distinguish the general cases when disequilibrium indicates life versus when disequilibrium is an anti-biosignature.

2.2 Methods

We model the change in atmosphere-ocean chemical disequilibrium between the prebiotic Earth, and Earth influenced by a chemotrophic ecosystem in two steps. First, we simulate atmospheric composition using a photochemical model coupled to a microbial biosphere (in the biotic case), and second, we calculate the atmosphere-ocean disequilibrium of this simulated atmosphere with multiphase Gibbs energy minimization. The following sections briefly describe both of these steps, and the Chapter Appendices 2.6.1 and 2.6.2 contain more detailed methods. The Python, Fortran and MATLAB source code is available on Github at `https://github.com/Nicholaswogan/Wogan_and_Catling_2020`.

2.2.1 Modeling the Hadean Atmosphere

For both the prebiotic and biotic atmospheric compositions, we use the 1-D photochemical-climate code contained within the open source software package *Atmos*. *Atmos* is derived from a model originally developed by the Kasting group (Pavlov et al., 2001), and versions of this code have been used to simulate the Archean and Proterozoic Earth atmosphere

(Zahnle et al., 2006), Mars (Sholes et al., 2019; Smith et al., 2014; Zahnle et al., 2008), and exoplanet atmospheres (Arney et al., 2016; Schwieterman et al., 2019). We use *Atmos* to model the prebiotic atmosphere and the atmosphere influenced by a chemotrophic ecosystem by setting lower boundary conditions appropriate to each scenario. Every model run achieves redox balance (i.e., conservation of chemical oxidants and reductants in the atmosphere) to better than approximately 0.01% (for an explanation of redox balance see Chapter 8 in Catling and Kasting (2017)).

Hadean Volcanic Outgassing

Modeling the atmosphere requires estimates of volcanic outgassing fluxes on the Hadean Earth. These fluxes depend on the redox state of the mantle, which is quantified by the mantle's oxygen fugacity (f_{O_2}). A more reduced mantle (lower O_2 fugacity) expels more reduced gases (e.g., H_2) relative to oxidized gases (e.g., H_2O). Recent oxygen fugacity proxies indicate that Earth's mantle was more reduced several billion years ago and slowly oxidized (Aulbach and Stagno, 2016; Nicklas et al., 2019). We linearly extrapolate O_2 fugacity data obtained by Aulbach and Stagno (2016) backward in time to estimate an O_2 fugacity of $\log_{10}(f_{O_2}) = \text{FMQ} - 1.48$ at ~ 4 Ga (Chapter Appendix 2.6.1) to represent mantle redox state around the time of the origin of life. Here, FMQ is the fayalite-magnetite-quartz buffer which is a synthetic reference f_{O_2} value at fixed temperature-pressure conditions. Sensitivity of calculated disequilibrium to f_{O_2} is relatively small. Changing the oxygen fugacity by 1 log unit changes the calculated atmosphere-ocean chemical disequilibrium by a factor of ~ 2 (Chapter Appendix 2.6.2), which is small compared to other uncertainties in chemical disequilibrium for an assumed prebiotic Earth at 4 Ga.

Volcanic outgassing in prebiotic times also depends on the total flux of all volcanic gases. This total depends on the tectonic regime of the ancient Earth, which is debated (Rosas and Korenaga, 2018). If Earth lacked plate tectonics and was in a "stagnant lid" regime, then the average heat flux could have been comparable to the modern flux despite a much warmer interior (Korenaga, 2009). On the other hand, if plate tectonics was active in the

Hadean, the heat flux on the 4 Ga Earth could have been 5 times higher than today (Sleep and Zahnle, 2001).

Volcanic outgassing is proportional to the heat flux to a power between 1 and 2. To be conservative, we take volcanic outgassing proportional to the square of heat flux (Sleep and Zahnle, 2001), so lower and upper bounds on heat flux suggest volcanic outgassing rates between 1 and 25 times the modern outgassing rate. We adopt this range here to estimate total volcanic outgassing fluxes (F_x) of hydrogen, carbon and sulfur at $\sim$ 4 Ga with the formulas

$$F_{\text{hydrogen}} = C F^{\text{mod}}_{\text{hydrogen}} \tag{2.1}$$

$$F_{\text{carbon}} = C F^{\text{mod}}_{\text{carbon}} \tag{2.2}$$

$$F_{\text{sulfur}} = C F^{\text{mod}}_{\text{suflur}} \tag{2.3}$$

Here, F^{mod}_x is the modern outgassing flux of species x, and C is an outgassing multiplier that we vary between 1 and 25. Fluxes are calculated in units of molecules cm^{-2} s^{-1}.

With estimates of O_2 fugacity and total outgassing fluxes, we use equilibrium chemistry of the mantle to calculate plausible outgassing fluxes of individual gases, H_2, H_2O, CH_4, CO_2, CO, H_2S, and SO_2 for C between 1 and 25. Details of these calculations are in Chapter Appendix 2.6.1.

Modeling a Prebiotic Atmosphere

We model the Earth's prebiotic atmosphere for each volcanic outgassing scenario between 1 and 25 times modern outgassing. We use calculated outgassing fluxes of H_2, CO, SO_2, and H_2S as lower boundary conditions to the *Atmos* photochemical model. Additionally, we set a CO deposition velocity to 10^{-8} cm s^{-1} to reflect the abiotic uptake of CO by the ocean (Kharecha et al., 2005). We assume that the abiotic surface flux of CH_4 is negligible. This assumption is supported by a recent work on the abiotic formation CH_4 on the modern Earth

(Fiebig et al., 2019) but is disputed by other studies (Etiope and Sherwood Lollar, 2013). All other boundary conditions are specified in Chapter Appendix 2.6.2. Given volcanic outgassing fluxes and other boundary conditions, *Atmos* calculates the mixing ratios of all species when the atmosphere is at photochemical equilibrium.

Modeling an Atmosphere Influenced by a Chemotrophic Ecosystem

For each volcanic outgassing scenario, we also model atmospheric composition influenced by a marine ecosystem of chemotrophic microbes. Our oceanic ecosystem is composed of four chemotrophic microorganisms with the following metabolisms:

$$CO_2 + 4H_2 \rightarrow CH_4 + 2H_2O \tag{2.4}$$

$$2CH_2O \rightarrow CH_3COOH \tag{2.5}$$

$$CH_3COOH \rightarrow CH_4 + CO_2 \tag{2.6}$$

$$4CO + 2H_2O \rightarrow 2CO_2 + CH_3COOH \tag{2.7}$$

These equations represent the metabolisms of chemosynthetic methanogens (Equation (2.4)), acetogenic bacteria (Equation (2.5)), acetotrophic methanogens (Equation (2.6)), and CO-consuming acetogens (Equation (2.7)). We have chosen this ecosystem to represent Earth's biosphere after the origin of life and before the origin of photosynthesis. The actual make-up Earth's biosphere at this time is unknown, but all organisms in our chosen ecosystem are phylogenetically ancient and should have preceded photosynthesis (Adam et al., 2018; Schönheit et al., 2016; Wolfe and Fournier, 2018), so they are a reasonable representation.

We model the impact of these various organism on atmospheric composition by setting lower boundary conditions in the photochemical model that reflect their metabolisms. This technique was used by Kharecha et al. (2005), and our ecosystem model is nearly identical to their "case 2" atmosphere-ecosystem model. The only difference is that the *Atmos* photochemical code is an updated version of the one used by Kharecha et al. (2005). Below,

we briefly describe how the model works, although a more in-depth account can be found in Kharecha et al. (2005) p. 58-61. Chapter Appendix 2.6.2 contains all the boundary conditions that are not listed in the main text.

Ground-level H_2 was likely much more plentiful than CH_4 on the prebiotic Earth because H_2 was produced by mantle-sourced volcanoes, and CH_4 was not because it is not thermodynamically favored compared to CO_2. When chemotrophic methanogens originated, they would have converted some of the prebiotic H_2 to CH_4 through their metabolism, although the total amount of hydrogen stored in these molecules would not have changed significantly. In other words, the weighted sum of the ground-level H_2 and CH_4 mixing ratios on the prebiotic Earth (denoted $n^{\rm pre}_{\rm H_2}$ and $n^{\rm pre}_{\rm CH_4}$, respectively) would have been approximately equal to the weighted sum of the ground-level H_2 and CH_4 mixing ratios on the Earth influenced by methanogens (denoted $n^{\rm eco}_{\rm H_2}$ and $n^{\rm eco}_{\rm CH_4}$, respectively):

$$n^{\rm eco}_{\rm H_2} + 2n^{\rm eco}_{\rm CH_4} \approx n^{\rm pre}_{\rm H_2} + 2n^{\rm pre}_{\rm CH_4} \tag{2.8}$$

Equation (2.8) is only approximately valid because burial of organic carbon, which contains hydrogen, would cause $n^{\rm eco}_{\rm H_2} + 2n^{\rm eco}_{\rm CH_4}$ to be less than $n^{\rm pre}_{\rm H_2} + 2n^{\rm pre}_{\rm CH_4}$ by no more than $\sim 1\%$. The precise difference depends on how efficiently organic carbon was buried in the past. Since this difference is small, we ignore organic carbon is burial, and assume that acetogenic bacteria and acetotrophic methanogens living in the ocean convert all organic carbon to methane and carbon dioxide. Our assumptions implicitly include heterotrophs in the model.

How much of the prebiotic atmospheric H_2 was converted to CH_4 by methanogens? Methanogens lived in the ocean, so their consumption or generation of atmospheric H_2 and CH_4 was modulated by gas transfer across the atmosphere-ocean interface. We model gas exchange using a stagnant boundary layer model (Kharecha et al., 2005; Liss and Slater, 1974). Within the ocean, life was probably energy limited, and not nutrient limited (i.e., life was not limited by phosphorus or biologically available nitrogen) on Earth before the

advent of oxygenic photosynthesis (Canfield et al., 2006; Kharecha et al., 2005; Ward et al., 2019). Therefore, we assume that methanogens consumed H_2 and expelled CH_4 in the ocean until they obtain 30 kJ mol^{-1} from Equation (2.4), which is the approximate Gibbs energy required to create 1 mol of ATP.

In practice, we simulate methanogens for each outgassing rate with the following steps. First, we arbitrarily set the ground-level H_2 and CH_4 mixing ratios in the photochemical model such that they satisfy Equation (2.8). Second, we run the photochemical model to retrieve the surface flux of H_2 and CH_4. Third, we check whether the calculated H_2 and CH_4 fluxes reflect energy-limited methanogens in an ocean which exchanges gases with the atmosphere via a stagnant boundary layer. Fourth, if the fluxes do not satisfy this requirement, then we select new H_2 and CH_4 mixing ratios which are closer to satisfying step 3 (which still satisfy Equation (2.8)). We iterate steps 2 through 4 until step 3 is satisfied.

To simulate CO-consuming acetogens, we set the CO deposition velocity to its maximum value of 1.2×10^{-4} cm s^{-1}. This maximum deposition velocity assumes that acetogens consume CO as soon as it enters the ocean. This assumption is reasonable because an energy limited chemotrophic biosphere which contains CO consumers should draw CO concentrations to negligible amounts in the ocean (Kharecha et al., 2005; Schwieterman et al., 2019). The photochemical code calculates the mixing ratio of CO corresponding to the maximum deposition velocity.

2.2.2 Quantification of Chemical Disequilibrium

For each prebiotic and biotic atmosphere, we calculate the atmosphere-ocean chemical disequilibrium with Gibbs energy minimization, using code described previously (Krissansen-Totton et al., 2018c). Given the chemical composition of an atmosphere-ocean system, the code reacts all molecules and atoms to thermodynamic equilibrium. The chemical disequilibrium is then defined by the Gibbs free energy difference between the initial and equilibrium state:

$$\Phi = G_{(T,P)}\left(\mathbf{n}_{\text{initial}}\right) - G_{(T,P)}\left(\mathbf{n}_{\text{final}}\right) \tag{2.9}$$

Here, Φ is the available Gibbs energy (J/mol atmosphere). The vector containing the abundance of all atmospheric and ocean species is $\mathbf{n}_{\text{initial}}$, while $\mathbf{n}_{\text{final}}$ contains abundances of the final equilibrium state. The quantification of chemical disequilibrium, Φ, is the maximum chemical energy that can be extracted from the atmosphere-ocean system that can be used to do work.

We determined the initial state of the atmosphere using the surface mixing ratios from the photochemical model (as described in the previous two sections), while the assumed initial state of the ocean is given in Table 2.1. Unless stated otherwise in Table 2.1, dissolved gas abundances were determined with Henry's law constants derived from NASA's thermodynamic database (Burcat and Ruscic, 2005) and SUPCRT database (Johnson et al., 1992). Additionally, we assumed atmospheric temperature and pressure to be 25°C and 1 bar respectively. Chemical disequilibrium is fairly insensitive to ocean composition, atmospheric pressure and temperature (Krissansen-Totton et al., 2018c); consequently, order of magnitude errors in these assumptions will result in a fairly small error (well within a factor of ~ 2) in the available Gibbs energy.

2.3 Results

2.3.1 Chemical disequilibrium on the prebiotic and chemotrophic Earth

The modeled mixing ratios of H_2, CH_4 and CO for both prebiotic and chemotrophic simulations are shown in Figure 2.1 as a function of the volcanic outgassing multiplier (from Equations (2.1) - (2.3)). All mixing ratios increase with increased volcanic outgassing, and CO in the prebiotic atmosphere increases rapidly. This behavior has been observed in other photochemical modeling studies and has been termed "CO runaway" (Kasting et al., 1983; Zahnle, 1986). The CO consumers in the chemotrophic model prevent "CO runaway". Additionally, $> 95\%$ of the H_2 present in the prebiotic model is converted to CH_4 by methanogens

Table 2.1: Assumed initial atmosphere-ocean composition for the prebiotic and biotic early Earth.

Ocean Species	Molality (mol/kg)	Reference/explanation
Na^+	0.586	Charge balance
Cl^-	0.545	Modern value
SO_4^{2-}	0	(Crowe et al., 2014)
NH_3	6.40×10^{-9}	Henry's law from atmospheric NH_3
NH_4^+	2.9×10^{-6}	Equilibrium with NH_3 and pH
H_2S	0	(Krissansen-Totton et al., 2018c)
pH	6.6 (dimensionless)	(Krissansen-Totton et al., 2018a)
HCO_3^-	0.02674	Equilibrium with CO_2 and pH
CO_3^{2-}	8.03×10^{-5}	Equilibrium with HCO_3^- and pH
Atmospheric Species	**Mixing Ratio**	**Reference/explanation**
NH_3	10^{-10}	Wolf and Toon (2010). Negligible, so not in photochemical model
H_2O	0.025	Global average value
CO_2	0.2	Nominal value (Kadoya et al., 2020; Krissansen-Totton et al., 2018a)

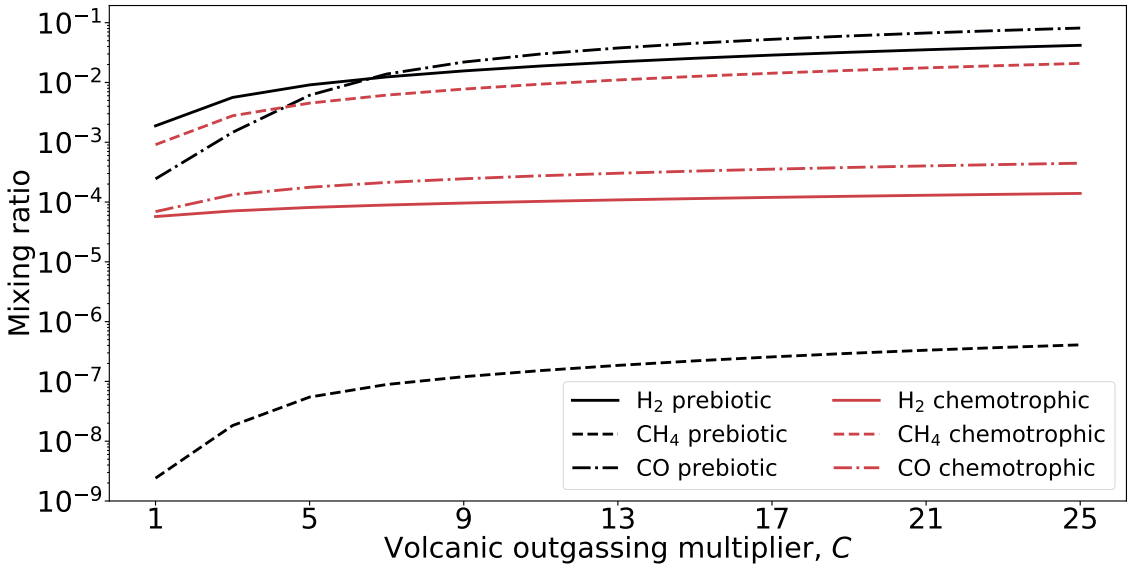

Figure 2.1: The mixing ratio of H_2, CH_4 and CO in the modeled prebiotic and chemotrophic early Earth atmospheres as a function of volcanic outgassing, relative to modern. Black lines represent mixing ratios for the prebiotic case. Red lines represent mixing ratios for the chemotrophic case where we have assumed an energy-limited ocean ecosystem. For both simulations, we also assume the mixing ratios of N_2 and CO_2 are 0.75 and 0.2 respectively. The presence of a chemotrophic biosphere drastically lowers H_2 abundances and increases CH_4 abundances due to methanogenesis, and lowers CO abundances because of acetogenesis.

once we implement the chemotrophic model.

Figure 2.2 shows the modeled atmosphere-ocean thermodynamic disequilibrium for the prebiotic and chemotrophic atmosphere as a function of the volcanic outgassing multiplier. For all outgassing scenarios, the chemotrophic atmosphere-ocean disequilibrium is lower than the prebiotic atmosphere-ocean disequilibrium because the biosphere exploits free energy for metabolism. Additionally, the atmosphere-only disequilibrium is always lower in the chemotrophic ecosystem than in the prebiotic ecosystem for the same reason.

The following sections explain which species contribute most to the available Gibbs energy in both the prebiotic and chemotrophic model.

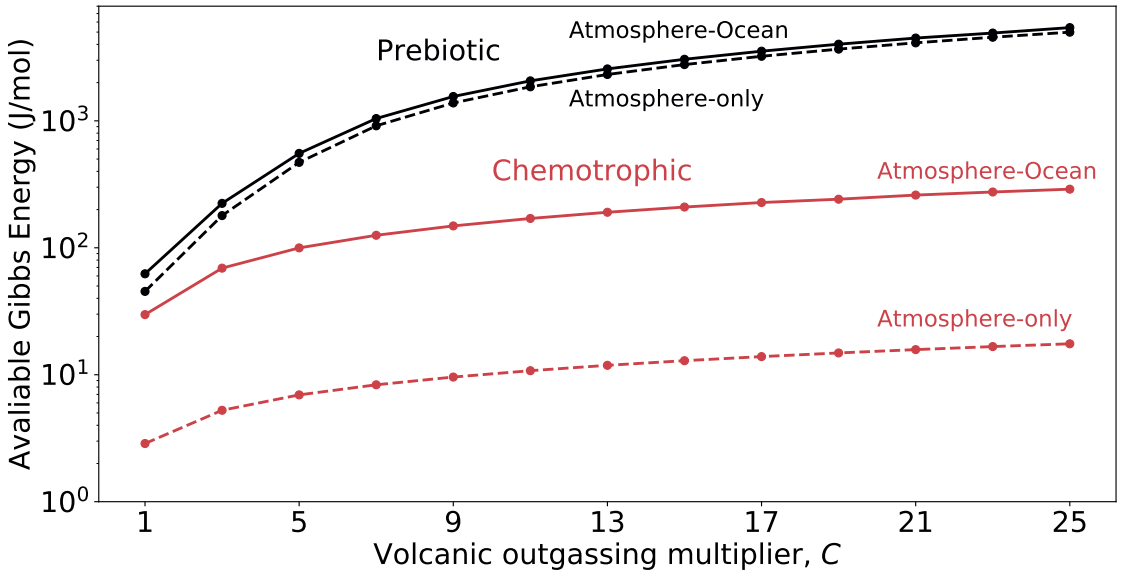

Figure 2.2: Chemical disequilibrium, as measured by available Gibbs energy, of the prebiotic (black lines) and chemotrophic (red lines) Earth as a function of a volcanic outgassing multiplier, relative to modern. The dotted lines are atmosphere-only Gibbs energy calculations, and the solid lines are atmosphere-ocean calculations. The presence of a chemotrophic ecosystem lowers both the atmosphere-ocean and atmosphere-only chemical disequilibrium by using the free energy for metabolism.

2.3.2 The prebiotic disequilibrium and the species that contribute to it

The available Gibbs energy of the prebiotic atmosphere-ocean system for modern volcanic outgassing rates ($C = 1$) is 62 J/mol of atmosphere (compared to 2326 J/mol for the modern biotic Earth (Krissansen-Totton et al., 2016)). The largest source of disequilibrium is due to the coexistence of CO_2 and H_2 which accounts for $\sim$ 40 J/mol (65%) of this total available Gibbs energy. These molecules should react and form CH_4 and water vapor in equilibrium:

$$4H_2 + CO_2 \leftrightarrow CH_4 + 2H_2O \tag{2.10}$$

The coexistence of CO and water vapor contributes $\sim$ 10 J/mol (16%), which is the second most important contributor to this available Gibbs energy. At equilibrium, H_2 and CO_2 will be replaced by CH_4 and CO_2 from the reaction

$$4CO + 2H_2O \leftrightarrow 3CO_2 + CH_4 \tag{2.11}$$

Both the H_2-CO_2 and CO-H_2O disequilibrium ultimately come from volcanic outgassing. Gases were once in equilibrium with magma but have been emitted into a colder environment of the atmosphere where they are in disequilibrium. For higher outgassing scenarios, the H_2-CO_2 and CO-H_2O reactions remain the most import contributors to the available Gibbs energy. Since these reactions are in the gas phase, the atmosphere-only disequilibrium is nearly as large ($\sim$ 80%) as the atmosphere-ocean disequilibrium for all outgassing rates. For a possible Hadean outgassing rate of $C = 9$, Φ is 1555 J/mol.

2.3.3 The chemotrophic disequilibrium and species that contribute to it

The atmosphere-ocean available Gibbs energy of the chemotrophic Earth for modern volcanic outgassing rates ($C = 1$) is 30 J/mol. The coexistence of CO_2, CH_4, N_2, and liquid water contribute $\sim$ 24 J/mol (80%) to this available Gibbs energy. These four species should react and deplete 99.9% of atmospheric methane in equilibrium

$$5CO_2 + 4N_2 + 3CH_4 + 14H_2O \leftrightarrow 8NH_4^+ + 8HCO_3^- \tag{2.12}$$

For volcanic outgassing 25 times modern fluxes ($C = 25$), this reaction accounts for ~ 273 J/mol (94%) of the available Gibbs energy (290 J/mol), which shows that these species are the most important for all modeled chemotrophic systems. The atmosphere-only disequilibrium is always much smaller than the atmosphere-ocean disequilibrium because Equation (2.12) involves disequilibrium with the liquid water ocean.

The H_2-CO_2 and CO-H_2O disequilibria, which dominate the prebiotic available Gibbs energy, contribute only ~ 0.8 J/mol and ~ 2.4 J/mol, respectively, for modern volcanic outgassing ($C = 1$). The minor contribution of these disequilibria persists for all volcanic outgassing scenarios.

2.3.4 Disequilibrium though Earth history

Figure 2.3 shows our estimates of the evolution of Earth's atmosphere-ocean and atmosphere-only disequilibrium through its history. The prebiotic and chemotrophic disequilibrium ranges are from this study (i.e., Figure 2.2), and the estimates from the late Archean to the present are from Krissansen-Totton et al. (2018c). Figure 2.3 has a broken axis between the chemotrophic ecosystem and the Archean because the advent of anoxygenic photosynthesis would have likely influenced how disequilibrium changed between these two eras. Our modeling does not capture this transition for reasons discussed below.

Like the chemotrophic Earth, the Archean disequilibrium was dominated by the coexistence of CO_2, CH_4, N_2, and liquid water (Krissansen-Totton et al., 2018c). After the Great Oxidation Event, the magnitude of the available Gibbs energy rose, and was instead dominated by the coexistence O_2, N_2 and liquid water, which should react to form nitric acid at equilibrium:

$$5O_2 + 2N_2 + 2H_2O \leftrightarrow 4H^+ + 4NO_3^- \tag{2.13}$$

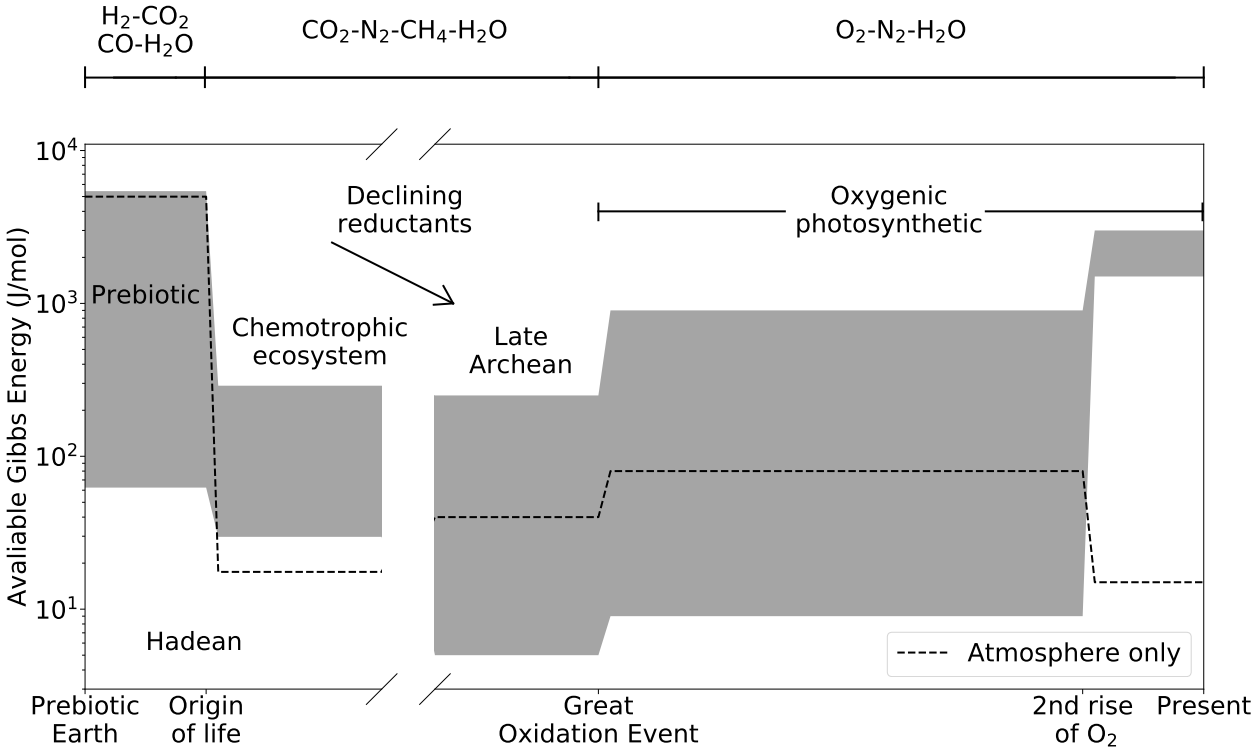

Figure 2.3: The chemical disequilibrium of Earth's atmosphere-ocean system through time. The shading indicates plausible ranges of atmosphere-ocean disequilibrium during intervals of Earth's history based on modeling (this study), and atmospheric proxies and models (Krissansen-Totton et al., 2018c). The plot is broken between the "chemotrophic ecosystem" and "Archean" because the advent of anoxygenic photosynthesis would have likely influenced how disequilibrium changed between these two eras which is uncertain. The dotted line is the maximum atmosphere-only disequilibrium. Above the plot are the disequilibria (e.g., H_2-CO_2) that contribute most to the atmosphere-ocean available Gibbs energy. Throughout Earth's history, disequilibrium fell with the rise of chemotrophic life, and rose after of the oxygenation of Earth's atmosphere from oxygenic photosynthesis.

The magnitude of the O_2-N_2-H_2O disequilibrium increased with the rise of O_2 until the present available Gibbs energy of 2326 J/mol (Krissansen-Totton et al., 2016).

2.4 Discussion

2.4.1 Life's impact on disequilibria through Earth's history

Our results show that life has both generated and destroyed chemical disequilibrium in Earth's atmosphere-ocean system (Figure 2.3). Pioneering work by Lovelock (1975), which proposed using disequilibrium as a sign of life, argued that abiotic worlds would be close to thermodynamic equilibrium. However, this thinking ignored volcanically active planets. We showed that disequilibrium was likely high (10^2 to 10^3 J/mol) in prebiotic times due to the volcanically produced H_2-CO_2 and CO-H_2O disequilibria.

Subsequently, if the first life was chemotrophic and metabolized H_2, CO_2, and CO, then the atmosphere-ocean disequilibrium would have dropped to $\sim 10^2$ J/mol with the rise of microbial life. This is an example of chemotrophic life destroying the disequilibrium of its environment and promoting chemical equilibrium on a global scale.

The invention of anoxygenic photosynthesis, which we did not consider, may have added to the Atmosphere-ocean disequilibrium in the late Archean. Iron oxidizing photosynthesis is an example:

$$4Fe^{2+} + CO_2 + 11H_2O + h\nu \rightarrow 4Fe(OH)_3 + CH_2O + 8H^+ \tag{2.14}$$

The CH_2O produced could have been processed by heterotrophs and methanogens yielding CH_4, which would have added to the Archean CO_2-N_2-CH_4-H_2O disequilibrium without the need for additional volcanic outgassing (Krissansen-Totton et al., 2018c). Additionally, the CH_2O would also degrade into CO in the ocean, which would have added a small amount to the CO-H_2O disequilibrium (Schwieterman et al., 2019). Figure 2.3 does not explicitly capture these effects because the evolutionary history of anoxygenic photosynthesis is uncertain, but Archean disequilibrium estimates allow for such photosynthesis (Krissansen-Totton

et al., 2018c).

Even though the rise of anoxygenic photosynthesis would have added to the late Archean disequilibrium, overall disequilibrium may have dropped because a lower flux of reductants would have been available to the biosphere. Before the rise of oxygenic photosynthesis, which uses ubiquitous water and sunlight, the biosphere is hypothesized to have been probably limited by the available reductants such as H_2, Fe^{2+}, and CO (Canfield et al., 2006). For example, H_2-using anoxygenic phototrophs ($CO_2 + 2H_2 + h\nu \rightarrow CH_2O + H_2O$) were likely limited by volcanically outgassed H_2. Volcanic outgassing of reductants probably declined from the Hadean to the late Archean as the Earth's interior cooled. Fewer available reductants would have lowered biological CH_4 production, resulting in smaller disequilibrium in the late Archean.

The increase of the available Gibbs energy and the rise of the O_2-N_2-H_2O disequilibrium after the Great Oxidation Event was primarily caused by oxygenic photosynthesis. Atmospheric O_2 comes directly from oxygenic photosynthesis, and N_2 is generated, in part, from denitrifying bacteria that are ultimately powered by organic material from photosynthesis. Disequilibrium increased again to near modern levels with a rise of O_2 to near modern levels through the Neoproterozoic and Paleozoic (Krause et al., 2018).

2.4.2 Why disequilibrium persists in Earth's atmosphere-ocean system despite the presence of biology

Chemotrophs consumed a large fraction of Earth's prebiotic disequilibrium (Figure 2.2), but microbes left the CO_2-N_2-CH_4-H_2O and O_2-N_2-H_2O disequilibrium uneaten in the Archean and Proterozoic eons and in modern times. Thus, a pertinent question is: Why didn't microbes evolve metabolisms to consume the "free lunch" that has persisted in Earth's atmosphere?

We propose that this lack of consumption is due to the kinetic barriers of the CO_2-N_2-CH_4-H_2O and O_2-N_2-H_2O reactions, which we hypothesize are insurmountable by enzymes. To illustrate this idea, consider the disequilibrium of O_2-N_2-H_2O. These species would react

slowly in the atmosphere in the absence of life via a number of steps:

$$\begin{aligned} N_2 + 2O &\rightarrow 2NO + 2N \\ 2N + 2O_2 &\rightarrow 2NO + 2O \\ 4NO + 2O_2 &\rightarrow 4NO_2 \\ 4NO_2 + O_2 + 2H_2O &\rightarrow 4HNO_3 \\ 4HNO_3 &\rightarrow 4H^+ + 4NO_3^- \end{aligned} \tag{2.15}$$

The first two reactions, which make NO, are Zeldovich's reactions (Dixon-Lewis, 1984) and require lightning to heat the air to $\sim 20,000$ K (Chameides et al., 1977). The third reaction occurs very quickly after the NO is generated (Murray, 2016). The final two reactions are ultimately (partially) responsible for acid rain (Platt, 1986). The rate limiting step to the net reaction is the first one, which has an activation energy of 316 kJ/mol (Dixon-Lewis, 1984). We take this to be a lower bound on the uncatalyzed activation energy of reacting O_2, N_2 and H_2O. This must be a lower bound because the rate limiting step requires the presence of atomic oxygen, which could only have come from splitting O_2 with additional energy.

Life harnesses the free energy of disequilibria by lowering activation energy barriers with enzymes. Figure 2.4a is a classic textbook graph of free energy during an exothermic chemical reaction. Uncatalyzed reactions can only occur if a relatively large activation energy barrier is overcome. Therefore, many uncatalyzed reactions (between disequilibria) occur extremely slowly because ambient thermal energy is insufficient. Microbes tap into the free energy stored in disequilibria by using enzymes to lower activation energy barriers to levels where thermal energy allows reactions to proceed at appreciable rates.

Figure 2.4b compares the uncatalyzed activation energy of O_2-N_2-H_2O to the uncatalyzed activation energy (blue bars) of reactions that enzymes lower to $\sim$ 30 to 60 kJ/mol, which allow reactions to proceed at normal temperatures. The reaction between O_2, N_2, and H_2O, which is not performed by life, has an activation energy that is higher than all other

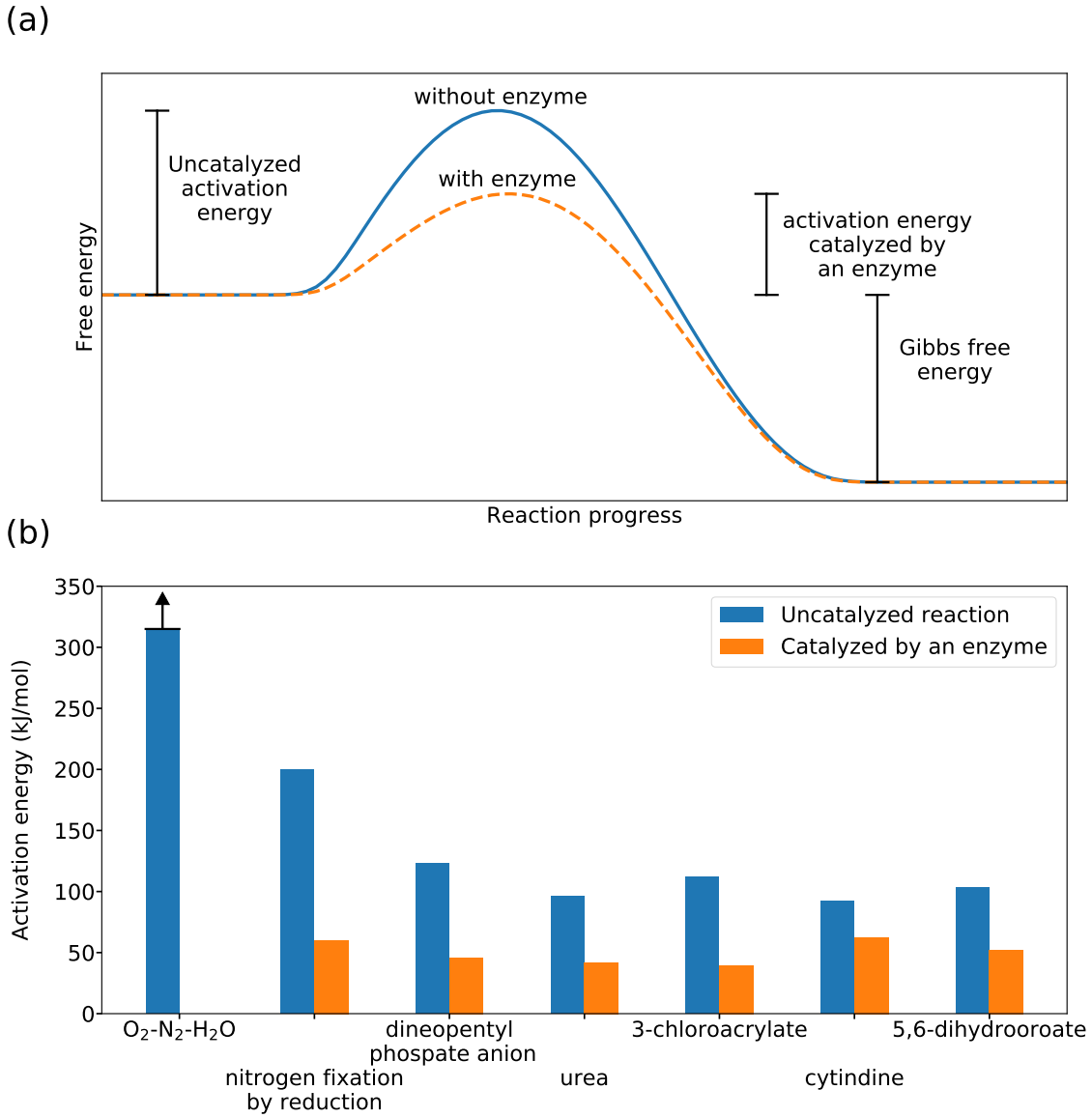

Figure 2.4: (a) Schematic of free energy during a chemical reaction. (b) The activation energy of several uncatalyzed reactions (blue), and reactions catalyzed by enzymes (orange). The lower bound for the uncatalyzed activation energy of O_2-N_2-H_2O (a reaction that life doesn't perform) is from Dixon-Lewis (1984), and the activation energy of nitrogen fixation is from a number of references (Andersen and Shanmugam, 1977; Hageman and Burris, 1980) (see Chapter Appendix 2.6.3 for a summary of our literature search of nitrogen fixation kinetics). The rest of the activation energies are from Table 4 in Wolfenden (2006). The uncatalyzed activation energy of O_2-N_2-H_2O is notably larger than the uncatalyzed activation energy of reactions that life manages to perform, which we hypothesize explains why no life has evolved that can exploit the O_2-N_2-H_2O disequilibrium.

uncatalyzed reactions. This suggests that Reaction (2.13) is not amenable to biological catalysis. The activation energy of O_2-N_2-H_2O is probably high because it involves breaking the triple bond in $N \equiv N$ by oxidation. The reaction between CO_2, N_2, CH_4, and H_2O (Equation (2.12)) also involves breaking an N_2 bond, so it potentially has an activation energy comparable to Reaction (2.13) (> 300 kJ/mol).

Nitrogen fixing bacteria are the only organisms that break $N \equiv N$ bonds by chemical reduction with the aid of the nitrogenase enzyme. The literature suggests that the uncatalyzed activation energy of nitrogen fixation by reduction is ~ 200 kJ/mol (Hageman and Burris, 1980), which is $< 63\%$ of the uncatalyzed activation energy of Reaction (2.13). These differing energy barriers might explain why biology has managed to catalyze nitrogen fixation by reduction of N_2 but not by direct oxidation of N_2.

In summary, we speculate that life has not evolved to consume the CO_2-N_2-CH_4-H_2O and O_2-N_2-H_2O disequilibrium because these reactions are kinetically insurmountable for biology. We hypothesize that these reactions will be biochemically prohibited elsewhere on Earth-like exoplanets, which is a testable hypothesis (Section 2.4.4).

2.4.3 Chemical disequilibrium as a biosignature or anti-biosignature

Throughout Earth's history, the available Gibbs energy of the atmosphere-ocean system varied substantially (Figure 2.3), and there is no one-to-one relationship between the magnitude of Gibbs energy and the presence of life. In both prebiotic and modern times, the atmosphere-ocean disequilibrium was relatively large ($\sim$ 1000s J/mol), so high disequilibrium alone is not a reliable sign of life. Lower disequilibrium ($\sim$ 100s) is also an ambiguous biosignature on its own because there were large spans of Earth's inhabited history when disequilibrium was comparable to the available Gibbs energy of Mars' atmosphere (136 J/mol) (Krissansen-Totton et al., 2016).

However, disequilibrium is useful to determine the presence or absence of life if you know which particular species are responsible for the disequilibrium. The species causing the prebiotic and modern disequilibrium are different even though the magnitude of disequilibrium

is similar. Before life appeared, atmospheric disequilibrium was dominated by H_2-CO_2, and CO-H_2O, while today the most important disequilibrium is O_2-N_2-H_2O.

Thus, biosignatures and anti-biosignatures arise from looking at both the magnitude of disequilibrium and how "edible" the disequilibrium gas mixture is, where "edibility" is associated with a low activation energy. An atmosphere-ocean with "edible" disequilibrium is an anti-biosignature because it is a sign that life is not consuming disequilibria that has kinetic barriers that are easily biologically surmountable (Table 2.2). One example is the prebiotic Earth, which likely had large amounts of "edible" free energy from the H_2-CO_2 and CO-H_2O disequilibria. If chemotrophs were present, these "edible" disequilibria would mostly be destroyed.

A separate example of an anti-biosignature is Mars' atmosphere, which has a fairly large available Gibbs energy ($\sim$ 136 J/mol) mostly because of photochemically produced CO and O_2 (Krissansen-Totton et al., 2016). This free energy could be consumed by aerobic carboxydotrophic organisms (Sholes et al., 2019). If a substantial biosphere were present, then it would consume this "edible" free lunch because a known enzyme (aerobic CO dehydrogenase) makes CO readily consumable with an activation energy ranging $\sim$ 20 to 95 kJ/mol (King, 2013; Xie et al., 2009). Strictly speaking, then, an anti-biosignature provides an upper limit on biomass (Sholes et al., 2019).

An atmosphere-ocean with primarily "inedible" disequilibrium (with an insurmountable activation energy barrier) is a biosignature (top right of Table 2.2). In this case, chemotrophs have consumed most of the "edible" free energy produced by geology or photosynthesis (if present) and have left "inedible" redox couples untouched. Some small amount of "edible" disequilibrium will always remain, because gas fluxes from the atmosphere into habitable bodies of water will be limited by the water boundary layer (Liss and Slater, 1974). The magnitude of the "inedible" disequilibrium should be larger if phototrophs are present. While life has been present on Earth, the coexistence of "inedible" CO_2-N_2-CH_4-H_2O or O_2-N_2-H_2O has persisted in Earth's atmosphere-ocean system (Figure 2.3), and "edible" disequilibrium has been absent because of chemotrophs.

Table 2.2: Chemical disequilibrium as a biosignature and anti-biosignature.

	Primarily "edible" disequilibria (low activation energy)	Primarily "inedible" disequilibria (high activation energy)
Atmosphere-ocean in disequilibrium	**Anti-biosignature** The presence of uneaten "edible" food should be consumed by biology.	**Biosignature** Life has consumed most of the "edible" food produced by geology and photosynthetic life (if present) and has left the "inedible" food untouched. The magnitude of the "inedible" disequilibrium should be larger if phototrophs are present, and smaller if only chemotrophs are present.
Atmosphere-ocean near equilibrium	**Anti-biosignature** Although chemotrophic life destroys disequilibrium, it is unlikely to drive a system to complete thermodynamic equilibrium. Chemotrophic metabolisms produce waste gases that are "inedible," so they leave some fraction of a planet's disequilibrium unconsumed. Therefore, a planet near equilibrium instead will be characterized by small abiotic disequilibrium resulting from photochemistry or small volcanic fluxes, if volcanism is present. The planet is very likely uninhabited although an extremely meager, undetectable biosphere cannot be excluded.	

A planet very near thermodynamic equilibrium most likely does not have life (lower row of Table 2.2). Although chemotrophs destroy disequilibrium, they did not drive Earth's atmosphere-ocean system to complete equilibrium in the Archean. Chemotrophs on Earth produce waste gas such as CH_4 (Equation (2.4)) that ultimately contribute to disequilibria and therefore life is unable to destroy all atmospheric disequilibrium.

The difference between the upper left and lower row of Table 2.2 is a question of degree. The upper left represents an anti-biosignature applicable to a large disequilibrium, such as prebiotic Earth $\sim$ 103 J/mol or of modern Mars $\sim$ 102 J/mol. In contrast, the lower row of Table 2.2 is applicable to a planet such as Venus, where the near-surface temperature drives the atmosphere very close to equilibrium with a disequilibrium of 0.06 J/mol (Krissansen-Totton et al., 2016). Also in this category are giant planets, such as Jupiter, where deep convective mixing produces a gas mixture very near chemical equilibrium ($\sim$ 0.001 and the small disequilibrium is purely photochemical.)

Some biospheres that are nutrient-limited (e.g., limited by fixed N or P) may not follow Table 2.2. For example, a nutrient-limited chemotrophic biosphere may not be able to consume all of the "edible" disequilibrium in the atmosphere. In this case, sizable "edible" disequilibrium might coexist with life, which contradicts the upper-left panel of Table 2.2. Most literature has argued that the pre-photosynthetic Earth was probably energy-limited (not nutrient-limited) (Canfield et al., 2006; Kharecha et al., 2005; Ward et al., 2019), therefore it might be reasonable to expect other purely chemotrophic biospheres to be energy-limited.

There are some cases where even a productive biosphere can coexist with edible atmospheric disequilibrium. This is because there are limits to how quickly gases can be transported from the atmosphere, into the ocean where they can be consumed by life (Kharecha et al., 2005). For example, consider a planet with a very large volcanic CO flux (e.g. 100$\times$ modern). CO could build up in this planet's atmosphere even if CO consumers were present in an ocean, because CO transport from the atmosphere to the ocean would not be sufficient to maintain low atmospheric CO (Schwieterman et al., 2019). While coexistence of productive biospheres and edible disequilibrium is conceivable, it might be unlikely on exoplanets,

given that it probably did not occur during all of Earth's history (Figure 2.3).

These aforementioned caveats to Table 2.2 highlights the importance of inferring fluxes of gases to further evaluate disequilibrium biosignatures (Krissansen-Totton et al., 2018c; Simoncini et al., 2013). The indicator of biology is a surface flux of gases not explained by geology, although the atmospheric composition resulting from a biological flux depends on many factors like the host star's spectrum, or volcanic outgassing rates (Segura et al., 2005). Therefore, it makes sense to infer surface fluxes of disequilibrium gases and then compare inferred fluxes to dead processes. Fluxes unexplained by dead processes are evidence for life. Detailed consideration of fluxes is beyond the scope of this paper.

2.4.4 Detecting the prebiotic Earth disequilibrium anti-biosignature

The prebiotic disequilibrium anti-biosignature is, in principle, remotely detectable on exoplanets. Strong spectral signatures of atmospheric CO_2, CO and H_2O exist, and could be detected with reflectance or transmission spectroscopy (see Table 3 in Catling et al. (2018)). The presence of prebiotic H_2 could be inferred with its spectral feature at 2.12 μm, or its continuous features in the near-infrared and < 0.08 μm. H_2 could also be detected by combining several spectral methods. Ultraviolet transmission spectroscopy can be used to observe hydrogen escape because hydrogen absorbs stellar Lyman-alpha. This has been done for warm Neptunes (Ehrenreich et al., 2015), and could be done for Earth sized planets with future telescopes (Fujii et al., 2018). If CH_4 and stratospheric H_2O were ruled out with transmission spectroscopy, then the hydrogen escape must result from H_2 in the atmosphere.

2.5 Conclusions

Given our current knowledge of photochemistry and Earth's Hadean atmosphere, we calculate that Earth's prebiotic atmosphere was in thermodynamic chemical disequilibrium due primarily to volcanic outgassing, and that the advent of chemosynthetic life destroyed much of this disequilibrium through its metabolism. Subsequently, disequilibrium rose for the rest of Earth's history primarily because oxygenic photosynthesis maintained high O_2 and N_2

levels, directly and indirectly, respectively.

In the prebiotic era, volcanically produced H_2-CO_2 and CO-H_2O were the largest contributors to the atmosphere-ocean available Gibbs energy. After the origin of life, chemotrophs consumed most of the prebiotic free energy, although the atmosphere-ocean system remained in disequilibrium because of biological waste gases: CO_2, CH_4, N_2 and liquid water. After the Great Oxidation Event, the magnitude of the available Gibbs energy rose, and was instead dominated by O_2, N_2 and liquid water.

Earth's history reveals a different relationship between life and atmospheric chemical disequilibrium than was first proposed by Lovelock (1965). Lovelock (1965) argued that planets with life should be in disequilibrium and that dead worlds should be near equilibrium, although we have shown that this was not true and was subtler for the first billion years of Earth history.

We suggest that chemotrophs never evolved to consume the CO_2-N_2-CH_4-H_2O disequilibrium prior to atmospheric oxygenation and O_2-N_2-H_2O disequilibrium after oxygenation because the reaction of these groups of species has insurmountable activation energy barriers. In contrast, the reactions between H_2 and CO_2 or CO and H_2O have activation energy barriers that can be lowered by enzymes, so that these redox couples readily support microbial metabolisms.

The large prebiotic "edible" disequilibrium between H_2 and CO_2 or CO and H_2O is therefore an anti-biosignature because these easily metabolized species should be consumed by chemotrophs. A planet that is dominated by "inedible" disequilibria such as CO_2-N_2-CH_4-H_2O or O_2-N_2-H_2O has signs of biology because these disequilibria show that life has consumed most the "edible" food produced by abiotic processes and has created "inedible" disequilibria with continuous fluxes of waste gases.

The mere detection of "edible" or "inedible" disequilibria is not a definitive sign of the presence or absence of life. A full evaluation of disequilibria would compare inferred surface fluxes of disequilibrium gases to plausible abiotic surface fluxes, which is further work beyond the focus of the present paper.

2.6 Chapter Appendix

2.6.1 Volcanic outgassing fluxes

One input for the model of photochemistry coupled to a microbial ecosystem is the flux of volcanic outgassing. Here we describe how plausible prebiotic volcanic fluxes are calculated.

We assume that gases emitted by a volcanic melt achieve thermodynamic equilibrium. The reactions governing equilibrium of volcanic gases are

$$\mathrm{H_2O} \leftrightarrow \mathrm{H_2} + \frac{1}{2}\mathrm{O_2} \tag{2.16}$$

$$\mathrm{CO_2} \leftrightarrow \mathrm{CO} + \frac{1}{2}\mathrm{O_2} \tag{2.17}$$

$$\mathrm{CO_2} + 2\mathrm{H_2O} \leftrightarrow \mathrm{CH_4} + 2\mathrm{O_2} \tag{2.18}$$

$$\mathrm{SO_2} + \mathrm{H_2O} \leftrightarrow \mathrm{H_2S} + \frac{3}{2}\mathrm{O_2} \tag{2.19}$$

At equilibrium, the ratios of the fugacities of volatile species (denoted f_x) are related to the equilibrium constant corresponding to each chemical reaction. The fugacities of each species are well approximated by magma chamber partial pressures (denoted P_x) because we consider low pressures and high temperatures (5 bar and 1473 K, following Holland (1984)), so non-ideal corrections can be ignored.

$$K_1 = \frac{f_{\mathrm{H_2}} f_{\mathrm{O_2}}^{0.5}}{f_{\mathrm{H_2O}}} = \frac{P_{\mathrm{H_2}} f_{\mathrm{O_2}}^{0.5}}{P_{\mathrm{H_2O}}} \tag{2.20}$$

$$K_2 = \frac{f_{\mathrm{CO}} f_{\mathrm{O_2}}^{0.5}}{f_{\mathrm{CO_2}}} = \frac{P_{\mathrm{CO}} f_{\mathrm{O_2}}^{0.5}}{P_{\mathrm{CO_2}}} \tag{2.21}$$

$$K_3 = \frac{f_{\mathrm{CH_4}} f_{\mathrm{O_2}}^{2}}{f_{\mathrm{CO_2}} f_{\mathrm{H_2O}}^{2}} = \frac{P_{\mathrm{CH_4}} f_{\mathrm{O_2}}^{2}}{P_{\mathrm{CO_2}} P_{\mathrm{H_2O}}^{2}} \tag{2.22}$$

$$K_4 = \frac{f_{\mathrm{H_2S}} f_{\mathrm{O_2}}^{1.5}}{f_{\mathrm{SO_2}} f_{\mathrm{H_2O}}} = \frac{P_{\mathrm{H_2S}} f_{\mathrm{O_2}}^{1.5}}{P_{\mathrm{SO_2}} P_{\mathrm{H_2O}}} \tag{2.23}$$

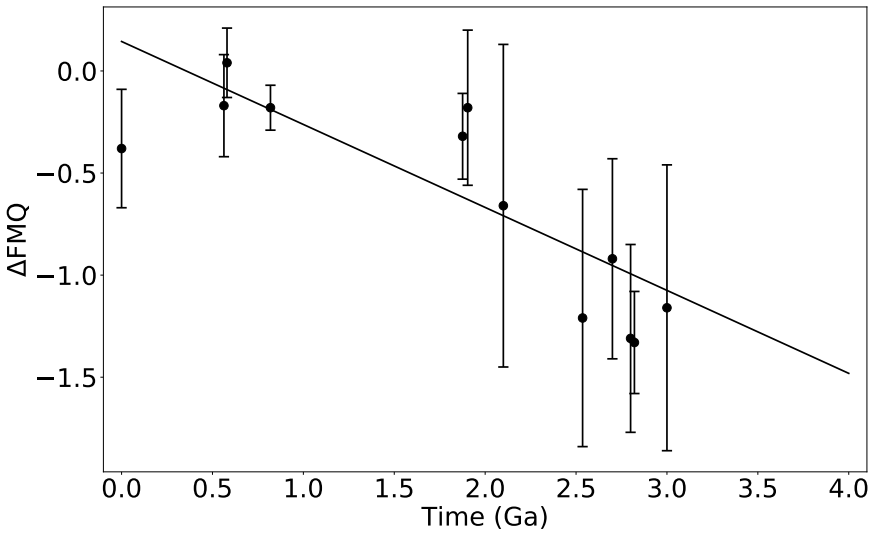

Figure 2.5: Weighted linear fit of mantle redox proxies from Aulbach and Stagno (2016). At 4 Ga, the linear fit predicts $\log_{10}(f_{O_2}) = \text{FMQ} - 1.48$.

We calculate equilibrium constants for temperature $T = 1473$ K using the NASA thermodynamic database (Burcat and Ruscic, 2005). Additionally, we estimate the oxygen fugacity (f_{O_2}) of prebiotic volcanic gases by a linear regression through data obtained from Aulbach and Stagno (2016) (Figure 2.5). We take $\log_{10}(f_{O_2}) = \text{FMQ} - 1.48$ at 4.0 Ga as a prebiotic value. At the temperatures and pressures we consider ($T = 1473$ K and $P = 5$ bar), $\log_{10}(\text{FMQ}) = -8.47$, our Gibbs energy calculations are fairly insensitive to the chosen oxygen fugacity at 4 Ga. Changing the oxygen fugacity by 1 log unit changes our calculated Gibbs energy results by a factor of ~ 2 (See Chapter Appendix 2.6.2).

We also assume that the ratio of carbon to hydrogen (χ_C), and sulfur to hydrogen (χ_S) in volcanic gases has remained constant through Earth's history. This is a reasonable assumption because these ratios depend most on the pressure of degassing (Gaillard and Scaillet, 2014), i.e., the atmospheric pressure into which the gases are released, and atmospheric pressure has probably has not changed by orders of magnitude over Earth's history (Som et al., 2012).

Table 2.3: Modern mantle-sourced volcanic outgassing fluxes and ratios

Modern Volcanic Fluxes ($\frac{\text{Tmol}}{\text{yr}}$)							Total Modern Fluxes ($\frac{\text{Tmol}}{\text{yr}}$)			Ratios	
CO_2	H_2O	SO_2	H_2	CO	CH_4	H_2S	$F^{\text{mod}}_{\text{hydrogen}}$	$F^{\text{mod}}_{\text{carbon}}$	$F^{\text{mod}}_{\text{sulfur}}$	χ_{C}	χ_{S}
8.5	95	1.8	2.0	0.25	0	0.03	97.03	8.75	1.83	0.090	0.019

Note - Fluxes of CO_2, H_2O, SO_2, and H_2S are from Catling and Kasting (2017) p. 203 and p. 212. Fluxes of H_2, CO, and CH_4 are calculated using equilibrium (e.g., Equation (2.20) with Equation (2.29)) and assuming $T = 1473$ K, $P = 5$ bar, and $\log_{10}(f_{O_2}) = \text{FMQ}$. The total modern fluxes (F^{mod}_x), and ratios χ_{C} and χ_{S} are calculated using the modern outgassing fluxes. Methods for this calculation are detailed in the text.

$$\frac{P_{CO_2} + P_{CO} + P_{CH_4}}{P_{H_2} + P_{H_2O} + 2P_{CH_4} + P_{H_2S}} = \chi_{\text{C}} \tag{2.24}$$

$$\frac{P_{H_2S} + P_{SO_2}}{P_{H_2} + P_{H_2O} + 2P_{CH_4} + P_{H_2S}} = \chi_{\text{S}} \tag{2.25}$$

We calculate χ_{C} and χ_{S} using modern values of total volcanic outgassing which we take from Catling and Kasting (2017), Chapter 7 (their Table 7.1). The total fluxes of hydrogen, carbon and sulfur are given by summing all species weighted by the number of atoms each species contains (e.g. $F_{H_2} + F_{H_2O} + 2F_{CH_4} + F_{H_2S} = F^{\text{mod}}_{\text{hydrogen}}$). The ratios of total fluxes are then calculated in the following way:

$$\chi_{\text{C}} = \frac{F^{\text{mod}}_{\text{carbon}}}{F^{\text{mod}}_{\text{hydrogen}}} \tag{2.26}$$

$$\chi_{\text{S}} = \frac{F^{\text{mod}}_{\text{sulfur}}}{F^{\text{mod}}_{\text{hydrogen}}} \tag{2.27}$$

Modern fluxes, and ratios are given in Table 2.3. We also assume that the partial pressures sum to the magma chamber total pressure:

$$P_{H_2} + P_{H_2O} + P_{CH_4} + P_{H_2S} + P_{SO_2} + P_{CO_2} + P_{CO} = P \tag{2.28}$$

Equations (2.20) - (2.25) and (2.28) are a system of 7 equations with 7 unknown partial

pressures (P_{H_2}, P_{H_2O}, etc.), which can be solved with some algebraic manipulation.

With the partial pressures in hand, we can calculate plausible prebiotic volcanic outgassing fluxes with another system of equations:

$$\frac{F_{H_2}}{F_{H_2O}} = \frac{P_{H_2}}{P_{H_2O}} \tag{2.29}$$

$$\frac{F_{CO}}{F_{CO_2}} = \frac{P_{CO}}{P_{CO_2}} \tag{2.30}$$

$$\frac{F_{CH_4}}{F_{CO_2}} = \frac{P_{CH_4}}{P_{CO_2}} \tag{2.31}$$

$$\frac{F_{H_2S}}{F_{SO_2}} = \frac{P_{H_2S}}{P_{SO_2}} \tag{2.32}$$

$$F_{H_2} + F_{H_2O} + 2F_{CH_4} + F_{H_2S} = F_{\text{hydrogen}} \tag{2.33}$$

$$F_{CO_2} + F_{CO} + F_{CH_4} = F_{\text{carbon}} \tag{2.34}$$

$$F_{SO_2} + F_{H_2S} = F_{\text{sulfur}} \tag{2.35}$$

The first four equations come from assuming that ratios between volcanic fluxes are equal to the corresponding ratios of the partial pressures. The final three equations are sums of the total hydrogen, carbon and sulfur fluxes weighted by the number of atoms in each species.

The total flux of each species (e.g. F_{hydrogen}) on the prebiotic Earth is uncertain and depends on the tectonic regime and its association with outgassing. If the Earth lacked plate tectonics and was in a "stagnant lid" regime, then heat fluxes could have been the same as modern fluxes despite a much warmer mantle (Korenaga, 2009). On the other hand, if plate tectonics or some similar precursor was active in the Hadean, heat fluxes on the 4 Ga Earth could have been 5 times higher than today's fluxes (Sleep and Zahnle, 2001). Volcanic outgassing can be related to heat flow with a power law.

$$F_x = F_x^{\text{mod}} Q^n \tag{2.36}$$

Here, Q is heat flow normalized to present, F_x is the outgassing flux of species x, and n is

between 1 and 2 (Krissansen-Totton et al., 2018a). Taking 5 and 1 for upper and lower bounds for heat flow (Q) at 4 Ga, respectively, and conservatively taking $n = 2$ gives outgassing rates between 1 and 25 times modern outgassing rates. We adopt this large range here to calculate F_{hydrogen}, F_{carbon}, and F_{sulfur}:

$$F_{\text{hydrogen}} = CF^{\text{mod}}_{\text{hydrogen}} \tag{2.37}$$

$$F_{\text{carbon}} = CF^{\text{mod}}_{\text{carbon}} \tag{2.38}$$

$$F_{\text{sulfur}} = CF^{\text{mod}}_{\text{sulfur}} \tag{2.39}$$

Here, C is the outgassing multiplier, which we vary between 1 and 25 to capture the most likely outgassing scenarios on the prebiotic Earth. Equations (2.29) - (2.35) are a system of 7 linear equations with 7 unknown volcanic fluxes (e.g. F_{H_2}), which can be reorganized and solved with matrix inversion. We solve this system for outgassing parameters (C) between 1 and 25, which yields a range of outgassing fluxes for each of each of the 7 species.

2.6.2 Photochemical modeling and Gibbs energy minimization

Photochemical modeling

Table 2.4 and Table 2.5 contains most of the boundary conditions used for modeling the prebiotic and chemosynthetic atmospheres respectively with the *Atmos* photochemical model. All species that are not listed in Table 2.4 and Table 2.5 that are in the *Atmos* code, have deposition velocities set to zero.

Photochemistry depends on the temperature and H_2O mixing ratio in the atmosphere (Figure 2.6). We acquire temperature and H_2O profiles by coupling the Atmos photochemical code with the Atmos 1-D radiative-convective climate model. This is done by running the photochemical code, then using its output as input for the climate model. The temperature and H_2O output of the climate model is then used as input for the photochemical code.

Table 2.4: Prebiotic boundary conditions.

Chemical Species	Deposition Velocity (cm s^{-1})	Mixing Ratio	Flux (molecules cm^{-2} s^{-1})
O	1.0	-	-
O_2	1.4×10^{-4}	-	-
H_2O	0.0	-	-
H	1.0	-	-
OH	1.0	-	-
HO_2	1.0	-	-
H_2O_2	2.0×10^{-1}	-	-
H_2	0.0	-	variable
CO	10^{-8}	-	variable
HCO	1.0	-	-
H_2CO	2.0×10^{-1}	-	-
CH_4	0.0	-	0.0
CH_3	1.0	-	-
C_2H_6	0.0	-	-
NO	3.0×10^{-4}	-	-
NO_2	3.0×10^{-3}	-	-
HNO	1.0	-	-
O_3	7.0×10^{-2}	-	-
HNO_3	2.0×10^{-1}	-	-
H_2S	2.0×10^{-2}	-	variable
SO_3	0.0	-	-
S_2	0.0	-	-
HSO	1.0	-	-
H_2SO_4	1.0	-	-
SO_2	1.0	-	variable
SO	0.0	-	-
H_2SO_4 aerosol	10^{-2}	-	-
S_8 aerosol	10^{-2}	-	-
hydrocarbon aerosol	10^{-2}	-	-
CO_2	-	2.0×10^{-1}	-

Note - Deposition velocities follow those used by Kharecha et al. (2005) and Schwieterman et al. (2019). All species in the photochemical model not listed here have zero deposition velocities. We assume that N_2 is a filler gas.

Table 2.5: Boundary conditions for the chemotrophic ecosystem model.

Chemical Species	Deposition Velocity (cm s^{-1})	Mixing Ratio	Flux (molecules cm^{-2} s^{-1})
O	1.0	-	-
O_2	1.4×10^{-4}	-	-
H_2O	0.0	-	-
H	1.0	-	-
OH	1.0	-	-
HO_2	1.0	-	-
H_2O_2	2.0×10^{-1}	-	-
H_2	-	variable	-
CO	1.2×10^{-4}	-	variable
HCO	1.0	-	-
H_2CO	2.0×10^{-1}	-	-
CH_4	-	variable	-
CH_3	1.0	-	-
C_2H_6	0.0	-	-
NO	3.0×10^{-4}	-	-
NO_2	3.0×10^{-3}	-	-
HNO	1.0	-	-
O_3	7.0×10^{-2}	-	-
HNO_3	2.0×10^{-1}	-	-
H_2S	2.0×10^{-2}	-	variable
SO_3	0.0	-	-
S_2	0.0	-	-
HSO	1.0	-	-
H_2SO_4	1.0	-	-
SO_2	1.0	-	variable
SO	0.0	-	-
H_2SO_4 aerosol	10^{-2}	-	-
S_8 aerosol	10^{-2}	-	-
hydrocarbon aerosol	10^{-2}	-	-
CO_2	-	2.0×10^{-1}	-

Note - Deposition velocities follow those used by Kharecha et al. (2005) and Schwieterman et al. (2019). All species in the photochemical model not listed here have zero deposition velocities. We assume that N_2 is a filler gas.

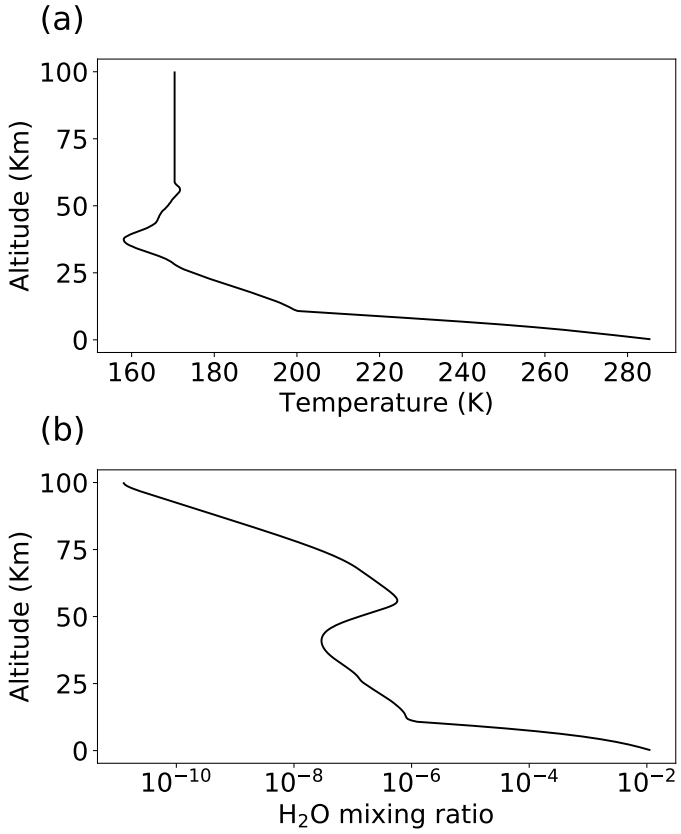

Figure 2.6: (a) Temperature profile and (b) H_2O profile used for every simulation in this study.

This coupling is continued until convergence is reached. We only couple the photochemical-climate code for the lowest volcanic outgassing scenario ($C = 1$) in the prebiotic case and use the resulting H_2O and temperature profiles for all simulations. Using the climate code for each simulation independently did not change the results significantly. The temperature and H_2O profile used in this study is shown in Figure 2.6.

Currently, the open-source version of *Atmos* has several rate constants which are inappropriately "zeroed." We updated these rate constants to their proper values following Harman et al. (2015). Table 2.6 shows a list of the updated rate constants.

All of our models include the modern production rate of NO from lightning, although

Table 2.6: Updated reaction rates for *Atmos*.

Rx #	Reaction	Rate (s^{-1})
61	$^3CH_2 + H_2 \rightarrow CH_3 + H$	5×10^{-14}
62	$^3CH_2 + CH_4 \rightarrow CH_3 + CH_3$	$6.1 \times 10^{12} \exp\left(\frac{-5051}{T}\right)$
116	$SO + HO_2 \rightarrow SO_2 + OH$	2.8×10^{-11}
123	$HSO_3 + OH \rightarrow H_2O + SO_3$	10^{-11}
124	$HSO_2 + H \rightarrow H_2 + SO_3$	10^{-11}
125	$HSO_2 + O \rightarrow OH + SO_3$	10^{-11}
130	$HS + O_2 \rightarrow OH + SO$	4×10^{-19}
143	$HS + H_2CO \rightarrow H_2S + HCO$	$1.7 \times 10^{-11} \exp\left(\frac{-800}{T}\right)$
163	$SO_2 + HO_2 \rightarrow SO_3 + OH$	10^{-18}
169	$S + CO_2 \rightarrow SO + CO$	10^{-20}
170	$SO + HO_2 \rightarrow HSO + O_2$	2.8×10^{-11}
174	$HSO + NO \rightarrow HNO + SO$	10^{-15}

Note - All updated reaction rates are taken from Harman et al. (2015). Harman et al. (2015) incorrectly lists the rate for Rx #169. Here, T is temperature in Kelvin.

this does not affect our results significantly. Every simulation uses the Sun's spectrum at 4 Ga calculated using the "Youngsun" routine (Claire et al., 2012).

Chemical disequilibrium calculation with Gibbs energy minimization

For each modeled prebiotic and biotic atmosphere, we calculate the atmosphere-ocean chemical disequilibrium with Gibbs energy minimization. Figure 2.7 and Figure 2.8 illustrate this calculation for the lowest volcanic outgassing scenario (outgassing multiplicative factor $C = 1$) for the prebiotic and biotic Earth respectively. For both figures, the blue bars are the initial or observed concentration of the atmosphere that we generated with the *Atmos* photochemical code. The red bars are the concentrations for the atmosphere-ocean system at chemical equilibrium.

The chemical reactions that contribute most to the chemical disequilibrium are apparent in Figure 2.7 and Figure 2.8. The main disequilibria in the prebiotic atmosphere are H_2-CO_2 and CO-H_2O. Figure 2.7 shows that the atmosphere at equilibrium has much less H_2 and

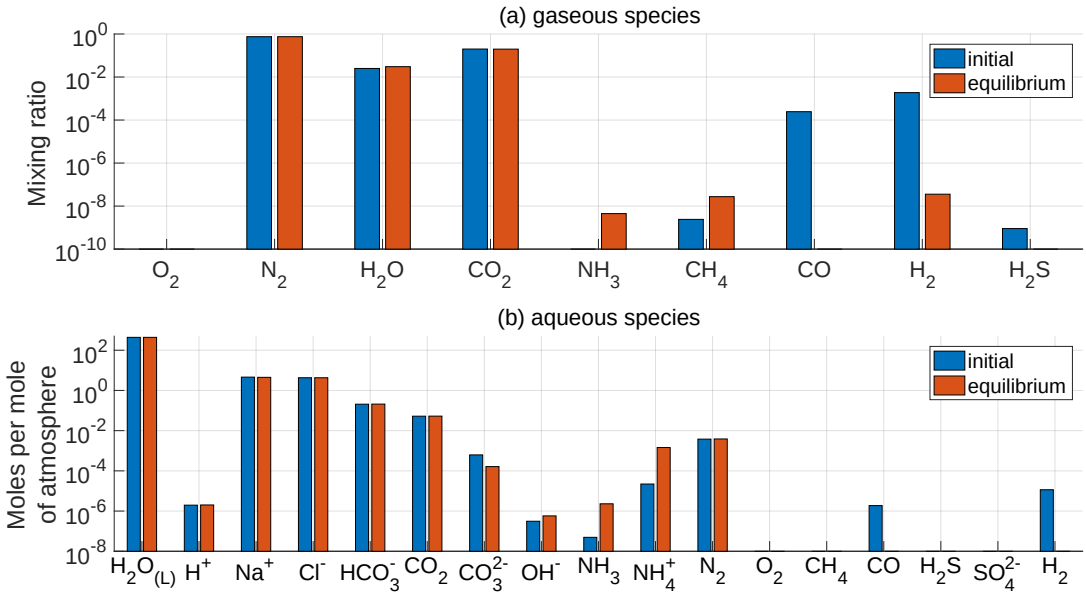

Figure 2.7: Atmosphere-ocean disequilibrium calculation for the prebiotic Earth (minimum outgassing scenario). Blue bars show the modeled atmosphere and ocean composition. Red bars show what happens to the species when thermodynamic equilibrium is imposed. (a) Shows all gas phase species, whereas (b) shows all aqueous species.

CO than the initial state. Additionally, the chemotrophic Earth's main disequilibrium was CO_2-N_2-CH_4-H_2O, which can be seen in Figure 2.8 because the equilibrium state has much less CH_4 than the initial state.

Sensitivity of chemical disequilibrium calculations to oxygen fugacity

Figure 2.9 shows that chemical disequilibrium is fairly insensitive to the mantle oxygen fugacity. Chemical disequilibrium, as measured by Gibbs energy, is plotted for the lowest volcanic outgassing scenario ($C = 1$) as a function of oxygen fugacity. Changing the oxygen fugacity by 1 log unit changes the calculated Gibbs energy results by a factor of ~ 2 (Figure 2.9). This effect is small compared to the uncertainty in volcanic outgassing rates, so it seems reasonable to ignore it.

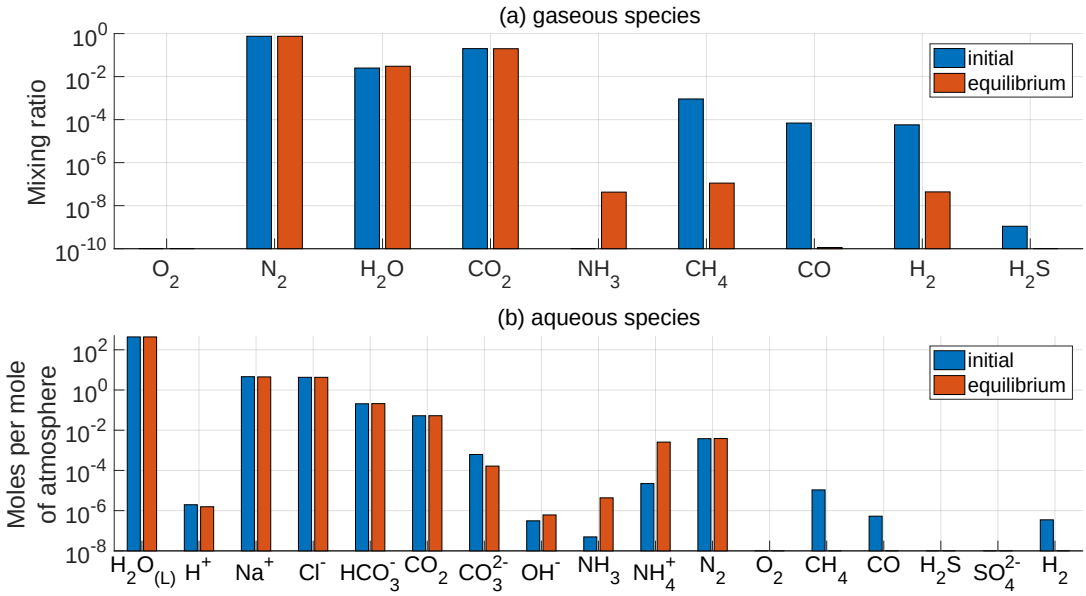

Figure 2.8: Atmosphere-ocean disequilibrium calculation for the chemotrophic Earth (minimum outgassing scenario). Blue bars show the modeled atmosphere and ocean composition. Red bars show what happens to the species when thermodynamic equilibrium is imposed. (a) Shows all gas phase species, whereas (b) shows all aqueous species.

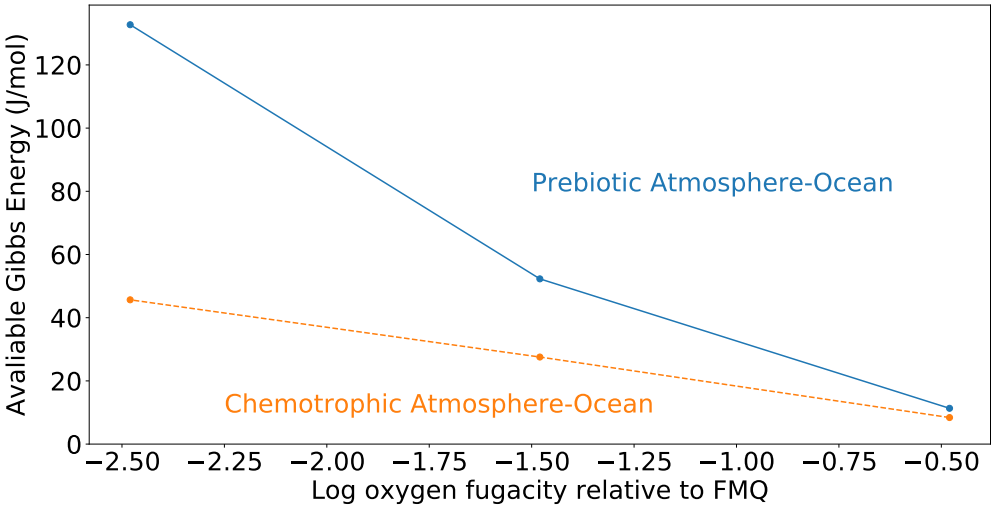

Figure 2.9: The effect of oxygen fugacity on the calculated available Gibbs energy for a volcanic outgassing coefficient for prebiotic Earth and after the advent of a chemotrophic biosphere. A change in 1 log unit in oxygen fugacity changes the calculated available Gibbs energy by a factor of ~ 2.

2.6.3 Uncatalyzed activation energy of nitrogen fixation

We suggest that life did not evolve to consume the O_2-N_2-H_2O and CO_2-N_2-CH_4-H_2O disequilibria because reactions of gases in these disequilibria have biologically insurmountable kinetic barriers. To substantiate this argument, we compare the uncatalyzed activation energy of O_2-N_2-H_2O (> 316 kJ/mol) to the uncatalyzed activation energy of nitrogen fixation reduction, because nitrogen fixation by reduction is arguably the most kinetically difficult reaction that biology has managed to catalyze. The net nitrogen fixation by reduction reaction is

$$3H_2 + H_2 \rightarrow 2NH_3 \tag{2.40}$$

Table 2.7 summarizes literature data on the uncatalyzed activation energy of this reaction. Estimates range from 150 kJ/mol to 200 kJ/mol, although we plot the 200 kJ/mol value in Figure 2.4b.

Table 2.7: Literature values for the activation energy of nitrogen fixation by chemical reduction.

Catalytic process	Activation Energy (kJ/mol)	Reference	Comments
With no catalyst	200	Gutschick (1982), p. 137	This is the Gibbs energy difference between H_2 and N_2 and the molecule N_2H_2 in the gas phase. N_2H_2 is not a step in nitrogen fixation, so this may be artificial.
	150	Hageman and Burris (1980), p. 281 - 282	This is the Gibbs energy difference between H_2 and N_2 and the molecule N_2H_2 in the aqueous phase.
	150	Ljones (1979)	They claim that the activation can be understood by the reaction of H_2 and N_2 to N_2H_2.
With enzyme	30	Andersen and Shanmugam (1977)	Between temperatures 20 and 35 °C in vivo.
	60	Hardy et al. (1968)	Between temperatures 20 and 35 °C in vivo.
	61	Burns (1969)	Above 21 °C
	163	Burns (1969)	Below 21 °C
With non-biological catalyst	103	Appl (1999)	On an iron surface.
	27 - 60	Dahl et al. (2000)	Activation energy of N_2 dissociation on Ru catalyst.
	131	Dahl et al. (2000)	Calculations of N_2 dissociation on Ru catalyst.
	101	Dahl et al. (2000)	Supersonic molecular beam experiments.
	100 - 200	Dahl et al. (2000)	Ammonia synthesis over stepped Ru catalyst.

Chapter 3

THE LIKELIHOOD OF CH_4+CO_2 BIOSIGNATURE FALSE POSITIVES FROM VOLCANISM

"Life is the hypothesis of last resort." - Sagan et al. (1993)

This chapter was originally published in collaboration with Joshua Krissansen-Totton and David C. Catling in the Planetary Science Journal (Wogan et al., 2020b), and is reproduced below with the permission of the journal.

Summary

The disequilibrium combination of abundant methane and carbon dioxide has been proposed as a promising exoplanet biosignature that is readily detectable with upcoming telescopes such as the James Webb Space Telescope. However, few studies have explored the possibility of non-biological CH_4 and CO_2 and related contextual clues. Here, we investigate whether magmatic volcanic outgassing on terrestrial planets can produce atmospheric CH_4 and CO_2 with a thermodynamic model. Our model suggests that volcanoes are unlikely to produce CH_4 fluxes comparable to biological fluxes. Improbable cases where volcanoes produce biological amounts of CH_4 also produce ample carbon monoxide. We show, using a photochemical model, that high abiotic CH_4 abundances produced by volcanoes would be accompanied by high CO abundances, which could be a detectable false positive diagnostic. Overall, when considering known mechanisms for generating abiotic CH_4 on terrestrial planets, we conclude that observations of atmospheric CH_4 with CO_2 are difficult to explain without the presence of biology when the CH_4 abundance implies a surface flux comparable to modern Earth's biological CH_4 flux. A small or negligible CO abundance strengthens the CH_4+CO_2 biosignature because life readily consumes atmospheric CO, while reducing volcanic gases likely cause CO to build up in a planet's atmosphere. Furthermore, the difficulty of volcanically-generated CH_4-rich atmospheres suitable for an origin of life may favor alternatives such as impact-induced reducing atmospheres.

3.1 Introduction

Large telescopes will soon be used to search for biogenic waste gases in exoplanet atmospheres. Oxygen is the most extensively studied biosignature gas (Meadows, 2017; Meadows et al., 2018). Although many studies have proposed ways of identifying scenarios where

non-living processes might mimic life by producing oxygen, i.e. false positives (Domagal-Goldman et al., 2014; Harman et al., 2015; Luger and Barnes, 2015; Schwieterman et al., 2019; Tian et al., 2014; Wordsworth and Pierrehumbert, 2014), the circumstances are unusual and contextual clues can distinguish abiotic scenarios (Meadows et al., 2018).

However, even when life is present, oxygen biosignatures may be uncommon. Oxygenic photosynthesis is a complex metabolism that only evolved once on Earth (Fischer et al., 2016). Additionally, oxygen was slow to accumulate in the Earth's atmosphere (Lyons et al., 2014), and other planets may have low O_2 concentrations for billions of years despite having oxygenic photosynthetic life if there are large oxygen sinks (Claire et al., 2006). Accumulation of oxygen may be especially challenging on planets orbiting M-dwarf stars due to their low visible photon flux, which potentially limits primary production (Lehmer et al., 2018).

One alternative to detecting oxygen-rich planets like the modern Earth is to look for methane on planets like the Archean Earth. Before the rise of oxygen, methanogenic life could have sustained a methane-rich atmosphere, which could be detected with remote spectroscopy (Kasting and Catling, 2003; Schindler and Kasting, 2000).

Recently, Krissansen-Totton et al. (2018c) proposed a criterion for methane biosignatures: finding abundant CH_4 in the presence of CO_2 (abbreviated CH_4+CO_2). This combination is compelling if the CH_4 mixing ratio is greater than 0.1% because it is difficult to explain such an abundance with the short atmospheric lifetime of CH_4 in terrestrial atmospheres and non-biological methane sources such as serpentinization (Krissansen-Totton et al., 2018c). This 0.1% threshold value is for planets that orbit stars like the Sun and must be adjusted for different stellar types. For example, planets orbiting M-stars typically receive less near-UV radiation than planets orbiting Sun-like stars resulting in different photochemistry that promotes the build up of CH_4 (Segura et al., 2005; Grenfell et al., 2007, 2014; Rugheimer et al., 2015; Rugheimer and Kaltenegger, 2018). Krissansen-Totton et al. (2018c) argued that the CH_4 biosignature is strengthened by a low CO abundance because volcanoes that produce CH_4 should also likely generate CO. Additionally, living planets might have low CO because microbes consume CO (Kharecha et al., 2005); coupled ecosystem-planetary

models of the early Earth suggest atmospheric CO/CH_4 ratios declined dramatically with the emergence of chemoautotrophic ecosystems (Sauterey et al., 2020).

Exploring false positives for methane biosignatures is timely. Biogenic O_2 or O_3 detections with upcoming telescopes such as the James Webb Space Telescope (JWST) will be extremely difficult (Barstow and Irwin, 2016; Krissansen-Totton et al., 2018b; Lustig-Yaeger et al., 2019; Wunderlich et al., 2020; Fauchez et al., 2019), whereas CH_4+CO_2 biosignatures are more readily detectable. Indeed, an Archean-Earth like CH_4+CO_2 biosignature is potentially detectable on the planet TRAPPIST-1e with just 10 transits (Krissansen-Totton et al., 2018b). Thus, exploration of potential methane biosignature false positives and their contextual discriminants is needed.

The literature exploring false positives for methane biosignatures has primarily focused on CH_4 generation in deep-sea serpentinizing hydrothermal vents. Guzmán-Marmolejo et al. (2013) estimated a maximum CH_4 surface flux of 0.18 Tmol/yr (6.8×10^8 molecules cm^{-2} $s^{-}1$) from hydrothermal vents for planets with the same mass as Earth. Additionally, Krissansen-Totton et al. (2018c) used Monte-Carlo simulations to estimate a probability distribution for maximum abiotic CH_4 production from this process. They suggest that >10 Tmol CH4/yr is highly unlikely. These estimated maximum fluxes are small compared to modern Earth's biological CH_4 flux of 30 Tmol/yr.

However, investigations of abiotic CH_4 on Earth suggest that these estimates of abiotic CH_4 from hydrothermal vents are potentially unrealistically large. Serpentinization reactions involving water and ultramafic oceanic crust generate H_2 then, purportedly, H_2 might react with inorganic carbon in hydrothermal systems to generate CH_4. Krissansen-Totton et al. (2018c) and Guzmán-Marmolejo et al. (2013) both estimated abiotic CH_4 fluxes assuming efficient reactions between H_2 and inorganic carbon. However, laboratory experiments have shown that, uncatalyzed, this reaction is extremely slow at hydrothermal vent temperatures and pressures preventing chemical equilibrium on timescales of at least months (Reeves and Fiebig, 2020). Additionally, various lines of evidence suggest that much of the CH_4 observed in deep-sea hydrothermal vent waters is ultimately from biology (Reeves and Fiebig, 2020).

Furthermore, lifeless planets without silica-secreting organisms should have high ocean-water SiO_2 concentrations which suppresses the H_2, and therefore abiotic CH_4, produced from serpentinization (Tutolo et al., 2020).

Impacts can likely generate abiotic CH_4 (Zahnle et al., 2020), although impact-generated CH_4 is only probable early in a solar system's lifetime. The cratering record on the Moon shows that Earth's impact flux decreased dramatically by 3.5 Ga (Marchi et al., 2014). Thus, extra solar systems that are several billion years old are probably unlikely to have abiotic CH_4 from this source.

Here, we investigate another potential false-positive for the CH_4+CO_2 biosignature: magma-sourced volcanic outgassing (i.e., not metamorphic). Negligible CH_4 has been observed in gases emitted by magmatic volcanoes on Earth (Reeves and Fiebig, 2020; Catling and Kasting, 2017), although it has not been investigated whether substantial CH_4 is feasible for volcanoes in vastly different thermodynamic regimes. We simulate outgassing speciation for a range of magma temperatures, outgassing pressures, oxygen fugacities, volatile composition, and variable partitioning between subaerial and submarine volcanism. We examine whether volcanoes can produce CH_4 fluxes comparable to biological fluxes. Using a photochemical model we also investigate atmospheric composition of hypothetical planets with reducing volcanic gases to see whether volcanic CH_4 coincides with large atmospheric CO, which could be a detectable false positive marker.

3.2 Methods

3.2.1 Model for calculating volcanic outgassing speciation

Below, we describe our model for predicting the gases produced by an erupting mantle-sourced volcano. We follow Gaillard and Scaillet (2014) and solve for the gas-gas and gas-melt equilibrium in a C-O-H system. Our model differs from Gaillard and Scaillet (2014) because we do not consider nitrogen or sulfur species. Despite these differences, we obtain similar results to calculations made in Gaillard and Scaillet (2014). We have also validated our code

against the work of Liggins et al. (2020) and Ortenzi et al. (2020), which have independently constructed similar outgassing models. Our Python code is published as an open-source software on the Github page `https://github.com/Nicholaswogan/VolcGases`.

Figure 3.1 shows a highly schematic conceptualization of volcanic degassing typical of low-viscosity magma. Gas bubbles form in the magma when molecules like H_2O and CO_2 are exsolved. Within the gas bubbles, reactions drive the system to chemical equilibrium. The oxygen fugacity (f_{O_2}) of the gas bubble is controlled by equilibrium with the oxygen fugacity of the magma (e.g. Kadoya et al., 2020). Gases bubbles are released from the magma and enter the overlying atmosphere or ocean.

A mathematical model describes the volatiles in gas bubbles and magma. The amount of carbon and hydrogen that are exsolved by the magma into bubbles is governed by the solubility of CO_2 and H_2O, which we calculate with the solubility relations for mafic magmas described in Iacono-Marziano et al. (2012):

$$\ln(x_{CO_2}) = x_{H_2O} d_{H_2O} + a_{CO_2} \ln(P_{CO_2}) + S_1 \tag{3.1}$$

$$\ln(x_{H_2O}) = a_{H_2O} \ln(P_{H_2O}) + S_1 \tag{3.2}$$

Here, x_{CO_2} and x_{H_2O} are mol fractions of CO_2 and H_2O in the magma, respectfully. Additionally, P_{CO_2} and P_{H_2O} are the partial pressure of CO_2 and H_2O in gas bubbles suspended in the magma. The other terms in Equations (3.1) and (3.2) are solubility parameters with values shown in Table 3.1 except S_1 and S_2, which are further described in Chapter Appendix 3.6.1. We use solubility relations appropriate for mafic magmas because rocky planets and moons in our solar system usually have basaltic crusts which suggests that mafic magma is common to most terrestrial bodies.

Volatile mol fractions (e.g., x_{H_2O}) can be converted to mass fractions with the formula

$$m_i = \frac{x_i \mu_i}{\mu_{\text{magma}}} \tag{3.3}$$

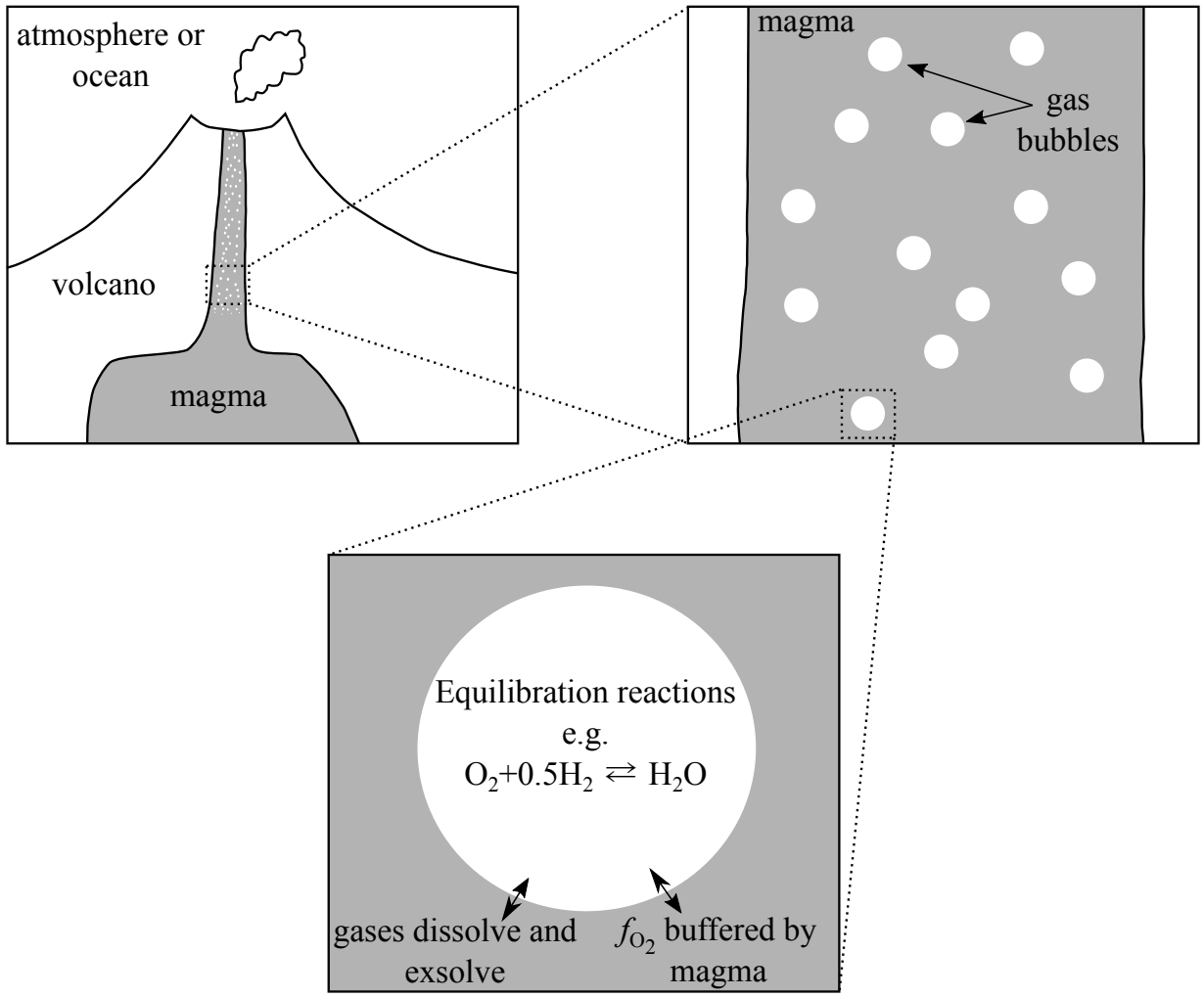

Figure 3.1: Qualitative sketch of degassing typical of low viscosity magma (e.g., Hawaiian volcanoes). Here, gas bubble reaches thermal and chemical equilibrium with a melt (no crystals are present). Note, degassing can occur in many different ways depending on magma viscosity and volatile content (Gonnermann and Manga, 2013).

Table 3.1: Model constants and variables

	Constant or Variable	Value	Units	Definition
Constants	d_{H_2O}	2.3	...	Solubility constant[a]
	a_{CO_2}	1	...	Solubility constant[a]
	a_{H_2O}	0.54	...	Solubility constant[a]
	S_1	...	...	Solubility constant[a]
	S_2	...	...	Solubility constant[a]
	μ_{magma}	64.52	$\frac{\text{g magma}}{\text{mol magma}}$	Molar mass of magma[b]
	μ_{H_2O}	18.02	$\frac{\text{g } H_2O}{\text{mol } H_2O}$	Molar mass of H_2O
	μ_{CO_2}	44.01	$\frac{\text{g } CO_2}{\text{mol } CO_2}$	Molar mass of CO_2
	K_1	$e^{-29755/T+6.55}$	$\text{bar}^{0.5}$	Equilibrium constant[c]
	K_2	$e^{-33979/T+10.42}$	$\text{bar}^{0.5}$	Equilibrium constant[c]
	K_3	$e^{-96444/T+0.22}$	-	Equilibrium constant[c]
Input	P	...	bar	Total pressure of degassing
	T	...	K	Temperature of magma and gas
	f_{O_2}	...	bar	Oxygen fugacity of the magma
	$m^{tot}_{CO_2}$	...	$\frac{\text{g } CO_2}{\text{g gas and magma}}$	mass fraction CO_2 in magma before degassing
	$m^{tot}_{H_2O}$	...	$\frac{\text{g } H_2O}{\text{g gas and magma}}$	mass fraction H_2O in magma before degassing
Output	x_{H_2O}	...	$\frac{\text{mol } H_2O}{\text{mol magma}}$	mol fraction of H_2O in the magma after degassing
	x_{CO_2}	...	$\frac{\text{mol } CO_2}{\text{mol magma}}$	mol fraction of CO_2 in the magma after degassing
	P_{H_2O}	...	bar	Partial pressure of H_2O
	P_{CO_2}	...	bar	Partial pressure of CO_2
	P_{H_2}	...	bar	Partial pressure of H_2
	P_{CO}	...	bar	Partial pressure of CO
	P_{CH_4}	...	bar	Partial pressure of CH_4
	α_{gas}	...	$\frac{\text{mol gas}}{\text{mol gas and magma}}$	mol fraction in gas phase

[a]From Iacono-Marziano et al. (2012). See Chapter Appendix 3.6.1 to calculate S_1 and S_2.
[b]Molar mass of Mt. Etna magma.
[c]Calculated from the NASA thermodynamic database (Burcat and Ruscic, 2005).

Here, m_i is mass fraction, μ_i is the volatile's molar mass, and i can be either H_2O or CO_2. Table 3.1 gives the units of each term.

We assume that after the hot gas exsolves from the magma into bubbles, it achieves thermodynamic equilibrium from the reactions

$$H_2O \leftrightarrow H_2 + \frac{1}{2}O_2 \tag{3.4}$$

$$CO_2 \leftrightarrow CO + \frac{1}{2}O_2 \tag{3.5}$$

$$CO_2 + 2H_2O \leftrightarrow CH_4 + 2O_2 \tag{3.6}$$

At thermodynamic equilibrium, the ratios of the fugacities of volatile species (denoted f_i) are related to the equilibrium constant corresponding to each chemical reaction. We assume that we can replace fugacities with partial pressures (denoted P_i). This approximation is reasonable for the temperatures and pressures involved in volcanic outgassing (Holland, 1984). Thus,

$$K_1 = \frac{f_{H_2} f_{O_2}^{0.5}}{f_{H_2O}} \approx \frac{P_{H_2} f_{O_2}^{0.5}}{P_{H_2O}} \tag{3.7}$$

$$K_2 = \frac{f_{CO} f_{O_2}^{0.5}}{f_{CO_2}} \approx \frac{P_{CO} f_{O_2}^{0.5}}{P_{CO_2}} \tag{3.8}$$

$$K_3 = \frac{f_{CH_4} f_{O_2}^2}{f_{CO_2} f_{H_2O}^2} \approx \frac{P_{CH_4} f_{O_2}^2}{P_{CO_2} P_{H_2O}^2} \tag{3.9}$$

We calculate equilibrium constants (e.g. K_1) using the NASA thermodynamic database (Burcat and Ruscic, 2005). We assume that the gas is thermally and chemically coupled to the magma so that the oxygen fugacity (f_{O_2}) of the gas is set by the oxygen fugacity of magma, as observed (Symonds, 1994). So far, we have 7 unknowns (x_{CO_2}, x_{H_2O}, P_{CO_2}, P_{H_2O}, P_{CO}, P_{H_2}, P_{CH_4}) and only 5 equations. To close the system, we add three more equations and one more unknown. The first equation requires that the partial pressures sum to the total pressure:

$$P_{H_2} + P_{H_2O} + P_{CO} + P_{CO_2} + P_{CH_4} = P \tag{3.10}$$

The final two equations are atom conservation equations for carbon and hydrogen:

$$\frac{m^{\text{tot}}_{\text{CO}_2}\mu_{\text{magma}}}{\mu_{\text{CO}_2}} = \frac{P_{\text{CO}_2} + P_{\text{CO}} + P_{\text{CH}_4}}{P}\alpha_{\text{gas}} + (1-\alpha_{\text{gas}})x_{\text{CO}_2} \tag{3.11}$$

$$\frac{m^{\text{tot}}_{\text{H}_2\text{O}}\mu_{\text{magma}}}{\mu_{\text{H}_2\text{O}}} = \frac{P_{\text{H}_2\text{O}} + P_{\text{H}_2} + 2P_{\text{CH}_4}}{P}\alpha_{\text{gas}} + (1-\alpha_{\text{gas}})x_{\text{H}_2\text{O}} \tag{3.12}$$

Equations (3.11) and (3.12) state that the total moles of either carbon or hydrogen should be equal to the moles of either element in the gas phase plus the moles in the magma. Here, α_{gas} is the final unknown. It is the total moles in the gas phase divided by the total moles in the gas and magma combined. See Chapter Appendix 3.6.1 for a full derivation of Equations (3.11) and (3.12).

Given a gas and magma temperature (T), pressure (P), oxygen fugacity (f_{O_2}), and the total mass fraction (or mol fraction) of CO_2 and H_2O in the magma ($m^{\text{tot}}_{\text{CO}_2}$, and $m^{\text{tot}}_{\text{H}_2\text{O}}$), Equations (3.1), (3.2), (3.7) - (3.12) are a system of 8 equations and 8 unknowns (x_{CO_2}, $x_{\text{H}_2\text{O}}$, P_{CO_2}, $P_{\text{H}_2\text{O}}$, P_{CO}, P_{H_2}, P_{CH_4},α_{gas}). We solve this system of equations numerically with the Scipy Python package.

The solution to this system of equilibrium equations provides an estimate of amount of each volatile species in gas bubbles in magma immediately before the gas leaves the magma. We assume bubbles remain in thermodynamic equilibrium with the surrounding melt until they are released into the overlying atmosphere or ocean, and volatile speciation does not continue evolve upon release. This does not exactly reflect real degassing. Observed outgassing chemistry suggest that volcanic gas re-equilibrates to temperatures slightly lower than the magma as the gas leaves the magma and is no longer chemically buffered by it (Moussallam et al., 2019; Kadoya et al., 2020; Oppenheimer et al., 2018). We do not capture this complexity in the main text, although, in Chapter Appendix 3.6.1 we investigate the closed system re-equilibration of volcanic gases and show that this process does not change our conclusions.

Once the unknowns are solved for, they can be used to calculate the gas production, i.e.,

the moles of gas produced per kilogram of magma erupted:

$$q_i = 10^3 \left(\frac{\alpha_{\text{gas}}}{\mu_{\text{magma}}(1 - \alpha_{\text{gas}})} \right) \frac{P_i}{P} \tag{3.13}$$

Here, q_i is the gas production of species i in mol gas/kg magma. Calculating q_i is useful because it is related to the flux F_i of gas i to the atmosphere by the magma production rate:

$$F_i = q_i Q_m \tag{3.14}$$

Here, Q_m is the magma production rate in kg magma/yr, and F_i is in mol/yr.

Several authors have shown that degassing can be affected by graphite saturation of magma (Hirschmann and Withers, 2008) or by the solubility of CO, CH_4, and H_2 in magma (Wetzel et al., 2013; Ardia et al., 2013; Hirschmann et al., 2012). The gas speciation model described above does not account for these processes. However, in Chapter Appendix 3.6.1 we introduce a more complex model that accounts for graphite saturation and CO, CH_4, and H_2 solubility, and show that this model produces very similar results to the simplified model described here.

3.2.2 Monte-Carlo Simulations

We investigate volcanic false positives to the CH_4+CO_2 biosignature on two types of worlds: An Earth-like world with subaerial and submarine outgassing (Figure 3.2), and an ocean-world with only submarine outgassing. For each type of planet, we search for false positive scenarios by calculating volcanic outgassing speciation with a wide range of input parameters.

To explore volcanism on Earth-like planets, we calculate outgassing speciation 10,000 times. For each calculation, we sample either uniform or $\log_{10}$-uniform distributions (See Table 3.2) of 10 parameters: $T_{\text{submarine}}$, $P_{\text{submarine}}$, $m^{\text{tot}}_{\text{CO}_2,\,\text{submarine}}$, $m^{\text{tot}}_{\text{H}_2\text{O},\,\text{submarine}}$, $T_{\text{subaerial}}$, $P_{\text{subaerial}}$, $m^{\text{tot}}_{\text{CO}_2,\,\text{subaerial}}$, $m^{\text{tot}}_{\text{H}_2\text{O},\,\text{subaerial}}$, f_{O_2}, and X . The width of each uniform sampling distribution are given and explained in Table 3.2. We use inputs with subscripts "subaerial"

Table 3.2: Monte-Carlo sampling distributions

Variable	Low	High	Sampling method	Justification
$T_{\text{submarine}}$	873 K	1973 K	linear uniform	Range of submarine magma temperatures observed on Earth[a]
$T_{\text{subaerial}}$	873 K	1973 K	linear uniform	Range of subaerial magma temperatures observed on Earth[a]
$P_{\text{submarine}}$	100 bar	1000 bar	linear uniform	Degassing pressure at 1 km to 10 km ocean depth[b]
$P_{\text{subaerial}}$	0.001 bar	100 bar	$\log_{10}$ uniform	Rough range of subaerial degassing pressure in solar system
$m^{\text{tot}}_{\text{CO}_2,\,\text{submarine}}$	10^{-5}	10^{-2}	$\log_{10}$ uniform	Approx. CO_2 mass fraction range in Earth magma (Wallace et al., 2015; Wallace, 2005; Anderson and Poland, 2017; Le Voyer et al., 2019)
$m^{\text{tot}}_{\text{CO}_2,\,\text{subaerial}}$	10^{-5}	10^{-2}	$\log_{10}$ uniform	Approx. CO_2 mass fraction range in Earth magma (Wallace et al., 2015; Wallace, 2005; Anderson and Poland, 2017; Le Voyer et al., 2019)
$m^{\text{tot}}_{\text{H}_2\text{O},\,\text{submarine}}$	10^{-5}	10^{-1}	$\log_{10}$ uniform	H_2O mass fraction range for Earth submarine outgassing (Wallace et al., 2015)
$m^{\text{tot}}_{\text{H}_2\text{O},\,\text{subaerial}}$	10^{-5}	10^{-1}	$\log_{10}$ uniform	H_2O mass fraction range for Earth subaerial outgassing (Wallace et al., 2015)
f_{O_2}	FMQ-4	FMQ+5	$\log_{10}$ uniform	Oxygen fugacity of most reducing Martian meteorite (Catling and Kasting, 2017) to most oxidized magma on Earth (Stamper et al., 2014)[c]
X	0	1	linear uniform	0% to 100% subaerial volcanism

[a]Coldest rhyolite magma, and hottest komatiites magmas (Huppert et al., 1984) .

[b]Assumes Earth's gravity. The solubility of H_2O in magma does not allow for significant CH_4 degassing at pressures greater than 1000 bar, equivalent to a depth of 10 km.

[c]FMQ is the fayalite-magnetite-quartz mineral redox buffer. See Chapter 7 in Catling and Kasting (2017) for a description of mineral redox buffers. We use the parameterization for the FMQ buffer defined by Wones and Gilbert (1969). This parameterization has only been experimentally validated to 1400 K (O'Neill, 1987), but we extrapolate using the parameterization to 1973 K

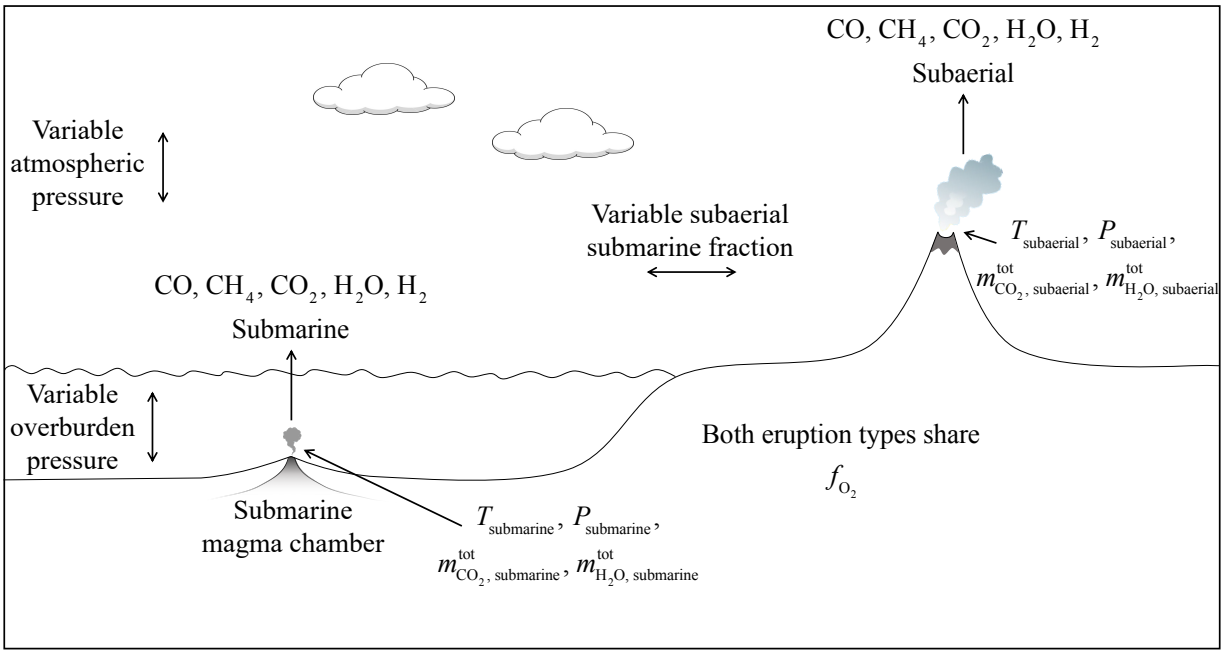

Figure 3.2: Illustration of the parameters considered in the Monte-Carlo simulations.

to calculate subaerial volcanic speciation and inputs with subscripts "submarine" to calculate submarine volcanic speciation, and then we combine the results of each calculation with the formula

$$n_i = \frac{P_{i,\,\text{subaerial}}}{P_{\text{subaerial}}} X + \frac{P_{i,\,\text{submarine}}}{P_{\text{submarine}}} (1 - X) \tag{3.15}$$

Here, n_i is the mixing ratio of averaged outgassed volatiles of species i produced by the combination of subaerial and submarine volcanoes and X is the fraction of subaerial volcanism ($0 < X < 1$). Also, $P_{i,\,\text{subaerial}}$ and $P_{i,\,\text{submarine}}$ are the partial pressure of species i in subaerial and submarine outgassing, respectively.

To investigate volcanism on an ocean-world, we also calculate outgassing speciation 10,000 times. For each calculation, we sample either uniform or $\log_{10}$-uniform distributions of inputs $T_{\text{submarine}}$, $P_{\text{submarine}}$, $m^{\text{tot}}_{\text{CO}_2,\,\text{submarine}}$, $m^{\text{tot}}_{\text{H}_2\text{O},\,\text{submarine}}$, and f_{O_2} with ranges defined and justified in Table 3.2.

3.2.3 Photochemical modeling: Uninhabited anoxic ocean-world with reducing volcanic gases

We further investigate the CH_4+CO_2 biosignature by modeling the atmospheric composition of hypothetical uninhabited ocean-worlds with reducing volcanic gases. We consider planets orbiting the Sun, and a late M star - the latter because planets orbiting M-dwarfs are the most feasible targets for near-term telescopes like JWST (Barstow and Irwin, 2016). Additionally, we simulate ocean-worlds because ocean-bottom degassing is most thermodynamically prone to produce CH_4, as revealed by our Monte-Carlo simulations and previous studies (**?**French, 1966) (see Section 3.4.1 for further discussion).

To simulate atmospheres on uninhabited planets, we use the 1-D photochemical model contained within the open source software package *Atmos*. *Atmos* is derived from a model originally developed by the Kasting group (Pavlov et al., 2001), and versions of this code have been used to simulate the Archean and Proterozoic Earth atmosphere (Zahnle et al., 2006), Mars (Sholes et al., 2019; Smith et al., 2014; Zahnle et al., 2008), and exoplanet atmospheres (Harman et al., 2015; Schwieterman et al., 2019).

3.3 Results

3.3.1 Monte-Carlo simulations

Figure 3.3 shows joint distributions of gas ratios CH_4/CO and CO_2/CO from the Monte-Carlo simulation described in Section 3.2.2. These results suggest that for most combinations of parameters volcanoes are most likely to produce more CO_2 than CO, and negligible CH_4, which is the case for the modern Earth (Catling and Kasting, 2017). About 7% and 2% of calculations produce more CH_4 than CO for ocean worlds and Earth-like worlds, respectfully. In the vast majority of cases, either CO or CO_2 is the dominant carbon-bearing species.

Figure 3.4a and 3.4b show CH_4 production from the Monte-Carlo simulations in terms of mol CH_4/kg magma. To give a sense for the gas fluxes implied by these CH_4 productions, we multiply the distributions in Figure 3.4a and 3.4b by the magma production rate of modern Earth of 9×10^{13} kg/yr (Crisp, 1984), which gives the gas fluxes shown in Figure

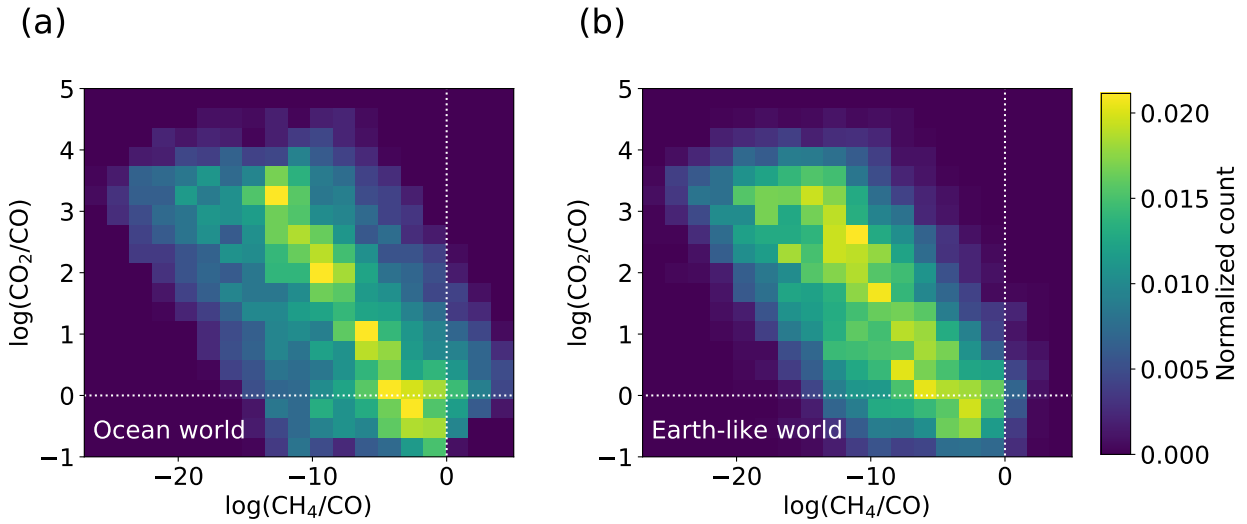

Figure 3.3: Results of the Monte-Carlo simulation described in Section 2.2. (a) and (b) show normalized count as a function of $\log(CH_4/CO)$ and $\log(CO_2/CO)$ for an ocean world and Earth-like world, respectively. The white dotted lines indicate where $CH_4/CO = 1$ and $CO_2/CO = 1$. For almost all calculated gas speciations, CO_2 and CO are much more abundant than CH_4.

3.4c and 3.4d, respectively. About 0.1% of calculations predict more than 10 Tmol CH_4/yr for both Earth-like worlds and ocean worlds. This small fraction suggests that for modern Earth magma production rates, volcanoes are unlikely to produce CH_4 fluxes comparable to modern Earth's biological flux of 30 Tmol/yr (Hauglustaine et al., 2007).

Magma production rates larger than modern Earth's increase the probability that volcanic fluxes of CH_4 become comparable to biological CH_4 fluxes. For example, the early Archean Earth could have had magma production rates up to about 25 times modern Earth's (Sleep and Zahnle, 2001). Such a magma production rate would shift the distributions in Figure 3.4c and 3.4d to larger values by a factor of 25 (or in $\log_{10}$-space, by a factor of 1.4). In this case, $\sim$2% of calculations (for either Earth-like world or ocean world) would predict more than 10 Tmol CH_4/yr.

Crucially, large CH_4 fluxes should almost always coincide with even larger CO fluxes (horizontal axis in Figure 3.3). Therefore, the unlikely cases where volcanoes mimic biological

CH_4 fluxes can be identified by detecting abundant CO in a planet's atmosphere. We further investigate CO as a CH_4+CO_2 biosignature discriminant using a photochemical model in the following section.

3.3.2 Photochemical modeling: Uninhabited anoxic ocean-world with reducing volcanic gases

We use the *Atmos* photochemical model to simulate the potential observable gas abundances of uninhabited Earth-sized ocean-worlds with reducing volcanic gases. We consider such planets because they are the most prone to mimic biology by producing volcanic CH_4 (see Section 3.4.1 for more details). Our hypothetical planets have 1 bar N_2 dominated atmospheres, 400 bars of ocean water, magma degassing at 1473 K and mantle redox states of FMQ-4. Here, FMQ is the fayalite-magnetite-quartz buffer which is a synthetic reference f_{O_2} value at fixed temperature-pressure conditions. Additionally, we assume that the magma contains 0.1 wt% CO_2, and 1 wt% H_2O. Our assumed H_2O concentration is comparable to those observed in submarine hot-spot magmas (0.2 to 1.5 wt%) (Wallace et al., 2015), however, the CO_2 concentration we assume is slightly lower (Anderson and Poland, 2017). Given these inputs, our speciation model (Section 3.2.1) predicts gas production from erupted magma of $q_{H_2} = 4.36 \times 10^{-2}$ mol gas/kg magma, $q_{CO} = 1.29 \times 10^{-2}$ mol gas/kg magma, and $q_{CH_4} = 7.39 \times 10^{-3}$ mol gas/kg magma.

The magnitude of gas fluxes to the atmosphere resulting from chemically reducing volcanism depends on the magma production rate (Equation (3.14)). We consider magma production rates between about 10^{-3} and 10^{2} Earth's modern magma production rate of 9×10^{13} kg magma/yr (Crisp, 1984).

For each magma production rate, we calculate the outgassing flux of CH_4, H_2, and CO and set these fluxes as lower boundary conditions to the *Atmos* photochemical model (the outgassing model also gives CO_2 and H_2O fluxes, but we don't use them in our photochemical modeling). *Atmos* only allows fixed CO_2 mixing ratios and not CO_2 fluxes so we consider cases with low and high CO_2 (100 ppm and 10%). Additionally, we set the deposition velocity of CO to 10^{-8} cm s^{-2} to reflect the abiotic uptake of CO by the ocean (Kharecha

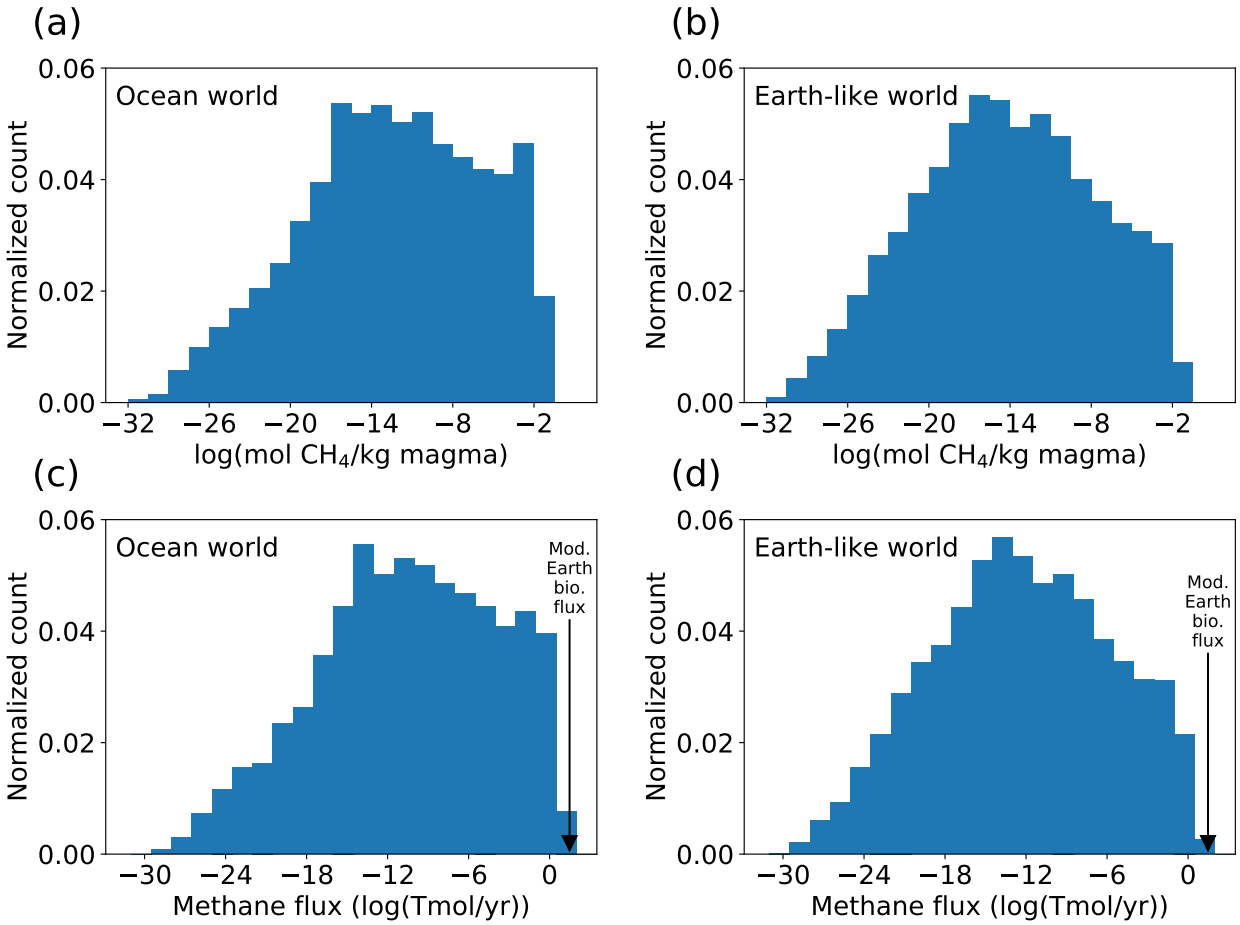

Figure 3.4: Normalized count of methane production (mol gas/kg magma) for (a) ocean worlds and (b) Earth-like worlds. Distributions were calculated by sampling the ranges in Table 3.2. Multiplying Earth's magma production rate of 9×10^{13} kg magma/yr by (a) and (b) gives the methane fluxes in (c) and (d), respectively. For modern Earth's magma production rate, volcanoes are likely to produce negligible CH_4.

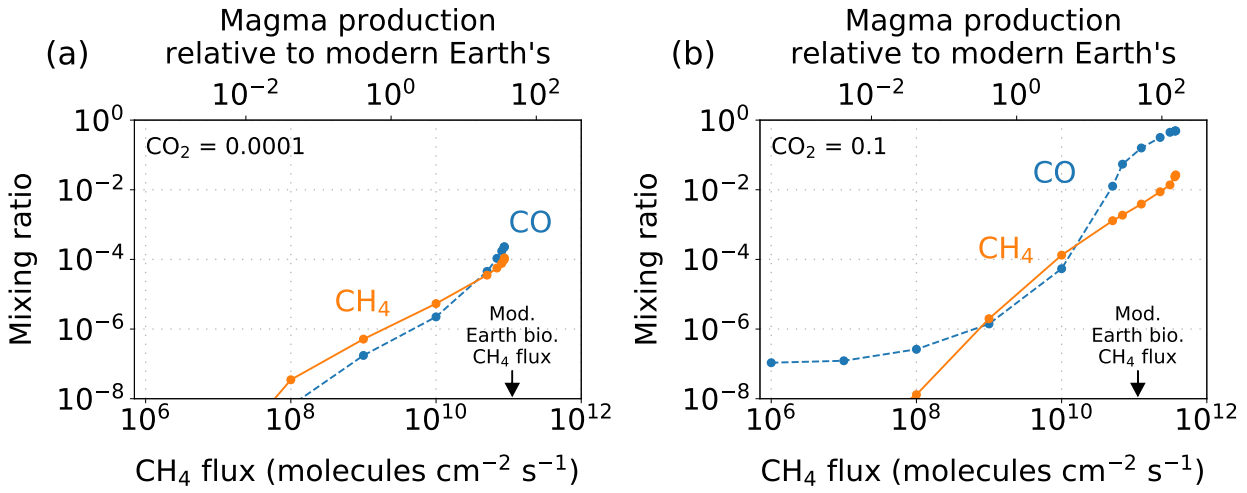

Figure 3.5: Atmospheric mixing ratios of CO and CH_4 as a function of magma production rate relative to modern Earth's (or CH_4 flux) on an anoxic ocean-world with reducing volcanic gases orbiting a sun-like star. (a) and (b) are identical model runs, except (a) assumes a constant atmospheric CO_2 mixing ratio of 0.0001, and (b) assumes a constant atmospheric CO_2 mixing ratio of 0.1. Modern Earth's biological CH_4 flux is indicated on the horizontal axes. Archean Earth-like CH_4 fluxes and abundances are only mimicked by volcanoes for magma production rates >10 times modern Earth's. Such false-positive cases can be distinguished from biology because the CO abundance exceeds the CH_4 abundance, which would likely not be the case for an inhabited planet.

et al., 2005). All other boundary conditions are specified in Chapter Appendix 3.6.2. Given volcanic outgassing fluxes and other boundary conditions, *Atmos* calculates the mixing ratios of all species when the atmosphere is at photochemical equilibrium.

Figure 3.5 shows the photochemical modeling results of reducing volcanic gases on an uninhabited Earth-sized ocean-world orbiting the Sun. Figure 3.5a assumes that the atmosphere has 100 ppmv CO_2 while Figure 3.5b assumes that atmospheric CO_2 is 10%. Carbon monoxide and methane are more abundant in the model with more CO_2 because CO_2 shields the lower atmosphere from hydoxyl (OH) production from water photolysis. In anoxic atmospheres, OH is a significant sink for both CO and CH_4 through the reactions $CO_2 + OH \rightarrow CO_2 + H$ and $CH_4 + OH \rightarrow CH_3 + H_2O$. OH is generated primarily from H_2O photolysis ($H_2O + h\nu[\lambda < 200\,\text{nm}] \rightarrow OH + H$), but CO_2 shields H_2O from photolysis in model runs with 10% CO_2, thus limiting the CH_4 and CO destruction from OH. Also, CH_4 is more abundant in atmospheres with more CO_2 because CO_2 shields CH_4 from direct photolysis in cases when CO_2 is >200 times as abundant as CH_4. This factor of ∼200 comes from comparing Lyman-α (λ = 121.6 nm) CO_2 and CH_4 cross sections. Lyman-α is the portion of the UV spectrum primarily responsible for photolyzing CH_4.

Figure 3.5 suggests that reducing volcanic gases on an ocean world orbiting a sun-like star will only mimic biological CH_4 fluxes and abundances for large magma production rates. Volcanism can generate Earth's modern biological CH_4 flux when the magma production rate is ∼50 times modern Earth's (Figure 3.5). In this case, the photochemical model predicts an atmospheric CH_4 abundance between 0.01% and 0.3%, depending on the CO_2 mixing ratio. Such CH_4 abundances are similar to the 0.01% to 1% expected in the early Archean Earth atmosphere (Catling and Zahnle, 2020). In contrast, magma production rates comparable to the modern Earth's result in a CH_4 flux of 2.4×10^9 molecules cm^{-2} s^{-1} (0.64 Tmol/yr) and CH_4 abundances < 30 ppm, which are likely to be considered abiotic levels in an anoxic atmosphere.

Figure 3.6 shows the CO and CH_4 mixing ratios on an Earth-sized ocean-world with reducing volcanic gases orbiting a cold M star. CO and CH_4 are more abundant on the

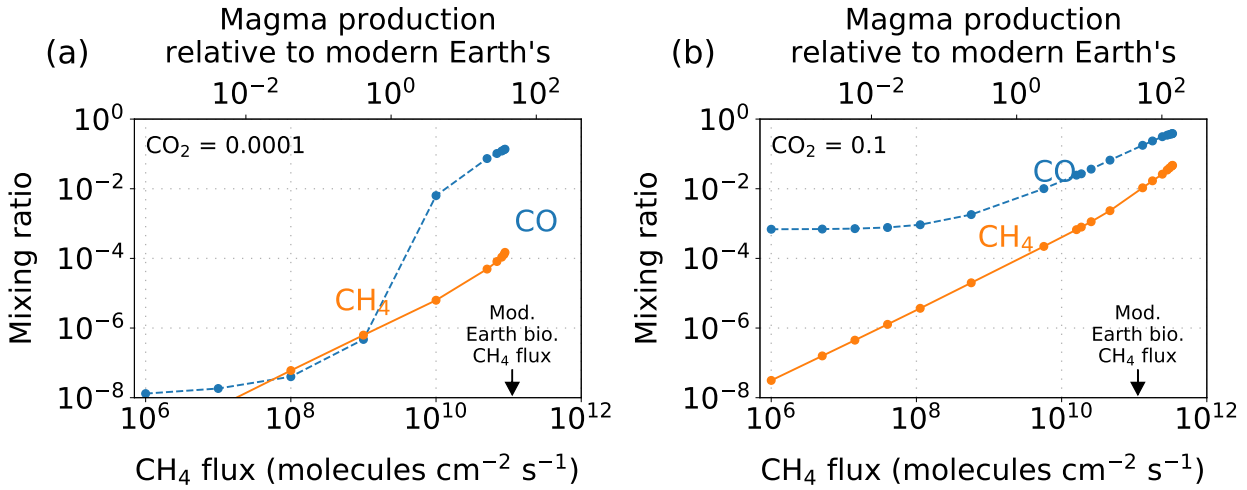

Figure 3.6: Identical to Figure 3.5, except for a planet that orbits a M8V star instead of a sun-like star.

ocean-world orbiting the M star compared to the ocean-world orbiting a Sun-like star (Figure 3.5). This is because M8V stars have a low flux of near-ultraviolet radiation compared to sun-like stars. The low near-ultraviolet flux reduces OH produce from H_2O photolysis, thus allowing for relatively high CO and CH_4 concentrations.

One consequence of M-dwarf photochemistry is a higher likelihood of Archean Earth-like CH_4 abundances on uninhabited planets with reducing gases from volcanism. Figure 3.6 shows that modern Earth magma production rates can result in CH_4 abundances up to 0.01% which is comparable to what is expected in the Archean atmosphere.

Potential CH_4 biosignature false positives from reducing volcanic gases might be discriminated from inhabited worlds using observations of CO. For planets orbiting Sun-like stars (Figure 3.5) or M stars (Figure 3.6) the CO abundance is higher than the CH_4 abundance in every case that is a potential outgassing false-positive. Some authors have argued that a large CO abundance is unlikely on an inhabited planet, because atmospheric CO should be readily consumed by biology (**?**). Conversely, Schwieterman et al. (2019) has demonstrated hypothetical cases where large CO can coincide with with biology in an anoxic atmosphere.

We further discuss CO as a false-positive discriminant in Section 3.4.2.

3.4 Discussion

3.4.1 The reasons why volcanoes produce little CH_4

Our modeling results show that for modern Earth magma production rates, volcanic fluxes of reducing gases are unlikely to produce more than 1 Tmol CH_4/yr even in an extreme case (Figure 3.4). This flux is relatively small compared to the flux of other volcanic gases on modern Earth. For example, Earth's modern volcanoes produce about 7.5 Tmol CO_2/yr and 95 Tmol H_2O/yr (Catling and Kasting, 2017, p. 203). There are three main reasons why the outgassing model predicts little CH_4, which we discuss below.

Volcanoes produce little CH_4 because of water solubility in magma

One reason for small CH_4 outgassing is the high solubility of water in magma at high pressures. Consider Equation (3.9), which can be re-arranged to the following

$$\frac{P_{\mathrm{CH_4}}}{P_{\mathrm{CO_2}}} = \frac{K_3 P_{\mathrm{H_2O}}^2}{f_{\mathrm{O_2}}^2} \tag{3.16}$$

The ratio $P_{\mathrm{CH_4}}/P_{\mathrm{CO_2}}$ in a gas bubble in magma is directly proportional to $P_{\mathrm{H_2O}}^2$ within that bubble. Generally speaking, $P_{\mathrm{H_2O}}$ increases as the total pressure of degassing increases because all partial pressures must sum to the total pressure (Equation (3.10)). For example, subaerial degassing at $\sim$1 bar will have a relatively small $P_{\mathrm{H_2O}}$, and thus a small $P_{\mathrm{CH_4}}/P_{\mathrm{CO_2}}$ ratio. On the other hand, submarine degassing at $\sim$400 bar should have a larger H_2O partial pressure, and thus a larger $P_{\mathrm{CH_4}}/P_{\mathrm{CO_2}}$ ratio. Here, the equilibrium constant and oxygen fugacity have extremely weak pressure dependencies, i.e. they are effectively constant as degassing pressure changes.

Figure 3.7a shows modeled gas speciation for highly reducing volcanism ($f_{\mathrm{O_2}}$ = FMQ-4) as a function of pressure. For small pressures ($<$ 100 bar), CH_4 increases with increasing pressure and then asymptotes for pressures $>$ 100 bar.

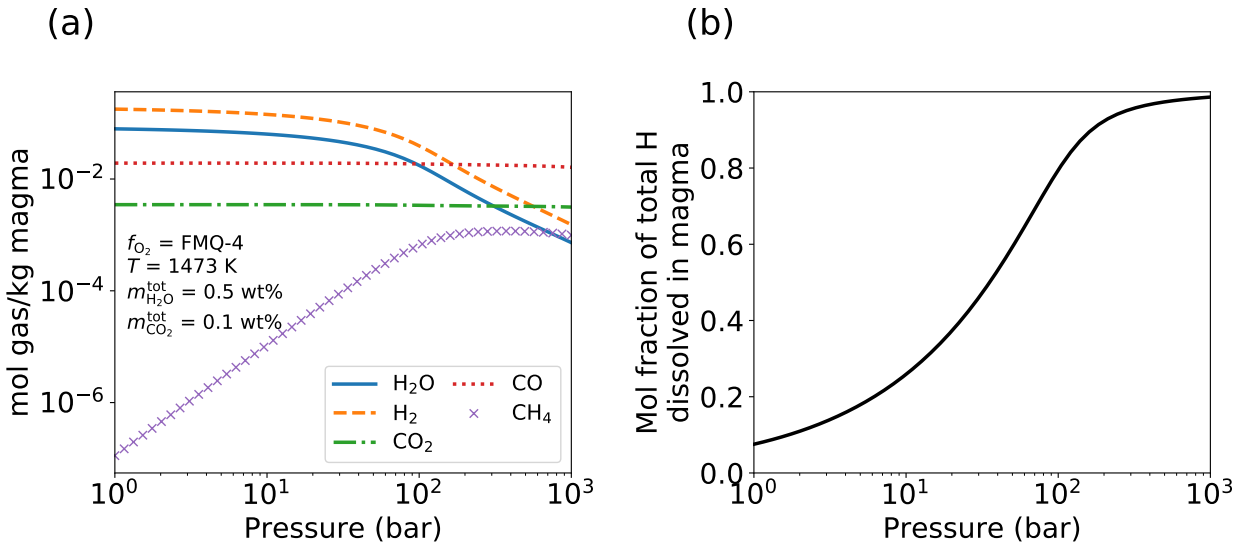

Figure 3.7: (a) Modeled gases speciation as a function of pressure. (b) Mole fraction of total hydrogen dissolved in the magma as a function of pressure. Model assumes f_{O_2} = FMQ-4, T = 1473 K, $m^{tot}_{H_2O}$ = 0.5 wt%, and $m^{tot}_{CO_2}$ = 0.1 wt%. Methane becomes more prevalent in volcanic gases at higher pressures, but asymptotes because hydrogen dissolves into the magma, reducing the total amount of H-bearing volatiles released from the magma.

CH_4 asymptotes because of the high solubility of water in magma at high pressure. High pressures dissolve a large fraction of the total available hydrogen as H_2O into the magma, which is shown in Figure 3.7b. Dissolving a large amount of H_2O into the magma limits the amount of hydrogen available in the gas phase for making H-bearing species, like CH_4, H_2O and H_2.

In summary, high pressure is in some ways thermodynamically favorable for making methane because $P_{CH_4}/P_{CO_2} \propto P_{H_2O}^2$, but also unfavorable because high pressure dissolves a large fraction of the available hydrogen in the magma as H_2O. Limited amounts of hydrogen in gas bubbles results in small amounts of CH_4 produced.

? used Equation (3.16) to argue that ∼1% of the carbon outgassed by submarine volcanoes should be CH_4 for magma with f_{O_2} = FMQ. They assumed that $P_{H_2O} \approx P$, the total pressure. This assumption is valid for oxidized subaerial volcanoes because ∼90% of the gas exsolved by Earth's subaerial volcanoes is H_2O (Catling and Kasting, 2017, p. 203). However, $P_{H_2O} < P$ for submarine volcanoes because of the high-water solubility in magma at high pressure. Our outgassing model, which accounts for water's solubility in magma, produces negligible methane.

Li and Lee (2004) also predict abundant CH_4 produced by subaerial and submarine volcanoes (their Figure 5). However they calculated equilibrium constants in units of bars, but then used units of Pascals for equilibrium chemistry calculations. The result was that they calculated speciation for pressures a factor 10,000 times greater than reported. For example, we were able to reproduce their subaerial outgassing case (their Figure 5a) by assuming $P = 10,000$ bar and not the $P = 1$ bar total pressure they intended. Additionally, like **?**, they did not account for the high solubility of H_2O in magma at high pressure. Their methods assume the total hydrogen outgassed for submarine volcanoes is the same as the total hydrogen outgassed by subaerial volcanoes. This should not be the case because at high pressure water dissolves in magma and is unavailable for making H-bearing gas species (Figure 3.7b).

The pressure dependence of volcanic outgassing has implications for planetary atmo-

spheres generally (Gaillard and Scaillet, 2014). Thin atmospheres will allow substantial degassing of both carbon and hydrogen bearing species. However, planets with thick atmospheres or large global oceans will have volcanic degassing dominated by CO_2 and CO, and almost no hydrogen bearing species. The overburden pressure where C-bearing species dominate depends primarily on the un-degassed concentrations of H_2O and CO_2 in the magma. In Figure 3.7, CO_2 and CO overwhelms H-bearing species at ∼1000 bar for initial volatile concentrations of $m^{\rm tot}_{\rm CO_2} = 0.1\%$, and $m^{\rm tot}_{\rm H_2O} = 0.5\%$. In contrast, Figure 8 in Gaillard and Scaillet (2014) illustrates a case with less volatiles ($m^{\rm tot}_{\rm CO_2} = 0.007\%$ and $m^{\rm tot}_{\rm H_2O} = 0.03\%$) where C-bearing species eclipse H-bearing species at ∼1 bar.

Volcanoes produce little CH_4 because magma is hot

Relatively little CH_4 is produced by volcanoes because CH_4 is generally not thermodynamically favorable at typical magma degassing temperatures. Figure 3.8 shows gas speciation as a function of temperature for a submarine outgassing case. For these chosen inputs, CH_4 is the dominant carbon-bearing species for $T < 1200$ K. Mid-ocean ridge basalts (MORB) are about 2/3 of total magma produced on Earth (Crisp, 1984). MORB magma erupt at temperatures between 1473 K and 1650 K (Scheidegger, 1973) and are thus in a temperature regime where CH_4 is unfavorable even from more reducing volcanism.

On the other hand, magma from arc volcanoes is generally much colder than MORB magma. Moussallam et al. (2019) report magma temperatures for many arc volcanoes (their Table S3), the coldest of which are 1123 K. Thus, it does seem possible for magma to be cold enough for CH_4 to be the dominant carbon-bearing outgassed species from an extremely reducing volcano with $f_{\rm O_2}$ = FMQ-4.

Recall that large magma production rates (∼30x modern) are required for volcanoes to produce CH_4 fluxes compared to biological ones (Figure 3.5). It seems unlikely that planets with large magma production rates will have magma temperatures cold enough to produce plentiful CH_4. For example, the Archean Earth may have had a larger magma production rate than the modern Earth because the Earth's mantle was hotter on the distant past

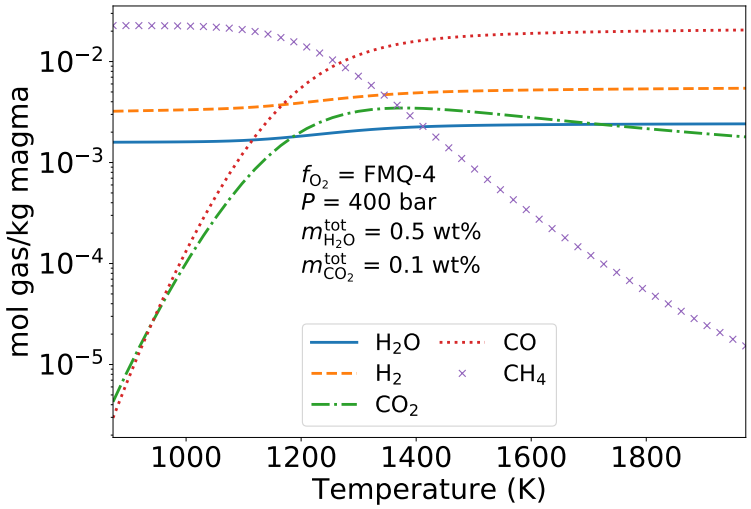

Figure 3.8: Modeled volcanic outgassing speciation as a function of temperature. Model assumes f_{O_2} = FMQ-4, $P = 400$ bar, $m^{tot}_{H_2O} = 0.5$ wt%, and $m^{tot}_{CO_2} = 0.1$ wt%. CH_4 is more thermodynamically favorable at lower degassing temperatures.

(Sleep and Zahnle, 2001). The hotter Archean mantle resulted in the eruption of ∼1800 K komatiite magmas (Huppert et al., 1984), or possibly only ∼1600 K (McKenzie, 2020). Such hot magma degassing is unfavorable for methane (Figure 3.8).

Volcanoes produce little CH_4 because very low oxygen fugacity is required

The final reason why volcanic CH_4 is unlikely on terrestrial planets is because very low f_{O_2} is required to make abundant methane. Figure 3.9 shows gas speciation as a function of oxygen fugacity for submarine volcanism. For these assumed inputs, methane is a substantial fraction of outgassed species for f_{O_2} < FMQ-3, and at FMQ-5 (roughly equivalent to the quartz-fayalite-iron buffer) half the carbon is converted to CH_4, while the other half is CO. Most degassing on Earth occurs at approximately f_{O_2} = FMQ (Catling and Kasting, 2017, p. 208), but magma spans FMQ-4 to FMQ+5 (Stamper et al., 2014). Additionally, the oxygen fugacity of Martian meteorites ranges between FMQ and FMQ-3.7 (Catling and Kasting, 2017, p. 363). Therefore, the f_{O_2} < FMQ-3 required for plentiful CH_4 outgassing is at the

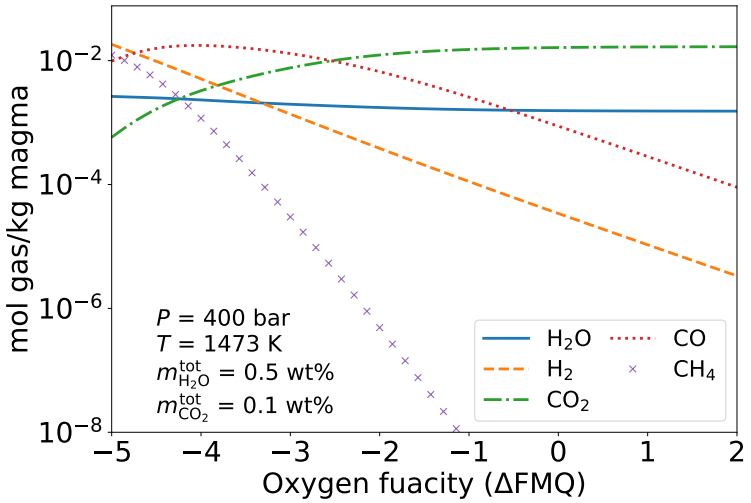

Figure 3.9: Modeled volcanic outgassing speciation as a function of oxygen fugacity. Model assumes $P = 400$ bar, $T = 1473$ K, $m^{\text{tot}}_{\text{H}_2\text{O}} = 0.5$ wt%, and $m^{\text{tot}}_{\text{CO}_2} = 0.1$ wt%. Methane is most favorable at low oxygen fugacity.

extremes of the oxygen fugacities observed for Earth and Mars.

Astronomical observations and geochemical experiments suggest Earth-sized planets should generally have relatively oxidized magmas. Doyle et al. (2019) spectroscopically measured the oxygen fugacity of material polluting the surface of several white dwarfs. Their observations suggest that rocky exoplanets are likely to have similar oxygen fugacities to Earth and Mars. Additionally, high pressure experiments suggest that the upper mantles of Earth-sized planets should self-oxidize by iron oxide disproportionation to roughly FMQ during the magma-ocean phase, early in a planet's life (Armstrong et al., 2019).

3.4.2 Carbon monoxide as a methane biosignature discriminant

CO-consuming life evolved very early on Earth (Adam et al., 2018) and is a relatively simple metabolism. Therefore, it seems possible that life on other planets will evolve to consume CO. Planets with atmospheric CH_4+CO_2 produced by life might also have relatively small amounts of atmospheric CO because of CO consumers. Consequentially, the presence of

abundant CO along with CH_4 can discriminate abiotic situations.

Monte-Carlo simulations shows that volcanoes should almost always produce more CO than CH_4 (Figure 3.3). Additionally, photochemical modeling (Figure 3.5 and 3.6) suggests that CO should build up in the atmospheres of uninhabited planets with reducing submarine volcanic gases. Thus, atmospheric CO_2+CH_4 produced by volcanoes is likely accompanied by a large CO concentration. This is distinct from an inhabited world, which can have lower CO concentrations due to CO consuming life.

However, the mere presence of large atmospheric CO is not a definitive sign of an uninhabited planet with reducing volcanic gases (Schwieterman et al., 2019). This is because there are limits to how quickly gases can be transported from the atmosphere, into the ocean where they can be consumed by life (Kharecha et al., 2005). For example, consider a planet with a very large volcanic CO flux (e.g., 100x modern). CO could build up in this planet's atmosphere even if CO consumers were present in an ocean because CO transport from the atmosphere to the ocean would not be sufficient to maintain low atmospheric CO.

In summary, the CH_4+CO_2 biosignature is most compelling when the CO abundance is low or negligible because lack of CO potentially implies the presence of CO consuming biology. In comparison, atmospheric CH_4+CO_2 and large CO is ambiguous, and can either be explained by reducing volcanic gases or by an inhabited world that is unable to sequester atmospheric CO.

JWST might be able to put a tentative upper limit on atmospheric CO. **?** simulated JWST retrievals of TRAPPIST-1e with an atmospheric composition similar to the Archean Earth containing 10 ppbv CO. Their synthetic retrieval suggested CO was below 652 ppmv with 90% confidence after 10 transits. CO constraints could be improved by co-adding more transits and positive CO detections may also be possible with JWST (Wunderlich et al., 2020).

However, even if observational CO constraints are poor, it may still be possible to say something about the abiotic or biotic origin of atmospheric CH_4. Reducing gases from volcanism are unlikely to mimic the modern biological CH_4 flux of 30 Tmol/yr (Section

3.4.1). Additionally, serpentinization is unlikely to produce 30 Tmol CH_4/yr, and impact-generated CH_4 might be distinguished with system age (**?**). Therefore, JWST observations of atmospheric CH_4+CO_2 would be challenging to explain without the presence of biology regardless of atmospheric CO, as long as the CH_4 abundance implies a surface flux similar to the modern Earth's.

3.4.3 CH_4 levels and implications for the origin on life

Much current origin of life research revolves around the "RNA world" hypothesis (Gilbert, 1986; Joyce and Szostak, 2018; Sasselov et al., 2020). This hypothesis proposes an interval of time when primitive life consisted of self-replicating, evolving RNA molecules, which, at some point, were encapsulated in cells. On a rocky world, "RNA world" requires that RNA is synthesized from early raw materials. Laboratory experiments that have successfully synthesized nucleobases, which are building blocks of RNA, require the following nitriles: hydrogen cyanide (HCN), cyanoacetylene (HCCCN), and cyanogen (NCCN) (Sutherland, 2016; Ritson et al., 2018; Benner et al., 2019). In addition, nitriles have also been used to synthesize amino acids (Miller and Urey, 1959; Sutherland, 2016).

The known natural source of nitriles is photochemistry in a chemically reducing atmosphere containing H_2, CH_4 and N_2 or perhaps NH_3. For example, Titan's photochemistry produces all the aforementioned nitriles (Strobel et al., 2009). Importantly, to make the simplest nitrile, HCN, requires abundant CH_4 because HCN is formed from photochemical products of CH_4 and nitrogen (Zahnle, 1986; Tian et al., 2011).

Our results show that volcanic gases generally are unlikely to cause high atmospheric CH_4 abundances in prebiotic atmospheres. Consequently, the results lend credence to alternative proposals for making early CH_4-rich, reducing atmospheres, such as impacts (Zahnle et al., 2020). Impacts can make a reducing atmosphere when reactions between iron-rich impact ejecta and shock-heated water vapor from an ocean generate copious H_2, CH_4 and NH_3. Subsequent photochemistry would generate HCN and other prebiotic nitriles over thousands to millions of years (Zahnle et al., 2020).

3.5 Conclusions

Our modeling of volcanic outgassing speciation suggests that chemically reducing volcanism on terrestrial planets is unlikely to mimic biological CH_4 fluxes. The improbable cases where volcanoes do produce biological CH_4 fluxes also often produce CO. Volcanoes are not prone to produce CH_4 for several reasons. First, the high solubility of H_2O in magma limits the amount of total hydrogen outgassed, thus preventing the production of H-bearing molecules like CH_4. Second, CH_4 outgassing requires relatively low magma temperatures compared to the majority of magma erupted on Earth. Finally, CH_4 outgassing requires a very low magma oxygen fugacity unlike that of most terrestrial planets inferred from astronomical data (Doyle et al., 2019).

We use a photochemical model to calculate atmospheric composition of planets with volcanoes that produce CH_4. We find that atmospheric CH_4 should coincide with abundant CO. On the other hand, biogenic CH_4 can coincide with a low CO abundance if CO-consuming microbial life is present.

Therefore, the CH_4-CO_2 biosignature is most compelling when little or no atmospheric CO is detected. Atmospheric CH_4-CO_2 and large CO is ambiguous and can be explained by an uninhabited planet with highly reducing volcanic gases, or an inhabited planet where biology is unable to sequester atmospheric CO (Schwieterman et al., 2019).

However, observations of CO are not required to make conclusions about the abiotic or biotic origin of observed atmospheric CH_4. Atmospheric CH_4 and CO_2 alone would have a reasonable probability of being biological if the observed CH_4 abundance implies a surface flux similar to modern Earth's biological CH_4 flux (30 Tmol/yr). Such a large CH_4 flux is difficult to explain with reducing volcanic gases or other abiotic processes that generate CH_4, such as serpentenization.

These conclusions should be taken with caution because they are based on what is understood about processes occurring on the Earth and our Solar System, which may be a very sparse sampling of what is possible.

3.6 Chapter Appendix

3.6.1 Details of outgassing speciation model

Solubility constants for of H_2O and CO_2

Our outgassing model uses solubility equations for H_2O and CO_2 in mafic magmas from Iacono-Marziano et al. (2012) (Equations (3.1) and (3.2)). The parameters S_1 and S_2 in the solubility equations depend on the chemical make-up of the magma. We found that different mafic magma compositions did not significantly effect the outputs of our outgassing speciation model (Section 3.2.1), therefore, for the purposes of calculating melt solubility, we fixed the chemical make-up of the magma to the magma erupting at Mt. Etna, Italy, reported by Iacono-Marziano et al. (2012). This reduced the complexity of the model without sacrificing any significant amount of accuracy.

Table 3.3 shows the chemical make-up of the magma at Mt. Etna, and Table 3.4 shows several solubility constants from Iacono-Marziano et al. (2012). Together these values define the solubility parameters S_1 and S_1:

$$\begin{aligned} S_1 = \ln\left(\frac{\mu_{\text{magma}}}{\mu_{CO_2}10^6}\right) + \frac{C_{CO_2}P}{T} + B_{CO_2} + b_{CO_2}\left[\frac{\text{NBO}}{\text{O}}\right] \\ + \left(\frac{x_{Al_2O_3}}{x_{CaO} + x_{K_2O} + x_{Na_2O}}\right) d_{Al_2O_3/(CaO\,+\,K_2O\,+\,Na_2O)} \\ + (x_{FeO} + x_{MgO})d_{FeO\,+\,MgO} + (x_{Na_2O} + x_{K_2O})d_{Na_2O\,+\,K_2O} \end{aligned} \tag{3.17}$$

$$S_2 = \ln\left(\frac{\mu_{\text{magma}}}{\mu_{H_2O}10^2}\right) + \frac{C_{H_2O}P}{T} + B_{H_2O} + b_{H_2O}\left[\frac{\text{NBO}}{\text{O}}\right] \tag{3.18}$$

$$\left[\frac{\text{NBO}}{\text{O}}\right] = \frac{2(x_{K_2O} + x_{Na_2O} + x_{CaO} + x_{MgO} + x_{FeO} - x_{Al_2O_3})}{2x_{SiO_2} + 2x_{TiO_2} + 3x_{Al_2O_3} + x_{MgO} + x_{FeO} + x_{CaO} + x_{Na_2O} + x_{K_2O}} \tag{3.19}$$

Here, T is magma temperature, P is the total pressure of degassing, and $\left[\frac{\text{NBO}}{\text{O}}\right]$ is the amount of non-bridging oxygen per oxygen in the melt.

Table 3.3: Mt. Etna magma composition

Magma component	Mole fraction
x_{SiO_2}	0.516
x_{TiO_2}	0.014
$x_{Al_2O_3}$	0.110
x_{FeO}	0.091
x_{MgO}	0.092
x_{CaO}	0.126
x_{Na2O}	0.035
x_{K_2O}	0.002
$x_{P_2O_5}$	0.016

Note. Taken from Iacono-Marziano et al. (2012).

Table 3.4: Solubility constants

Constant	Value
C_{CO_2}	0.14
B_{CO_2}	-5.3
b_{CO_2}	15.8
B_{H_2O}	-2.95
b_{H_2O}	1.24
$d_{Al_2O_3/(CaO+K_2O+Na_2O)}$	3.8
$d_{FeO+MgO}$	-16.3
$d_{Na_2O+K_2O}$	20.1

Note. "Anhydrous" case from Iacono-Marziano et al. (2012).

Derivation of Equations (3.11) *and* (3.12)

Following is the derivation for the atom conservation equation for carbon used in our outgassing model (Equation (3.11)). The derivation for the atom conservation equation for hydrogen follows the exact same procedure, so we do not include it.

Consider some volume of magma with gas bubbles in it which contains a total number of moles γ_{tot}. The total moles is the sum of the moles of magma (γ_{magma}), and the moles of gas in bubbles suspended in that magma (γ_{gas}):

$$\gamma_{\text{tot}} = \gamma_{\text{gas}} + \gamma_{\text{magma}} \tag{3.20}$$

Within this same volume of magma, the total moles of carbon ($\gamma_{\text{C}}^{\text{tot}}$) is equal to the moles of carbon in the gas phase ($\gamma_{\text{C}}^{\text{gas}}$) and the moles of carbon dissolved in the magma ($\gamma_{\text{C}}^{\text{magma}}$) combined.

$$\gamma_{\text{C}}^{\text{tot}} = \gamma_{\text{C}}^{\text{gas}} + \gamma_{\text{C}}^{\text{magma}} \tag{3.21}$$

We assume that the only carbon bearing molecule that can dissolve in the magma is CO_2, therefore $\gamma_{\text{C}}^{\text{magma}} = \gamma_{\text{CO}_2}^{\text{magma}}$. Dividing by γ_{tot} and expanding gives

$$\frac{\gamma_{\text{C}}^{\text{tot}}}{\gamma_{\text{tot}}} = \frac{\gamma_{\text{gas}}}{\gamma_{\text{tot}}}\frac{\gamma_{\text{C}}^{\text{gas}}}{\gamma_{\text{gas}}} + \frac{\gamma_{\text{magma}}}{\gamma_{\text{tot}}}\frac{\gamma_{\text{CO}_2}^{\text{magma}}}{\gamma_{\text{magma}}} \tag{3.22}$$

We can replace $\frac{\gamma_{\text{magma}}}{\gamma_{\text{tot}}}$ with $1 - \frac{\gamma_{\text{gas}}}{\gamma_{\text{tot}}}$ using Equation (3.20). This leaves us with

$$\frac{\gamma_{\text{C}}^{\text{tot}}}{\gamma_{\text{tot}}} = \frac{\gamma_{\text{gas}}}{\gamma_{\text{tot}}}\frac{\gamma_{\text{C}}^{\text{gas}}}{\gamma_{\text{gas}}} + \left(1 - \frac{\gamma_{\text{gas}}}{\gamma_{\text{tot}}}\right)\frac{\gamma_{\text{CO}_2}^{\text{magma}}}{\gamma_{\text{magma}}} \tag{3.23}$$

Here, $\frac{\gamma_{\text{CO}_2}^{\text{magma}}}{\gamma_{\text{magma}}}$ is just x_{CO_2} (the mol fraction of CO_2 in the magma, see Table 3.1). Also, we assume that CO_2, CO and CH_4 are the only carbon-bearing gas species, so $\gamma_{\text{C}}^{\text{gas}} = \gamma_{\text{CO}_2}^{\text{gas}} +$

$\gamma_{\mathrm{CO}}^{\mathrm{gas}} + \gamma_{\mathrm{CH_4}}^{\mathrm{gas}}$. Making substitutions gives

$$\frac{\gamma_{\mathrm{C}}^{\mathrm{tot}}}{\gamma_{\mathrm{tot}}} = \frac{\gamma_{\mathrm{gas}}}{\gamma_{\mathrm{tot}}} \frac{\gamma_{\mathrm{CO_2}}^{\mathrm{gas}} + \gamma_{\mathrm{CO}}^{\mathrm{gas}} + \gamma_{\mathrm{CH_4}}^{\mathrm{gas}}}{\gamma_{\mathrm{gas}}} + \left(1 - \frac{\gamma_{\mathrm{gas}}}{\gamma_{\mathrm{tot}}}\right) x_{\mathrm{CO_2}} \tag{3.24}$$

Assuming the ideal gas law, $\gamma_i^{\mathrm{gas}}/\gamma_{\mathrm{gas}} = P_i/P$. Also, to make the equation more manageable, we substitute $\alpha_{\mathrm{gas}} = \frac{\gamma_{\mathrm{gas}}}{\gamma_{\mathrm{tot}}}$, which is the total mols in the gas phase divided by the moles in the gas phase and magma combined.

$$\frac{\gamma_{\mathrm{C}}^{\mathrm{tot}}}{\gamma_{\mathrm{tot}}} = \frac{P_{\mathrm{CO_2}} + P_{\mathrm{CO}} + P_{\mathrm{CH_4}}}{P} \alpha_{\mathrm{gas}} + (1 - \alpha_{\mathrm{gas}})\, x_{\mathrm{CO_2}} \tag{3.25}$$

Magma sometimes freezes deep in the Earth as a glass before it releases any volatiles. Measurements of volatiles like CO_2, in such glasses are reported in terms of mass fractions (Wallace et al., 2015). To stay consistent with these unit conventions, we indicate the total carbon in undegassed magma as a mass fraction of CO_2 ($m_{\mathrm{CO2}}^{\mathrm{tot}}$). We can convert the mass fraction to a mole fraction using Equation (3.3):

$$\frac{m_{\mathrm{CO2}}^{\mathrm{tot}} \mu_{\mathrm{magma}}}{\mu_{\mathrm{CO_2}}} = x_{\mathrm{CO2}}^{\mathrm{tot}} = \frac{\gamma_{\mathrm{CO_2}}^{\mathrm{tot}}}{\gamma_{\mathrm{tot}}} = \frac{\gamma_{\mathrm{C}}^{\mathrm{tot}}}{\gamma_{\mathrm{tot}}} \tag{3.26}$$

Substituting Equation (3.26) into Equation (3.25) gives

$$\frac{m_{\mathrm{CO_2}}^{\mathrm{tot}} \mu_{\mathrm{magma}}}{\mu_{\mathrm{CO_2}}} = \frac{P_{\mathrm{CO_2}} + P_{\mathrm{CO}} + P_{\mathrm{CH_4}}}{P} \alpha_{\mathrm{gas}} + (1 - \alpha_{\mathrm{gas}}) x_{\mathrm{CO_2}} \tag{3.27}$$

Equation (3.27) is identical to Equation (3.11).

Graphite saturation and the solubility of CO, CH_4, and H_2

Several studies have shown that degassing can be affected by graphite saturation of of magma (Hirschmann and Withers, 2008) or by the solubility of CO, CH_4, and H_2 in magma (Wetzel et al., 2013; Ardia et al., 2013; Hirschmann et al., 2012). Our model for outgassing speciation used throughout the main text does not account for these complications. Here, we show that

our assumption is valid because it does not significantly change our results.

Consider the following equilibrium.

$$C + O_2 \leftrightarrow CO_2 \tag{3.28}$$

$$K_9 = \frac{f_{CO_2}}{a_C f_{O_2}} \approx \frac{P_{CO_2}}{a_C f_{O_2}} \tag{3.29}$$

Here, K_9 is the equilibrium constant given by $\exp(47457/T + 0.136)$, and a_C is the activity of carbon. To incorporate graphite saturation into our model, we first calculate outgassing speciation using the model described in the main text (Section 3.2.1). Next, we check for graphite saturate by calculating the activity of carbon using Equation (3.29). If $a_C < 1$, then we assume the melt is not graphite saturated and that the calculation is valid. If $a_C > 1$, then we assume graphite is saturated and recalculate outgassing speciation by replacing the carbon conservation equation (Equation (3.11)), with the graphite saturation equation with $a_C = 1$ (Equations (3.29)). Here, we are considering graphite saturation in the magma just before degassing occurs. Our treatment is different than, for example, the methods of Ortenzi et al. (2020) because they are accounting for graphite saturation much deeper in a planet during partial melting of the mantle.

Figure 3.10 is identical to Figure 3.3, except Figure 3.10 accounts for graphite saturation. Graphite saturation appears to have a small effect on the results, therefore it is justified to ignore it.

To incorporate the solubility of H_2, CH_4, and CO into our model, we add the following solubility relationships to or system of original outgassing equations (Section 3.2.1).

$$\exp(-11.403 - 0.000076P) = K_5 = \frac{x_{H_2}}{f_{H_2}} \approx \frac{x_{H_2}}{P_{H_2}} \tag{3.30}$$

$$\exp(-7.63 - 0.000193P) = K_6 = \frac{x_{CH_4}}{f_{CH_4}} \approx \frac{x_{CH_4}}{P_{CH_4}} \tag{3.31}$$

$$\exp(-41.02 - 0.00056P) = K_7 = \frac{x_{Fe(CO)_5}}{a_{Fe} f_{CO}^5} \approx \frac{x_{Fe(CO)_5}}{a_{Fe} P_{CO}^5} \tag{3.32}$$

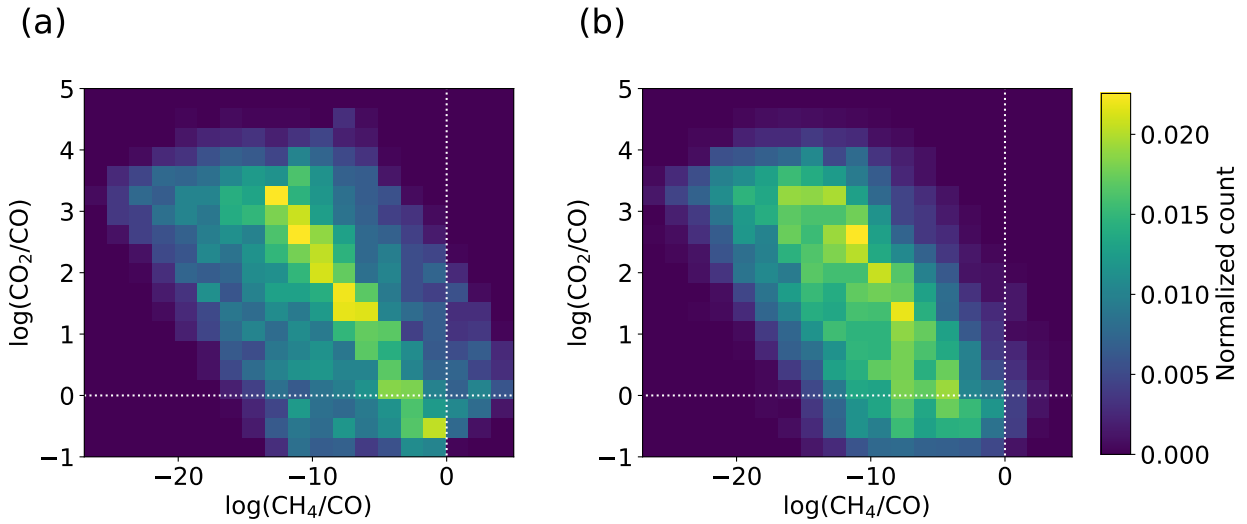

Figure 3.10: Identical to Figure 3.3, except here we account for graphite saturation in the melt. Like Figure 3.3 (a) is for ocean worlds and (b) is for Earth-like worlds. Graphite saturation has a small effect on the results.

Here, pressure dependent equilibrium constants K_5, K_6 and K_7 are from Hirschmann et al. (2012), Ardia et al. (2013), and Wetzel et al. (2013), respectively. For Equation (3.32), we take the activity of iron to be $a_{\rm Fe} = 0.6$ based on the experiments in Wetzel et al. (2013). Also, we only include the Equation (3.32) when the $f_{\rm O_2}$ < IW-0.55 (IW is the Iron-Wustite mineral buffer) because Wetzel et al. (2013) only observed CO dissolved in magma for these low oxygen fugacities.

We also alter the carbon and hydrogen atom conservation equations to accommodate for new molecules in the melt.

$$\frac{m^{\rm tot}_{\rm CO_2}\mu_{\rm magma}}{\mu_{\rm CO_2}} = \frac{P_{\rm CO_2} + P_{\rm CO} + P_{\rm CH_4}}{P}\alpha_{\rm gas} + (1-\alpha_{\rm gas})\left(x_{\rm CO_2} + x_{\rm CO} + x_{\rm CH_4}\right) \tag{3.33}$$

$$\frac{m^{\rm tot}_{\rm H_2O}\mu_{\rm magma}}{\mu_{\rm H_2O}} = \frac{P_{\rm H_2O} + P_{\rm H_2} + 2P_{\rm CH_4}}{P}\alpha_{\rm gas} + (1-\alpha_{\rm gas})\left(x_{\rm H_2O} + x_{\rm H_2} + 2x_{\rm CH_4}\right) \tag{3.34}$$

Here, x_i is the mol fraction of species i in the melt.

Figure 3.11 is identical to Figure 3.3, except Figure 3.11 accounts for H_2, CH_4 and CO

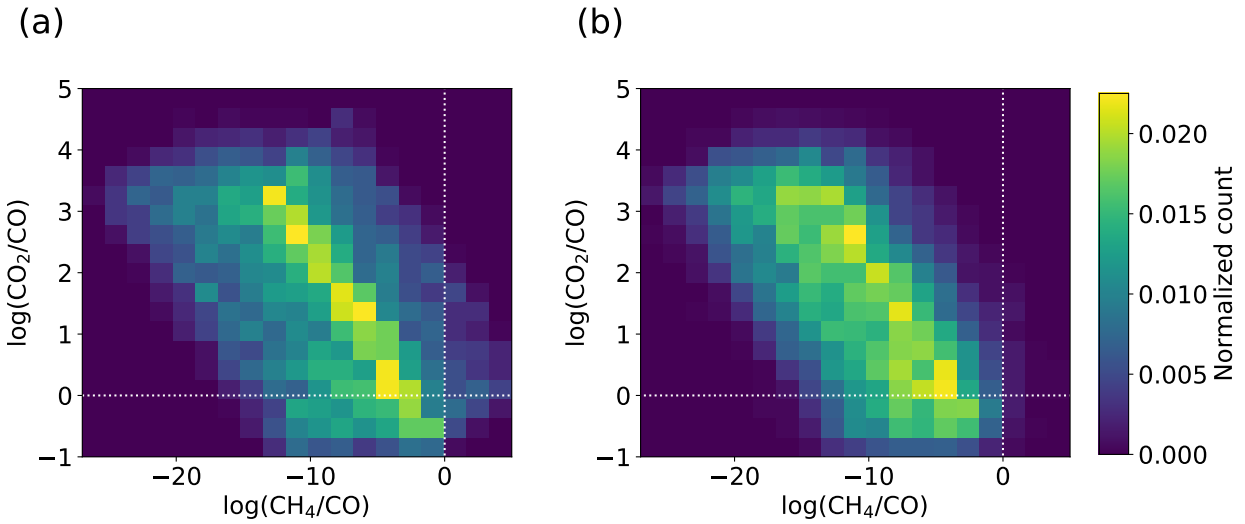

Figure 3.11: Identical to Figure 3.3, except here we account for the solubility of H_2, CH_4 and CO in the melt. Like Figure 3.3 (a) is for ocean worlds and (b) is for Earth-like worlds. H_2, CH_4 and CO solubility has a small effect on the results.

solubility in magma. The solubility of these three molecules has a small effect on the results, therefore they can be ignored.

Closed system cooling and chemical kinetics

Our model for volcanic outgassing is a thermodynamic equilibrium model. We assume that during magma eruptions gas bubbles chemically and thermally equilibrate with magma, and then are released to the atmosphere unaltered (Figure 3.1). This does not exactly reflect real degassing.

In reality, the chemical composition of gas bubbles changes as bubbles leave the magma and enter the atmosphere (Moussallam et al., 2019; Kadoya et al., 2020). As a bubble leaves magma, it cools down, and new chemical equilibria are preferred. When the gas bubble first begins cooling, it is still very hot, so chemical reactions keep the bubble near chemical equilibrium. Once the bubble is cold enough, chemical reactions slow, and ultimately cease, quenching or freezing the chemical composition of the gas bubble. Therefore, the cooling

process alters the chemistry of the gas.

Gas re-equilibration to lower temperatures explains the observed chemistry of volcanic gases globally (Moussallam et al., 2019), and Oppenheimer et al. (2018) provides a specific example of this phenomenon at Kilauea volcano, Hawaii. During eruptions at Kilauea, gas bubbles in the magma would rise to the surface. As the bubbles rose in the magma, they adiabatically expanded, which cooled the gas below the temperature of the magma. Chemical reactions during adiabatic expansion changed the chemical make-up of the bubble.

For the purposes of understanding potential CH_4 biosignature false positives from volcanoes, we need to know if bubble cooling might generate a substantial amount of CH_4. Here, we first consider the kinetics of methane generation and show that reactions are likely too slow to generate substantial CH_4 during gas cooling. Next, we show that our Monte Carlo simulation results (Figure 3.4) remain qualitatively unchanged even if our kinetics calculations are wrong, and CH_4 can be generated during gas cooling.

CO or CO_2 is converted to CH_4 through either of the net reactions (Schaefer and Fegley Jr, 2010)

$$CO + 3H_2 \leftrightarrow CH_4 + H_2O \tag{3.35}$$

$$CO_2 + 4H_2 \leftrightarrow CH_4 + 2H_2O \tag{3.36}$$

The rate limiting step to either CO or CO_2 conversion to CH_4 is debated in the literature (Zahnle and Marley, 2014), but following are two good candidates and their corresponding rate constants:

$$H_2 + H_2CO \rightarrow CH_3 + OH \tag{3.37}$$

$$k_{10} = 2.3 \times 10^{-10} \exp(-36200/T) \tag{3.38}$$

$$H + H_2CO \rightarrow CH_3 \tag{3.39}$$

$$k_{12} = 4.0 \times 10^{-11} \exp(-2068/T) \tag{3.40}$$

Here, k_{10} and k_{12} are rate constants ($cm^3\ s^{-1}$). The lifetime of CO or CO_2 conversion to

CH_4 is thus one of the following

$$\tau_{10}(\mathrm{CO}) = \frac{N_{\mathrm{CO}}}{k_{10} N_{\mathrm{H_2}} N_{\mathrm{H_2CO}}} \tag{3.41}$$

$$\tau_{12}(\mathrm{CO}) = \frac{N_{\mathrm{CO}}}{k_{12} N_{\mathrm{H}} N_{\mathrm{H_2CO}}} \tag{3.42}$$

$$\tau_{10}(\mathrm{CO_2}) = \frac{N_{\mathrm{CO_2}}}{k_{10} N_{\mathrm{H_2}} N_{\mathrm{H_2CO}}} \tag{3.43}$$

$$\tau_{12}(\mathrm{CO_2}) = \frac{N_{\mathrm{CO_2}}}{k_{12} N_{\mathrm{H}} N_{\mathrm{H_2CO}}} \tag{3.44}$$

Here, τ is chemical lifetime in seconds, and N_i is number density of species i in molecules cm^{-3}.

Figure 3.12 shows timescales of CH_4 generation (Equations (3.41)-(3.44)) during the closed system cooling of submarine volcanic gas. To determine gas chemistry just before a bubble is released from magma we use our speciation model (section 3.2.1). At 1473 K we calculate gas speciation assuming $P = 400$ bar, $f_{\mathrm{O_2}} = \mathrm{FMQ}$-4, $m^{\mathrm{tot}}_{\mathrm{CO_2}} = 0.1\%$, $m^{\mathrm{tot}}_{\mathrm{H_2O}} = 0.5\%$. We then calculate new chemical equilibrium as the gas cools assuming it is a closed system, i.e. we assume the gas is thermally and chemically decoupled from the magma (Figure 3.12a). Figure 3.12b shows the corresponding timescale of CH_4 generation (Equations (3.41)-(3.44)) at each temperature.

The "quench" temperature, i.e. the temperature where outgassing chemistry is frozen-in due to slow kinetics, of CH_4 depends on the cooling timescale of volcanic gases (not shown in Figure 3.12). CH_4 should quench where the cooling timescale is about the same as the timescale of CH_4 generation. After gases are released from a submarine volcano, we suspect they cool from magma temperatures to ocean temperatures on the order of seconds. If this is the case, then the CH_4 quench temperature is probably >1400 K. This would result in a negligible increase in the CH_4 content of the gas (Figure 3.12a).

Suppose that the CH_4 quench temperature was instead 1000 K. In this case, the CH_4 content of the gas would be increased by about a factor of 5 (Figure 3.12a). There are two

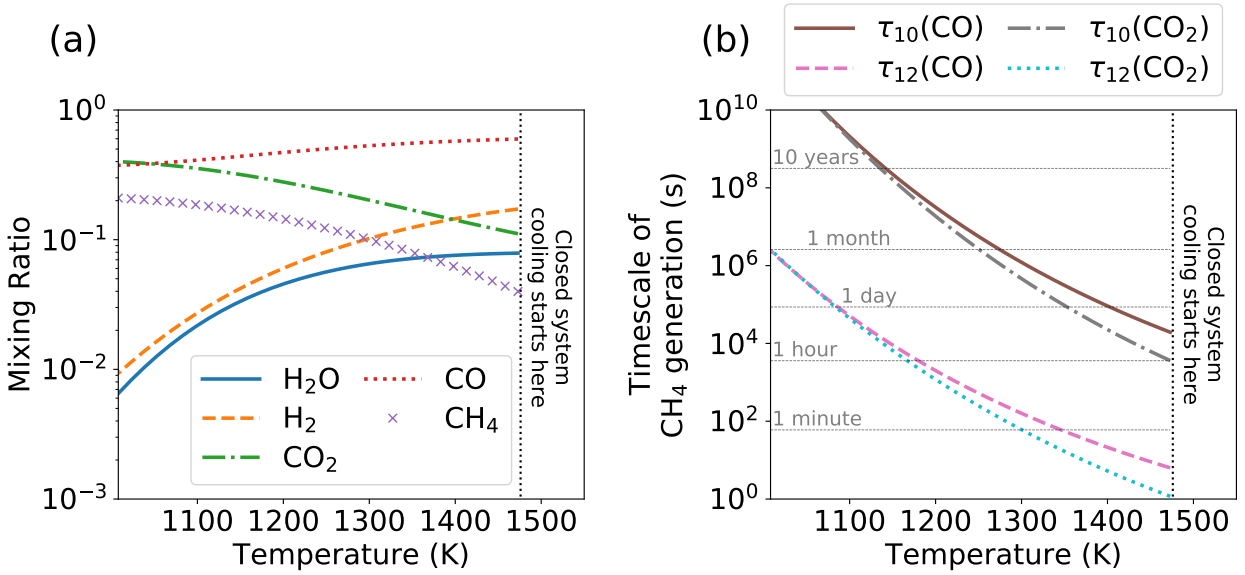

Figure 3.12: (a) Equilibrium composition as a function of temperature for a submarine volcanic gas which is cooled as a closed system and (b) timescales of CH_4 formation during closed system cooling. Timescales of volcanic gas cooling are not shown or calculated.

ways that a ∼1000 K CH_4 quench is possible. First, gas cooling could occur on timescales of months rather than seconds. According to Figure 3.12b, month-long gas cooling should quench CH_4 by 1000 K. Second, catalysts could dramatically speed up the reactions creating CH_4, which might allow for quench temperatures near 1000 K for even gas cooling timescales of seconds. In the following two paragraphs we show that either of these scenario would not significantly change our results.

To demonstrate that re-equilibration of gases to feasible lower temperatures does not change our conclusions, assuming low CH_4 quench temperatures can be achieved, we perform another Monte-Carlo simulation identical to the one described in Section 3.2.2 except we account for closed system cooling of volcanic gases. In the Monte-Carlo simulation we first calculate gas composition using our outgassing model (Section 3.2.1), then we re-equilibrate this gas mixture to the uniformly sampled gas equilibrium temperature between 800 and 1500 K. This range of gas equilibrium temperatures is the range observed in Earth's volcanic gases

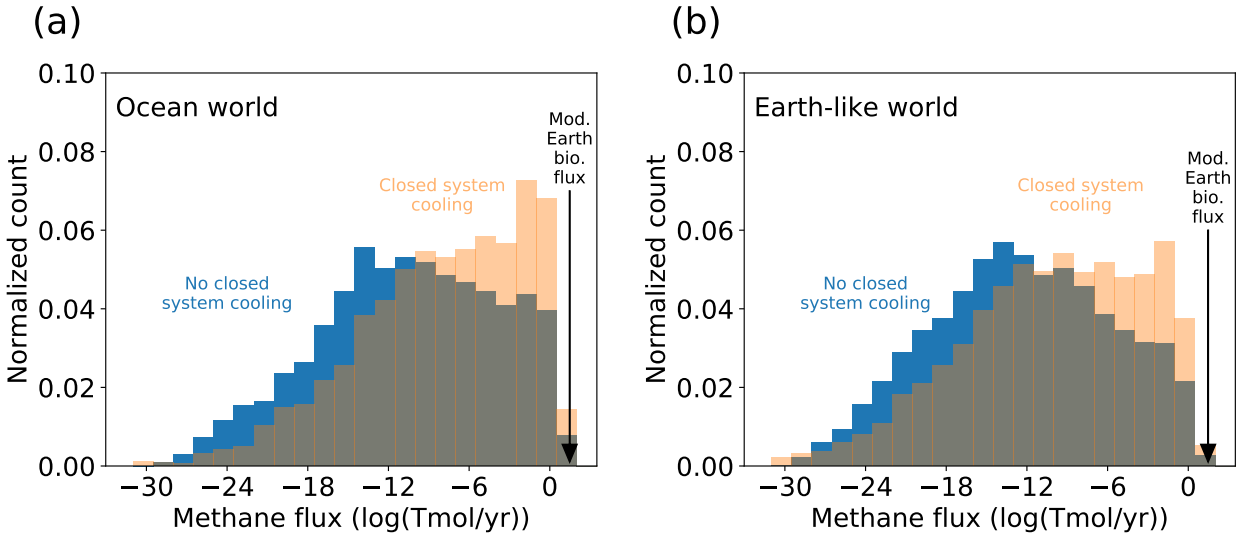

Figure 3.13: The blue histograms in (a) and (b) are identical to Figure 3.4c and 3.4d, and orange histograms are identical Monte Carlo simulations except they account for the closed system cooling of volcanic gases to equilibrium temperatures observed on Earth (800 to 1500 K). To calculate CH_4 fluxes, we used modern Earth's magma production rate.

(Moussallam et al., 2019). In cases where the randomly drawn gas equilibrium temperature is higher than the magma temperature, we assume no closed system cooling occurs.

Figure 3.13 is identical to Figure 3.4c and 3.4d, except Figure 3.13 accounts for closed system cooling of gases. Closed system cooling allows more CH_4 production on average, but still only 0.3% and 0.1% of calculations for ocean worlds or earth-like worlds respectively produce more than 10 Tmol CH_4/yr. The probability of volcanic CH_4 fluxes being comparable to modern Earth's biological flux (30 Tmol/yr) is still low.

In summary, changes in gas chemistry during cooling might cause our speciation model to under-predict the CH_4 produced by an amount that does not change our conclusions significantly. Further consideration of the kinetics of CH_4 generation in volcanic gases is beyond the scope of this paper.

3.6.2 Photochemical model boundary conditions

Table 3.5 shows boundary conditions used for the *Atmos* photochemical model. We used the same H_2O and temperature profile as Kharecha et al. (2005) for all simulations. The version of Atmos that we used has updated rate constants and H_2O cross sections following Ranjan et al. (2020).

Every simulation for planets orbiting the Sun uses a solar spectrum at 2.7 Ga calculated using methods described in Claire et al. (2012), although our results are not sensitive to age of the Sun. For planets orbiting a M8V star, we use estimates of TRAPPIST-1's spectrum derived by Lincowski et al. (2018), scaled so that the solar constant of the planet is 0.822 relative to modern Earth's. We use this solar constant because it places the simulated planet at the same relative distance from the inner edge of the habitable zone as Earth today (Kopparapu et al., 2013).

All of our models include the modern production rate of NO from lightning.

Table 3.5: Boundary conditions for photochemical modeling

Chemical Species	Deposition Velocity (cm s^{-1})	Mixing Ratio	Flux (molecules cm^{-2} s^{-1})
O	1	...	...
O_2	1.4×10^{-4}	...	...
H_2O	0	...	...
H	1	...	...
OH	1	...	...
HO_2	1	...	...
H_2O_2	2×10^{-1}	...	...
H_2	0	...	$5.9F_{CH_4}$
CO	1×10^{-8}	...	$1.7F_{CH_4}$
HCO	1	...	...
H_2CO	2×10^{-1}	...	...
CH_4	0	...	variable
CH_3	1	...	...
C_2H_6	0	...	...
NO	3×10^{-4}	...	...
NO_2	3×10^{-3}	...	...
HNO	1	...	...
O_3	7×10^{-2}	...	...
HNO_3	2×10^{-1}	...	...
H_2S	2×10^{-2}	...	$0.1F_{CH_4}$
SO_3	0	...	...
S_2	0	...	...
HSO	1	...	...
H_2SO_4	1	...	...
SO_2	1	...	$0.1F_{CH_4}$
SO	0	...	...
SO_4 aerosol	1×10^{-2}	...	...
S_8 aerosol	1×10^{-2}	...	...
hydrocarbon aerosol	1×10^{-2}	...	...
CO_2	...	variable	...
N_2	...	0.8	...

Notes. Species included in the photochemical scheme with a deposition velocity and flux of 0 include N, C_3H_2, C_3H_3, CH_3C_2H, CH_2CCH_2, C_3H_5, C_2H_5CHO, C_3H_6, C_3H_7, C_3H_8, C_2H_4OH, C_2H_2OH, C_2H_5, C_2H_4, CH, CH_3O_2, CH_3O, CH_2CO, CH_3CO, CH_3CHO, C_2H_2, $(CH_2)_3$, C_2H, C_2, C_2H_3, HCS, CS_2, CS, OCS, S, and HS. Here, deposition velocities follow those used by Schwieterman et al. (2019).

Chapter 4

RAPID TIMESCALE FOR AN OXIC TRANSITION DURING THE GREAT OXIDATION EVENT AND THE INSTABILITY OF LOW ATMOSPHERIC O_2

"To evaluate f_l, the fraction of such planets on which life develops, we perform a simple series of spectrographic observations. We first search for large amounts of molecular oxygen - a sure sign that something strange is happening on that planet." - Owen (1980)

This chapter was originally published in collaboration with David C. Catling, Kevin J. Zahnle and Mark W. Claire in the Proceedings of the National Academy of Sciences (Wogan et al., 2022), and is reproduced below with the permission of the journal.

Summary

The Great Oxidation Event (GOE), arguably the most important event to occur on Earth since the origin of life, marks the time when an oxygen-rich atmosphere first appeared. However, it is not known whether the change was abrupt and permanent or fitful and drawn out over tens or hundreds of millions of years. Here, we developed a 1-D time-dependent photochemical model to resolve time-dependent behavior of the chemically unstable transitional atmosphere as it responded to changes in biogenic forcing. When forced with step-wise changes in biogenic fluxes, transitions between anoxic and oxic atmospheres take between only 10^2 and 10^5 years. Results also suggest that O_2 between $\sim 10^{-8}$ and $\sim 10^{-4}$ mixing ratio is unstable to plausible atmospheric perturbations. For example, when atmospheres with these O_2 concentrations experience fractional variations in the surface CH_4 flux comparable to those caused by modern Milankovitch cycling, oxygen fluctuates between anoxic ($\sim 10^{-8}$) and oxic ($\sim 10^{-4}$) mixing ratios. Overall, our simulations are consistent with possible geologic evidence of unstable atmospheric O_2, after initial oxygenation, which could occasionally collapse from changes in biospheric or volcanic fluxes. Additionally, modeling favors mid-Proterozoic O_2 exceeding 10^{-4} - 10^{-3} mixing ratio, otherwise O_2 would periodically fall below 10^{-7} mixing ratio, which would be inconsistent with post-GOE absence of sulfur isotope mass-independent fractionation.

4.1 Introduction

Abundant atmospheric O_2 at 21% by volume is the most distinctive and consequential feature of Earth's atmosphere. Produced by cyanobacteria, algae and plants, O_2 is a clear sign of our biosphere that is detectable across interstellar space by telescopic spectroscopy (Meadows et al., 2018). Oxygen permits aerobic respiration, the only known metabolism with sufficient

energy yield that can sustain complex animal life (Catling et al., 2005). However, for about the first half of Earth's 4.5-billion-year-old history, the atmosphere had negligible O_2 (e.g. Catling and Zahnle, 2020). This changed ∼2.4 billion years ago.

The timing of the GOE, and magnitude of atmospheric O_2 concentrations before and after the GOE can be constrained by the geologic record of sulfur isotopes in combination with photochemical models. Archean and earliest Proterozoic sedimentary minerals contain sulfur isotopes with characteristic mass independent fractionation (MIF) which abruptly disappears 2.4 billion years ago (Warke et al., 2020). Sulfur MIF in marine sediments likely requires that atmospheric photochemistry produce elemental sulfur, S_8 (for explanation, see the introduction in Zahnle et al., 2006) (Pavlov and Kasting, 2002; Farquhar et al., 2000). Zahnle et al. (2006) used a 1-D photochemical model to show that atmospheric S_8 production only occurs when atmospheric O_2 is below $\sim 2 \times 10^{-7}$ mixing ratio. An often cited threshold of 2×10^{-6} was from an earlier photochemical model that did not simulate atmospheres with surface O_2 mixing ratios between 2×10^{-6} and $\sim 10^{-15}$ (Pavlov and Kasting, 2002). Therefore, the disappearance of the sulfur isotope MIF signal at 2.4 Ga is strong evidence that O_2 first rose above 2×10^{-7} mixing ratio.

Geologic evidence may suggest that the GOE was not a single monotonic rise of oxygen but characterized by oscillations. Using U-Pb dating, Gumsley et al. (2017) updated the chronology of sulfur isotope MIF in the stratigraphic record, finding evidence for two oxic-to-anoxic transitions between ~ 2.4 and ~ 2.3 Ga. More recently, Poulton et al. (2021) report 2.3 - 2.2 Ga marine sediments with sulfur isotopes consistent with approximately five oxic-to-anoxic transitions. Fluctuating O_2 levels coincide with three to four widespread glaciations, indicating extreme climate instability (Rasmussen et al., 2013). Overall, geochemical evidence tentatively suggests that O_2 concentrations and climate were unstable for 200 million years until ~ 2.2 Ga, which marks the most recent estimated timing of the permanent oxygenation of the atmosphere (Poulton et al., 2021). However, interpretations of oscillating O_2 have been questioned (Izon et al., 2022). While the geologic evidence for the O_2 oscillations remains equivocal, the data has raised significant questions regarding the

feasibility and timescales for Earth's great oxidation. Some have argued that the oxygen-rich atmosphere is more stable than an oxygen-poor atmosphere (Goldblatt et al., 2006), which favors a single rise of O_2 instead of O_2 oscillations.

Evidence for O_2 instability and the time-dependent behavior of O_2 concentrations have not been reconciled with atmospheric photochemical models. All previous models treated the GOE as successive photochemical steady states (Kasting and Donahue, 1980; Segura et al., 2003; Pavlov et al., 2001; Pavlov and Kasting, 2002; Zahnle et al., 2006; Gregory et al., 2021; Claire et al., 2014; Izon et al., 2017; Kurzweil et al., 2013). A photochemical steady state occurs when no atmospheric species changes concentration over time because their production and loss from reactions and surface sources (e.g. volcanoes or biology) are balanced. Such steady state calculations have been crucial for understanding the GOE by contextualizing sulfur isotope MIF observations (Pavlov and Kasting, 2002; Zahnle et al., 2006), and establishing the relationship between atmospheric O_2 concentrations and the degree to which O_3 blocks UV photons from Earth's surface (i.e. O_3 shielding) (Kasting and Donahue, 1980; Pavlov et al., 2001; Gregory et al., 2021), but they do not evaluate time-dependent changes and transient imbalances, or characteristic timescales.

Several theories for the rise of O_2 suggest that it relied on a global redox titration over 10^8 - 10^9 years involving oxidation of the upper mantle and/or crust, plausibly driven by hydrogen escape, which led to a tipping point where the source flux of O_2 exceeded a kinetically rapid O_2 sink from volcanic and metamorphic reductants (Catling et al., 2001; Claire et al., 2006; Kadoya et al., 2020; Holland, 2002; Kasting et al., 1993). Beyond the tipping point, O_2 flooded the atmosphere, reaching a new, long-term balance limited by oxidative weathering.

Here, we developed a novel, time-dependent 1-D photochemical model capable of investigating changes of O_2 at the tipping point itself over timescales 10^2 - 10^5 years rather than the longer-term planetary changes which initiated the GOE. We simulate changing O_2 as a time-dependent evolution, in contrast to the steady-state approach used in previous studies (e.g. Kasting and Donahue, 1980), because O_2 can change on relatively rapid timescales that are not well characterized by steady-states. With our model, we compute the time required

for an anoxic-to-oxic atmospheric transition, and the time required for de-oxygenation. Additionally, we investigate the stability of O_2 concentrations against perturbations to surface gas fluxes produced by biology. Finally, we use our model results to better constrain O_2 levels and stability during the GOE (starting $\sim$ 2.4 Ga), and during the mid-Proterozoic eon (1.8 to 0.8 Ga).

4.2 Methods

To investigate the transition between an anoxic and oxygen rich Earth, we use a photochemical model with one spatial dimension of altitude, approximating a global average vertical profile. One-dimensional photochemical models are typically governed by a simplification of the continuity equation for molecules:

$$\frac{\partial n_i}{\partial t} = -\frac{\partial}{\partial z}\Phi_i + P_i - L_i + R_{\text{i, rainout}} + Q_{\text{i, lightning}} \tag{4.1}$$

Table 4.1 defines all the variables and their units. Here, the flux (Φ_i) is given by

$$\Phi_i = -Kn\frac{\partial}{\partial z}\left(\frac{n_i}{n}\right) - D_i n_i \left(\frac{1}{n_i}\frac{\partial n_i}{\partial z} + \frac{1}{H_i} + \frac{1+\alpha_{\text{Ti}}}{T}\frac{\partial T}{\partial z}\right) \tag{4.2}$$

The above system of partial differential equations (PDEs) describes how the number density (n_i) of each chemical species i changes over altitude and time.

In our photochemical model, we solve a simplified version of Equation (4.1) which assumes that the total number density does not change over time ($\partial n/\partial t \approx 0$). This assumption is valid for atmospheric transitions which maintain approximately constant surface pressure and atmospheric temperature. The continuity equations can then be written in terms of mixing ratios (f_i) instead of number densities (see Appendix B.1 in Catling and Kasting (2017) for a derivation):

$$\frac{\partial f_i}{\partial t} = -\frac{1}{n}\frac{\partial}{\partial z}\Phi_i + \frac{P_i}{n} - \frac{L_i}{n} - \frac{R_{\text{i, rainout}}}{n} + \frac{Q_{\text{i, lightning}}}{n} \tag{4.3}$$

$$\Phi_i = -\left(K + D_i\right) n \frac{\partial f_i}{\partial z} - \zeta_i n f_i \tag{4.4}$$

$$\zeta_i = D_i \left(\frac{1}{H_i} - \frac{1}{H_a} + \frac{\alpha_{\mathrm{Ti}}}{T} \frac{\partial T}{\partial z} \right) \tag{4.5}$$

To approximate Equation (4.3), the model replaces the spatial derivatives with finite difference approximations, turning the system of PDEs into a larger system of ordinary differential equations (ODEs). This is the "method of lines" approach to solving a PDE. Catling and Kasting (2017), their Appendix B.2, provides a detailed description of how to do this with Equation (4.3), therefore we will omit a detailed description here, except to point out a sign error. The first two terms for the equation for B in their equation B.16 should have minus signs instead of plus signs.

The system of ODEs derived from finite differencing Equation (4.3) can be evolved forward in time with numerical integration. However, the photochemical ODEs are "stiff", meaning that some dependent variables (i.e. the mixing ratios) change much more quickly than others. For example, in the modern atmosphere, OH typically has a chemical lifetime of about 1 second, while CH_4 has a chemical lifetime of $\sim$10 years. Stiff equations require special, high stability, "implicit" integration methods. For more details on stiff equations and the implicit methods used to solve them, see Hairer and Wanner (1996).

Often, we solve for steady states of the photochemical continuity equation ($\frac{\partial f_i}{\partial t} = 0$). To find steady states, we begin with some initial atmospheric composition, then integrate Equation (4.3) forward in time until the atmosphere ceases to change, i.e. a steady state is reached. The assumption of photochemical steady state is approximately valid for most periods of Earth's history because the atmosphere changes slowly enough to be in a quasi-steady state.

However, the Paleoproterozoic rise of O_2 was a relatively fast atmospheric transition that is not well modeled as a photochemical steady state process. Therefore, describing it requires accurately solving the continuity equation over time.

Table 4.1: Variables in Equation (4.1)

Variable	Definition	Units
f_i	Mixing ratio of species i	dimensionless
n_i	Number density of species i	molecules cm^{-3}
z	Altitude	cm
t	Time	seconds
n	Total number density	molecules cm^{-3}
P_i	Total chemical production of species i	molecules cm^{-3} s^{-1}
L_i	Total chemical loss of species i	molecules cm^{-3} s^{-1}
$R_{\text{i, rainout}}$	Production and loss of species i from rainout	molecules cm^{-3} s^{-1}
$Q_{\text{i, lightning}}$	Production and loss of species i from lightning	molecules cm^{-3} s^{-1}
Φ_i	Vertical flux of species i	molecules cm^{-2} s^{-1}
K	Eddy diffusion coefficient	cm^2 s^{-1}
D_i	Molecular diffusion coefficient	cm^2 s^{-1}
H_i	$= N_a kT/\mu_i g$, The scale heights of species i	cm
H_a	$= N_a kT/\overline{\mu} g$, The average scale height.	cm
N_a	Avogadro's number	molecules mol^{-1}
k	Boltzmann's constant	erg K^{-1}
μ	Molar mass. $\overline{\mu}$ is mean molar mass of the atmosphere, and μ_i is the molar mass of species i	g mol^{-1}
g	Gravitational acceleration	cm s^{-2}
α_{Ti}	Thermal diffusion coefficient of species i. We neglect this term ($\alpha_{\text{Ti}} = 0$)	dimensionless
T	Temperature	K

Table 4.2: Fixed surface flux boundary conditions for SO_2, H_2S, H_2, and CO used in this study. All fluxes have units of molecules cm^{-2} s^{-1}

Model	SO_2	H_2S	H_2	CO
Archean Outgassing[a]	10^{10}	10^9	3×10^{10}	3×10^9
Modern Values[b]	3.5×10^9	3.5×10^8	1.22×10^8	2.65×10^{11}

[a] The same fluxes as the "Archean High" values from Table 1 in Zahnle et al. (2006).
[b] Surface flux values required to reproduce the concentration of each gas in the modern Earth's atmosphere. These values are also the "Case 1" fluxes described in Gregory et al. (2021).

To model the photochemistry of the GOE, we modified the photochemical model contained within the *Atmos* modeling suite (described in Appendix B of Catling and Kasting (2017)) so that it can accurately solve the time dependent behavior of Equation (4.3). We call the modified version of the model PhotochemPy. Instead of using a Backward Euler as in *Atmos*, we used CVODE BDF ODE solver from Sundials Computing (Hindmarsh et al., 2005). CVODE BDF is an implementation of the backward differential formulas (BDF) and is a gold-standard for solving large chemical kinetics problems. For details, see Section 4.6.

PhotochemPy is open source under an MIT license. The version of the code (v0.2.14) used in this paper and the corresponding Python scripts to reproduce work done in this article is at `https://doi.org/10.5281/zenodo.6824092`. However, the most up to date version of the code can be found at the following Github link: `https://github.com/Nicholaswogan/PhotochemPy`.

4.3 Results

To investigate the time-dependent behavior of O_2 during the GOE, we first computed grids of photochemical steady state atmospheres. These steady states establish context for time-dependent photochemical modeling described in subsequent sections. Figure 1 shows

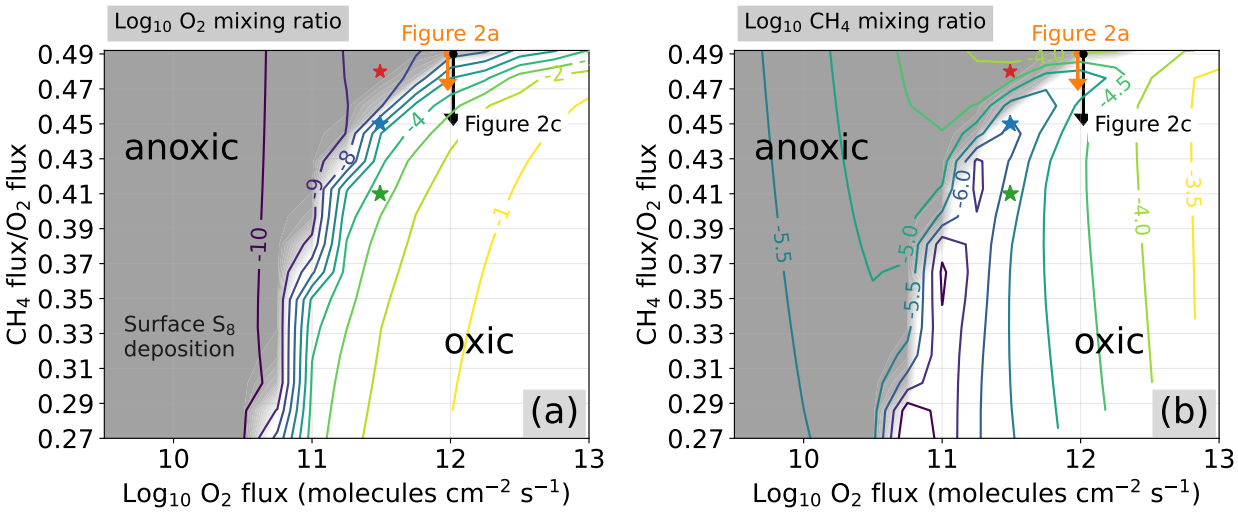

Figure 4.1: Colored contours show photochemical steady states of (a) $\log_{10}$ surface O_2 mixing ratio, and (b) $\log_{10}$ surface CH_4 mixing ratio as a function of $\log_{10}$ O_2 surface flux and CH_4 flux / O_2 flux. Grey shading indicates the magnitude of elemental S_8 production in the atmosphere, which is considered essential for the preservation of sulfur isotope mass independent fractionation in marine sediments. Peak S_8 production is $\sim 10^7$ molecules cm^{-2} s^{-1}. Grey shading fades to white for S_8 production less than 10^{-10} molecules cm^{-2} s^{-1}, a negligibly small value. Arrows labeled "Figure 4.2a" and "Figure 4.2c" indicate start and endpoints for time-dependent photochemical models of the oxic transition shown in Figures 4.2a and 4.2c. Red, blue and green stars are the initial conditions used in the simulations shown in Figures 4.4b, 4.4c, and 4.4d, respectfully.

predicted steady state surface O_2 mixing ratio (Figure 4.1a), surface CH_4 mixing ratio (Figure 4.1b), and the precipitation of atmospheric S_8 (gray shading) as a function of surface O_2 flux between 3×10^9 and 10^{13} molecules cm^{-2} s^{-1}, and CH_4 flux / O_2 flux ratios between 0.27 to 0.49 where gas fluxes are those entering the atmosphere. The surface O_2 fluxes reported here are net emissions into the atmosphere which exclude recycling within the biosphere. For reference, a comparable model of the modern Earth requires a surface O_2 flux of 10^{12} molecules cm^{-2} s^{-1}, and a CH_4 flux / O_2 flux of 0.09 (CH_4 flux = $\sim 9 \times 10^{10}$ molecules cm^{-2} s^{-1}) (Gregory et al., 2021). We consider a CH_4 flux / O_2 flux ratio close to 0.5 to be more realistic for the late Archean, prior to the GOE, because this ratio is expected if oxygenic photosynthesis is balanced by methanogenesis. In net (Claire et al., 2006), where "CH_2O" represents organic matter:

$$\begin{aligned} CO_2 + H_2O &\rightarrow CH_2O + O_2 \qquad \text{(Oxygenic Photosynthesis)} \\ 2CH_2O &\rightarrow CH_4 + CO_2 \qquad \text{(Methanogenesis)} \\ CO_2 + 2H_2O &\rightarrow CH_4 + 2O_2 \qquad \text{(Net)} \end{aligned} \tag{4.6}$$

The CH_4 flux / O_2 flux ratio is smaller than 0.5 on the modern Earth largely because of the microbial anerobic oxidation of methane via SO_4^{2-} in ocean sediments, a process that was unimportant in the anoxic mid-Archean ocean with little sulfate (Canfield et al., 2000; Catling et al., 2007; Olson et al., 2016). We include O_2 fluxes several orders of magnitude smaller than the modern value ($\sim 10^{12}$ molecules cm^{-2} s^{-1}) because of evidence for smaller primary productivity during the Proterozoic eon (Laakso and Schrag, 2019; Kipp et al., 2021).

Recall that atmospheric S_8 deposition is considered necessary to preserve sulfur isotope MIF in ocean sediments (Pavlov and Kasting, 2002). We find that S_8 production is not possible above $\sim 10^{-7}$ O_2 mixing ratio (the gray-to-white shading boundary in Figure 4.1), consistent with previous results (Zahnle et al., 2006).

Figure 4.1 uses Archean outgassing surface fluxes for CO, H_2, H_2S, and SO_2 listed in

Table 4.2, with the CO_2 surface mixing ratio fixed to 1% for all model runs - a reasonable value for the late Archean according to carbon cycle modeling (Krissansen-Totton et al., 2018a). Additionally, over the same span of surface O_2 fluxes and H_2 flux / O_2 flux ratios, we compute photochemical steady states for the modern fluxes for CO, CH_4, H_2S, and SO_2 listed in Table 4.2, again fixing CO_2 to 1%. The results are shown in Figure 4.5 in Chapter Appendix 4.6.1.

In the following sections, we calculate the time required to transition between different steady state atmospheres shown in Figures 4.1 and 4.5.

4.3.1 The timescale of atmospheric oxygenation

The orange arrow labeled "Figure 4.2a" in Figure 4.1 corresponds to the approximate start and end states of the time-dependent photochemical model run shown in Figure 4.2a. The model starts with an atmosphere at a steady state, then at $t = 0$ years, we impose a stepwise decrease in the surface methane flux from 4.9×10^{11} to 4.7×10^{11} molecules cm^{-2} s^{-1} (we keep the surface O_2 flux constant at 10^{12} molecules cm^{-2} s^{-1}). This perturbation causes O_2 to rise from 3×10^{-8} to 3×10^{-5} mixing ratio over $\sim$ 3500 years, eliminating photochemical S_8 production.

The O_2 transition in Figure 4.2a(i) is modulated by O_3 shielding of tropospheric H_2O (Kasting and Donahue, 1980). When a stratospheric O_3 layer begins to develop, OH production from H_2O decreases (Figure 4.2a(ii)). Decreasing OH concentrations prevent the mutual annihilation of O_2 and CH_4 (by $CH_4 + OH \rightarrow CH_3 + H_2O$ followed by $CH_3 + O_2 \rightarrow$ products), so O_2 levels increase. The mixing ratio of CH_4 also rebounds. O_3 shielding (protecting life on the surface from harmful solar UV radiation) is just barely beginning to operate in this example compared to the modern Earth. After the atmosphere reaches a new steady state, the atmospheric column has 3×10^{17} O_3 molecules cm^{-2}, some 26 times smaller than the modern value of 8×10^{18} molecules cm^{-2}. Note, the extent to which O_3 shields tropospheric H_2O can be strongly modulated by 3-D dynamical effects (Cooke et al., 2022), which we do not account for.

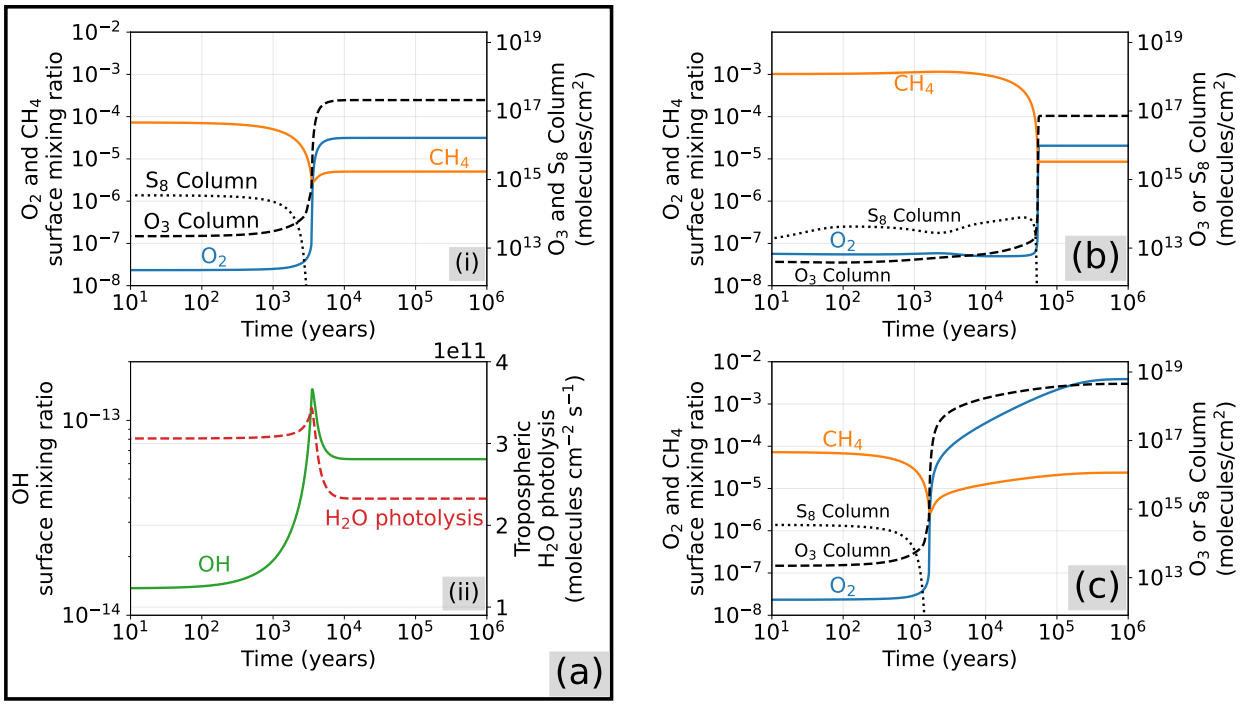

Figure 4.2: Three models of anoxic to oxic transitions. (a) Shows atmospheric oxygenation caused by a step-wise decrease in the methane flux from 4.9×10^{11} to 4.7×10^{11} molecules cm^{-2} s^{-1} (orange arrow in Figure 4.1). Panel (i) shows surface O_2 and CH_4 mixing ratios, and O_3 and S_8 column abundance over time; Panel (ii) shows OH surface mixing ratio and tropospheric H_2O photolysis rate. (b) Shows transition caused by step-wise increase in the O_2 flux from 10^{12} to 1.8×10^{12} molecules cm^{-2} s^{-1} and a stepwise increase in the CH_4 flux to maintain constant CH_4 flux / O_2 flux = 0.45 (Figure 4.5 in Chapter Appendix 4.6.1). Transition in (c) results from a step-wise decrease in the CH_4 flux from 4.9×10^{11} to 4.5×10^{11} molecules cm^{-2} s^{-1} (black arrow in Figure 4.1).

Like Figure 4.2a, Figure 4.2b also shows a transition between 5×10^{-8} and 2×10^{-5} O_2 mixing ratio, but this model uses the modern outgassing fluxes for CO, H_2, H_2S, and SO_2 listed in Table 4.2 instead of presumptive Archean outgassing values. Also, at $t = 0$ years, we impose a stepwise increase of the O_2 flux from 10^{12} to 1.8×10^{12} molecules cm^{-2} s^{-1} while keeping the CH_4 flux / O_2 flux ratio at 0.45 (see Figure 4.5 for context). While the anxoic-to-oxic transition itself still occurs rapidly, the atmosphere simulated in Figure 4.2b takes 60,000 years to reach the tipping point, which is much longer than the comparable O_2 transition shown in Figure 4.2a.

The time required for O_2 to begin to rise in concentration is controlled by the reservoir of reducing gases, primarily CH_4, H_2 and CO, in the pre-oxygenated atmosphere. Big reservoirs of reducing gases slow the timescale of oxygenation because reducing gases must be mostly removed before O_2 can increase. O_2 cannot increase while reducing gases are abundant because large oxygen sinks from reactions with reducing gases prevent it. That is why 3,500 years elapse before O_2 begins to rise in Figure 4.2a, and why 60,000 years elapse before O_2 rises in Figure 4.2b. Figure 4.2b starts with more reducing gases, which take longer to eradicate.

We can roughly estimate the time required for O_2 to begin to rise with a back-of-the-envelope calculation of the rate that reducing gases are eliminated from the anoxic atmosphere. The total reservoir of reducing gases in the pre-oxygenated atmosphere in O-equivalent units is

$$N_{\text{reducing}} = \sum_j N_j \alpha_j \approx -4N_{\text{CH}_4} - N_{\text{CO}} - N_{\text{H}_2} \tag{4.7}$$

Here, N_{reducing} is the O-equivalent column abundance of reducing gases (O_{equiv} molecules cm^{-2}), which is equal to the sum of all reducing gases in the atmosphere (N_j) multiplied by α_j, the redox state of each gas. Redox state is a relative quantity that requires defining redox-neutral reference species. Following previous models of the early Earth (Zahnle et al., 2006), we define H_2O, SO_2, CO_2 and N_2 as redox-neutral, with the oxygen redox parameter

$\alpha_{\rm O} = +1$. Therefore, $\alpha_{\rm H} = -0.5$, $\alpha_{\rm S} = -2$, and $\alpha_{\rm C} = -2$, from redox stoichiometry of hydrogen, sulfur and carbon, respectfully. It then becomes straight-forward to calculate the α_j for any molecule. For example, $\alpha_{\rm CH_4} = \alpha_{\rm C} + 4\alpha_{\rm H} = -2 - 2 = -4$. For a more in-depth explanation of atmospheric redox, see Section 3 in Harman et al. (2015) or Chapter 8 in Catling and Catling and Kasting (2017). $N_{\rm reducing}$ is approximately equal to the weighted sum of CH_4, H_2, and CO because these are the main reducing gases in an Archean Earth-like atmosphere.

The change in column abundance of reducing gases is the difference between the redox columns at the finial and initial atmospheric states.

$$\Delta N_{\rm reducing} = N^{\rm final}_{\rm reducing} - N^{\rm initial}_{\rm reducing} \tag{4.8}$$

In Figures 4.2a and 4.2b, we initiate the rise of oxygen by changing the surface flux of CH_4 and/or O_2 flux. We can quantify this flux perturbation in units of $O_{\rm equiv}$ molecules cm^{-2} s^{-1} ($\Delta F_{\rm O_{equiv}}$):

$$\begin{aligned} \Delta F_{\rm O_{equiv}} &= \sum_i F_i^{\rm final}\alpha_i - \sum_i F_i^{\rm initial}\alpha_i \\ &= (2F^{\rm final}_{\rm O_2} - 4F^{\rm final}_{\rm CH_4}) - (2F^{\rm initial}_{\rm O_2} - 4F^{\rm initial}_{\rm CH_4}) \end{aligned} \tag{4.9}$$

Therefore, the time required to oxidize the reducing gases in the atmosphere and permit oxygen to begin rising is approximately

$$\tau_{\rm oxy} = \left| \frac{\Delta N_{\rm reducing}}{\Delta F_{\rm O_{equiv}}} \right| \tag{4.10}$$

Plugging in values for the O_2 transition in Figure 4.2b yields $\tau_{\rm oxy}$ = 2,900 years, a value only slightly smaller than the 3,500 years predicted by the time-dependent photochemical model. For Figure 4.2b, $\tau_{\rm oxy}$ = 29,000 years, which is about a factor of 2 smaller than the figure from 1-D photochemistry. Our estimate is too small in this case because the reducing

column and its destruction rate is not constant prior to the rise of oxygen (see Section 4.6). This calculation illustrates that the time required for oxygen to begin rising, once a tipping point of fluxes is reached, mostly depends on the quantity of reducing gases in the pre-oxygenated atmosphere.

Figure 4.2c shows a more substantial anoxic-to-oxic transition compared to simulations shown thus far. We start with the same steady state atmosphere as in Figure 4.2a, except we decrease the methane flux by twice as much at $t = 0$, from 4.9×10^{11} to 4.5×10^{11} molecules cm^{-2} s^{-1} instead of 4.7×10^{11} molecules cm^{-2} s^{-1} (we keep the surface O_2 flux constant at 10^{12} molecules cm^{-2} s^{-1}). O_2 begins to rise and eliminates S_8 production after ~ 1500 years, but O_2 will reach higher levels because of the lower CH_4 flux. It takes $\sim 300,000$ years for O_2 to reach its final steady state abundance of 4×10^{-3} mixing ratio. While the switch from 10^{-8} to 10^{-5} O_2 mixing ratio remains as rapid as in Figure 4.2a, the predicted increase in O_2 concentrations to 4×10^{-3} requires far longer. This timescale is roughly analogous to the time required to deplete H_2 and CH_4 reservoirs to allow O_2 to initially rise in concentration.

In summary, the timescale for O_2 to rise in concentration depends on the reservoir of redox gases in the atmosphere, and the magnitude of the perturbation to redox surface fluxes. For O_2 to rise from 10^{-8} to 10^{-5}, reducing gases must first be removed, which can take 1000s to 10,000s of years (Figures 4.2a and 4.2b). Increasing O_2 concentrations beyond 10^{-5} to near % levels, requires filling a large O_2 reservoir, which occurs on 10^5 year timescales in our model run (Figure 4.2c).

4.3.2 The time required for deoxygenation

Here, we use our time-dependent photochemical model to address the controversy of the reversibility of the oxic transition (Poulton et al., 2021; Izon et al., 2022). Figure 4.3a, 4.3b, and 4.3c show the reverse of model runs shown in Figure 4.2a, 4.2b, and 4.2c. For each model run, we start with an atmosphere initially at a steady state at the end of the simulations shown in Figures 4.2a - 4.2c. Then we impose a stepwise change in the O_2 and CH_4 flux at $t = 0$ years to return the atmosphere to anoxia. The reversal of Figures 4.2a, 4.2b, and

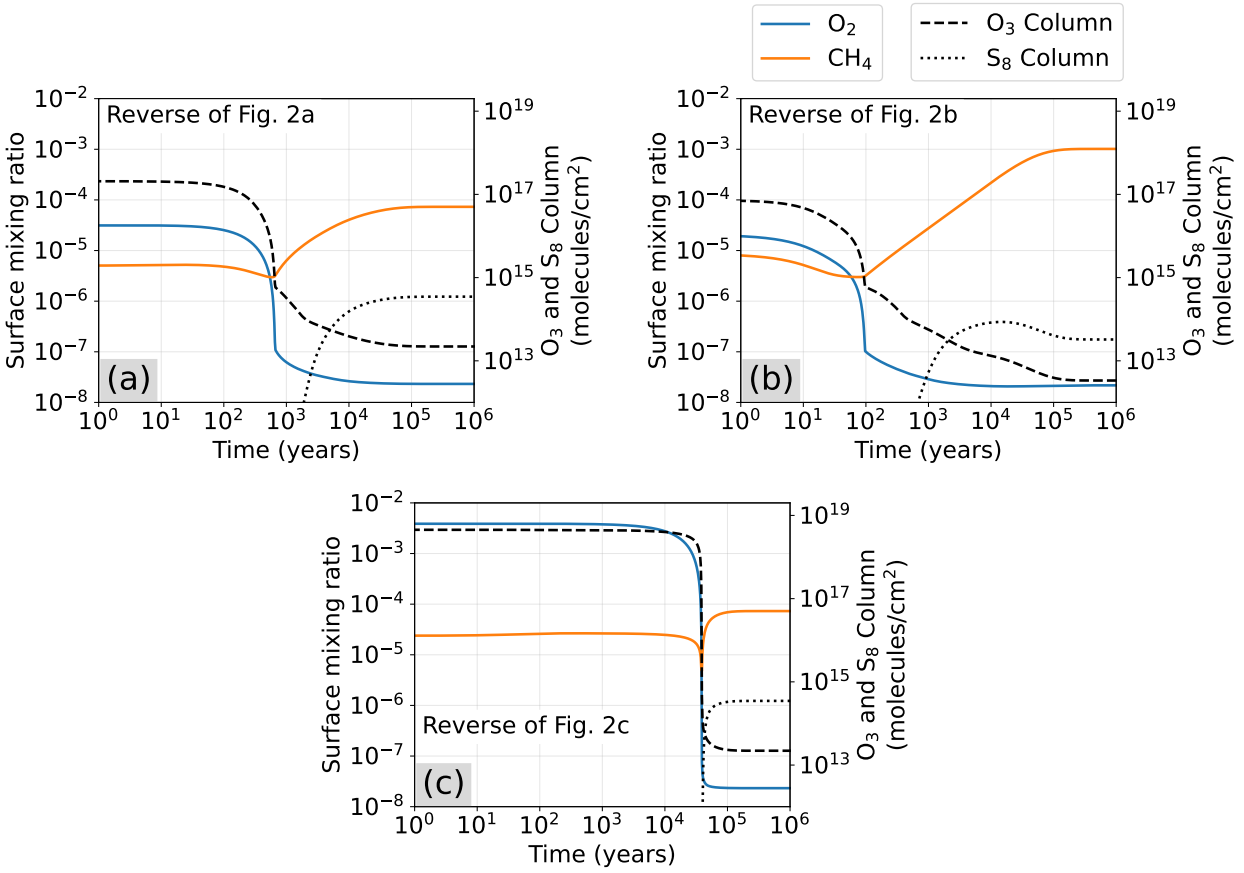

Figure 4.3: (a), (b) and (c) show simulated reversal of the oxic transitions shown in Figures 4.2a, 4.2b, and 4.2c, respectfully. Each oxic to anoxic transition is caused by a stepwise change of the CH_4 flux and O_2 flux at $t = 0$ years.

4.2c take approximately 700, 100, and 40,000 years, respectively, in comparison to the 3,500, 60,000, and the 300,000 years required for oxygenation.

Like the timescale for oxygenation, the timescale of de-oxygenation depends on the column abundance of redox sensitive gases. In the previous section, we established that the timescale required for O_2 to begin to rise is merely the time required to deplete the reservoirs of CH_4 and other reducing gases. Analogously, the timescale of deoxygenation is determined by the reservoir of O_2 and other oxidizing gases in the oxygenated atmosphere. The reversal shown in Figure 4.3b starts with only 2×10^{-5} O_2, which can be depleted very quickly, allowing the return of an anoxic atmosphere. In contrast, the reversal shown in Figure 4.3c takes 40,000 years because the atmosphere starts with 4×10^{-3} O_2, which takes longer to deplete.

4.3.3 The stability of post-GOE atmospheric oxygen

In the previous two sections we show that reservoirs of redox gases, primarily methane and oxygen, give the atmosphere chemical inertia, controlling the timescale of O_2 changes. When reservoirs are big, for similar flux perturbations, the O_2 mixing ratio will change relatively slowly over time; however, when reservoirs are small, photochemistry permits rapid O_2 transitions. Therefore, the abundance of redox gases in an atmosphere is closely linked to the photochemical stability of oxygen.

Figure 4.4a shows the steady state inertial timescale of redox gases, τ_{inertia}, over the same axes as Figure 4.1, which shows mixing ratios. τ_{inertia} is the sum of all redox gases in the atmospheric column (O-equivalent molecules cm^{-2}), divided by a characteristic flux perturbation, which we take to be 10% of the O_2 flux:

$$\tau_{\text{inertia}} = \frac{N_{\text{redox}}}{F_{\text{redox perturb.}}} = \frac{\sum_i |\alpha_i| N_i}{0.1 \alpha_{O_2} F_{O_2}} \tag{4.11}$$

We choose the characteristic flux perturbation to be 10% of the O_2 flux because it is the same order of magnitude as natural redox variations that occur on the modern Earth during

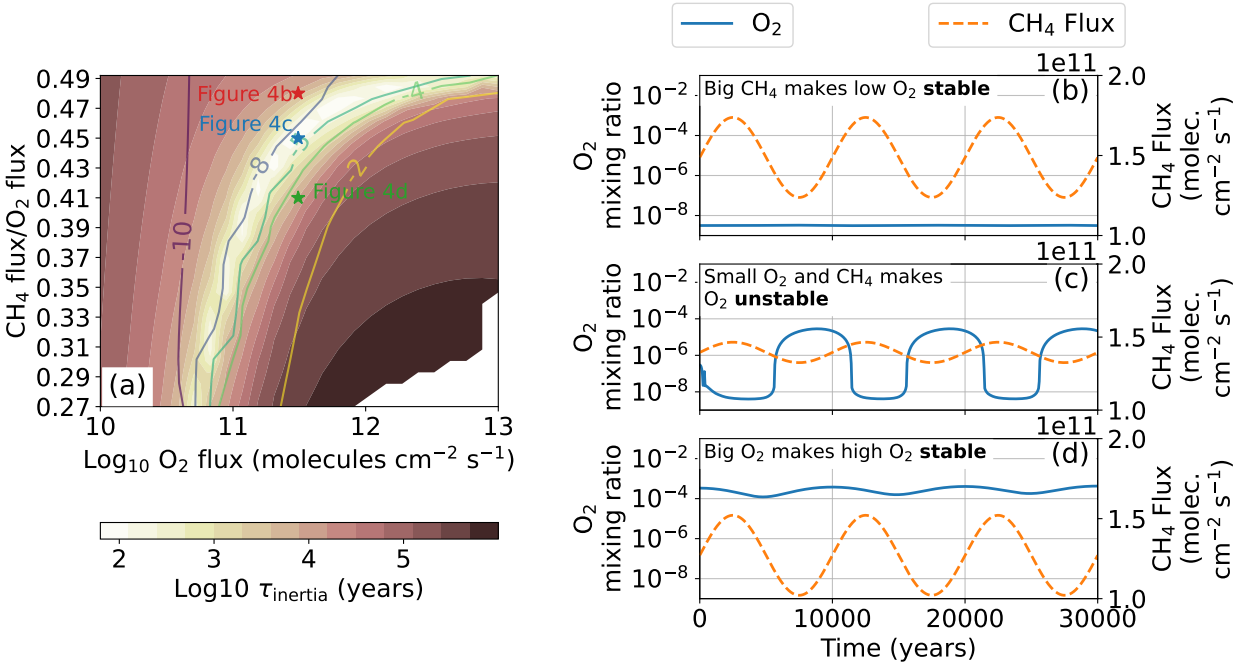

Figure 4.4: The photochemical stability of O_2. Shading in (a) shows the steady state inertial timescale of redox gases (Equation (4.11)), and colored contours are the steady state $\log_{10}$ surface O_2 mixing ratio (same as Figure 4.1a). (b), (c), and (d) are time-dependent photochemical simulations with oscillating CH_4 surface fluxes, each beginning with steady state atmospheres indicated in (a). O_2 stability is directly proportional to the column abundance of redox gases in the atmosphere.

Milankovitch cycling (see the Discussion section). An upper limit for the characteristic flux perturbation would be 100% of the O_2 flux. This would decrease all τ_{inertia} values in Figure 4.4a by a factor of 10, which would not change our interpretation. Since CH_4, CO, H_2, and O_2 are the most important redox gases, the numerator in Equation (4.11) is well approximated by $4N_{CH_4} + N_{CO} + N_{H_2} + 2N_{O_2}$. Oxygen is the most prone to change for the smallest τ_{inertia} values, coinciding with O_2 mixing ratios between $\sim 10^{-8}$ and $\sim 10^{-5}$ shown in the whitish region of Figure 4.4a.

The time-dependent photochemical models shown in Figures 4.4b - 4.4d illustrate the relationship between τ_{inertia} and O_2 instability. To produce Figure 4.4b, we started with the steady state atmosphere indicated on Figure 4.4a, then imposed 17% amplitude oscillations to the CH_4 flux with a period of 10,000 years. This forcing had no perceptible effect on the 3×10^{-9} atmospheric O_2. A similar 20% CH_4 flux oscillations also did not significantly perturb an oxic atmosphere starting with 3×10^{-4} O_2 (Figure 4.4d). However, just 5% CH_4 flux oscillations cause ~ 4 orders-of-magnitude oscillations in surface oxygen concentrations for an incipiently oxic atmosphere starting with 3×10^{-7} O_2 (Figure 4.4c). O_2 is most unstable where the abundance of all redox gases is smallest relative to a characteristic redox surface flux (the whitish area of Figure 4.4a) between $\sim 10^{-8}$ and $\sim 10^{-5}$ O_2 mixing ratio. Stability continually increases outside of this range of O_2 concentrations.

While O_2 was relatively stable in the Figure 4.4b and 4.4d simulations, it does not mean these atmospheres and initial oxygen concentrations are stable to all atmospheric perturbations. The stability of any O_2 mixing ratio depends on the atmospheric forcings that are likely in nature. In the discussion section, we argue that the CH_4 flux oscillations used in Figure 4.4 are realistic because comparable fractional changes in the methane flux have occurred over the past 650,000 years.

Flux oscillations over timescales greater than $\sim$ 10 years are required to significantly affect O_2 concentrations. Imposing 100% amplitude fluctuations to the CH_4 flux with a period of 1 year, starting with the same atmosphere as Figure 4.4c, did not significantly alter the atmosphere over time. Atmospheres with between $\sim 10^{-8}$ and $\sim 10^{-5}$ O_2 contain

some CH_4 and O_2, which gives the atmosphere inertia against annual to decadal change.

4.4 Discussion

Recently, Gregory et al. (2021) computed photochemical steady state atmospheres for a wide range of surface O_2 and CH_4 fluxes and found bistable O_2 concentrations. Their model allows steady state atmospheres for O_2 concentrations below 6×10^{-7} and above 2×10^{-3} mixing ratio but admits few steady state solutions in between. They hypothesized that feedbacks between O_2 and O_3 shielding eliminate most solutions with these intermediate O_2 concentrations. In contrast, our model can yield a steady state solution with intermediate O_2 concentrations given the right constant surface flux boundary conditions (e.g. Figure 4.2b; see also Gregory et al. Figure 8). The difference might be caused by different steady state convergence criteria, chemical reaction networks, boundary conditions, or a combination of these factors.

However, a photochemical steady state, e.g., at 10^{-6} O_2 mixing ratio, does not mean that such an atmosphere is stable and realistic over 10^5 to 10^6 year timescales. Gas fluxes from Earth's surface can vary during these timescales and significantly change O_2 concentrations (results section).

For example, in the past 650,000 years, the biogenic methane flux has oscillated with an amplitude of 25% (6×10^9 molecules cm^{-2} s^{-1}) and a 100,000 year period (Hopcroft et al., 2018; Spahni et al., 2005). On the modern Earth, methanogens in wetlands are a major source of atmospheric methane (Canadell et al., 2021). Every 100,000 years, ice sheets have advanced and retreated, covering and uncovering wetlands, changing the CH_4 flux to the atmosphere. These ice ages and methane flux variations are in response to Milankovitch cycles with characteristic periods between 20,000 and 100,000 years. This exact same methane oscillation would not have occurred in the late Archean or early Proterozoic because modern wetlands did not exist then, but a similar process involving microbial mats is conceivable.

Zhao et al. (2018) modeled cyanobacterial mats on Proterozoic land, finding that they

could have been a substantial CH_4 source to the atmosphere. Ice sheets covering and uncovering microbial mats could have affected global CH_4 fluxes. Figure 4.4c illustrates the effect of 5% methane flux variations over Milankovitch timescales on an atmosphere starting with 3×10^{-7} O_2. O_2 oscillates nearly four orders of magnitude between $\sim 10^{-8}$ (anoxic) and $\sim 10^{-4}$ (oxic) (Figure 4.4).

An oscillating methane flux is only one of many possible atmospheric perturbations. The early Proterozoic geologic record preserves evidence of large igneous provinces (LIPs), or massive volcanic eruptions (Gumsley et al., 2017). In Section 4.6, we show that the H_2 and CO outgassed from a significant LIP eruption could cause the O_2 surface mixing ratio to drop from 2×10^{-5} to 4×10^{-9} in $\sim$ 100 years, causing a return to sulfur isotope MIF. In this simulation, we use the maximum LIP eruption rates reported in the literature (Bryan et al., 2010). In addition to LIPs, a Snowball Earth event concurrent with the GOE would have presumably affected gases produced by the biosphere (Rasmussen et al., 2013).

Constant surface gas fluxes from biology and volcanism for millions of years in the aftermath of the initial rise of O_2 are unlikely. Additionally, our photochemical modeling shows that for atmospheres with transitional O_2 concentrations, relatively small atmospheric perturbations (e.g. a CH_4 flux change of 5%) over timescales as short as 100s of years can cause O_2 to change by orders of magnitude (e.g. Figure 4.3b). Therefore, substantial variability of O_2 during the GOE appears possible.

For these reasons, our photochemical modeling results are compatible with recently published evidence of fluctuating sulfur isotope MIF (Poulton et al., 2021; Gumsley et al., 2017) indicating that O_2 was unstable between 2.4 and 2.2 Ga. We find that shut-off of S_8 aerosol production, which is required to produce sulfur isotope MIF, occurs at $\sim 10^{-7}$ O_2 mixing ratio, a region of the parameter space where O_2 is prone to rapid change (Figure 4.4). But, oxygen surface levels between $\sim 10^{-8}$ and $\sim 10^{-4}$ mixing ratio were likely unstable. Short period changes to the biosphere, or volcanic outgassing rates could have caused order of magnitude O_2 changes over 100 to 100,000 year timescales. Occasionally, big perturbations to the atmosphere, such as a LIP, might have lowered O_2 concentrations enough for sulfur

isotope MIF to reoccur. Note, the above explanation for the cause of O_2 oscillations prior to 2.2 Ga is complicated by S-MIF data presented in Izon et al. (2022), which do not suggest the same O_2 variability found by Poulton et al. (2021).

After 2.2 Ga, and during the mid-Proterozoic, sulfur isotope MIF never returned. Therefore, this time must have had O_2 concentrations large enough to prevent O_2 collapse. Our modeling shows that larger O_2 concentrations give the atmosphere chemical inertia, slowing atmospheric deoxygenation (Figure 4.3). It is therefore challenging to reconcile our modeling results with the interpretation of Planavsky et al. (2014b), who used Proterozoic chromium isotopes to argue that O_2 could not have been larger than 2×10^{-4} mixing ratio. Such a small O_2 reservoir would have been unstable to LIP eruptions, or variations in the CH_4 flux from Milankovitch cycles (Figure 4.4), which both have evidence for occurring in the mid-Proterozoic stratigraphic record (Zhang et al., 2015; Meyers and Malinverno, 2018; Le-Cheminant and Heaman, 1989). We conclude that for stability, mid-Proterozoic O_2 levels should have exceeded $\sim 10^{-4}$. This conclusion is compatible with mid-Proterozoic Fe isotopes in ironstones, which suggest O_2 levels between approximately 2×10^{-4} - 2×10^{-3} mixing ratio (Wang et al., 2022).

Our results are not sensitive to the changing solar UV photon flux between the GOE ($\sim$ 2.4 Ga) and the mid-Proterozoic. Re-calculating Figure 4.1 using the solar UV flux at 1.3 Ga (Claire et al., 2012) results in surface O_2 and CH_4 surface mixing ratios within a factor of 2 of Figure 4.1.

Our work also has implications for the most likely oxygen levels before the GOE. Johnson et al. (2021) analyzed molybdenum isotopes in the Archean sedimentary record for signs of continental oxidative weathering. Their work is compatible with two end-member interpretations: (1) if Archean O_2 was evenly distributed over the globe, then the surface O_2 mixing ratio was $> 3\times10^{-8}$ and $< 2\times10^{-7}$, or (2) if O_2 accumulation was geographically restricted, then the O_2 surface flux was greater than 0.01 Tmol yr^{-1} (3×10^7 molecules cm^{-2} s^{-1}). Our modeling suggests (1) is unlikely because we find that O_2 is likely unstable over geologic time for this range of oxygen levels.

In our modeling, we do not explicitly consider redox reservoirs in the oceans, sediments, crust, and mantle for good reason. These reservoirs are coupled to the atmosphere and can modulate O_2 levels. However, the timescale of equilibration between the atmosphere and other redox reservoirs is often relatively long (e.g. 100 Myr for organic carbon in continental sediments), so we consider them to be approximately constant over the timescale of O_2 transitions ($< 10^5$ years).

A caveat is the coupling between redox reservoirs in the atmosphere, crust or sediments might depend on atmospheric composition. An example is the pyrite oxidation rate, which depends on the partial pressure of oxygen (Gregory et al., 2021). We do not explicitly consider such feedbacks, which could affect the timescale of changing O_2 levels.

An additional, related caveat is that our model does not consider biological feedbacks. The rise of O_2 would limit habitats for anaerobes, and permit more widespread aerobic respiration, potentially dropping the CH_4 flux / O_2 flux ratio further than we have modeled here. Also, a stronger ozone UV shield would make new habitats for cyanobacteria and allow the expansion of life on land, promoting chemical and oxidative weathering. All these changes, which we do not explicitly model, would modulate oxygen levels. In this article, we impose changes in the CH_4 and O_2 flux that are suppose to be representative of a changing biosphere, but a better model would determine more realistic changes in gas fluxes by directly coupling 1-D photochemistry and biology.

4.5 Conclusions

Our time-dependent photochemical modeling of the Great Oxidation Event suggests that oxygen can rise and fall over geologically short periods of time. For an anoxic to oxic transition, once a tipping point of imbalanced redox fluxes is reached, the reservoir of reducing gases in the atmosphere must be eliminated before O_2 can begin to rise. This takes 100s to 10,000s of years. O_2 accumulation to just hundredths or tenths of percent levels requires filling a large O_2 reservoir, which may occur on a 10^5 year timescales. Atmospheric de-oxygenation occurs over similar periods of time, mainly controlled by the magnitude of the

initial O_2 abundance.

We also find O_2 instability, especially for mixing ratios between $\sim 10^{-8}$ and $\sim 10^{-5}$. For these O_2 concentrations, photochemistry demands that both CH_4 and O_2 be relatively small in concentration. This small reservoir of redox sensitive gases permits rapid changes to the atmosphere's redox state. For example, for an atmosphere starting with 3×10^{-7} O_2, 5% amplitude oscillations to the methane flux with a period of 10,000 years cause oxygen to fluctuate four orders of magnitude between anoxic and oxic. Additionally, we show that a LIP eruption could cause the collapse of O_2 and the return of sulfur isotope MIF for an atmosphere starting with 2×10^{-5} O_2 mixing ratio (Supporting Information).

We emphasize that the short term (10^2 - 10^5 year) variability in O_2 levels considered here occurred on the backdrop of the billion year oxidation of the crust and mantle, and long-term organic burial, which are argued to be the ultimate causes of the rise of oxygen on Earth (e.g. Catling et al., 2001).

Overall, our modeling is compatible with, but does not prove, proposed geologic evidence for fluctuating and unstable atmospheric O_2 after the initial rise of oxygen 2.4 billion years ago. A single, uni-directional, oxidation event remains plausible, although would require strong and perhaps biological feedbacks promoting permanent substantial changes in the global CH_4 flux / O_2 flux ratio. While this is evident between the Archean (CH_4 flux / O_2 flux $\sim$ 0.5) and modern (CH_4 flux / O_2 flux $\sim$ 0.1) biospheres, the dynamics of the Proterozoic biosphere remain largely unexplored. Also, our results suggest that a stable, post-GOE, mid-Proterozoic atmosphere would need an O_2 mixing ratio exceeding a value in the 10^{-4} - 10^{-3} range.

4.6 Chapter Appendix

4.6.1 Photochemical modeling details

All Great Oxidation Event (GOE) simulations use the solar spectrum at 2.4 Ga, calculated with methods described in Claire et al. (2012). We also always include chemical rainout and

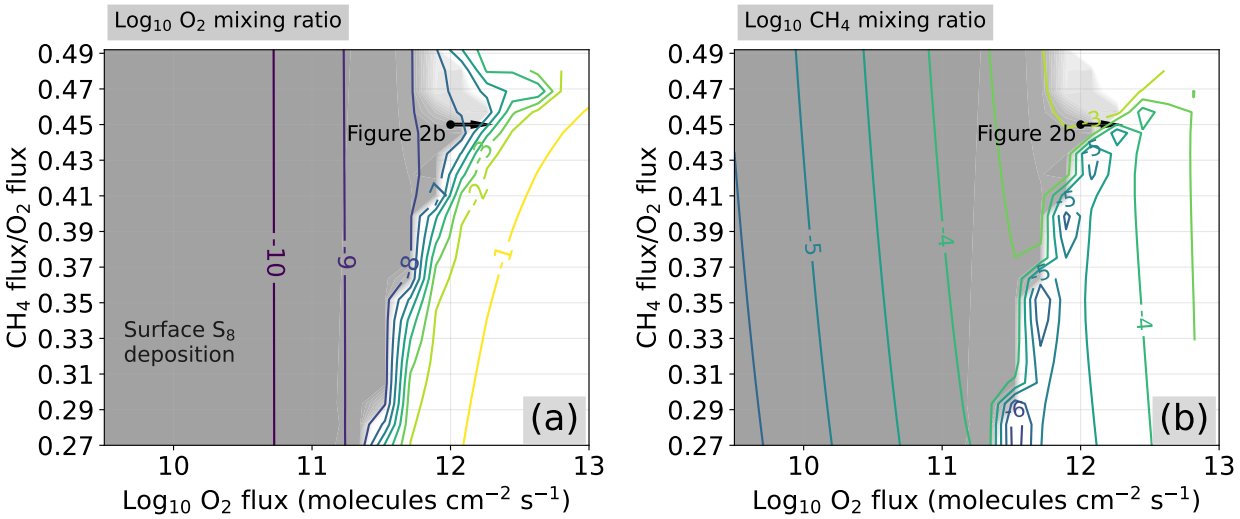

Figure 4.5: Identical to Figure 4.1, except we use the "Modern Values" surface fluxes in Table 4.2. The time-dependent photochemical simulation shown in Figure 4.2b, is indicated with a black arrow.

NO production from lightning. 95% of steady state simulations conserve redox to a factor better than 10^{-6}. 3% of models, all with $> 0.1\%$ steady-state O_2, conserve redox to a factor of $\sim 10^{-3}$. Figure 4.5 shows results from steady-state photochemical simulations over the same parameter space as Figure 4.1, except using the "Modern Values" fluxes from Table 4.2. Figure 4.6 shows assumed eddy diffusion and temperature profiles.

4.6.2 Estimating the timescale of the rise of O_2

In Section 4.3, we estimated the timescale for the rise of O_2 using the following equation:

$$\tau_{\text{oxy}} = \left| \frac{\Delta N_{\text{reducing}}}{\Delta F_{\text{O}_{\text{equiv}}}} \right| \tag{4.12}$$

Applying this equation to the Figure 4.2b simulation:

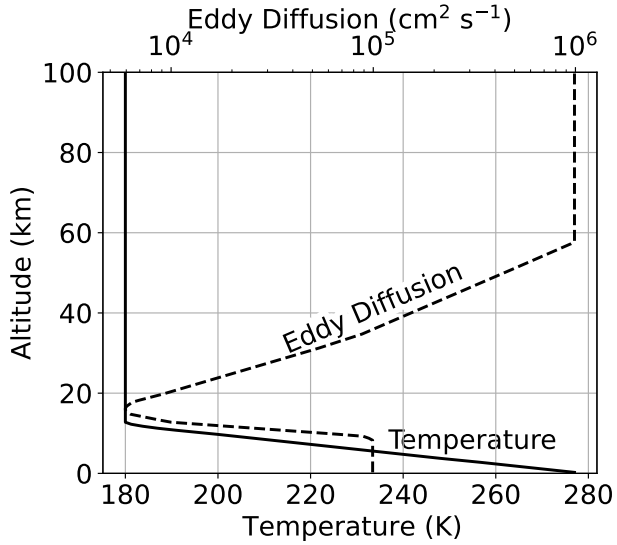

Figure 4.6: The temperature and eddy diffusion used for every simulation.

$$\begin{aligned}\Delta F_{\mathrm{O_{equiv}}} &= (2F_{\mathrm{O_2}}^{\mathrm{final}} - 4F_{\mathrm{CH_4}}^{\mathrm{final}}) - (2F_{\mathrm{O_2}}^{\mathrm{initial}} - 4F_{\mathrm{CH_4}}^{\mathrm{initial}}) \\ &= (2(1.8\times10^{12}) - 4(8.1\times10^{11})) - (2(1.0\times10^{12}) - 4(4.5\times10^{11})) \\ &= 1.6\times10^{11}\ \mathrm{molecules\,cm^{-2}\,s^{-1}}\end{aligned} \tag{4.13}$$

$$\tau_{\mathrm{oxy}} = \left|\frac{\Delta N_{\mathrm{reducing}}}{\Delta F_{\mathrm{O_{equiv}}}}\right| = \left|\frac{1.47\times10^{23}}{1.6\times10^{11}}\right| = 9.8\times10^{11}\ \mathrm{s} = 29,000\ \mathrm{years} \tag{4.14}$$

This estimation is about a factor of two smaller than the ∼60,000 years predicted by our time-dependent photochemical model.

Figure 4.7 shows the column of reducing gases and its destruction rate during the Figure 4.2b simulation. Our estimation for the timescale of oxygenation (Equation (4.14)) is off by a factor of two because the reducing column evolves over time, and our estimation of its destruction rate ($\Delta F_{\mathrm{O_{equiv}}}$) is too large. In the photochemical model, chemistry and transport does not permit a reducing column destruction rates identical to the imposed change in redox

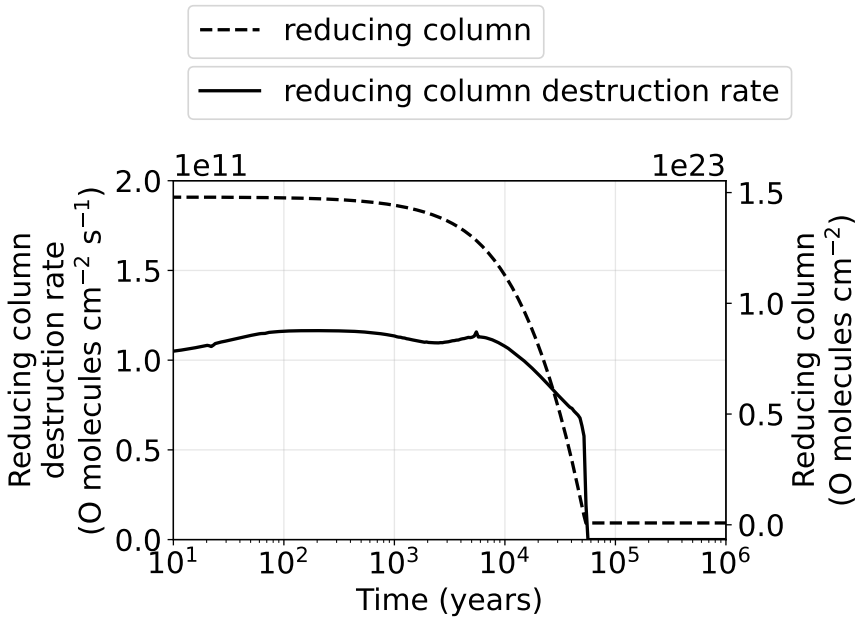

Figure 4.7: Reducing gas column and its destruction rate for the simulation shown in Figure 4.2b.

fluxes at the surface (1.6×10^{11} O molecules cm^{-2} s^{-1}).

4.6.3 A Large Igneous Province may have destabilized atmospheric oxygen

Here, we show that the H_2 and CO outgassing from large igneous provinces (LIPs), or massive volcanic eruptions, could have potentially caused the collapse of transitional O_2 concentrations ($\sim 10^{-8}$ to $\sim 10^{-4}$ mixing ratio).

To compute H_2 and CO outgassing rates from LIPs, we use the outgassing model described in Wogan et al. (2020b). To briefly summarize, the model estimates the composition of gas bubbles suspended in magma just prior to release into the overlying atmosphere or ocean. Gas composition is computed by solving a system of equations including solubility relationships for H_2O and CO_2, gas-phase equilibrium relationships, and mass conservation of hydrogen and carbon. The model has five inputs: Magma oxygen fugacity, temperature, and overburden pressure, and the H_2O and CO_2 mass fractions ($m^{\mathrm{tot}}_{\mathrm{H_2O}}$, and $m^{\mathrm{tot}}_{\mathrm{CO_2}}$) in the magma

before degassing occurs. For LIPs, we assume a magma oxygen fugacity one log-unit below the fayalite-magnetite-quartz mineral redox buffer (i.e. ΔFMQ-1) following Archean proxies (Aulbach and Stagno, 2016). See Chapter 7 in Catling and Kasting (2017) for a description of the fayalite-magnetite-quartz redox buffer. Additionally, we use $m^{\text{tot}}_{\text{H}_2\text{O}} = 0.5$ wt% and $m^{\text{tot}}_{\text{CO}_2} = 0.05$ wt% which agrees with estimates of LIP volatile concentrations (Wallace et al., 2015). Finally, we take the degassing temperature and pressure to be 1473 K and 1 bar, respectfully. With these inputs, our outgassing model predicts 1.6×10^{-2} mol H_2/kg magma and 1.7×10^{-3} mol CO/kg magma.

Converting gas production rates (e.g. mol H_2/kg magma) into gas fluxes to the atmosphere requires estimations of magma eruption rates during LIPs. Basaltic LIPs typically last several million years and cumulatively produce $> 3 \times 10^{18}$ kg magma (Self et al., 2015). This magma is release over 10s to 100s of eruptions each lasting several years to 10s of years with eruptions rates between 3×10^{13} to 3×10^{15} kg magma yr^{-1} (Bryan et al., 2010). Multiplying these eruption rates by calculated gas production yields H_2 fluxes between 1.9×10^9 and 1.9×10^{11} molecules cm^{-2} s^{-1} and CO fluxes between 2.0×10^8 and 2.0×10^{10} molecules cm^{-2} s^{-1}.

The time-dependent photochemical simulation shown in Figure 4.8 shows how atmospheric O_2 responds to maximum LIP H_2 and CO outgassing scenario. The simulation starts with an atmosphere initially at equilibrium, then at $t = 0$ years, we increase the H_2 and CO outgassing fluxes by 1.9×10^{11} and 2.0×10^{10} molecules cm^{-2} s^{-1}, respectfully. O_2 drops from 2×10^{-5} to 4×10^{-9} in 100 years. Basaltic LIP eruptions can last for 10s of years (Bryan et al., 2010), so a 100 year eruption, which is required to cause O_2 to collapse, is within the realm of possibility. However, the period of anoxia would likely be maintained for only a few hundred years, until the eruption ceased. Several periods of anoxia, each corresponding to a significant eruption, might occur during an entire several-million-year LIP event.

It is unclear whether a 100 year period of anoxia is detectable in the geologic record of multiple sulfur isotopes. A single sample from the sedimentary record might represent a

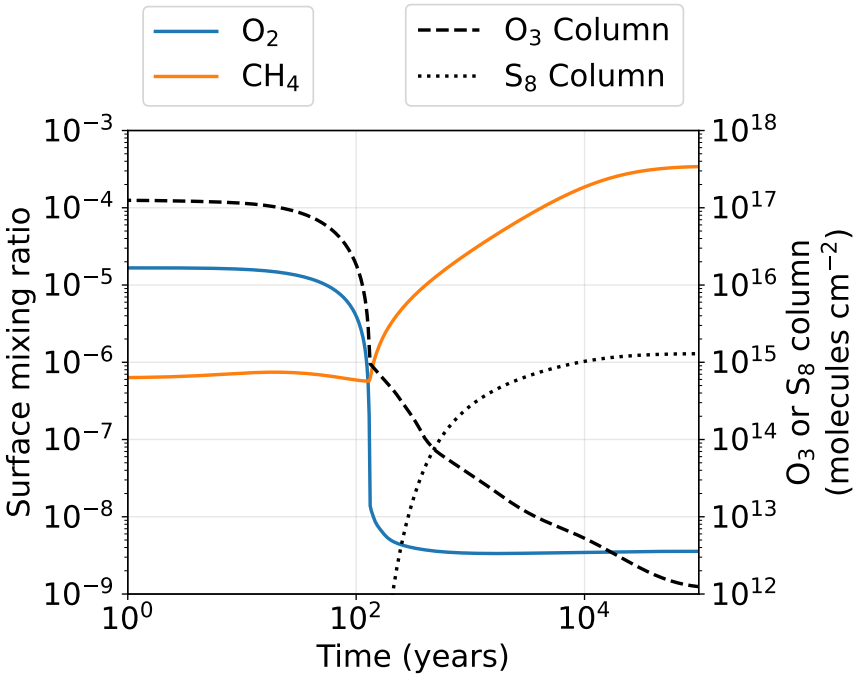

Figure 4.8: Modeled oxic to anoxic transition caused by H_2 and CO outgassing from a large igneous province eruption. The simulation begins with a photochemical equilibrium atmosphere, and then is perturbed by a stepwise increase of the H_2 and CO flux by 1.9×10^{11} and 2.0×10^{10} molecules cm^{-2} s^{-1}, respectfully. A LIP eruption should able to produce these outgassing fluxes for the 100 years required to cause O_2 to collapse (see text).

period of time greater than 100 years, thus containing sulfur from both an oxic and anoxic atmosphere, diluting the S-MIF signal. Evaluating the detectability of short-term anoxia in the sedimentary record of sulfur isotopes is an interesting target for future work coupling in-situ and bulk rock measurements (Meyer et al., 2017).

LIPs may have additional effects on the atmosphere that we are not accounting for in the above calculations. For example, increased Cl outgassing could catalyze O_3 and CH_4 destruction (e.g. $Cl + O_3 \rightarrow ClO + O_2$ and $Cl + CH_4 \rightarrow HCl + CH_3$), which could have a non-trivial effect on the O_2 concentration.

Part II

ORIGIN OF LIFE ATMOSPHERIC CHEMISTRY

Chapter 5

ORIGIN OF LIFE MOLECULES IN THE ATMOSPHERE AFTER BIG IMPACTS ON THE EARLY EARTH

"At the time such objects were falling on the moon similar objects fell on the Earth... Its materials would have fallen through the atmosphere in the form of iron and silicate rains and would have reacted with the atmosphere in the process... Thus it is very difficult to see how the primitive atmosphere of the Earth contained more than trace amounts of other compounds of carbon, nitrogen, oxygen and hydrogen than CH_4, H_2O, NH_3 (or N_2) and H_2."
- Urey (1952)

At the time of writing, this chapter is accepted for publication in the Planetary Science Journal written in collaboration with David C. Catling, Kevin J. Zahnle, and Roxana Lupu.

Summary

The origin of life on Earth would benefit from a prebiotic atmosphere that produced nitriles, like HCN, which enable ribonucleotide synthesis. However, geochemical evidence suggests that Hadean air was relatively oxidizing with negligible photochemical production of prebiotic molecules. These paradoxes are resolved by iron-rich asteroid impacts that transiently reduced the entire atmosphere, allowing nitriles to form in subsequent photochemistry. Here, we investigate impact-generated reducing atmospheres using new time-dependent, coupled atmospheric chemistry and climate models, which account for gas-phase reactions and surface-catalysis. The resulting H_2-, CH_4- and NH_3-rich atmospheres persist for millions of years, until hydrogen escapes to space. HCN and HCCCN production and rainout to the surface can reach 10^9 molecules cm^{-2} s^{-1} in hazy atmospheres with a mole ratio of $CH_4/CO_2 > 0.1$. Smaller CH_4/CO_2 ratios produce HCN rainout rates $< 10^5$ molecules cm^{-2} s^{-1}, and negligible HCCCN. The minimum impactor mass that creates atmospheric $CH_4/CO_2 > 0.1$ is 4×10^{20} to 5×10^{21} kg (570 to 1330 km diameter), depending on how efficiently iron reacts with a steam atmosphere, the extent of atmospheric equilibration with an impact-induced melt pond, and the surface area of nickel that catalyzes CH_4 production. Alternatively, if steam permeates and deeply oxidizes crust, impactors $\sim 10^{20}$ kg could be effective. Atmospheres with copious nitriles have > 360 K surface temperatures, perhaps posing a challenge for RNA longevity, although cloud albedo can produce cooler climates. Regardless, post-impact cyanide can be stockpiled and used in prebiotic schemes after hydrogen has escaped to space.

5.1 Introduction

Two essential aspects of life are a genome and catalytic reactions, so the presence of ribonucleotide molecular "fossils" in modern biochemistry (White, 1976; Goldman and Kacar,

2021) and the ability of RNAs to store genetic information and catalyze reactions have led to the hypothesis that RNA-based organisms originated early (Cech, 2012; Gilbert, 1986). This hypothesis proposes a stage of primitive life with RNA as a self-replicating genetic molecule that evolved by natural selection, which, at some point, became encapsulated in a cellular membrane and may have interacted with peptides from the beginning in the modified hypothesis of the RNA-Peptide World (e.g. Di Giulio, 1997; Muller et al., 2022). In any case, RNA must be produced abiotically on early Earth for such scenarios. Chemists have proposed several prebiotic schemes that require nitriles - hydrogen cyanide (HCN), cyanoacetylene (HCCCN), cyanamide (H_2NCN), and cyanogen (NCCN) - to synthesize ribonucleobases, which are building blocks of RNA (Benner et al., 2020; Sutherland, 2016; Yadav et al., 2020).

Abiotic synthesis of nitriles in nature is known to occur efficiently from photochemistry in reducing N_2-CH_4 atmospheres (Zahnle, 1986; Tian et al., 2011). Indeed, Titan's atmosphere, composed of mostly N_2 and CH_4, makes HCN, HCCCN and NCCN (Strobel et al., 2009).

Geochemical evidence does not favor a volcanic source for a CH_4-rich prebiotic atmosphere. Redox proxies in old rocks indicate that Earth's mantle was only somewhat more reducing 4 billion years ago (Aulbach and Stagno, 2016; Nicklas et al., 2019). Therefore, volcanoes would have mostly produced relatively oxidized gases like H_2O, CO_2 and N_2 instead of highly reduced equivalents, H_2, CH_4 and NH_3 (Holland, 1984; Catling and Kasting, 2017; Wogan et al., 2020a). Thus, steady-state volcanism would have likely produced Hadean (4.56 - 4.0 Ga) air with CO_2 and N_2 as bulk constituents, whereas reducing gases, such as CH_4, would have been minor or very minor.

However, Urey (1952) suggested that the prebiotic atmosphere was transiently reduced by large asteroid impacts. In more detail, Zahnle et al. (2020) argued that iron-rich impact ejecta could react with an impact-vaporized ocean to generate H_2 ($Fe + H_2O \leftrightarrow FeO + H_2$). As the H_2O- and H_2-rich atmosphere cools, their chemical equilibrium modeling with parameterized quenching finds that H_2 can combine with atmospheric CO or CO_2 to generate CH_4. After several thousand years of cooling, the steam condenses to an ocean, leaving a H_2 dominated

atmosphere containing CH_4. Zahnle et al. (2020) used a photochemical box model to show that such a reducing atmosphere would have generated prebiotic molecules like HCN. The reducing atmospheric state terminates when H_2 escapes to space after millions of years.

Model simplicity in Zahnle et al. (2020) left critical questions unanswered. Their model of a cooling steam post-impact atmosphere did not explicitly simulate chemical kinetics pertinent to Earth, which may inaccurately estimate the generated CH_4. Additionally, their photochemical box model did not include all relevant reactions or distinguish between different prebiotic nitriles (e.g. HCN and HCCCN). Finally, Zahnle et al. (2020) only crudely computed the climate of post-impact atmospheres, yet surface temperature is important for understanding the possible fate of prebiotic feedstock molecules. These molecules are needed to initiate prebiotic synthesis and must be available in the prebiotic environment.

Here, we improve upon the calculations made in Zahnle et al. (2020) using more sophisticated and accurate models of post-impact atmospheres. We estimate post-impact H_2 production by considering reactions between the atmosphere and delivered iron, and equilibration between the atmosphere and impact-generated melt. Our model explicitly simulates the 0-D chemical kinetics of a cooling steam atmosphere, considering gas-phase reactions, as well as reactions occurring on nickel surfaces which catalyze CH_4 production given that nickel is expected to be delivered by big impactors. After post-impact steam condenses to an ocean, we simulate the long-term evolution of a reducing atmosphere with a 1-D photochemical-climate model, quantifying HCN and HCCCN production and the climate in which they are deposited on Earth's surface. Additionally, we discuss the possible fate and preservation of prebiotic molecules in ponds or lakes on Hadean land. Finally, we discuss how "lucky" primitive life was if created by post-impact molecules, given a need to not be subsequently annihilated by further impactors.

5.2 Methods

We organize our investigation of post-impact Hadean atmospheres in three phases of atmospheric evolution depicted in Figure 5.1. Below, we briefly describe our numerical models

for each phase and complete descriptions can be found in the Chapter Appendix.

In Phase 1, an impactor collides with Earth, vaporizing the ocean, and H_2 is generated by reactions between the atmosphere and iron-rich impact ejecta, and atmospheric reactions with an impact-produced melt pond. Our model of this phase (Chapter Appendix 5.6.1) accounts for H_2 generation from impactor iron by assuming each mole of iron delivered to the atmosphere removes one mole of oxygen. For example, Fe can sequester O atoms from steam:

$$\mathrm{Fe} + \mathrm{H_2O} \rightarrow \mathrm{FeO} + \mathrm{H_2} \tag{5.1}$$

Simulations that consider reactions between the atmosphere and impact-melted crust follow a similar procedure to the one described in Itcovitz et al. (2022). Our model requires that the atmosphere and melt have the same oxygen fugacity. The oxygen fugacity of the melt is governed by relative amounts of ferric and ferrous iron (Kress and Carmichael, 1991):

$$0.5\mathrm{O_2} + 2\mathrm{FeO} \leftrightarrow \mathrm{Fe_2O_3} \tag{5.2}$$

We assume that oxygen atoms can flow from the atmosphere into the melt (or visa-versa), and use an equilibrium constant for Reaction 5.2 from Kress and Carmichael (1991). Finally, we compute a chemical equilibrium state of the atmosphere (or atmosphere-melt system) at 1900 K using thermodynamic data from NIST for 96 gas-phase species (Chapter Appendix 5.6.3). The result gives the estimated amount of H_2 generated by an impact.

In Phase 2 of Figure 5.1, the steam atmosphere cools for thousands of years generating CH_4 and NH_3, and eventually, the steam condenses to an ocean. We simulate these events with the 0-D kinetics-climate box model fully described in Chapter Appendix 5.6.2. The gas-phase model tracks 96 species connected by 605 reversible reactions (Chapter Appendix 5.6.3), but we do not account for photolysis. The model also optionally accounts for reactions that occur on nickel surfaces using the chemical network described in Schmider et al. (2021). As discussed later in Section 5.3.2, nickel is potentially delivered to Earth's surface by impacts

which may catalyze methane production. In the model, atmospheric temperature changes as energy is radiated to space and is modulated by latent heat released from water condensation. We estimate the net energy radiated to space by using a parameterization of calculations performed with our radiative transfer code (Chapter Appendix 5.6.4).

Table 5.1: Opacities used in climate modeling

Line absorption	Continuum CIA absorption	Rayleigh Scattering
H_2O, CO_2, CH_4	CO_2-CO_2, N_2-N_2, CH_4-CH_4, H_2-CH_4, H_2-H_2, H_2O-H_2O, H_2O-N_2	N_2, CO_2, H_2O, H_2

During Phase 3, photochemistry generates HCN and other prebiotic molecules. Hydrogen in the H_2 dominated atmosphere escapes to space over millions of years, ushering in the return of a CO_2 and N_2 atmosphere. We use our time-dependent photochemical-climate model, *Photochem* (Chapter Appendix 5.6.3), to simulate this phase of atmospheric evolution. The model solves a system of partial differential equations approximating molecular transport in the vertical direction and the effect of chemical reactions, photolysis, condensation, rainout in droplets of water, and hydrogen atmospheric escape. Specifically, the model rains out haze particles and HCN among a few other atmospheric species listed in Chapter Appendix 5.6.3. We simulate diffusion-limited and hydrodynamic hydrogen escape using Equation (47) in Zahnle et al. (2020). Our reaction network (Chapter Appendix 5.6.3) acceptably reproduces the steady-state composition of Earth and Titan (Figure 5.20 in Chapter Appendix 5.6.3). When reproducing the chemistry of Earth and Titan we fix the temperature profile to measured values, rather than self-consistently compute the climate. We evolve the model equations accurately over time using the CVODE Backward Differential Formula (BDF) method (Hindmarsh et al., 2005). As the atmosphere evolves, we compute self-consistent temperature structures using the radiative transfer code described and validated in Chapter Appendix 5.6.4. Unless otherwise noted in the text, our climate calculations use the opacities in Table 5.1, which is a subset of the opacities available in our radiative transfer code (Table

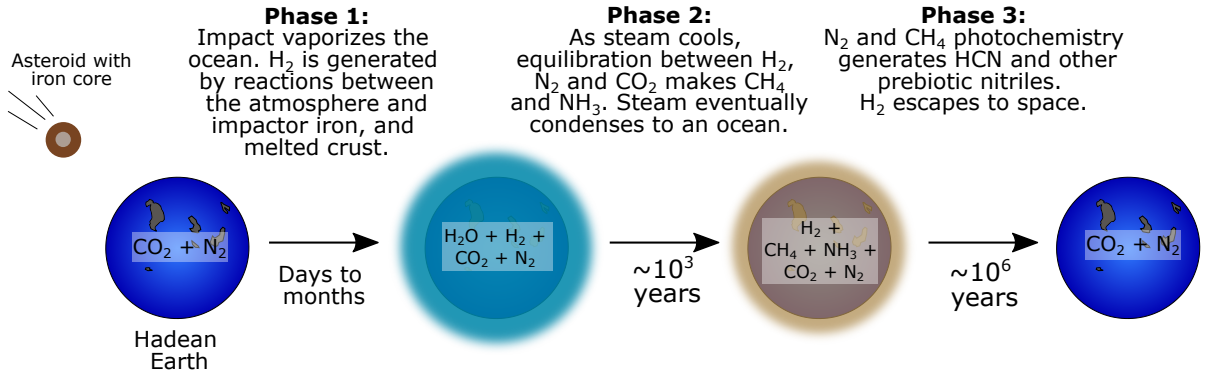

Figure 5.1: The three phases of atmospheric evolution after a large asteroid impact on the Hadean Earth. In Phase 1, the impactor vaporizes the ocean and heats up the atmosphere. Iron delivered by the impactor reacts with hot steam to make H_2. H_2 is also modulated by equilibration between the atmosphere and an impact-generated melt pond. In Phase 2, as the steam-rich atmosphere cools for thousands of years, H_2 reacts with CO_2 to make atmospheric CH_4. Ultimately, the steam condenses to an ocean. Finally, in Phase 3, N_2 and CH_4 photochemistry generates HCN and other prebiotic nitriles. The H_2 dominated atmosphere escapes to space over millions of years, causing the return of a more oxidizing N_2 and CO_2 atmosphere.

5.4 in Chapter Appendix 5.6.4). Climate calculations do not account for the radiative effects of clouds or hazes. However, our UV radiative transfer for computing photolysis rates do account for haze absorption and scattering.

5.3 Results

The following sections simulates the three post-impact phases of atmospheric evolution shown in Figure 5.1 for impactor masses between 10^{20} and 10^{22} kg (360 to 1680 km diameter) under various modeling assumptions.

5.3.1 Phase 1: Reducing the steam-generated atmosphere with impactor iron

Within days, a massive asteroid impact would leave the Hadean Earth with a global ~2000 K rock and iron vapor atmosphere, the iron derived from the impactor's core (Itcovitz et al.,

2022). In the following months to years, energy radiated downward from the silicates would vaporize a large fraction of the ocean, adding steam to the atmosphere (Sleep et al., 1989). At this point, steam should rapidly react with iron to generate H_2. Eventually, the iron vapor and then rock would rain out leaving behind a steam-dominated atmosphere containing H_2, as well as CO_2 and N_2 from the pre-impact atmosphere. The sequence of metal followed by silicate condensation with falling temperature is loosely analogous to that of the well-known condensation sequence of the solar nebula.

Furthermore, the massive impact would generate a melt pool on Earth's surface inside the impact crater, which may contain reducing impact-derived iron. The atmosphere and melt pool could react to a redox-equilibrium state. This could add or sequester H_2 from the atmosphere, depending on whether the melt was more or less reducing than the atmosphere (Itcovitz et al., 2022).

Recently, Itcovitz et al. (2022) used a smoothed-particle hydrodynamics (SPH) code with 0.5×10^6 - 3×10^6 particles of 150 - 250 km diameter to estimate the amount of H_2 generated as these processes unfold under several different impact scenarios on the Hadean Earth. In their fiducial case (i.e. their "Model 1A"), they assume that 100% of iron delivered by an impactor is available to react and reduce a post-impact steam atmosphere. In another scenario, they assume that only $\sim$15 - 30% of impactor iron reacts with the steam atmosphere based on their SPH simulations (their "Model 1B") (Citron and Stewart, 2022). For both cases, they also consider equilibration between the atmosphere and a melt pool (their "Model 2", "Model 3A" and "Model 3B"). In their simulations, the melt pool is extremely reducing or more oxidizing depending on whether they assume it contains a fraction of the impactor's iron, and they use SPH models to predict the amount of iron accreted to the melt pool (Citron and Stewart, 2022). Overall, they conclude that melt-atmosphere equilibration generates about as much H_2 as their fiducial case as long as the iron delivered to the melt-atmosphere system can equilibrate. However, if iron delivered to the melt pool sinks into Earth and cannot react with the atmosphere, then approximately 2 - 10 times less H_2 is produced compared to their fiducial scenario (see the erratum in Itcovitz et al. (2022)).

Itcovitz et al. (2022) considers impactors between 2×10^{21} and 2×10^{22} kg, and assumes the pre-impact Earth has 1.85 oceans of water, 100 bars CO_2 and 2 bars of N_2. However, we investigate impacts as small as 10^{20} kg, and our nominal model (Table 5.2) assumes only 0.5 bars of pre-impact CO_2 motivated by models of the Hadean carbonate-silicate cycle (Kadoya et al., 2020) and assuming little mantle-hosted carbonate is vaporized. Therefore, we use a similar model (Chapter Appendix 5.6.1) to the one described in Itcovitz et al. (2022) to predict the post-impact H_2 for our alternative model assumptions (Table 5.2) and impactor sizes. Figure 5.2 shows the results.

Our calculations give two end-member scenarios for impact H_2 production which we consider for subsequent calculations in this article. The more optimistic case assumes that 100% of the impactor's iron reacts with an atmosphere that is chemically isolated from a melt pool ("Model 1A" in Figure 5.2). Following Zahnle et al. (2020), we adopt this scenario as our nominal model throughout the main text. This assumption produces a similar amount of H_2 as an atmosphere-melt system that retains most of the impactor's iron (e.g. "Model 2" in Figure 5.2), which is consistent with Itcovitz et al. (2022). The "Model 2" calculation assumes the melt pool has an initial oxygen fugacity of ΔFMQ-2.3 which is appropriate for a peridotite melt (Itcovitz et al., 2022).[1] However, our results are not sensitive to this assumption because, for "Model 2", initial melt oxygen fugacities between ΔFMQ and ΔFMQ-4 changes the generated H_2 by a factor of at most ~ 1.3.

The less-optimistic case for H_2 production is "Model 1B" in Figure 5.2, which assumes that only a fraction of the impactor iron reacts with an atmosphere ($\sim 15\%$ to $\sim 30\%$), and that the latter does not react with a melt pool. We compute the fraction of available iron by extrapolating SPH simulations of impacts traveling at twice Earth's escape velocity and colliding with Earth at a 45° angle (Figure 5.12 in the Chapter Appendix), which is the most probable angle (Citron and Stewart, 2022). Most simulations shown in the main text have a complementary figure in the Chapter Appendix that makes this alternative pessimistic

[1] FMQ is the fayalite-magnetite-quartz redox buffer. See Chapter 7 in Catling and Kasting (2017) for a discussion of redox buffers.

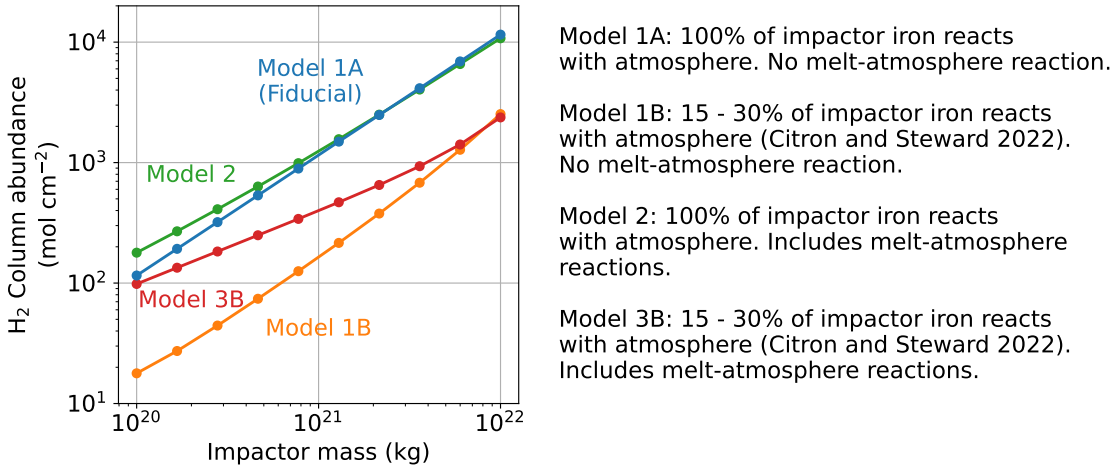

Figure 5.2: Post-impact H_2 generation as a function of impactor mass under different modeling assumptions. Models 1A, 1B, 2 and 3B are identical to those describe in Figure 1 of Itcovitz et al. (2022). The simulation's pre-impact volatile inventories, impact angle, and impact velocity are listed in Table 5.2. In Model 1A, all iron delivered by an impact reacts with steam to produce H_2. The resulting atmosphere does not equilibrate with a impact-generated melt pool. Model 1B assumes that a fraction ($\sim$ 15% to $\sim$ 30%) of impactor iron reduces the steam atmosphere based on SPH simulations (Citron and Stewart, 2022), and that the atmosphere is chemically isolated from a melt pool. Model 2 is like Model 1A while also including post-impact equilibration with a melt pool with a redox state of ΔFMQ-2.3 to represent peridotite (Itcovitz et al., 2022). Model 3B assumes that a fraction ($\sim$ 15% to $\sim$ 30%) of impactor iron reacts with the steam atmosphere based on SPH simulations, and includes melt-atmosphere redox equilibration with a pool magma initially at ΔFMQ-2.3. As stated in Section 5.3.1, we nominally assume Model 1A throughout the main text calculations. We also include simulations in the Chapter Appendix that instead adopt Model 1B, which we consider to be a plausible lower bound for post-impact H_2 generation.

assumption regarding post-impact H_2 generation.

5.3.2 Phase 2: The cooling post-impact steam atmosphere

After reactions between impact-derived iron and steam produce H_2, the atmosphere would radiate at a rate determined by the optical properties of water vapor (Zahnle et al., 2020). Chemical reactions would initially be rapid, forcing the whole atmosphere to chemical equilibrium. Methane is thermodynamically preferred at lower temperatures (e.g., more methane is prefered in a gas at 1000 K than a gas at 1500 K), so it should become more abundant as the atmosphere cools. Eventually the atmosphere would reach a temperature where the reactions producing methane would be extremely sluggish compared to the rate of atmospheric cooling. At this point, the methane abundance would freeze, or quench. Ammonia would exhibit the same behavior as methane by initially rising in abundance then quenching when kinetics become slow. After several thousand years, water vapor condenses and rains out of the atmosphere to form an ocean.

We use the 0-D kinetics-climate box model described in Chapter Appendix 5.6.2 to simulate these events. By simulating each elementary chemical reaction, the model automatically computes methane and ammonia quenching as the atmosphere cools and temperature-dependent reactions slow. We first consider gas-phase kinetics, and later we will also consider nickel-surface kinetics.

Figure 5.3 shows our model applied to a 1.58×10^{21} kg ($\sim$ 900 km diameter) impactor. As the steam cools, ammonia quenches when the atmosphere is $\sim$ 1200 K, followed by CH_4 quenching at $\sim$ 950 K. After quenching, nearly half of the total carbon in the atmosphere exists as CH_4. After 4200 years, the steam has largely rained out to form an ocean, leaving behind a H_2-dominated atmosphere containing CH_4 and NH_3. NH_3 is soluble in water, so a fraction should be removed from the atmosphere by dissolution in the newly formed ocean; however our simulations (e.g. Figure 5.3) do not account for this effect.

Figure 5.4 shows predicted atmospheric composition at the end of the steam atmosphere (e.g. at 4200 years in Figure 5.3) as a function of impactor mass. The calculations use gas-

Table 5.2: Nominal model assumptions

Parameter	symbol	value
Pre-impact ocean inventory	N_{H_2O}	1.5×10^4 mol cm^{-2} (i.e. 1 ocean)[a]
Pre-impact CO_2 inventory	N_{CO_2}	12.5 mol cm^{-2} (i.e. "0.5 bars")[b]
Pre-impact N_2 inventory	N_{N_2}	36 mol cm^{-2} (i.e. "1 bar")[c]
Impactor mass	M_{imp}	10^{20} - 10^{22} kg
Iron mass fraction of the impactor	$m_{Fe,imp}$	0.33
Fraction of iron that reacts with atmosphere	$X_{Fe,atmos}$	1.0[d]
Impact angle	-	45°
Impact velocity relative to Earth	-	20.7 km s^{-1}
Eddy diffusion coefficient[e]	K_{zz}	10^6 cm^2 s^{-1}
Aerosol particle radius[e]	-	0.1 μm
Troposphere relative humidity	ϕ	1
Surface Albedo	A_s	0.2
Temperature of the stratosphere	T_{strat}	200 K
Rainfall rate	R_{rain}	1.1×10^{17} molecules cm^{-2} s^{-1} (Modern Earth's value)
HCN deposition velocity[f]	$v_{dep,HCN}$	7×10^{-3} cm s^{-1}
HCCCN deposition velocity[g]	$v_{dep,HCCCN}$	7×10^{-3} cm s^{-1}

[a] The source and inventory of surface H_2O throughout the Hadean is debated (Miyazaki and Korenaga, 2022; Korenaga, 2021; Johnson and Wing, 2020) and even how much water is present on the modern Earth (e.g., Lécuyer et al. (1998) estimates 0.3-3 oceans in Earth's mantle). Our nominal case of one modern ocean is one possibility among several.

[b] Based on Hadean carbon cycle modeling in Kadoya et al. (2020).

[c] Based on Figure 5 in Catling and Zahnle (2020).

[d] This is the "Model 1A" scenario for H_2 production described near the end of Section 5.3.1 and in Figure 5.2.

[e] Assumed to be constant as a function of altitude.

[f] Estimated based on the HCN hydrolysis rate in the ocean (Chapter Appendix 5.6.3).

[g] Assumed to the the same as HCN.

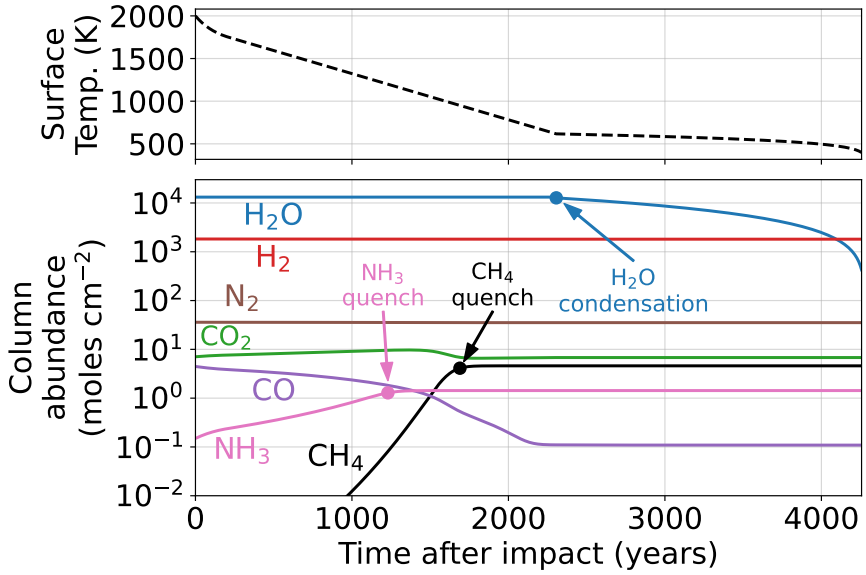

Figure 5.3: A kinetics-climate simulation of a cooling steam atmosphere caused by a 1.58×10^{21} kg impactor. The model uses the Table 5.2 nominal parameters. The top panel is surface temperature and the bottom panel shows atmospheric composition.

phase reactions, and our nominal model parameters (Table 5.2), including the assumption that 100% of the iron delivered by the impactor reacts with the steam atmosphere to make H_2. For example, a 10^{20} kg impactor generates 1.2×10^2 H_2 moles cm^{-2} which would have a partial pressure of 1.2 bars if the atmosphere did not contain water vapor. A 10^{22} kg impactor generates 1.1×10^4 H_2 moles cm^{-2} which would have a "dry" partial pressure of 23.8 bars.[2] We find that most of the CO_2 in the atmosphere is converted to CH_4 for impactors larger than 1.6×10^{21} kg ($\sim$ 900 km diameter), and that bigger impacts generate more NH_3, e.g., a 10^{22} kg impactor makes 0.013 "dry" bars of NH_3. Reduced species like CH_4 and NH_3 are thermodynamically preferred in the thick H_2 atmospheres generated by bigger impacts.

[2]Partial pressures depend on the mean molecular weight of the atmosphere. The 10^{22} kg simulation in Figure 5.4 has 65.0 bars H_2 before ocean vapor condenses, and would have 23.8 bars H_2 if there was no water vapor in the atmosphere. Both scenarios have the same number of H_2 molecules in the atmosphere, but have different partial pressures because of dissimilar mean molecular weights. To avoid ambiguity, we occasionally report partial pressures in "dry" bars, which is the partial pressure of a gas if the atmosphere had no water vapor.

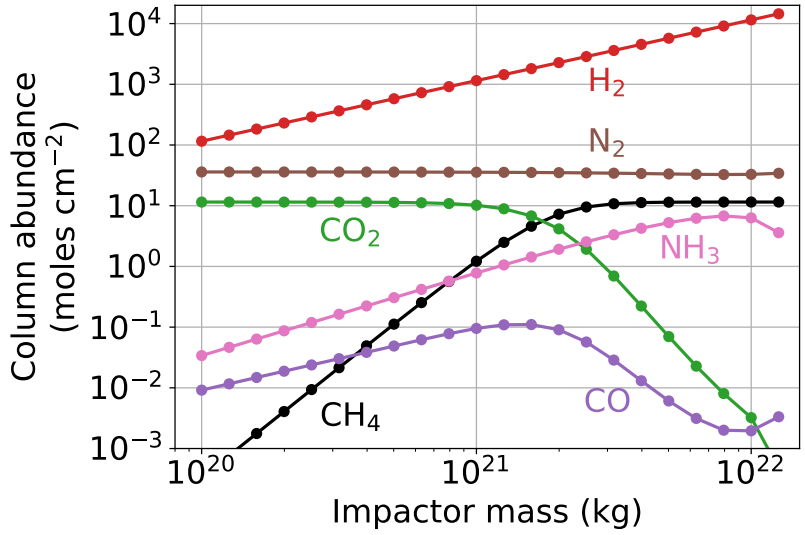

Figure 5.4: Predicted atmospheric composition as a function of impactor mass after steam has condensed to an ocean. We use our nominal modeling assumptions (Table 5.2), and also use gas-phase kinetics. Most CO_2 is converted to CH_4 for impactors larger than 1.6×10^{21} kg.

Large impacts generate big amounts of hydrogen because they deliver more iron which more thoroughly reduces the atmosphere.

The Figure 5.4 calculations might underestimate the CH_4 produced in the post-impact atmosphere because they ignore reactions occurring on nickel surfaces that can catalyze CH_4 generation. If the impactors that struck the Earth during the Hadean resembled enstatite chondrite or carbonaceous chondrite composition then they would have contained 1% - 2% nickel (Lewis, 1992, Table 15). This nickel would have coexisted with the rock and iron vapor atmosphere that lasted months to years following a massive impact (Phase 1 in Figure 5.1). Metals along with silicates would have rained out as spherules covering the entire planet (Genda et al., 2017). As the impact-generated steam cooled, chemical reactions catalyzing CH_4 production could have occurred on nickel surfaces in the bed of spherules (Schmider et al., 2021). These surface reactions could lower the quench temperature of CH_4, causing more of the gas to be produced.

To estimate the effect of nickel catalysis on CH_4 production, we use our kinetics-climate box model (Chapter Appendix 5.6.2) with the nickel-surface reaction network developed by Schmider et al. (2021). The network is based on quantum chemistry calculations and about a dozen experiments from the literature. Our micro-kinetics approach is distinct from the empirical one taken by, e.g. Kress and McKay (2004), because our model tries to capture each elementary step of catalysis, rather than use a parameterization that is specific to certain experimental conditions.

Figure 5.5 shows the quenched methane abundance as a function of impactor mass predicted by our model that includes nickel catalysts. The amount of CH_4 generated depends strongly on the amount of available nickel surface area. Nickel areas bigger than 0.1 cm^2 nickel / cm^2 Earth permit more CH_4 production compared to our gas-phase only model. Assuming a nickel area of 1000 cm^2 nickel / cm^2 Earth, then a Vesta-size impactor (2.6×10^{20} kg, 500 km diameter) could convert most CO_2 in the pre-impact atmosphere to CH_4.

Unfortunately, a precise nickel surface area is hard to estimate. The correct value depends on how the rock, iron and nickel spherules mix and precipitate to the surface, and furthermore, how effectively the atmosphere can diffuse through and react on exposed nickel. We do not attempt to compute these effects here, and instead estimate possible upper bounds. Consider a 2.6×10^{20} kg impactor (Vesta-sized) of enstatite chondrite composition, containing 2% by mass Ni (Lewis, 1992). If all this nickel is gathered into 1 mm spheres, a plausible droplet size according to Genda et al. (2017), then the total nickel surface area is 3.4×10^3 cm^2 nickel / cm^2 Earth. An impactor ten times more massive would deliver ten times more nickel resulting in an upper bound Ni area that is one order of magnitude larger. Significantly smaller nickel particles are conceivable. There is experimental support for the formation of ultra-fine < 300 nm particles in the wake of impacts colliding with an ocean (Furukawa et al., 2007). For a Vesta-sized impactor, collecting all nickel into 100 nm particles has a nickel area six orders of magnitude large than the 1 mm case - 3.4×10^9 cm^2 nickel / cm^2 Earth. Overall, the larger nickel areas shown in Figure 5.5 may be within the realm of possibility. Alternatively, nickel might be buried by rock and iron when these materials condense out of

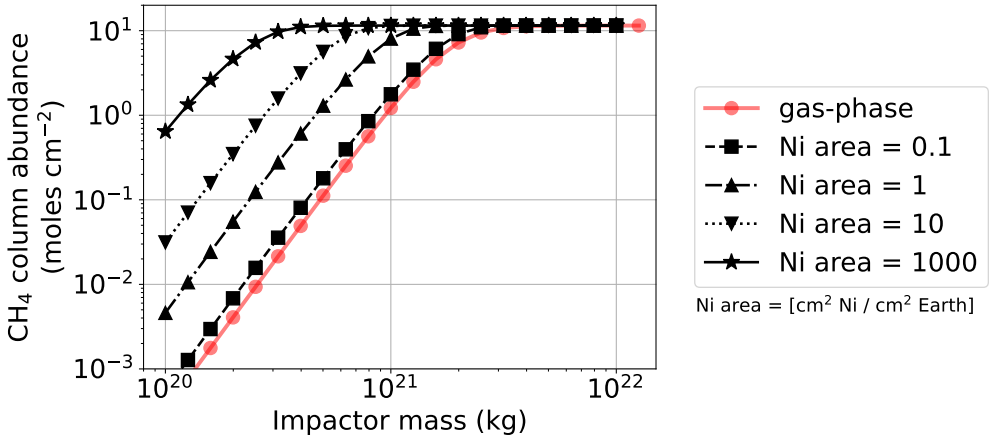

Figure 5.5: The effect of nickel catalysts on post-impact methane production. The calculations use the Table 5.2 model parameters and the Schmider et al. (2021) surface reaction network. Ni areas larger than 0.1 cm^2 nickel / cm^2 Earth generates more methane than our model that uses gas-phase reactions, e.g., Figure 5.4.

the post-impact atmosphere, and that < 0.1 cm^2 nickel / cm^2 Earth is available for catalysis. In this case, gas-phase kinetics would determine the conversion of CO_2 to CH_4.

Figures 5.4 and 5.5 optimistically assume that all iron delivered by the impactor reacts with steam to make H_2, however, this may not be the case (see Section 5.3.1). Therefore, in the Chapter Appendix we recalculate Figures 5.4 and 5.5, but assume that only a fraction of the impactor's iron reduces the steam atmosphere by extrapolating SPH simulations of impacts ("Model 1B" in Figure 5.2). The resulting H_2, CH_4, and NH_3 production appear similar, except shifted by a factor of ~ 5 to larger impactors. The results are shifted by this amount because SPH simulations suggest approximately $\sim 1/5$ of impactor iron is delivered to the atmosphere, while the rest is either embedded in Earth, or ejected to space. We consider these supplementary calculations lower-bounds for impactor generated CH_4 and NH_3.

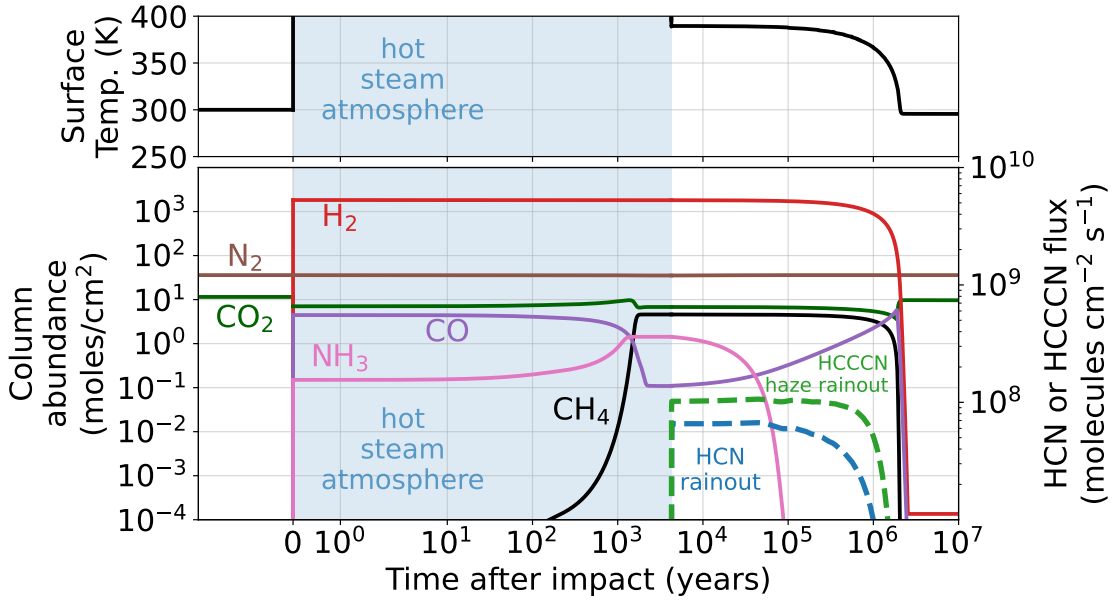

Figure 5.6: Simulated composition and climate of the Hadean atmosphere after a 1.58×10^{21} kg impactor that produces 7.0 bars of H_2 once vaporized ocean water condenses. We use the Table 5.2 model parameters. The blue shaded region labeled "hot steam atmosphere", also called Phase 2 in Figure 5.1, is simulated by the kinetics-climate model described in Chapter Appendix 5.6.2. After this time-period, during Phase 3 of a post-impact atmosphere, we evolve the atmosphere with 1-D photochemical-climate model (Chapter Appendix 5.6.3), which maintains 0.018 bar of CH_4 between 4×10^3 and $\sim 10^6$ years. Dashed lines are referenced to the right-hand axis. "HCN rainout" is HCN molecules raining out in droplets of water. "HCCCN haze rainout" is the rainout rate of HCCCN incorporated into particles formed from the reaction $C_4H + HCCCN \rightarrow$ polymer. CH_4 and N_2 photochemistry generates HCN and HCCCN for about one million years until H_2 escapes to space.

5.3.3 Phase 3: Long-term photochemical-climate evolution

Several thousand years after a massive impact, the steam-dominated atmosphere would condense to an ocean leaving behind a H_2-dominated atmosphere containing CH_4 and NH_3 (e.g. at 4200 years in Figure 5.3). The reducing atmospheric state should persist for millions of years until hydrogen escapes (Zahnle et al., 2020).

We simulate the long-term evolution of this hydrogen-rich atmosphere using a coupled one-dimensional photochemical-climate model (Chapter Appendix 5.6.3). Figure 5.6 shows

our model applied to the atmosphere following a 1.58×10^{21} kg ($\sim$ 900 km diameter) impactor. We assume a pre-impact atmosphere with 1 bar N_2 and 0.5 bars of CO_2, and simulate the cooling steam atmosphere with our kinetics-climate climate model (Section 5.3.2). Next, we use the end of the steam atmosphere simulation as initial conditions for our 1-D photochemical-climate model.

We find that N_2 and CH_4 photochemistry generates HCN in a hazy Titan-like atmosphere for about one million years until it is halted by hydrogen escape to space. In this model, the dominant channel producing HCN is $N + {}^3CH_2 \rightarrow HCN + H$ where ${}^3CH_2$ is ground (triplet) state of the methylene radical derived form methane photolysis. There are two other important paths. The first is $N + CH \rightarrow CN + H$ followed by $H_2 + CN \rightarrow HCN + H$, and the second is $N + CH_3 \rightarrow H + H_2CN$ and $H_2CN + H \rightarrow HCN + H_2$. In all pathways, hydrocarbon radicals (e.g., ${}^3CH_2$ and CH_3) are sourced from photolyzed CH_4 and atomic N is derived from photolyzed N_2, which both occur at high altitudes ($p < 10^{-5}$ bar, Figure 5.16) in the Chapter Appendix. The largest chemical loss of HCN is photolysis followed by $N + CN \rightarrow N_2 + C$. Other significant losses are paths that form HCCCN haze aerosols. HCN production and loss is our model is comparable to pathways discussed in similar studies (Zahnle, 1986; Tian et al., 2011; Rimmer and Rugheimer, 2019). We determined the chemical paths most important for producing and destroying HCN by studying column integrated reaction rates at 14,200 years in Figure 5.6.

In Figure 5.6, HCN mixes to the surface and rains out in droplets of water at a rate of $\sim 10^7$ molecules cm^{-2} s^{-1}. HCN also dissolves into the ocean at a similar rate, where we assume it is eventually destroyed by hydrolysis (not shown in Figure 5.6). To emulate HCN dissolution and destruction in the ocean, we assume a 7×10^{-3} cm s^{-1} deposition velocity justified in Chapter Appendix 5.6.3. Additionally, a relatively small amount of HCN polymerizes to haze particles in our model via $H_2CN + HCN \rightarrow$ polymer following Lavvas et al. (2008a), which falls and rains out in water droplets to the surface.

Our results differ from the simulations of Zahnle et al. (2020), which suggested that the duration of HCN production after an impact was limited by rapid photolysis of methane.

The Figure 5.6 simulation finds that the CH_4 lifetime is 4.8 million years because, following photolysis, CH_4 efficiently recombines in a hydrogen rich atmosphere from the following reaction, which is well known in the atmospheres of the giant planets in out solar system (Figure 5.15 in the Chapter Appendix).

$$CH_3 + H + M \rightarrow CH_4 + M \tag{5.3}$$

Zahnle et al. (2020) did not account for Reaction 5.3. The lifetime of cyanide production is therefore instead determined by the timescale of hydrogen escape to space. Significant hydrogen escape permits the destruction of most atmospheric CH_4 because Reaction 5.3 becomes inefficient, which in turn ceases CH_4-driven HCN production.

In Figure 5.6, HCCCN is primarily destroyed by photolysis and produced by the following reaction from acetylene and the cyanide radical,

$$C_2H_2 + CN \rightarrow HCCCN + H \tag{5.4}$$

A fraction of produced HCCCN reacts to form aerosols via C_4H + HCCCN $\rightarrow$ polymer following Lavvas et al. (2008a). These polymers fall and mix toward the surface where they rainout in droplets of water at a rate of $\sim 10^8$ molecules cm^{-2} s^{-1}. Most gas-phase HCCCN is either destroyed by photolysis or incorporated into aerosols, causing vanishingly small surface HCCCN gas pressures ($< 10^{-16}$ bar).

Our model approximates haze formation with the following three reactions: C_2H + C_4H_2 $\rightarrow$ polymer + H, H_2CN + HCN $\rightarrow$ polymer, and C_4H + HCCCN $\rightarrow$ polymer. At 14,200 years in Figure 5.6, the first pathway dominates, forming $\sim 1.8 \times 10^{13}$ g haze yr^{-1}. At this same point in time the second and third pathways produce 9×10^7 g yr^{-1} and 2.8×10^{12} g yr^{-1}, respectively. The total haze production rate (2.1×10^{13} g yr^{-1}) is comparable to values estimated by Trainer et al. (2006) for the early Earth based on laboratory experiments. Haze particles fall and rainout to the surface where they can hydrolyze and participate in prebiotic chemistry (Neish et al., 2010; Poch et al., 2012).

In Figure 5.6, impact-generated ammonia persists for nearly 10^5 years. NH_3 is primarily destroyed by photolysis, but then recombines from reactions with hydrogen:

$$NH + H_2 + M \rightarrow NH_3 + M \tag{5.5}$$

$$NH_2 + H + M \rightarrow NH_3 + M \tag{5.6}$$

Reactions 5.5 and 5.6 are relatively efficient in a hydrogen-rich atmosphere. Ammonia photolysis primarily occurs at the 10^{-3} bar altitude, while haze is largely produced above the 10^{-5} bar altitude. Therefore, haze particles partially shield ammonia from photolysis, extending the NH_3 lifetime (Sagan and Chyba, 1997). Our model assumes the haze particles are perfect spheres with optical properties governed by Mie theory. Observations of Titan's haze have revealed that hydrocarbon haze particles have a fractal structure which absorb and scatter UV more effectively than Mie spheres (Wolf and Toon, 2010). Therefore, our model likely overestimates NH_3 photolysis in post-impact atmospheres.

Figure 5.6 assumes that all NH_3 is in the atmosphere and that it does not rainout, but the gas is highly soluble in water and should dissolve in the ocean where it hydrolyzes to ammonium, NH_4^+. Later in Section 5.4.4, we show that for an atmosphere with 0.3 mol cm^{-2} NH_3 and a 371 K ocean at pH = 7, 4% of NH_3 would persist in the atmosphere, while the rest is dissolved in the ocean. For a hotter 505 K atmosphere with 6.8 mol cm^{-2} NH_3, only 20% of ammonia dissolves in the ocean because solubility decreases with increasing temperature (Section 5.4.4). Ammonia dissolution in the ocean would protect it from photolysis perhaps lengthening the lifetime of ammonia in the atmosphere-ocean system. Overall, since our photochemical-climate model neglects NH_3 ocean dissolution and likely overestimates NH_3 photolysis, then we probably underestimate the lifetime of NH_3 in Figure 5.6.

While HCN and HCCCN are produced in Figure 5.6, the surface temperature would be $\sim$ 390 K primarily caused by H_2-H_2 collision-induced absorption (CIA), which has a significant greenhouse effect in thick H_2 atmospheres like this one of 8.5 bars total pressure.

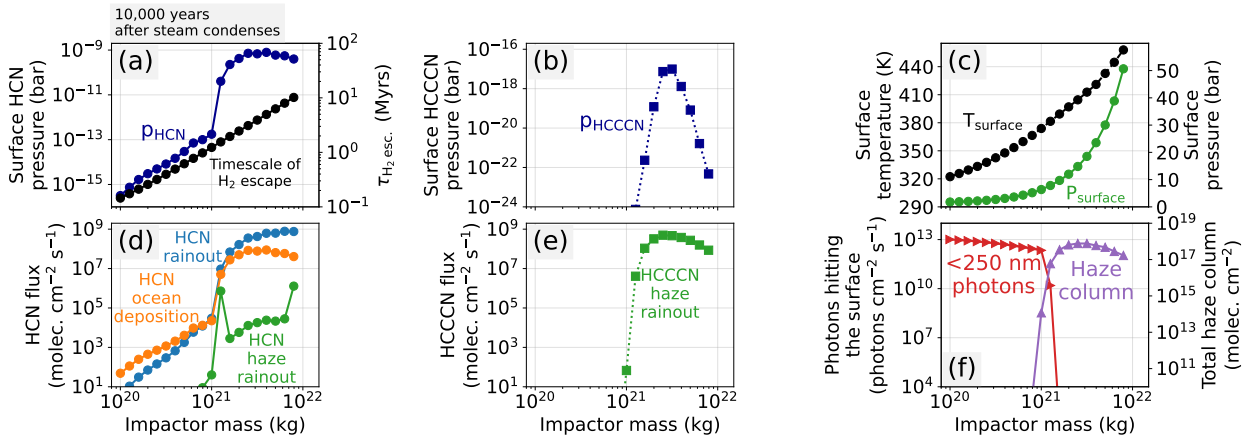

Figure 5.7: The state of the Hadean post-impact atmospheres 10,000 years after steam condenses to an ocean. This time period is within Phase 3 of a post-impact atmosphere indicated in Figure 5.1. The simulations assume the Table 5.2 parameters and gas-phase reactions during the cooling steam atmosphere. (a) The surface HCN pressure and timescale of H_2 escape, which can be interpreted as the approximate duration of HCN and HCCCN production. (b) The HCCCN surface pressure. (c) The surface temperature and pressure. (d) The HCN deposition rate in the ocean and the rate HCN leaves the atmosphere in rain drops. "HCN haze rainout" is the rainout rate of a aerosol created via the reaction $H_2CN + HCN \rightarrow$ polymer. (e) The rainout rate of an aerosol formed from the reaction $C_4H + HCCCN \rightarrow$ polymer. (f) The < 250 nm photons hitting the surface, and the total hydrocarbon haze column abundance. Impactors larger than 10^{21} kg produce haze-rich atmospheres and a stepwise increase in HCN and HCCCN production.

The atmosphere cools to ~ 300 K after H_2 escapes to space.

Figure 5.7 applies our model to various impactor masses. The results show the Hadean atmosphere 10,000 years after the post-impact generated steam atmosphere has condensed to an ocean. We choose 10,000 years after ocean condensation because this is adequate time for the atmosphere to reach a quasi-photochemical steady-state that does not change significantly until hydrogen escapes (e.g. Figure 5.6). Figure 5.7d and 5.7e show a sharp increase in the HCN and HCCCN production for impactors larger than 10^{21} kg (~ 780 km). Such large impacts generate $CH_4/CO_2 > 0.1$ (Figure 5.4), which makes a thick Titan-like haze (Trainer et al., 2006). Haze shielding causes CH_4 photolysis to be higher in the atmosphere and closer to N_2 photolysis, therefore the photolysis products of both species can more ef-

ficiently combine to make cyanides (Figure 5.16 in the Chapter Appendix). Additionally, HCCCN production requires acetylene (Reaction 5.4), which is a haze precursor that accumulates when $CH_4/CO_2 > 0.1$. These Titan-like atmospheres have $\sim 10^{-9}$ bar surface HCN, and HCN ocean deposition and rainout rates between 10^7 and 10^9 HCN molecules cm^{-2} s^{-1} persisting on hydrogen escape timescales ($>$ 1 million years). HCCCN is incorporated into aerosols before raining out to the surface at a rate of up to 10^9 HCCCN molecules cm^{-2} s^{-1}.

In addition to photochemistry, lightning should also generate HCN (Chameides and Walker, 1981; Stribling and Miller, 1987). Figure 5.19 in the Chapter Appendix shows HCN production from lighting for the same time period as the Figure 5.7 simulation using methods described in Chameides and Walker (1981). Assuming the same lightning dissipation rate as modern Earth's, we find that lightning produces up to $\sim 10^4$ HCN molecules cm^{-2} s^{-1}. This value is small compared to the 10^7 - 10^9 HCN molecules cm^{-2} s^{-1} produced from photochemistry after $> 10^{21}$ kg impacts.

Larger impacts generate a thicker H_2 atmosphere which make the atmosphere warmer (Figure 5.7c). For impactors $> 10^{21}$ kg, which generate substantial HCN and HCCCN, the surface temperature is $>$ 380 K. Figure 5.7f shows that impactors that produce substantial haze shield the surface from $<$ 250 nm photons, which means that prebiotic schemes that require high energy UV light (e.g., Patel et al., 2015) would need to rely on stockpiling of the nitriles for later use.

The Hadean Earth CO_2 concentration is uncertain. Models of the Hadean geologic carbon cycle argue for CO_2 levels between $\sim 10^{-5}$ and 1 bar at 4 Ga with a median value of $\sim$ 0.5 bar and a 95% uncertainty spanning 10^{-5} to 1 bar (Kadoya et al., 2020). However, these values might be unrealistically small because a large impact would warm surface rocks possibly causing carbonates to degass thereby increasing the atmospheric CO_2 reservoir. Up to $\sim$ 80 bars of CO_2 may potentially be liberated from surface carbonates (Krissansen-Totton et al., 2021b).

Figure 5.8 explores the effect of different pre-impact CO_2 abundances on HCN and HCCCN production in post-impact atmospheres. The simulations are snapshots of the atmo-

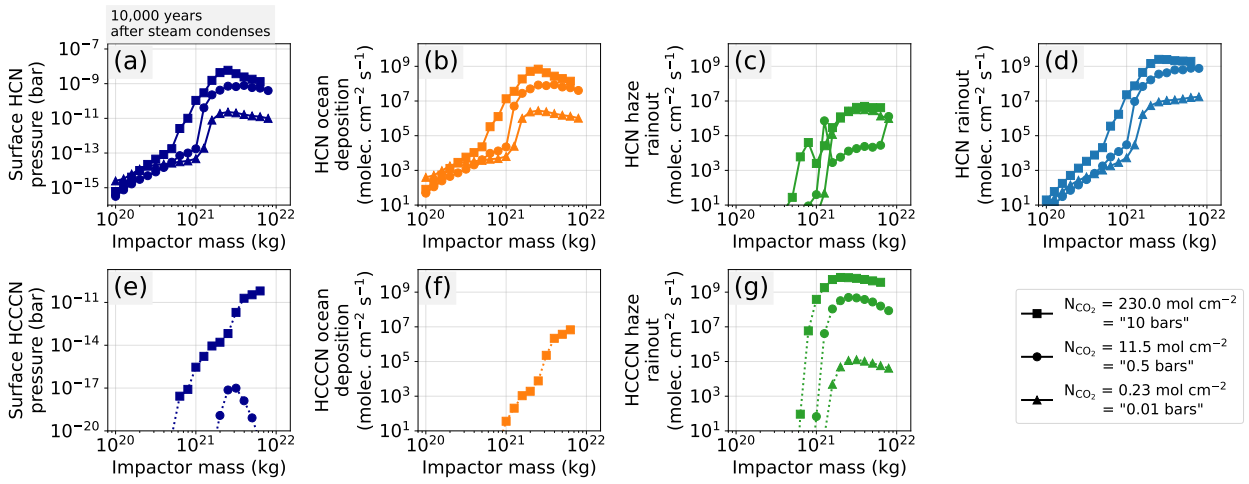

Figure 5.8: The effect of the pre-impact CO_2 abundance on HCN and HCCCN production in post-impact atmospheres. All values are for the atmosphere 10,000 years after the steam condenses to an ocean, which is within Phase 3 of a post-impact atmosphere (Figure 5.1). The simulations assume the Table 1 parameters, except vary the pre-impact CO_2 inventory between 0.01 bar (triangles), 0.5 bar (circles), and 10 bars (squares). The calculations use gas-phase chemistry during the cooling steam atmosphere. Panels (a) - (d) show the surface HCN abundance and fluxes, while (e) - (g) show HCCCN production. Our model assumes that HCCCN is not soluble in water and does not rainout, therefore we omit a panel showing HCCCN rainout. Prebiotic nitrile production is directly correlated with the pre-impact CO_2 inventory.

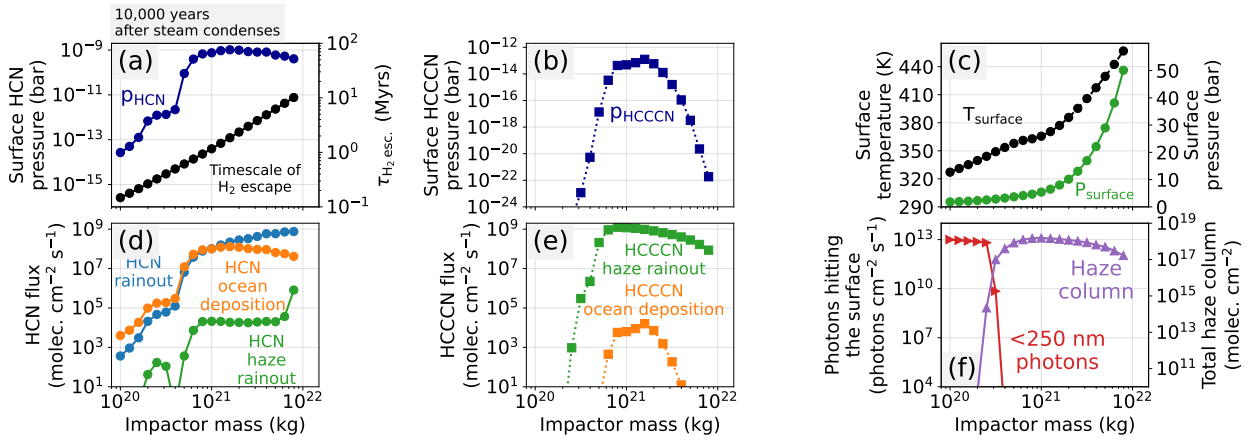

Figure 5.9: Identical to Figure 5.7, except simulations account for nickel-surface reactions which catalyze methane production as the steam atmosphere cools (Schmider et al., 2021). We assume a nickel surface area of 10 cm^2 nickel / cm^2 Earth (for context, see Figure 5.5). Nickel catalysts cause more efficient CH_4 generation, permitting bigger HCN and HCCCN production for smaller impactors compared to the gas-phase only scenario (Figure 5.7).

sphere 10,000 years after the impact-vaporized steam has condensed to an ocean. Larger pre-impact CO_2 causes larger HCN and HCCCN production because it allows more CH_4 to form in the cooling steam atmosphere. As discussed previously, CH_4 is closely tied to photochemical cyanide generation. Regardless of the pre-impact CO_2 concentrations, HCN and HCCCN production sharply increases for impactors larger than $\sim 10^{21}$ kg due to more efficient haze production (Figure 5.7, and corresponding text).

Figure 5.9 shows the state of the atmosphere after impacts of various size assuming 10 cm^2 nickel / cm^2 Earth is present in the steam atmosphere to catalyze methane production. The nickel causes more efficient conversion of CO_2 to CH_4 compared to the gas-phase only scenario (Figure 5.7) permitting greater production of HCN and HCCCN for smaller impactors. For example, a 5×10^{20} kg ($\sim$ 610 km) impactor which accounts for nickel catalysts (Figure 5.9) has comparable HCN and HCCCN production to a 1.6×10^{21} kg ($\sim$ 900 km diameter) impactor if no nickel catalysts are assumed in the cooling steam atmosphere (Figure 5.7).

A critical assumption in this section is that 100% of the iron delivered by impactors

reacts with steam to generate H_2. As discussed in Section 5.3.1, it is possible that the post-impact atmosphere is less thoroughly reduced by impactor iron. Figures 5.17 and 5.18 in the Chapter Appendix recalculate main text Figures 5.7 and 5.9, assuming that a fraction (approximately 15% to 30%) of impactor iron reduces the steam atmosphere based on SPH simulations ("Model 1B" in Figure 5.2). This alternative assumption requires that impactors ~ 5 times more massive are required to generate a haze-rich post-impact atmosphere with copious HCN and HCCCN production. For example, in Figure 5.7, recall that there is a sharp increase in cyanide production for impactors larger than 10^{21} kg ($\sim$ 780 km). Figure 5.17 in the Chapter Appendix, which instead assumes a fraction of iron reduces the steam atmosphere, finds that the sharp increase in cyanide production occurs for impacts larger than 5×10^{21} kg ($\sim$ 1330 km). However, the presence of nickel catalysts may permit large prebiotic nitrile production for smaller impactors, even under pessimistic post-impact H_2 generation (Figure 5.18 in the Chapter Appendix).

5.4 Discussion

5.4.1 Comparison to previous work

Recently, Zahnle et al. (2020) performed calculations of post-impact atmospheres using simpler models than the ones used in this article. Our results differ in several important ways. First, we find that our purely gas-phase model of the post-impact steam atmosphere (Section 5.3.2) predicts less CH_4 generation than the model used in Zahnle et al. (2020). For example, Figure 5.4 predicts that most CO_2 is converted to CH_4 for impactors larger than 1.6×10^{21} kg. Figure 2 (top panel) in Zahnle et al. (2020), which is a comparable scenario, suggests a 5×10^{20} kg impactor is required to convert most of the atmospheric CO_2 to CH_4. The difference is likely caused by different approaches to computing CH_4 quenching, or freeze-out, as the atmosphere cools. Our kinetics-climate model automatically computes CH_4 quenching by tracking the elementary reactions producing and destroying CH_4 along with many other atmospheric species. In most of our simulations of cooling post-impact atmospheres, CH_4

quenches when the temperature is between 900 and 1000 K. Zahnle et al. (2020) instead used equilibrium chemistry modeling with a parameterization for CH_4 quenching derived from kinetics calculations of H_2-dominated brown dwarf atmospheres (Zahnle and Marley, 2014). This parameterization predicts $\sim$ 800 K CH_4 quenching temperatures. The different quenching temperatures between our model and the Zahnle et al. (2020) model suggests that the Zahnle et al. (2020) kinetics parameterization is likely not suitable for a cooling steam-rich atmosphere.

The new photochemical model predicts longer post-impact CH_4 lifetimes than the Zahnle et al. (2020) model. As mentioned previously, Zahnle et al. (2020) included CH_4 photolysis, but neglected Reaction 5.3, which efficiently recombine photolysis products in hydrogen-rich atmospheres. In our model, these recombination reactions allow CH_4 to persist in most post-impact atmospheres until hydrogen escapes to space ($\sim$ millions of years). Zahnle et al. (2020) instead finds that CH_4 is eradicated from the atmosphere before hydrogen escape.

Finally, nitrile production and rainout in our new model depend strongly on the presence of haze and the CH_4/CO_2 ratio, which was not the case in Zahnle et al. (2020). Our model finds that up to $\sim 10^9$ molecules cm^{-2} s^{-1} HCN and HCCCN is rained out in hazy post-impact atmospheres with $CH_4/CO_2 > 0.1$ (Figure 5.7). When $CH_4/CO_2 < 0.1$, there is little haze, and HCN production is $<\sim 10^5$ molecules cm^{-2} s^{-1} and HCCCN production is negligible. Haze causes CH_4 and N_2 photolysis products to be close in altitude so that they efficiently react to make cyanides (Figure 5.16 in the Chapter Appendix). Additionally, HCCCN generation requires C_2H_2 in our model (Reaction 5.4), which is only abundant in hazy atmospheres. In contrast, Zahnle et al. (2020) finds that cyanide production rate in post-impact atmospheres is 10^8 to 10^{10} molecules cm^{-2} s^{-1} regardless of the presence of haze and the CH_4/CO_2 ratio. Our results differ largely because our model is 1-D (has vertical transport), while the Zahnle et al. (2020) is a zero dimensional box model. HCN production depends on the proximity of CH_4 and N_2 photolysis, but a box model cannot account for this 1-D effect. Furthermore, Zahnle et al. (2020) does not distinguish between different prebiotic nitriles (e.g. HCN and HCCCN), or determine their surface concentrations and

rainout rates. Also, Zahnle et al. (2020) does not have a coupled climate model.

Cometary and lightning sources of HCN are relatively small compared to our estimated photochemical production rates in haze-rich post-impact atmospheres. Todd and Öberg (2020) calculated that comets could deliver $\sim 1.8 \times 10^5$ HCN molecules cm^{-2} s^{-1} to the Hadean Earth, a value ~ 4 orders of magnitude smaller than HCN from photochemistry in our most optimistic models. As discussed in Section 5.3.3, we find that HCN production from lightning in post-impact atmospheres to be at most $\sim 10^4$ HCN molecules cm^{-2} s^{-1} which is also small compared to UV photochemistry in a CH_4 rich atmosphere. This result agrees with Pearce et al. (2022), who also finds that lightning-produced HCN is relatively insignificant.

Rimmer and Shorttle (2019) suggested that localized ultra-reducing magma rich in carbon and nitrogen might outgas HCN and HCCCN. They imagine this gas interacting with subsurface water causing high concentrations of dissolved prebiotic molecules, and therefore a setting for origin of life chemistry. While this idea may have merit, their calculations do not account for graphite saturation in magma, which may inhibit outgassing of reduced carbon-bearing species, like HCN (Hirschmann and Withers, 2008; Wogan et al., 2020a; Thompson et al., 2022). Additionally, Rimmer and Shorttle (2019) did not self-consistently account for the solubility of gases in magma, which has been been hypothesized to prevent the outgassing of H-bearing gases, like CH_4 or HCN (Wogan et al., 2020a). Therefore, we argue that a hypothesized volcanic source of HCN and HCCCN requires further modeling and experiments before it can be compared to a photochemical source, but, in general, seems challenging.

Cerrillo (2022) recently used a climate model to predict the surface temperature of post-impact atmospheres with compositions predicted by Zahnle et al. (2020). They find surface temperatures > 600 K in some cases. However, the Cerrillo (2022) calculations do not include the effects of water vapor on the lapse rate in the troposphere. Latent heat from water condensation alters convection in the troposphere, greatly reducing the lapse rate when compared to a dry lapse rate. The result is a much cooler surface. Our climate

calculations include the effects of water vapor on the lapse rate, which is why we predict surface temperatures $\lesssim$ 500 K, even in the wake of a 7.9×10^{21} kg impact in Figure 5.7. All our climate simulations of post-impact atmospheres allow surface liquid water.

If a post-impact atmosphere of 2000 mol cm^{-2} H_2 is all lost to space ($\sim$ 4 bar pure H_2 atmosphere, or $\sim$ 13% of the H_2 in an ocean), that would shift D/H of the ocean heavier by 1.4% by hydrodynamic escape and Rayleigh fractionation (following Equation (16) in Zahnle et al. (2019) using an escape fractionation factor $\sim$ 0.9 appropriate for an atmosphere where H_2 dominates over CO_2). This may be an underestimate of the D/H shift because the immediate post-impact oxidation of iron by steam probably produce H_2 with a lower concentration of D than the steam that condense into an ocean. Experiments show isotopic fractionation in reaction of iron powder with steam at low temperatures (Smith and Posey, 1957), but we are unaware of high temperature experiments corresponding to post-impact conditions. In any case, cumulative big impacts during the Hadean that created highly reducing atmospheres would be expected to increase oceanic D/H additively, raising the ocean D/H from starting values that were ten (Piani et al., 2020) to tens of percent (Alexander et al., 2012) lighter than the modern ocean. Such an evolution with intermittent hydrogen escape in the Hadean is consistent both with D/H constraints and with the xenon isotope record (Avice et al., 2018), in which ionic xenon is dragged out to space by early hydrogen escape and the distribution of xenon isotopes becomes heavier (Zahnle et al., 2019).

5.4.2 Origin of life setting and stockpiling of cyanides

The Hadean Earth may have had less land but was likely speckled with hot-spot volcanic islands similar to modern-day Hawaii (Bada and Korenaga, 2018), and possibly had continental land (Korenaga, 2021) where nitriles could accumulate. The majority of HCCCN and HCN produced in post-impact atmospheres would dissolve or rainout into the ocean where it would be diluted and gradually removed by hydrolysis reactions (Miyakawa et al., 2002) or complexation with dissolved ferrous iron (Keefe and Miller, 1996). However, some of the nitriles would be deposited in lakes or ponds on land. We consider, first, equilibrium with

atmospheric p_{HCN} and, second, time-integrated deposition.

Nitrile concentrations in waterbodies on land in equilibrium with the atmosphere according to Henry's law would be too small to participate in prebiotic schemes that form ribonucleotides. Our models predict HCN surface pressures up to 10^{-9} bar (Figure 5.7). For a warm 373 K pond, Henry's law predicts the dissolved HCN concentration is 4×10^{-11} mol L^{-1}. Yet, $\sim$ 0.01 mol L^{-1} HCN is required for polymerization (Sanchez et al., 1967) and published prebiotic schemes can use 1 mol L^{-1} HCN (Patel et al., 2015).

Additionally, while nitriles are produced in post-impact atmospheres, waterbodies on land would likely be too warm for prebiotic chemistry. In the Figure 5.6 simulation, substantial HCN and HCCCN production occurs in the aftermath of big impacts when the surface temperature is $\sim$ 390 K caused by a H_2-H_2 CIA greenhouse. Nickel catalysts permit big HCN and HCCCN production for surface temperatures as small as $\sim$ 360 K (Figure 5.9). Nucleotide building blocks are fragile at such hot temperatures and conditions may not be conducive to an RNA world (Bada and Lazcano, 2002).

We propose that cyanides produced in hot post-impact atmospheres may instead be preserved, stockpiled, and concentrated, and used in prebiotic schemes at a later time when the climate is colder. Cyanide rainout and stockpiling could occur for millions of years until HCN production is halted by H_2 escape to space (Figure 5.6). For example, if HCN rains out at 10^9 molecules cm^{-2} s^{-1} over one million years (Figure 5.7), then $\sim$ 1.4 g cm^{-2} HCN could be stockpiled assuming all molecules are preserved. Once H_2 escapes, the surface temperature would drop to $\sim$ 300 K (Figure 5.6), and over longer timescales the carbonate-silicate cycle might settle on even colder climates because impact ejecta promotes CO_2 sequestration (Kadoya et al., 2020). In this cold climate, cyanide stockpiled into salts could be released as HCN or CN^- into water bodies on land because of rehydration, volcanic or impact heating (Patel et al., 2015; Sasselov et al., 2020), or UV exposure (Todd et al., 2022). Liberation of cyanide could enable the prebiotic schemes that make RNA.

Toner and Catling (2019) investigated a mechanism for stockpiling cyanides. Their thermodynamic calculations show that HCN can be preserved as ferrocyanide salts in evaporating

carbonate-rich lakes. However, the Toner and Catling (2019) numerical experiments were at 273 K and 298 K, which are far colder environments than the > 360 K surface temperatures that coincide with large HCN production in post-impact atmospheres (Figure 5.9). Although, Toner and Catling (2019) did not address stockpiling of HCCCN, cyanoacetylene can be captured by 4,5-dicyanoimidazole (DCI), a byproduct of adenine synthesis, to make crystals of 4,5-dicyanoimidazole (CV-DCI) (Ritson et al., 2022) and it is possible that other capture mechanisms are yet to be discovered. Overall, the feasibility of stockpiling prebiotic nitriles in post-impact conditions requires further geochemical modeling and experiments.

5.4.3 Impactor size and the likelihood of the origin of life

We hypothesize that $CH_4/CO_2 > 0.1$ might be an important threshold required for a post-impact atmosphere to produce useful concentrations of nitriles for origin of life chemistry. Figure 5.10 shows HCN and HCCCN haze rainout as a function of the atmospheric CH_4/CO_2 mole ratio for every post-impact simulation in this article. When $CH_4/CO_2 > 0.1$, the atmosphere is hazy, and HCN and HCCCN are delivered to the surface at a rate of up to $\sim 10^9$ molecules cm^{-2} s^{-1}. In contrast, atmospheres with $CH_4/CO_2 < 0.1$ rainout less than 10^5 HCN molecules cm^{-2} s^{-1} and have surface HCN concentrations less than 10^{-13} bar (Figure 5.7). Such small HCN concentrations may be challenging to stockpile as ferrocyanides (Toner and Catling, 2019). Additionally, modeled atmospheres with $CH_4/CO_2 < 0.1$ produce negligible HCCCN, yet the molecule is required in prebiotic schemes to synthesize pyrimidine (cytosine and uracil) nucleobase precursors to RNA (Powner et al., 2009; Okamura et al., 2019; Becker et al., 2019).

The impactor mass required to generate an atmosphere with $CH_4/CO_2 > 0.1$ is uncertain. Our optimistic model, which considers the effect of nickel-catalyzed methane production, requires a $> 4 \times 10^{20}$ kg (> 570 km) impactor (Figure 5.9). The lunar cratering record and abundance of highly siderophile elements Earth's mantle imply that between 4 and 7 such impacts occurred during the Hadean (Marchi et al., 2014; Zahnle et al., 2020). Our least optimistic model needs a $> 5 \times 10^{21}$ kg (> 1330 km) impact to create a post-impact

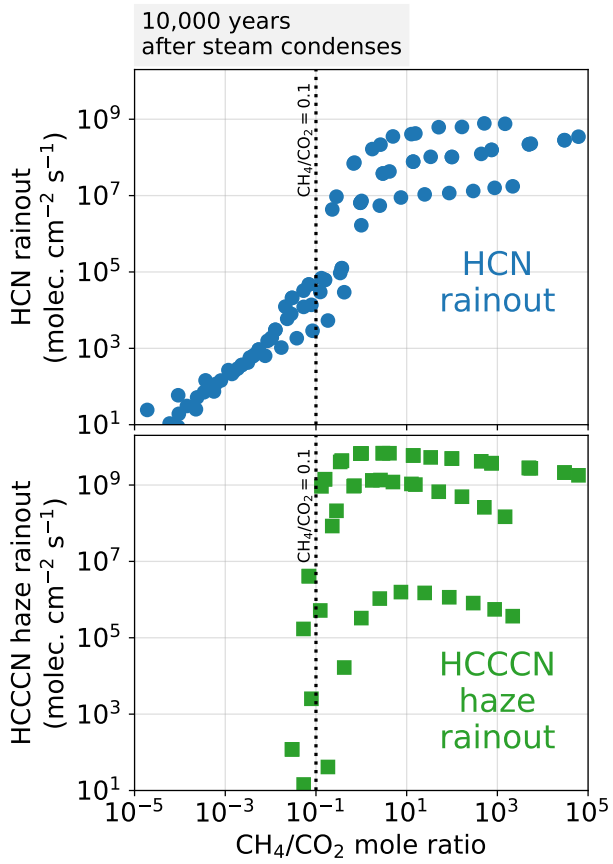

Figure 5.10: HCN rainout and HCCCN haze rainout as a function of the CH_4/CO_2 mole ratio in all simulated post-impact atmospheres. The figure considers simulations shown in main text Figure 5.7, 5.8, 5.9 and Figures 5.17 and 5.18 in the Chapter Appendix. All values are for the atmosphere 10,000 years after steam has condensed to an ocean. The HCN and HCCCN haze production is significantly larger for atmospheres with $CH_4/CO_2 > 0.1$.

atmosphere with $CH_4/CO_2 > 0.1$ because it assumes only a fraction of iron delivered to Earth reacts with the ocean to create atmospheric H_2 (Figure 5.17 in the Chapter Appendix). The Hadean only experienced 0 to 2 collisions this large (Zahnle et al., 2020). The precise minimum impactor mass to make an atmosphere with $CH_4/CO_2 > 0.1$ depends on the importance of atmospheric equilibration with a melt pond (Section 5.3.1, and Itcovitz et al. (2022)), the fraction of impactor iron that reduces the atmosphere, and the effect of Nickel and other surface catalysts on CH_4 kinetics.

An additional consideration is that any progress toward the origin of life caused by an impact could be erased by a subsequent impact that sterilizes the planet. For example, suppose a > 500 km impact that vaporizes the ocean sterilizes the globe (Citron and Stewart, 2022). With our most pessimistic calculations for post-impact CH_4 generation a > 1330 km ($> 5 \times 10^{21}$ kg) impact is required to create an atmosphere that generates significant HCN and HCCCN. In this scenario, the last > 1330 km impact favorable for prebiotic chemistry would likely be followed by a 500 to 1330 km impact that would destroy any primitive life without rekindling it. Alternatively, our optimistic model for post-impact CH_4 generation only requires a $> 4 \times 10^{20}$ kg (> 570 km) impact to create an atmosphere with $CH_4/CO_2 > 0.1$. In this case, the final > 570 km impact that might kickstart the origin of life is unlikely to be followed by a slightly smaller 500 km to 570 km sterilizing impact.

A caveat to the reasoning in the previous paragraph is that ocean-vaporization may not have sterilized the planet because microbes could have possibly survived in the deep subsurface (Sleep et al., 1989; Grimm and Marchi, 2018).

In summary, we suggest that $CH_4/CO_2 > 0.1$ may be an important threshold for post-impact atmospheres to be conducive to the origin of life because they generate > 4 orders of magnitude larger surface HCN concentrations, and are the only modeled atmospheres capable of generating HCCCN. We find that the minimum impactor mass required to create a post-impact atmosphere with $CH_4/CO_2 > 0.1$ is between 4×10^{20} and 5×10^{21} kg (570 to 1330 km). The value is uncertain because we do not know how effectively iron delivered by an impact reduces the atmosphere (Section 5.3.1), the importance of atmospheric equilibration

with a melt pond (Section 5.3.1), and because it is hard to estimate a realistic surface area of nickel catalysts available during the cooling steam atmosphere (Section 5.3.2).

5.4.4 Model caveats and uncertainties

Hydrogen from crust-atmosphere reactions

Perhaps the most significant caveat to the modeling effort described above is that we did not consider H_2 production from reactions between a hot post-impact atmosphere and solid, non-melted crust. Section 5.3.1 explores impact H_2 made by two mechanisms: (1) reduction of the atmosphere by impact-derived iron and (2) atmospheric equilibration with a melt pond made by the impact. However, it is also conceivable that while the atmosphere is hot and steam-rich in the $\sim 10^3$ years following an impact (i.e. Phase 2), water vapor could permeate through and react with the solid crust to produce H_2 by a process like serpentinization. Specifically, H_2O reduction by FeO in the solid crust could make H_2:

$$H_2O + 3FeO \rightarrow H_2 + Fe_3O_4 \tag{5.7}$$

In our nominal model (Figure 5.4 and 5.7), we require a post-impact atmosphere has $> 2 \times 10^3$ H_2 mol cm^{-2} (i.e. the equivalent of converting 13% of Earth's ocean to H_2) in order to reach a $CH_4/CO_2 > 0.1$ and big nitrile production rates. Assuming a crustal FeO content of 8 wt% (Takahashi, 1986), then 2×10^3 H_2 mol cm^{-2} could be produced by reacting water with FeO in the top $\sim$ 16 km of Earth's lithosphere. The feasibility of extensive water-rock H_2 generation depends on the permeability of the crust and the pressure gradients driving subsurface fluid circulation. For example, low permeability rocks with slow water circulation may not permit serpentinization of the upper crust within $\sim 10^3$ years while the atmosphere is hot and steam-rich. A comprehensive model is out of the scope of this article, but if attainable, significant water-rock reactions might produce a thick H_2 atmosphere after relatively small impacts (e.g. 10^{20} kg) which favors a $CH_4/CO_2 > 0.1$ and significant nitrile generation.

Another possibility, which we do not investigate in detail, is that atmosphere-crust reactions occur in the immediate aftermath of a giant impact (i.e. Phase 1), rather than over $\sim 10^3$ as previously discussed. A large impact could produce a global ejecta blanket several kilometers thick of mixed hot water and rock. As water was vaporized to form a steam atmosphere, the water and rock slurry could chemically equilibrate, producing H_2.

Zahnle et al. (2020) attempted to account for atmosphere-crust interaction by equilibrating the post-impact steam atmosphere (Phase 2) to a mineral redox buffer. For example, their Figure 5 assumes the atmosphere has a fixed oxygen fugacity set by the FMQ buffer at an assumed 650 K methane quench temperature. The calculation predicts most CO_2 is converted to CH_4 for impacts as small as $\sim 5 \times 10^{19}$ kg, but Zahnle et al. (2020) did not determine whether such significant atmosphere-crust interaction is physically plausible.

Climate

A shortcoming of this work is that our climate model is relatively simple. Throughout the Results section, our climate code assumes an isothermal 200 K stratosphere, a saturated adiabatic troposphere (i.e. relative humidity, $\phi = 1.0$), and ignores clouds. However, many of our simulated post-impact atmospheres contain a hydrocarbon haze which should absorb sunlight and warm the stratosphere (Arney et al., 2016). Also, in a hydrogen-dominated atmosphere, water vapor has a larger molecular weight compared to the background gas which could inhibit convection (Leconte et al., 2017) and perhaps cause low relative humidities. Furthermore, low-altitude clouds reflect sunlight and should cool a planet while high clouds have a greenhouse warming effect (Goldblatt and Zahnle, 2011).

Figure 5.11 attempts to show the uncertainty in our climate calculations as a function of three free parameters: stratosphere temperature, relative humidity, and low-altitude clouds which we crudely approximate by varying the surface albedo. The calculation uses the composition of the atmosphere after a 5×10^{20} kg impact in Figure 5.9 immediately after the steam atmosphere has condensed to an ocean. Our nominal climate parameters ($T_{\rm strat} = 200$ K, $\phi = 1$, $A_s = 0.2$) predict a 361 K surface temperature. A warm stratosphere caused by

hydrocarbon UV absorption and high albedo low altitude clouds might cause the surface to be ~ 30 K colder than our nominal model, assuming water vapor is saturated. On the other hand, low relative humidities, which might be favored in convection-inhibited H_2 dominated atmospheres, increase the troposphere lapse rate which warms the surface (Leconte et al., 2017). While Figure 5.11 gives a sense for the possible uncertainty in our climate calculations, it does not self-consistently simulate haze, relative humidity and clouds feedbacks. A more comprehensive model is required to resolve these nuances.

A further caveat is that our climate calculations ignore greenhouse warming from NH_3 (Table 5.1). We choose to disregard the influence of NH_3 because a substantial fraction of the gas should dissolve in the ocean (Zahnle et al., 2020), a process that our coupled photochemical-climate model cannot self-consistently account for. However, our climate model (Chapter Appendix 5.6.4), when uncoupled to photochemistry, can partition gases between the atmosphere and ocean according to gas solubility and ocean chemistry. Below, we use this stand-alone climate model to determine the climate affects of NH_3 in a post-impact atmosphere. NH_3 should dissolve into an ocean by henry's law, then hydrolyze to NH_4^+:

$$NH_3(g) \leftrightarrow NH_3(aq) \tag{5.8}$$

$$NH_3(aq) + H_2O \leftrightarrow NH_4^+ + OH^- \tag{5.9}$$

$$H_2O \leftrightarrow OH^- + H^+ \tag{5.10}$$

Therefore, the concentration of aqueous NH_3 (in mol kg^{-1}) is given by $m_{NH_3} = p_{NH_3}\alpha_{NH_3}$, where p_{NH_3} is the surface partial pressure of NH_3 in bars and α_{NH_3} is the Henry's law constant (mol kg^{-1} bar^{-1}). Reactions 5.9 and 5.10 give the ammonium concentration to be $m_{NH_4^+} = (K_9/K_{10})m_{NH_3}m_{H^+}$, where K_9 and K_{10} are equilibrium constants for each reaction. The Henry's law constant for NH_3 (in mol kg^{-1} bar^{-1}) is $\alpha_{NH_3} = 61\exp(4200(\frac{1}{T} - \frac{1}{298.15}))$ (Linstrom and Mallard, 1998). The equilibrium constants for Reactions 5.9 and 5.10 are approxi-

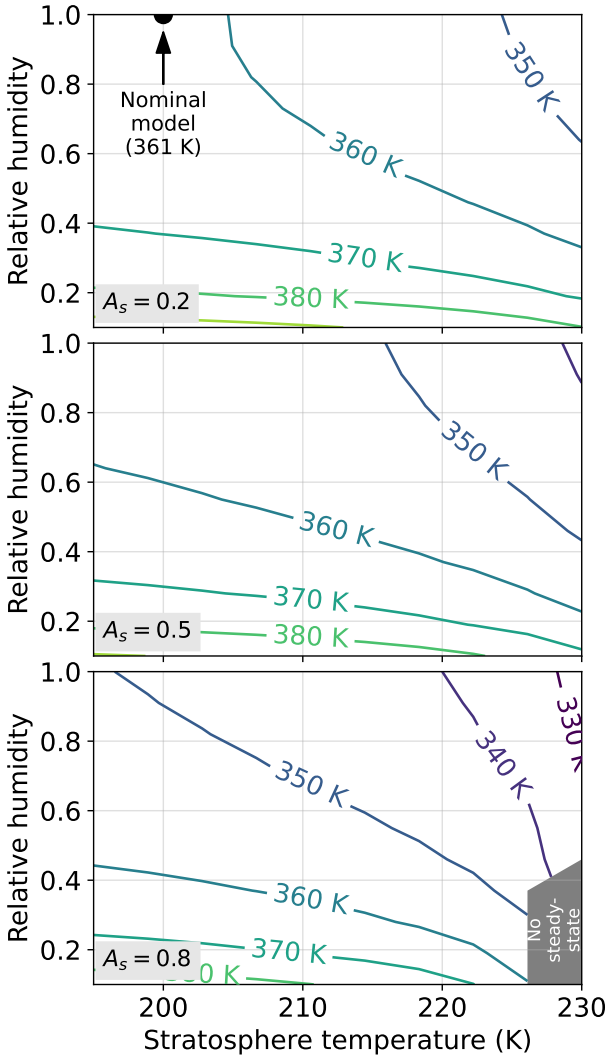

Figure 5.11: Surface temperature of a post-impact atmosphere as a function of stratosphere temperature, relative humidity, and surface clouds which we crudely approximate with the surface albedo (A_b). The atmosphere has 5.9 mol cm^{-2} CO_2, 5.6 mol cm^{-2} CH_4, 35.8 mol cm^{-2} N_2, 556 mol cm^{-2} H_2, 0.01 mol cm^{-2} CO, 0.3 mol cm^{-2} NH_3, and a liquid water ocean at the surface. This is the same composition of the atmosphere after a 5×10^{20} kg impact in Figure 5.9 once steam has condensed to an ocean. The gray shaded region labeled "no steady-state" has no steady-state climate solutions that balance incoming shortwave and outgoing longwave energy. Uncertainties in our assumed stratosphere temperature, relative humidity and the effects of low-altitude clouds predict surface temperatures from $\sim$ 330 K to $\sim$ 390 K with a nominal value of 361 K.

mately $\log_{10}(K_9) = -84.63\exp(-0.0161T) - 4.05$ and $\log_{10}(K_{10}) = -39.96\exp(-0.00639T) - 8.06$. We derived both of these parameterizations using the SUPCRT thermodynamic database (Johnson et al., 1992).

We implement this ocean chemistry into our stand-alone climate model (Chapter Appendix 5.6.4), and compute the surface temperature after the 5×10^{20} kg impact in Figure 5.9 once the steam atmosphere has condensed to an ocean. The mol cm^{-2} of each gas are given in the Figure 5.11 caption. We use our nominal climate parameters ($T_{\rm strat} = 200$ K, $\phi = 1$, $A_s = 0.2$), assume the total H_2O reservoir is 1 modern ocean (15,000 mol cm^{-2}) with pH = 7, and account for the radiative affects of NH_3 in addition to the Table 5.1 opacities. The model predicts a 371 K surface temperature, which is 10 K warmer than calculations that do not include NH_3 opacities or ocean dissolution. 96% of the ammonia reservoir is dissolved in the ocean.

Ammonia has a more substantial effect on climate after larger impactors. Consider the atmosphere after a 7.9×10^{21} kg impact in Figure 5.5 once steam has condensed to an ocean (0.008 mol cm^{-2} CO_2, 11.5 mol cm^{-2} CH_4, 32.6 mol cm^{-2} N_2, 9122 mol cm^{-2} H_2, 0.002 mol cm^{-2} CO, and 6.8 mol cm^{-2} NH_3). Our climate model, which includes NH_3 opacities and ocean dissolution, predicts a 505 K surface temperature with only 20% of the NH_3 dissolved in the ocean because solubility decreases with increased temperature. This is 42 K hotter than our model that ignores NH_3 greenhouse contributions (Figure 5.7). Overall, our climate calculations throughout most of this article perhaps underestimate the greenhouse warming by 10 to $\sim$ 40 K by ignoring NH_3 opacities, but instead may overestimate surface temperature because do not account for the cooling effects of haze and low altitude clouds (Figure 5.11). Additional warming from NH_3 would only be relevant for a fraction of the post-impact atmosphere, before ammonia is destroyed by photolysis (Figure 5.6).

Unknown chemical reactions and the effect of ions

While our chemical scheme for HCCCN successfully reproduces the HCCCN abundances in Titan's atmosphere (Figure 5.20 in the Chapter Appendix), it may lack many reactions

relevant to post-impact atmospheres. Our sparse HCCCN network is necessary because currently few kinetic measurements are published in the literature.

Our photochemical model does not include ion chemistry, which is likely a reasonable simplification because ions are not important for HCN or HCCCN formation on Titan (Loison et al., 2015). Only some heavy hydrocarbons, like benzene (C_6H_6), rely on coupled neutral-ion chemistry to explain their observed abundances in Titan's atmosphere (Hörst, 2017).

5.5 Conclusions

We use atmospheric models to investigate the production of prebiotic feedstock molecules in impact-generated reducing atmospheres on the Hadean Earth, updating simpler calculations made by Zahnle et al. (2020). We find that massive asteroid impacts can generate temporary H_2-, CH_4- and NH_3-rich atmospheres, which photochemically generate HCN and HCCCN for the duration of hydrogen escape to space (10^5 to 10^7 years). The production of nitriles increases dramatically for haze-rich atmospheres that have mole ratios of $CH_4/CO_2 > 0.1$. In these cases, HCN can rain out onto land surfaces at a rate of $\sim 10^9$ molecules cm^{-2} s^{-1}, and HCCCN incorporated in haze rains out at a similar rate. Atmospheres with $CH_4/CO_2 < 0.1$ produce 3 to 4 orders of magnitude less HCN, and generate negligible HCCCN. The impactor mass required to create an atmosphere with $CH_4/CO_2 > 0.1$ is uncertain and depends on how efficiently atmosphere-iron, atmosphere-melt and atmosphere-crust reactions generate H_2 and the surface area of nickel catalysts exposed to the cooling steam atmosphere. In an optimistic modeling scenario a $> 4 \times 10^{20}$ kg (> 570 km) impactor is sufficient, while in our least optimistic scenario a $> 5 \times 10^{21}$ kg (> 1330 km) impactor is required.

We find that post-impact atmospheres that generate significant prebiotic molecules have > 360 K surface temperatures caused by a H_2-H_2 greenhouse which may be too hot for prebiotic chemistry, although the temperature may be cooler if reflective clouds occur. An alternative is that HCN and HCCCN generated in post-impact atmosphere are stockpiled. Cyanide can plausibly be stockpiled and concentrated in ferrocyanide salts and cyanoacetylene could be captured by byproducts of adenine synthesis into imidazole-based crystals

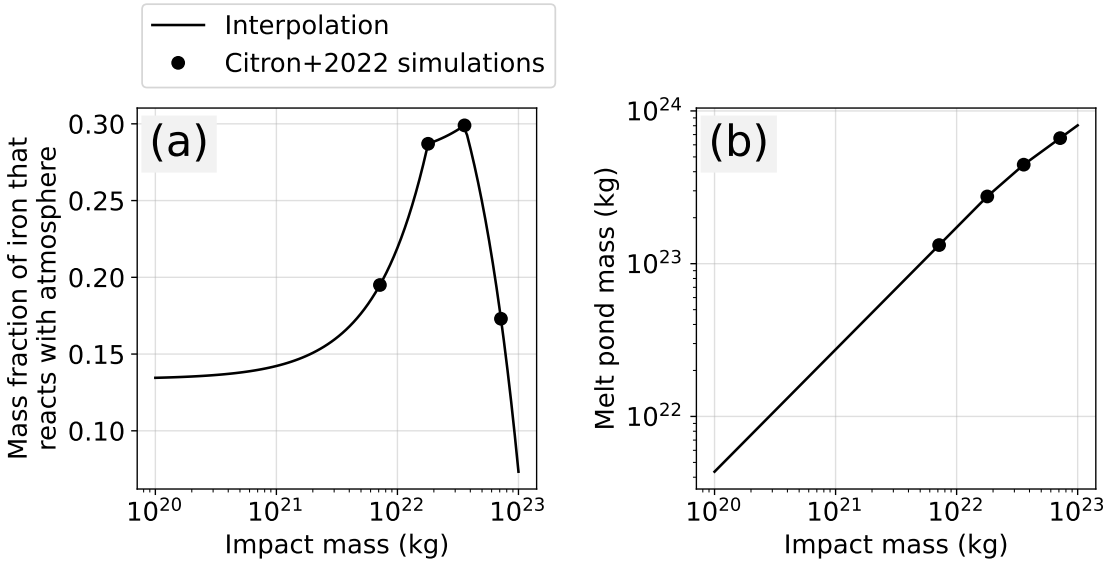

Figure 5.12: Interpolation and extrapolation of the Citron and Stewart (2022) SPH simulations of impacts that collide with Earth at a 45° angle and with a velocity of twice Earth's escape velocity. (a) is the mass fraction of iron that reacts with the atmosphere and (b) is the mass of the melt pool produced by an impact. These interpolations are relevant to Figure 5.2 in the main text, and Figures 5.13, 5.14, 5.17, and 5.18 in the Chapter Appendix.

(Ritson et al., 2022). HCN and HCCCN can be used to create nucleotide precursors to RNA millions of years after the impact, once the H_2 has escaped to space, and the atmosphere has cooled to a more temperate state.

Nominally, the Hadean Earth appears to have experienced several impacts that would have produced an atmosphere that made significant prebiotic feedstock molecules. Like Earth, all rocky exoplanets accreted from impacts. Consequently, impact-induced reducing atmospheres may be a common planetary processes that provides windows of opportunity for the origin of exoplanet life.

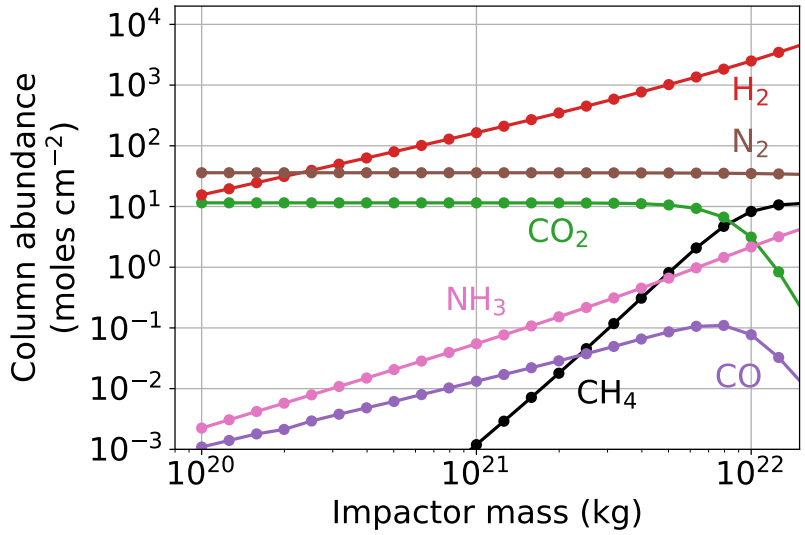

Figure 5.13: Identical to Figure 5.4 in the main text, but instead assumes post-impact H_2 generation if governed by "Model 1B" described in Figure 5.2.

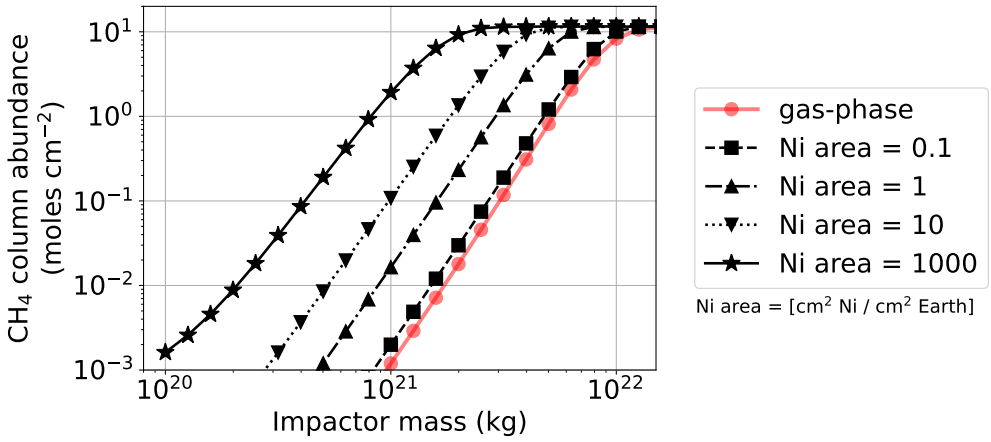

Figure 5.14: Identical to Figure 5.5 in the main text, but instead assumes post-impact H_2 generation if governed by "Model 1B" described in Figure 5.2.

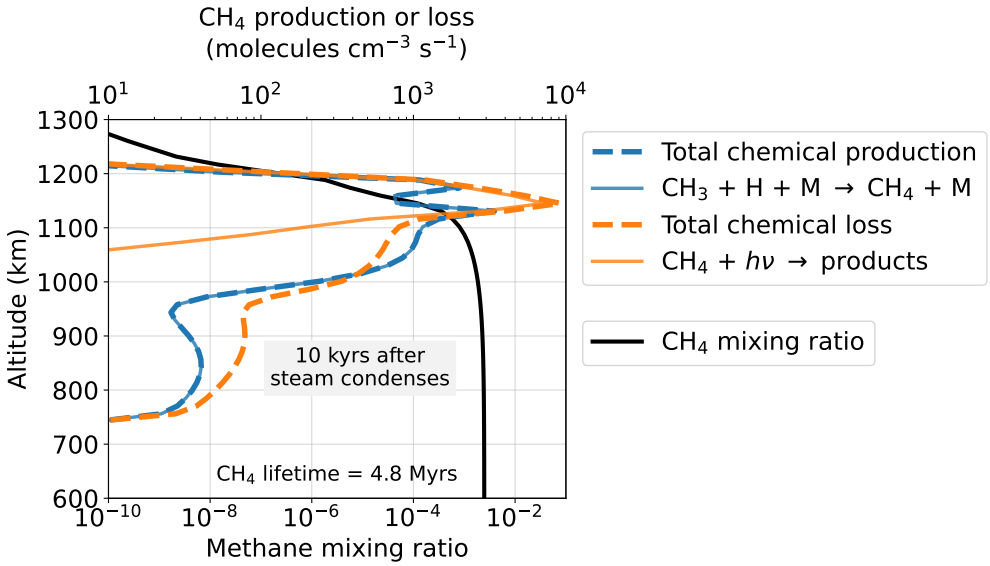

Figure 5.15: The methane photochemical lifetime in post-impact atmospheres. The plot shows the CH_4 mixing ratio and production and loss as a function of altitude 10,000 years after the steam atmosphere has condensed to an ocean following the 1.58×10^{21} kg impact described in Figure 5.6. CH_4 is primarily destroyed by photolysis, but reforms efficiently in the H_2 rich atmosphere from $CH_3 + H + M \rightarrow CH_4 + M$. The result is a 4.8 million year CH_4 photochemical lifetime. CH_4 only persists in the atmosphere for about one million years because H_2 escapes to space in this amount of time which inhibits CH_4 recombination.

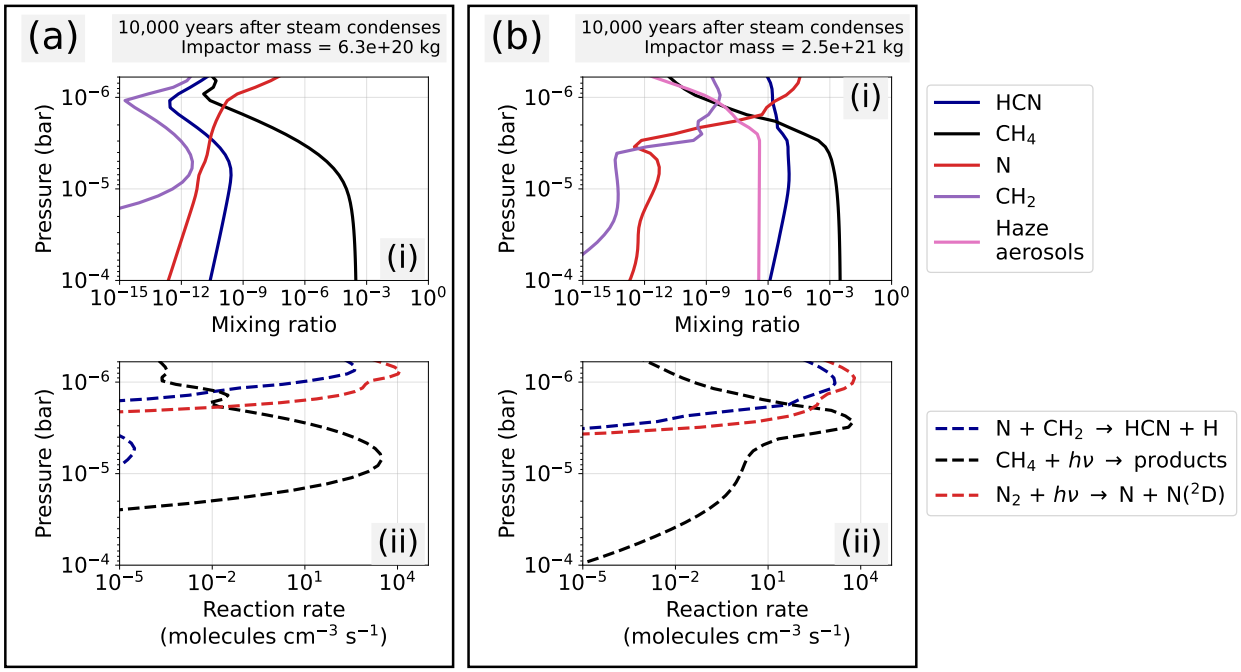

Figure 5.16: HCN production and precursor species after a (a) 6.3×10^{20} kg and (b) 2.5×10^{21} kg impactor. In both (a) and (b) panels (i) shows mixing ratios, while (ii) shows photolysis and reaction rates. Panel (b) contains haze aerosols which cause CH_4 photolysis to be higher in the atmosphere compared to panel (a). High altitude CH_4 photolysis, closer to N_2 photolysis, promotes HCN production because photolysis produced can more readily combine to make cyanides.

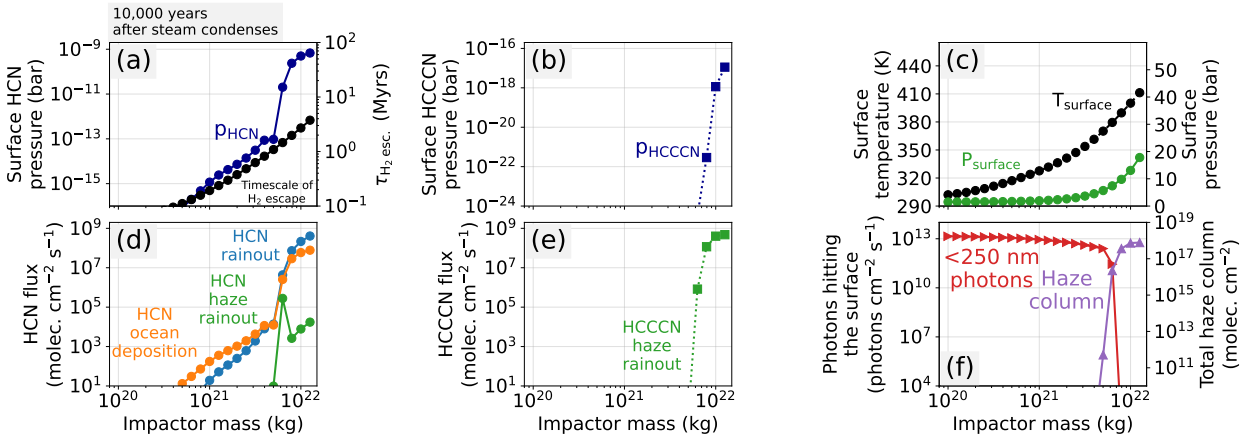

Figure 5.17: Identical to Figure 5.7 in the main text, but instead assumes post-impact H_2 generation if governed by "Model 1B" described in Figure 5.2.

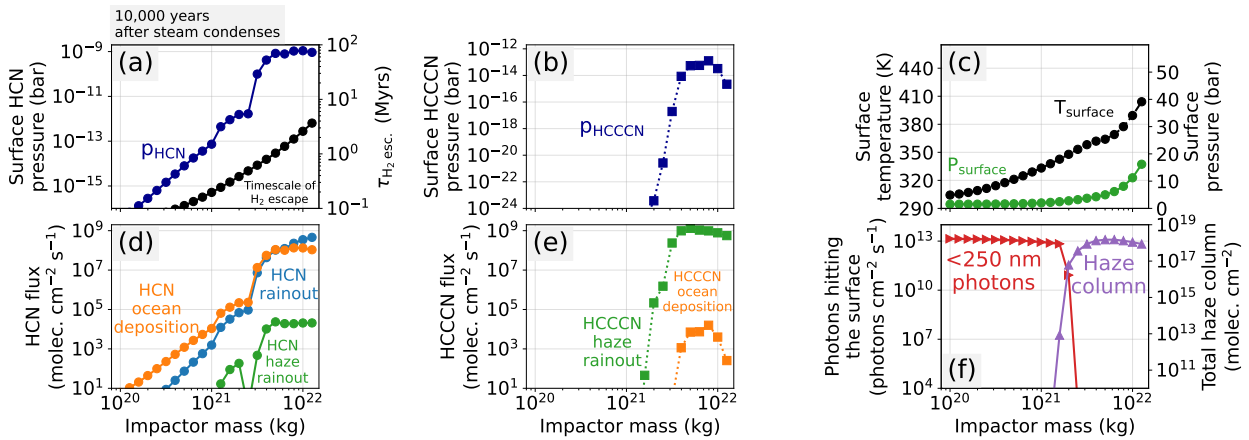

Figure 5.18: Identical to Figure 5.9 in the main text, but instead assumes post-impact H_2 generation if governed by "Model 1B" described in Figure 5.2.

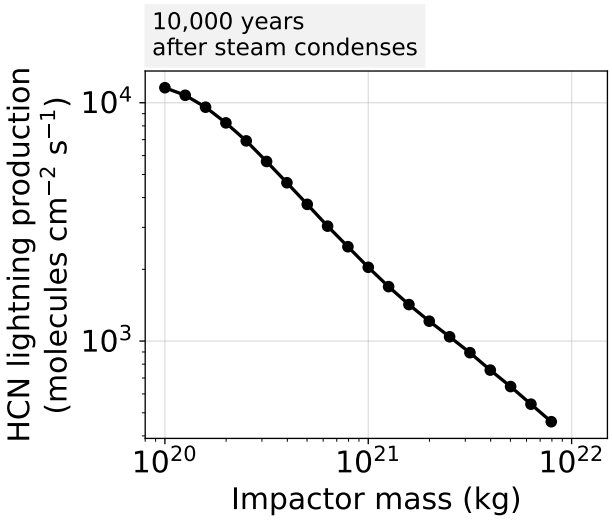

Figure 5.19: HCN production from lighting for the same simulations and time-period shown in Figure 5.7. The calculations use methods described in Chameides and Walker (1981) assuming modern Earth's lightning dissipation rate (9.8×10^{-9} J cm^{-2} s^{-1}), and a 2250 K HCN freeze-out temperature. HCN production from lightning is small compared to what is achievable with photochemistry.

5.6 Chapter Appendix

5.6.1 Hydrogen generation from iron and molten crust

Here, we describe our model for atmospheric H_2 generation in the days to months following a massive asteroid impact (Phase 1 in Figure 5.1). All our simulations assume a pre-impact atmosphere containing CO_2, N_2, and ocean water. First, we assume that half of the impactor's kinetic energy heats the atmosphere and ocean water to $\sim$ 2000 K. We assume the atmosphere is heated to $\sim$ 2000 K because this is roughly the evaporation temperature of silicates. For our assumed impact velocity of 20.7 km s^{-1}, all impactor masses that we consider in the main text (10^{20} to 10^{22} kg) have kinetic energies $> 2 \times 10^{28}$ joules delivering $> 10^{28}$ joules to the atmosphere which is larger than the 5×10^{27} joules required to vaporize an ocean (Sleep et al., 1989).

Next, our model assumes each mole of iron delivered reacts with the atmosphere and removes one mole of oxygen. The moles cm^{-2} of iron delivered to the atmosphere is

$$N_{\mathrm{Fe,atmos}} = \frac{X_{\mathrm{Fe,atmos}} X_{\mathrm{Fe,imp}} M_{\mathrm{imp}}}{\mu_{\mathrm{Fe}} A_{\oplus}} \tag{5.11}$$

Here, M_{imp} is the mass of the impact in grams, $X_{\mathrm{Fe,imp}}$ is the iron mass fraction of the impact, $X_{\mathrm{Fe,atmos}}$ is the fraction of the impactor iron that reacts with the atmosphere, μ_{Fe} is the molar weight of iron, and $A_{\oplus}$ is the area of Earth in cm^2. Following Zahnle et al. (2020) we take $X_{\mathrm{Fe,imp}} = 0.33$. In main text, we assume $X_{\mathrm{Fe,atmos}} = 1$ (e.g. "Model 1A" in Figure 5.2), while the Chapter Appendix contains calculations with $X_{\mathrm{Fe,atmos}} = 0.15$ to 0.3 based on extrapolations of the Citron and Stewart (2022) SPH impact simulations for 45° impactors traveling at 20.7 km s^{-1} (e.g. "Model 1B" in Figure 5.2). To approximate equilibration between the delivered iron and the atmosphere, we simply remove $N_{\mathrm{Fe,atmos}}$ of oxygen atoms from the atmosphere.

Our model also optionally considers reactions between the atmosphere and a melt pond generated by the impact. Our approach is similar to the one described in Itcovitz et al.

(2022). We estimate the total mass of the melt pond (M_{melt}) by interpolating SPH impact simulations from Citron and Stewart (2022) for a 45° impact angle. The smallest impact they consider is 7×10^{21} kg, so we extrapolate their results down to 10^{20} kg. We additionally take the melted crust to be basaltic in composition except with variable initial amounts of ferric and ferrous iron. Effectively, this means that the initial oxygen fugacity of the melted crust is a free parameter because iron redox state is related to oxygen fugacity through the equilibrium reaction,

$$0.5O_2 + 2FeO \leftrightarrow Fe_2O_3 \tag{5.12}$$

We assume the oxygen atoms can flow from the atmosphere into the melt (or vice-versa) in order to bring Reaction 5.12 to an equilibrium state defined by Kress and Carmichael (1991) thermodynamic data. Our model also considers H_2O gas dissolution in the melt using the Equation (19) solubility relation in Itcovitz et al. (2022).

Finally, given a heated post-impact atmosphere that has been reduced by impactor iron and, optionally, in contact with an melt pool, we compute thermodynamic equilibrium of the atmosphere-melt system at 1900 K. We choose 1900 K because any impact-produced silicate vapors should have condensed and rained out of the atmosphere, and the melt pool should have not yet solidified (Itcovitz et al., 2022). To find an equilibrium state, we first compute an equilibrium composition for the atmosphere alone using the equilibrium solver in the Cantera chemical engineering package (Goodwin et al., 2022) with our thermodynamic data (Chapter Appendix 5.6.3). Next, to equilibrate the atmosphere-melt system, we perform a zero-dimensional kinetics integration for 1000 years at constant temperature and pressure with our reaction network (Chapter Appendix 5.6.3). All reactions in our network are reversible thermodynamically, therefore integrating the kinetics forward in time should ultimately reach a state of thermodynamic equilibrium. Our integration includes additional reactions representing Reaction 5.12 and H_2O dissolution in the melt. We arbitrarily choose forward reaction rates of 10^{-10} s^{-1} for both reactions, then reverse the rates using the Kress

and Carmichael (1991) equilibrium constant, and the Equation (19) solubility relation in Itcovitz et al. (2022). Overall, our approach finds a chemical equilibrium state between the atmosphere and the melt pond, and therefore an estimation of the amount of H_2 generated from atmosphere-iron and atmosphere-melt reactions.

Our code for solving melt-atmosphere equilibrium is available at the following Zenodo link: `https://doi.org/10.5281/zenodo.7802966`.

5.6.2 Kinetics model of a cooling steam atmosphere

We simulate the chemistry of a cooling post-impact atmosphere using a zero-dimensional kinetics-climate model. We assume the atmosphere's composition, pressure, and temperature are homogeneous in all directions, and has a vertical extent of one atmospheric scale height (H_a). For these assumptions, the following system of ordinary differential equations govern our model:

$$\frac{\partial N_i}{\partial t} = \frac{H_a}{N_a}(P_i - L_i) + \frac{A_c}{N_a}(P_{i,\text{surf}} - L_{i,\text{surf}}) \tag{5.13}$$

$$\frac{\partial T_s}{\partial t} = -\frac{1}{\rho c_p}\left(\frac{F_{\text{net}}}{H_a}\right) - \frac{1}{\rho c_p}\left(\frac{dM_{\text{H}_2\text{O}}}{dt}\frac{l_{\text{H}_2\text{O}}}{A_\oplus H_a}\right) \tag{5.14}$$

All variables and units are in Table 5.3. In Equation (5.13), N_i is the column abundance of species i in mole cm^{-2}, which changes because of gas-phase chemical reactions (production rate P_i and loss rate L_i) and reactions occurring on surfaces ($P_{i,\text{surf}}$ and $L_{i,\text{surf}}$). In Equation (5.14), T is surface temperature, which changes because of energy radiated to space (F_{net}), and because of latent heat from H_2O condensation ($\frac{dM_{\text{H}_2\text{O}}}{dt}$), where $M_{\text{H}_2\text{O}}$ is the mass of H_2O in the atmosphere. We approximate the energy radiated to space in ergs cm^{-2} s^{-1} from a steam-dominated atmosphere with the following parameterization:

$$F_{\text{net}} = 8.3 \times 10^4 + 1000 \max(T_s - 1750, 0) \tag{5.15}$$

This parameterization fits calculations from our radiative transfer model (see Chapter Ap-

pendix 5.6.4), which uses the a solar spectrum at 4.0 Ga derived from methods described in Claire et al. (2012).

We can rewrite Equation (5.14), replacing ρH_a using the ideal gas law and the definition of atmospheric scale height,

$$\rho H_a = \frac{p\bar{\mu}}{N_a kT}\frac{N_a kT}{\bar{\mu}g} = \frac{p}{g} \tag{5.16}$$

Here, p is the total atmospheric pressure in dynes cm^{-2}, g is gravitational acceleration in cm s^{-2}, k is the Boltzmann constant, $\bar{\mu}$ is the mean molecular weight in g mol^{-1}, and N_a is Avogadro's number. Therefore,

$$\frac{\partial T_s}{\partial t} = -\frac{g}{pc_p}F_{\text{net}} - \frac{g}{pc_p}\left(\frac{dM_{\text{H}_2\text{O}}}{dt}\frac{l_{\text{H}_2\text{O}}}{A_\oplus}\right) \tag{5.17}$$

Next, we must derive an expression for the steam condensation rate ($dM_{\text{H}_2\text{O}}/dt$) in terms of known variables. Working in CGS units, the total pressure of the atmosphere is given by its gravitational force divided by Earth's surface area (5.1×10^{18} cm^2):

$$p = \frac{Mg}{A_\oplus} \tag{5.18}$$

Here, M is the mass of the atmosphere in grams. We are considering steam-dominated atmospheres, therefore, the mass and pressure in the above relation is approximately equal to the mass of atmospheric H_2O and the H_2O partial pressure.

$$p_{\text{H}_2\text{O}} \approx \frac{M_{\text{H}_2\text{O}}g}{A_\oplus} \tag{5.19}$$

$$M_{\text{H}_2\text{O}} \approx \frac{p_{\text{H}_2\text{O}}A_\oplus}{g} \tag{5.20}$$

Taking a time derivative of Equation (5.20) yields

$$\frac{dM_{\mathrm{H_2O}}}{dt} \approx \frac{A_\oplus}{g}\frac{dp_{\mathrm{H_2O}}}{dt} \tag{5.21}$$

We assume that the only processes changing the H_2O mass in the atmosphere is condensation, which occurs in our model when steam becomes saturated. We further assume that the H_2O partial pressure is fixed at saturation once steam condensation begins. We approximate the saturation vapor pressure of H_2O, $p^{\mathrm{sat}}_{\mathrm{H_2O}}$, using the Clausius-Clapeyron equation, assuming a temperature-independent latent heat, $l_{\mathrm{H_2O}}$,

$$p^{\mathrm{sat}}_{\mathrm{H_2O}} = p_0 \exp\left(\frac{l_{\mathrm{H_2O}}\mu_{\mathrm{H_2O}}}{R}\left(\frac{1}{T_0} - \frac{1}{T}\right)\right) \tag{5.22}$$

p_0 and T_0 are reference pressures and temperatures, respectively. Taking a time derivative of Equation (5.22) yields

$$\frac{dp^{\mathrm{sat}}_{\mathrm{H_2O}}}{dt} = \left(\frac{l_{\mathrm{H_2O}}\mu_{\mathrm{H_2O}}}{RT^2}\right)\frac{dT_s}{dt}p^{\mathrm{sat}}_{\mathrm{H_2O}} \tag{5.23}$$

Substituting Equation (5.23) into Equation (5.21) gives

$$\frac{dM_{\mathrm{H_2O}}}{dt} = \frac{A_\oplus}{g}\left(\frac{l_{\mathrm{H_2O}}\mu_{\mathrm{H_2O}}}{RT^2}\right)\frac{dT_s}{dt}p^{\mathrm{sat}}_{\mathrm{H_2O}} \tag{5.24}$$

Finally, we can substitute Equation (5.24) into Equation (5.17) and rearrange to solve for dT/dt. The result below gives the rate of change of temperature when the steam is too hot to condense ($p_{\mathrm{H_2O}} > p^{\mathrm{sat}}_{\mathrm{H_2O}}$), and when the steam is condensing ($p_{\mathrm{H_2O}} = p^{\mathrm{sat}}_{\mathrm{H_2O}}$).

$$\frac{dT_s}{dt} = \begin{cases} -\frac{g}{pc_p}F_{\mathrm{net}} & p_{\mathrm{H_2O}} > p^{\mathrm{sat}}_{\mathrm{H_2O}} \\ -\frac{g}{pc_p}F_{\mathrm{net}}\left(1 + \frac{l^2_{\mathrm{H_2O}}\mu_{\mathrm{H_2O}}p^{\mathrm{sat}}_{\mathrm{H_2O}}}{pc_pRT^2}\right)^{-1} & p_{\mathrm{H_2O}} = p^{\mathrm{sat}}_{\mathrm{H_2O}} \end{cases} \tag{5.25}$$

Equations (5.13) and (5.25) are a system of ordinary differential equations, which we approximately solve over time using the CVODE BDF method developed by Sundials Computing (Hindmarsh et al., 2005). Additionally, for either gas-phase or surface reactions, we

make use of the Cantera software library (Goodwin et al., 2022) to compute chemical production and destruction rates. Our code for solving the equations derived in this section is available at the following Zenodo link: `https://doi.org/10.5281/zenodo.7802966`.

Table 5.3: Variables

Variable	Definition	Units
f_i	Mixing ratio of species i	dimensionless
n_i	Number density of species i	molecules cm^{-3}
n	Total number density	molecules cm^{-3}
N_i	Column abundance of species i	mol cm^{-2}
N	Total column abundance	mol cm^{-2}
ρ	Density of the atmosphere	g cm^{-3}
c_p	Specific heat capacity of the atmosphere	erg g^{-1} K^{-1}
F_{net}	Net radiative energy leaving the atmosphere	erg cm^{-2} s^{-1}
z	Altitude	cm
t	Time	seconds
P_i	Total chemical production of species i	molecules cm^{-3} s^{-1}
L_i	Total chemical loss of species i	molecules cm^{-3} s^{-1}
$P_{i,\text{surf}}$	Total chemical production of species i from surface reactions	molecules cm^{-2} s^{-1}
$L_{i,\text{surf}}$	Total chemical loss of species i from surface reactions	molecules cm^{-2} s^{-1}
$R_{\text{i, rainout}}$	Production and loss of species i from rainout	molecules cm^{-3} s^{-1}
$Q_{i,\text{ cond}}$	Production and loss of species i from condensation and evaporation	molecules cm^{-3} s^{-1}
Φ_i	Vertical flux of species i	molecules cm^{-2} s^{-1}
K_{zz}	Eddy diffusion coefficient	cm^{-2} s^{-1}
D_i	Molecular diffusion coefficient	cm^{-2} s^{-1}
H_i	$= N_a\text{kT}/\mu_i g$, The scale heights of species i	cm
H_a	$= N_a\text{kT}/\overline{\mu} g$, The average scale height.	cm
N_a	Avogadro's number	molecules mol^{-1}
k	Boltzmann's constant	erg K^{-1}
R	Gas constant	erg mol^{-1} K^{-1}
μ	Molar mass. $\overline{\mu}$ is mean molar mass of the atmosphere, and μ_i is the molar mass of species i	g mol^{-1}

A_c	Catalyst surface area per atmospheric column	cm^2 catalyst / cm^2 Earth
$l_{\mathrm{H_2O}}$	Latent heat of H_2O condensation	erg g^{-1}
$A_\oplus$	Area of Earth's surface	cm^2
ϕ	Relative humidity	dimensionless
A_s	Optical surface albedo	dimensionless
p	Atmospheric pressure. p_i is the partial pressure of species i.	dynes cm^{-2}
M	Mass of the atmosphere. M_i is the mass of species i. M_imp is the mass of an impactor.	g
g	Gravitational acceleration	cm s^{-2}
α_Ti	Thermal diffusion coefficient of species i. We neglect this term ($\alpha_\mathrm{Ti} = 0$)	dimensionless
w_i	Fall velocity of a particle	cm s^{-1}
T	Temperature. T_s is the surface temperature.	K

5.6.3 The Photochem *model*

To simulate the photochemistry of post-impact reducing atmospheres, we developed a photochemical model called *Photochem*. The model is a re-written and vastly updated version of *PhotochemPy* (Wogan et al., 2022). *Photochem* is written in modern Fortran and C, with a Python interface made possible by Cython (Behnel et al., 2010). This article uses *Photochem* version v0.3.14 archived in the following Zenodo repository: `https://doi.org/10.5281/zenodo.7802921`.

The following sections briefly describe the fundamental model equations solved by *Photochem*, our chemical network, and validates the model against observations of Earth and Titan.

Model equations

We begin our derivation of the equations governing *Photochem* with modified versions of Equations B.1, B.2 and B.29 in Catling and Kasting (2017):

$$\frac{\partial n_i}{\partial t} = -\frac{\partial}{\partial z}\Phi_i + P_i - L_i - R_{i,\text{ rainout}} + Q_{i,\text{ cond}} \tag{5.26}$$

$$\Phi_{i,\text{gas}} = -K_{zz} n \frac{\partial}{\partial z}\left(\frac{n_i}{n}\right) - n_i D_i \left(\frac{1}{n_i}\frac{\partial n_i}{\partial z} + \frac{1}{H_i} + \frac{1}{T}\frac{\partial T}{\partial z} + \frac{\alpha_{Ti}}{T}\frac{\partial T}{\partial z}\right) \tag{5.27}$$

$$\Phi_{i,\text{particle}} = -K_{zz} n \frac{\partial}{\partial z}\left(\frac{n_i}{n}\right) - w_i n_i \tag{5.28}$$

Table 5.3 explains the variables and their units. Equation (5.26) states that molecule concentration (n_i in molecules cm^{-3}) changes over time at a point in space because of vertical movement of particles ($\frac{\partial}{\partial z}\Phi_i$), and chemical reactions, rainout or condensation/evaporation (P_i, L_i, $R_{i,\text{ rainout}}$, and $C_{i,\text{ cond}}$). The equation is 1-D, because it only considers vertical gas transport and differs from Equation B.1 in Catling and Kasting (2017) because we explicitly include rainout and condensation. Equation (5.27) states that the flux of gases ($\Phi_{i,\text{gas}}$) is determined by eddy and molecular diffusion, and Equation (5.28) assumes that the flux of particles ($\Phi_{i,\text{particle}}$) is given by eddy diffusion and the rate particles fall through the atmosphere.

Many 1-D photochemical models further simplify Equation (5.26) by assuming that total number density does not change over time ($\partial n/\partial t \approx 0$). Using this assumption, Equation (5.26) is recast in terms of evolving mixing ratios (f_i) rather than number densities (see Appendix B.1 in Catling and Kasting (2017) for a derivation). Such models assume a time-constant temperature profile. The surface pressure is also prescribed, and pressures above the surface are computed with the hydrostatic equation. In order to guarantee that all mixing ratios in the atmosphere sum to 1, models assume a background filler gas with a mixing ratio $f_{\text{background}} = 1 - \sum_i f_i$. N_2, CO_2 or H_2 are common choices for the background gas, depending on the atmosphere under investigation. By definition, the background gas

is not conserved. This approach is valid for steady-state photochemical calculations, and is also reasonable for atmospheric transitions which maintain approximately constant surface pressure and atmospheric temperature. The *Photochem* code contains an implementation of this traditional approach to photochemical modeling.

Unfortunately, solving a simplified version of Equation (5.26) in terms of mixing ratios does not work well for post-impact atmospheric modeling. For example, a post-impact atmosphere can contain 10 bars of H_2 which escapes to space over millions of years, lowering the surface pressure to a 1 bar N_2 dominated atmosphere (e.g. Figure 5.6). Traditional photochemical models fail to simulate this scenario because it is not reasonable to assume a single background gas and time-constant surface pressure. Additionally, most models fix atmospheric temperature during any single model integration, but surface temperature should change significantly as impact-generated H_2 escapes to space.

Therefore, *Photochem* implements a code that solves Equation (5.26) in terms of number densities (n_i) without the assumption of fixed surface pressure or a background gas. This approach requires slight modifications to Equation (5.27) and (5.28) which we describe below. Consider the hydrostatic equation and ideal gas law

$$\frac{\partial p}{\partial z} = \frac{-gp\bar{\mu}}{N_a k T} \tag{5.29}$$

$$p = nkT \tag{5.30}$$

Substituting the ideal gas law in the hydrostatic equation yields

$$\frac{\partial}{\partial z}(nT) = \frac{-gn\bar{\mu}}{N_a k} \tag{5.31}$$

$$n\frac{\partial T}{\partial z} + T\frac{\partial n}{\partial z} = \frac{-gn\bar{\mu}}{N_a k} \tag{5.32}$$

After rearrangement and substituting the definition of scale height,

$$\frac{1}{n}\frac{\partial n}{\partial z} = -\frac{1}{H_a} - \frac{1}{T}\frac{\partial T}{\partial z} \tag{5.33}$$

Now consider the following expansion using the quotient rule

$$\frac{\partial}{\partial z}\left(\frac{n_i}{n}\right) = \frac{1}{n}\frac{\partial n_i}{\partial z} - \frac{n_i}{n^2}\frac{\partial n}{\partial z} \tag{5.34}$$

Substituting Equation (5.33) into Equation (5.34) and rearrangement gives

$$n\frac{\partial}{\partial z}\left(\frac{n_i}{n}\right) = \frac{\partial n_i}{\partial z} + \frac{n_i}{H_a} + \frac{n_i}{T}\frac{\partial T}{\partial z} \tag{5.35}$$

Finally, we can substitute Equation (5.35) into Equations (5.27) and (5.28) to derive new equations for the flux of gases and particles

$$\Phi_{i,\text{gas}} = -K_{zz}n_i\left(\frac{1}{n_i}\frac{\partial n_i}{\partial z} + \frac{1}{H_a} + \frac{1}{T}\frac{\partial T}{\partial z}\right) - n_i D_i\left(\frac{1}{n_i}\frac{\partial n_i}{\partial z} + \frac{1}{H_i} + \frac{1}{T}\frac{\partial T}{\partial z} + \frac{\alpha_{Ti}}{T}\frac{\partial T}{\partial z}\right) \tag{5.36}$$

$$\Phi_{i,\text{particle}} = -K_{zz}n_i\left(\frac{1}{n_i}\frac{\partial n_i}{\partial z} + \frac{1}{H_a} + \frac{1}{T}\frac{\partial T}{\partial z}\right) - w_i n_i \tag{5.37}$$

We then apply a finite-volume approximation to the Equation (5.26) system of particle differential equations using fluxes for gases and particles given by Equations (5.36) and (5.37), which results in a system of ordinary differential equations. We use a second-order centered scheme for all spatial derivatives except falling particles, which use a first-order upwind scheme for stability. *Photochem* evolves the finite volume approximate forward in time using the CVODE BDF method developed by Sundials Computing (Hindmarsh et al., 2005). The model assumes no background gas, and surface pressure can evolve over time as, for example, gases escape to space. Additionally, our model computes a self-consistent temperature structure within each time step using the *Clima* radiative transfer code (Chapter Appendix 5.6.4) assuming a pseudo-moist adiabatic troposphere connected to an isothermal upper atmosphere.

An additional challenge of post-impact atmospheres is that the scale height changes by a factor of $\sim$ 10 or more when H_2 escapes leaving behind a N_2 or CO_2 dominated atmosphere (Figure 5.6). Most relevant photochemistry occurs at pressures $> 10^{-7}$ bar, and so we choose a model domain which starts at the surface and extends to an altitude that is approximately this pressure. However, suppose we choose a model domain extending to $\sim$ 1000 km (i.e. the 10^{-7} bar level) appropriate for an H_2 dominated atmosphere. After H_2 escapes to space, all relevant photochemistry would occur below 100 km, in the bottom several grid cells of the model. Therefore, the important photochemistry would be poorly resolved and inaccurate, and the extremely small pressures at the top of the model domain would likely cause numerical instability. Our solution is to adaptively adjust the model domain so it is always appropriate for atmospheres scale height. We use the root finding functionally in CVODE BDF to halt integration whenever the pressure at the top of the atmosphere falls below 10^{-7} bar and lower the top of the model domain before continuing integration. This procedure is done automatically tens to hundreds of times during each post-impact integration.

Chemical network, photolysis cross sections and thermodynamic data

Our chemical reactions, photolysis cross sections, and thermodynamic data used for all gas-phase kinetics are archived in the following Zenodo repository: `https://doi.org/10.5281/zenodo.7802962`. Chemical reactions and thermodynamic data are in the file "reaction_mechanisms/zahnle_earth.yaml", and photolysis cross sections are in the folder "xsections/". All thermodynamic data is from the NIST Chemistry WebBook (Linstrom and Mallard, 1998). The chemical and photolysis reactions are an updated version of rates presented in Zahnle et al. (2016).

In this article, our model simulates rainout in droplets of water for the following species: particles, OH, CN, HCN, C_2H_4, NO, HO_2, N_2O, H_2O_2, O_3, NO_2, NO_3, HNO_2, HNO_3, C_2H_6, CH_3OH, CH_3CHO, C_3H_6, CH_3CN.

Model validation

Figure 5.20 shows *Photochem* applied to Earth and Titan compared to observations gathered from the literature. All boundary conditions and settings for each model are archived in the "ModernEarth" and "Titan" templates in the following Zenodo repository: `https://doi.org/10.5281/zenodo.7802921`. Our model of Titan fixes the surface CH_4 mixing ratio to 0.015 volume mixing ratio, permits H_2 escape at the diffusion-limited rate, and allows aerosols to fall to Titan's surface, but otherwise has zero-flux boundary conditions. We ignore the effects of galactic cosmic rays, which causes our model to under-predict the nitrile haze production in the lower atmosphere (Lavvas et al., 2008b). Additionally, we neglect ion chemistry which is argued to be important for the formation of large hydrocarbons (e.g., C_6H_6), but inconsequential for smaller molecular weight species. Despite these omissions, *Photochem* broadly reproduces the main cyanide chemistry on Titan.

Deposition velocity of HCN

Our photochemical-climate simulations of post-impact atmosphere assume a HCN surface deposition velocity of 7×10^{-3} cm s^{-1}. Here, we describe a simple model of HCN hydrolysis in the ocean which justifies this value.

Motivated by Appendix 3 in Kharecha et al. (2005), we imagine a two-box ocean model with a surface ocean of depth $\sim$ 100 m and a deep ocean ($\sim$ 4 km). We assume HCN transport into the ocean is governed by a stagnant boundary layer model (see Figure 3 in Kharecha et al. (2005)), where it is destroyed by hydrolysis reactions. HCN is mixed between the surface and deep ocean reservoirs by a turnover velocity, $v_{\rm over}$, which we nominally take to be 1.2×10^{-5} cm s^{-1} which is appropriate for modern Earth. Under these circumstances, the following system of ordinary differential equations governs the concentration of HCN in the surface and deep ocean.

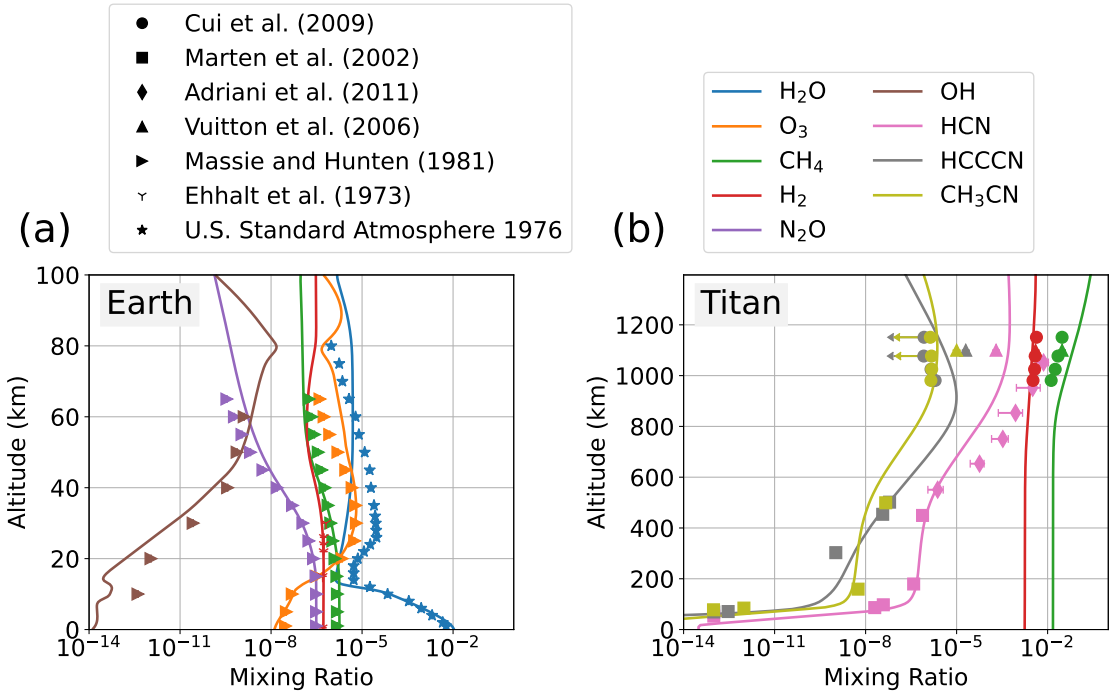

Figure 5.20: Earth and Titan photochemical model validation. (a) and (b) shows the *Photochem* model applied to Earth and Titan, respectively, compared to data from the literature (Cui et al., 2009; Marten et al., 2002; Adriani et al., 2011; Vuitton et al., 2006; Massie and Hunten, 1981; Ehhalt et al., 1975).

$$\frac{dm_{\mathrm{HCN,s}}}{dt} = \frac{\Phi_{\mathrm{HCN}}}{Cz_s} - k_{\mathrm{tot}} m_{\mathrm{HCN,s}} - \left(\frac{v_{\mathrm{over}}}{z_s}\right)(m_{\mathrm{HCN,s}} - m_{\mathrm{HCN,d}}) \tag{5.38}$$

$$\frac{dm_{\mathrm{HCN,d}}}{dt} = -k_{\mathrm{tot}} m_{\mathrm{HCN,s}} + \left(\frac{v_{\mathrm{over}}}{z_d}\right)(m_{\mathrm{HCN,s}} - m_{\mathrm{HCN,d}}) \tag{5.39}$$

Here, $m_{\mathrm{HCN,s}}$ and $m_{\mathrm{HCN,d}}$ are the concentration of HCN in the surface and deep ocean, respectively, in mol L^{-1}, C is a constant equal to 6.022×10^{20} molecules mol^{-1} L cm^{-3}, z_s is the depth of the surface ocean, and z_d is the depth of the deep ocean. We compute the temperature and pH dependent hydrolysis rate coefficient, k_{tot}, following Miyakawa et al. (2002). Φ_{HCN} is the HCN flux into the ocean in molecules cm^{-2} s^{-1}, which is determined by a stagnant boundary layer model:

$$\Phi_{\mathrm{HCN}} = v_{\mathrm{p,HCN}}(\alpha_{\mathrm{HCN}} 10^{-6} p_{\mathrm{HCN}} - m_{\mathrm{HCN,s}})C \tag{5.40}$$

We assume the piston velocity of HCN is 5×10^{-3} cm s^{-1}, which is the same as the piston velocity of CO (Kharecha et al., 2005, Table 1). Also, α_{HCN} is the henry's law coefficient for HCN. The flux of a gas can also be parameterized with a deposition velocity ($v_{\mathrm{d,HCN}}$):

$$\begin{aligned} \Phi_{\mathrm{HCN}} &= n_{\mathrm{HCN}} v_{\mathrm{d,HCN}} \\ &= \frac{p_{\mathrm{HCN}}}{kT} v_{\mathrm{d,HCN}} \end{aligned} \tag{5.41}$$

Assuming a steady state ($dm_{\mathrm{HCN,s}}/dt = dm_{\mathrm{HCN,d}}/dt = 0$) and solving for $v_{\mathrm{d,HCN}}$ in Equations (5.38) - (5.41) yields

$$v_{\mathrm{d,HCN}} = 10^{-6} kT \alpha_{\mathrm{HCN}} C k_{\mathrm{tot}} v_{\mathrm{p,HCN}} \frac{k_{\mathrm{tot}} z_d z_s + v_{\mathrm{over}}(z_d + z_s)}{k_{\mathrm{tot}} z_d (v_{\mathrm{p,HCN}} + k_{\mathrm{tot}} z_s) + v_{\mathrm{over}}(v_{\mathrm{p,HCN}} + k_{\mathrm{tot}}(z_d + z_s))} \tag{5.42}$$

Here, we assume that the temperature and pH of the ocean is uniform, and that the tem-

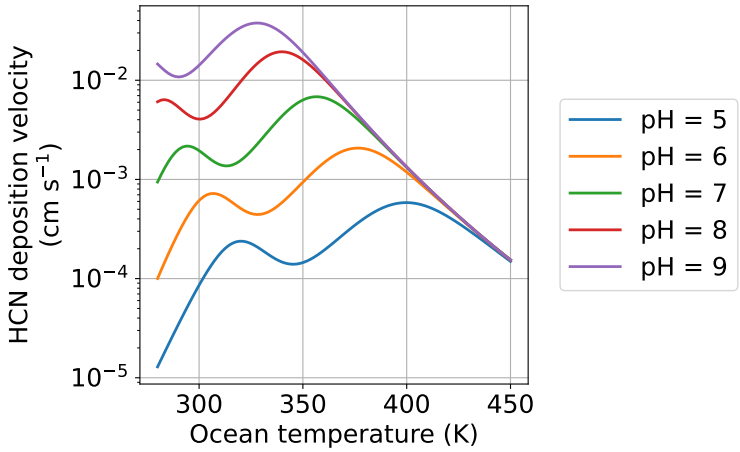

Figure 5.21: The deposition velocity of HCN caused by hydrolysis in the ocean. Calculations use Equation (5.42) assuming $v_{\rm over} = 1.2 \times 10^{-5}$ cm s^{-1}, $z_s = 10^4$ cm, $z_d = 4 \times 10^5$ cm.

perature of the surface air is the same as the temperature of the ocean.

Figure 5.21 computes the deposition velocity of HCN using Equation (5.42) over a wide range of ocean temperatures and pH. Kadoya et al. (2020) used a model of the geologic carbon cycle to argue that the Hadean ocean was moderately alkaline (pH ≈ 8). Therefore, we choose a HCN deposition velocity of 7×10^{-3} cm s^{-1} for our nominal model because it a reasonable approximation of the pH $= 8$ case over a wide range of temperatures. Additionally, we assume that HCCCN has the same deposition velocity as HCN, also caused by hydrolysis reactions in the ocean.

We have re-run our photochemical-climate simulations of post-impact atmospheres with order-of-magnitude larger and smaller HCN deposition velocities. The results are qualitatively unchanged. For example, assuming $v_{\rm d,HCN} = 7 \times 10^{-4}$ cm s^{-1} for a 2×10^{21} kg impactor in Figure 5.7 causes one order of magnitude smaller HCN ocean deposition. However, the HCN rainout and HCN surface pressure is unchanged because HCN rainout dominates over the HCN ocean deposition.

5.6.4 The Clima *radiative transfer and climate model*

To simulate the climate of post-impact atmospheres, we developed a new radiative transfer and climate code called *Clima*. We approximately solve the radiative transfer equation using standard two-stream methods (Toon et al., 1989). The code includes opacities representing photolysis, Rayleigh scattering, collision-induced absorption, and approximates line absorption with k-distributions. All available opacities and citations, except photolysis cross sections, are listed in Table 5.4. In this article, to account for line absorption of multiple species, we use the "random overlap with resorting and rebinning" method described in Amundsen et al. (2017).

Figure 5.22 shows a thermal emission spectra computed with *Clima* for a two bar pure CO_2 atmosphere on Mars with a 250 K surface temperature. This same benchmark has been computed by several other radiative transfer codes: SOCRATES (Wolf et al., 2022, Figure 2), ExoRT (Wolf et al., 2022, Figure 2), SMART (Figure 5.22), and the radiative transfer code used in Kopparapu et al. (2013) (their Figure 1). All codes estimate the total outgoing thermal energy to be between 86 and 94 W m^{-2}, which is comparable to the value computed by *Clima* (92.9 W m^{-2}).

The *Clima* code also includes an adiabatic climate model which we use in Section 5.4.4. Given partial pressures of gases at the surface, the code draws a pseudo-adiabat temperature profile upward using Equation (1) in Graham et al. (2021) until the temperature reaches an assume isothermal stratosphere. The code is general and can consider any number of condensing species, but H_2O is the only relevant condensible for post-impact atmospheres. Finally, to find an equilibrium climate, we solve a nonlinear equation for the surface temperature that balances incoming solar and outgoing longwave radiation. Each iteration of the nonlinear solve involves drawing an adiabat upward then computing the solar and infrared radiative fluxes.

We have validated the stand-alone climate model in *Clima* by reproducing the calculations in Wordsworth et al. (2017) of early Mars with CO_2 and H_2 atmospheres (left panel of Figure

2 in Wordsworth et al. (2017)). Furthermore, we predict the runaway greenhouse limit to be 291 W m^{-2}, which is in acceptable agreement with the literature (e.g., Kopparapu et al., 2013). Finally, we have also confirmed that our code for drawing pseudo-moist adiabats reproduces the code used in Graham et al. (2021).

The version of *Clima* used in this article (v0.3.7) is archived on Zenodo (`https://doi.org/10.5281/zenodo.8060772`), while the most up-to-date version can be found on GitHub (`https://github.com/Nicholaswogan/clima`).

Table 5.4: Opacities used in the *Clima* radiative transfer code

Opacity type	Opacity	Notes	Citation
k-distributions[a]	H_2O	HITEMP2010 for 0 to 30,000 cm^{-1} and HITRAN2016 for 30,000 to 42,000 $^{-1}$. Voigt line shape with 25 cm^{-1} cutoff. Assumes Earth air broadening coefficients. Plinth or base is removed because this opacity is combined with MT_CKD H_2O continuum.	Rothman et al. (2010); Gordon et al. (2017)
	CO_2	HITEMP2010. Sub-Lorentzian line shape with 500 cm^{-1} cutoff. Assumes self-broadening coefficients.	Rothman et al. (2010)
	CH_4	HITEMP2020. Voigt line shape with 25 cm^{-1} cutoff. Assumes Earth air broadening coefficients.	Hargreaves et al. (2020)
	CO	HITEMP2019. Voigt line shape with 25 cm^{-1} cutoff. Assumes self-broadening coefficients.	Li et al. (2015)
	O_2	HITRAN2016. Voigt line shape with 25 cm^{-1} cutoff. Assumes Earth air broadening coefficients.	Gordon et al. (2017)
	O_3	HITRAN2016. Voigt line shape with 25 cm^{-1} cutoff. Assumes Earth air broadening coefficients.	Gordon et al. (2017)

	NH_3	HITRAN2016. Voigt line shape with 25 cm^{-1} cutoff. Assumes Earth air broadening coefficients.	Gordon et al. (2017)
CIA	H_2-H_2	-	Mollière et al. (2019)
	H_2-He	-	Mollière et al. (2019)
	N_2-N_2	-	Mollière et al. (2019)
	CH_4-CH_4	-	Karman et al. (2019)
	N_2-O_2	-	Karman et al. (2019)
	O_2-O_2	-	Karman et al. (2019)
	H_2-CH_4	-	Karman et al. (2019)
	CO_2-CO_2	-	Karman et al. (2019)
	CO_2-CH_4	-	Karman et al. (2019)
	CO_2-N_2	-	Karman et al. (2019)
	N_2-H_2	-	Karman et al. (2019)
Rayleigh scattering[b]	N_2	-	Keady and Kilcrease (2002); Penndorf (1957)
	CO_2	-	Keady and Kilcrease (2002); Shemansky (1972)
	O_2	-	Keady and Kilcrease (2002); Penndorf (1957)
	H_2O	-	Keady and Kilcrease (2002); Ranjan and Sasselov (2017); Murphy (1977)
	H_2	-	Keady and Kilcrease (2002)

[a] All k-distributions are computed using HELIOS-K (Grimm et al., 2021).
[b] Rayleigh scattering opacities are computed using a parameterization from Vardavas and Carver (1984).

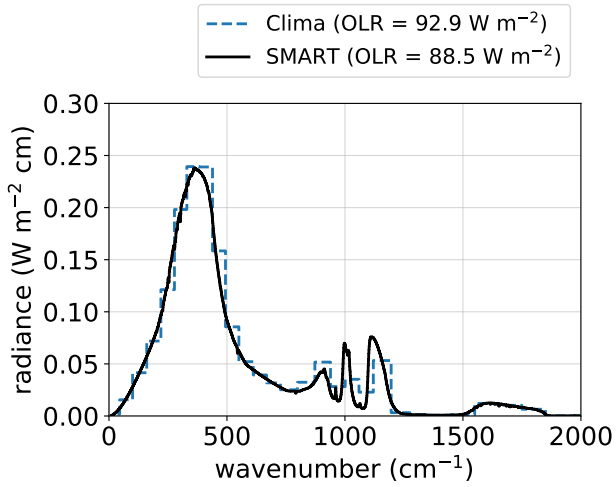

Figure 5.22: Outgoing longwave radiation of a 2 bar CO_2 atmosphere on Mars with a 250 K surface temperature, computed with *Clima* (this work) and SMART (Meadows and Crisp, 1996). The agreement between the two codes validates *Clima*.

Chapter 6

TIMING AND LIKELIHOOD OF THE ORIGIN OF LIFE DERIVED FROM POST-IMPACT HIGHLY REDUCING ATMOSPHERES

"At some point a particularly remarkable molecule was formed by accident. We will call it the Replicator. It may not necessarily have been the biggest or the most complex molecule around, but it had the extraordinary property of being able to create copies of itself. This may seem a very unlikely sort of accident to happen. So it was. It was exceedingly improbable... But in our human estimates of what is probable and what is not, we are not used to dealing in hundreds of millions of years." - Richard Dawkins in The Selfish Gene

This chapter was written in collaboration with David C. Catling and Kevin J. Zahnle, and will soon be submitted for publication in an academic journal.

Summary

Big impacts on the early Earth would have created highly reducing atmospheres that generated molecules needed for the origin of life, such as nitriles. However, such impactors can be followed by collisions that were still sufficiently big to vaporize the ocean and destroy any pre-existing life. Thus, a post-impact reducing atmosphere that gives rise to life needs to be followed by a lack of subsequent sterilizing impacts for life to persist. Using statistics and limits for the impact history on early Earth and the impact mass needed to generate post-impact highly reducing atmospheres, we show that the median timing of impact-driven biopoiesis (i.e., the origin of life) is favored early in the Hadean eon. However, uncertainties are large because impact bombardment is stochastic, so biopoiesis could have occurred in ~ 0.5 billion year window from 4.45 to 3.9 Ga within 95% uncertainty. Previous claims of a far narrower window for the origin of life are unsupported. In an optimistic scenario for life starting from post-impact reducing atmospheres, we find that the origin of life is possible in $\sim 90\%$ of stochastic impact realizations. In our most pessimistic case, life's origin is still fairly likely ($\sim 20\%$ chance). This potentially bodes well for life on rocky planets elsewhere because they will have experienced an early episode of enhanced impact bombardment given how planets form.

6.1 Introduction

Benner et al. (2020) argued that the most likely time for the origin of life in an RNA-world scenario would have been 4.36 ± 0.1 Ga in the wake of a $\sim 2 \times 10^{22}$ kg (~ 2100 km) asteroid impact called Moneta. They suggested that iron delivered by Moneta's core would have reacted with impact-vaporized ocean water to generate a reducing Hadean atmosphere conducive to the photochemical generation of essential prebiotic nitriles like HCN and HCCCN. Nitriles are required in prebiotic schemes that synthesize ribonucleotide precursors to RNA

(Patel et al., 2015; Powner et al., 2009; Becker et al., 2019). A transient period of profuse nitrile production after a Moneta impact could have been a window of opportunity for the origin of RNA and, ultimately, life.

A single Moneta impact could also explain the highly-siderophile elements (i.e. iron-loving, abbreviated HSEs) in the Moon's and the Earth's mantles. During the Moon-forming impact, HSEs should have been sequestered in each planetary core, so over-abundant HSEs in today's mantles are commonly interpreted as evidence for late-accretion impactors. Earth's mantle has substantially more HSEs than the Moon by an amount that cannot be accounted for by Earth's greater gravitational cross section (Day and Walker, 2015). A single massive Moneta impact could explain the Earth-Moon HSE discrepancy because, by the statistics of small numbers, Moneta could have missed the Moon and hit the Earth (Sleep et al., 1989; Bottke et al., 2010).

However, the lunar HSE depletion may be explained without a Moneta impact. Lunar HSEs could have been lost to space during impact-delivery because of the Moon's small gravity (Kraus et al., 2015). Alternatively, HSEs delivered to the Moon during its $\sim$ 150 million-year magma ocean could have been sequestered in the core due to iron sulfide exsolution (Morbidelli et al., 2018; Rubie et al., 2016). Finally, there is some chance that the Earth's HSEs do not record late impacts because the Moon-forming impact delivered HSEs (Sleep, 2016). Another explanation for Earth's HSEs that does not require impacts is that HSEs are gradual core contributions over time from mantle plumes (Halliday and Canup, 2023; Mundl-Petermeier et al., 2020). If indeed Earth's HSEs reflect asteroid bombardment after the Moon formed, then the HSEs can be explained by multiple $\sim$ 500 to 2000 km impacts rather than a single big ($\sim$ 2100 km) collision.

Chapter 5 and Zahnle et al. (2020) used photochemical models of post-impact atmospheres to show that impacts significantly smaller than Moneta can efficiently produce prebiotic molecules. In their simulations, impactor iron equilibrates with vaporized ocean water to generate atmospheric H_2, CH_4 and NH_3 that form thermochemically as the reducing steam atmosphere cools. Once steam condenses to an ocean, subsequent photochemistry of a Titan-

like, hazy atmosphere produces prebiotic nitriles. Zahnle et al. (2020) was a preliminary study that used simple atmospheric models, and Chapter 5 improves upon their calculations with more sophisticated and accurate simulations. Photochemical modeling in Chapter 5 shows that the production of both HCN and HCCCN only occurs when $CH_4/CO_2 \gtrsim 0.1$ while the atmosphere is hazy. In an optimistic scenario, which includes nickel-catalyzed methane production, results suggests that $CH_4/CO_2 > 0.1$ (i.e. significant nitriles) occurs for impacts $> 4 \times 10^{20}$ kg ($>$ 570 km diameter). In a pessimistic case, which assumes only a fraction of impactor iron reacts with the atmosphere (Citron and Stewart, 2022), a $> 5 \times 10^{21}$ kg ($>$ 1330 km diameter) impactor is required to produce substantial HCN and HCCCN (Chapter 5). Regardless of uncertainty, atmospheric models suggest that an impactor much smaller than Moneta could deliver the nitriles needed for an RNA origin of life.

Here, we use the Chapter 5 results, along with Monte-Carlo simulations of Earth's impact history, to make an alternative estimate for when life most likely emerged during an RNA-first process. Our calculations account for the possibility of planet sterilization by impacts that vaporize the ocean (Sleep et al., 1989). We assume that a life-starting impact is one that produces significant prebiotic nitriles and is not subsequently followed by an ocean-vaporizing impact that destroys the biosphere. By considering the fraction of stochastic impact realizations that do not have a life-starting impact, we also estimate the probability of life beginning if Earth history was rerun.

6.2 Methods

The rate impacts hit Earth bigger than mass m at age t can be written

$$f(t, m) = F_0(t) S_0(m) \tag{6.1}$$

Here, $S_0(m)$ is the size-frequency distribution of impactors normalized to a reference mass m_0 so that $S_0(m_0) = 1$. Also, $F_0(t)$ is the number of impacts per billion years with mass

greater than m_0.

We assume that the the majority of the size-frequency distribution of impactors is identical to the main-belt asteroids (Extended Data Figure 1 in Marchi et al., 2014). Data for the frequency of main-belt asteroids only extends down to about 1 km diameter (1.3×10^{12} kg). To extend the distribution to smaller objects, we use the observed 1400 ratio between the frequency of $>$ 1 km and $>$ 20 km craters on the Moon following Morbidelli et al. (2018). Crater scaling relations suggest that 1 km and 20 km craters on the Moon corresponds to 50 m and 1 km asteroids, respectively (Morbidelli et al., 2018). The largest main belt asteroid is $\sim$ 1000 km, so we must extrapolate to larger impactors. Through the main text, we use the same extrapolation as Marchi et al. (2014), which extends the distribution to big impacts with a slope $d(\ln S_0)/d(\ln m) = -0.415$ (Figure 6.1). In Chapter Appendix 6.6.1 we show that instead extrapolating with the red dashed line in Figure 6.1a (with slope $d(\ln S_0)/d(\ln m) = -1.0$) does not significantly change our overall conclusions. Finally, we normalize the size-frequency distribution to the impact mass required to make a 1 km crater on the moon (50 m object, $m_0 = 1.64 \times 10^8$ kg). Figure 6.1a shows the resulting size-frequency distribution.

The flux of impactors, $F_0(t)$, can be estimated from the lunar cratering record. We adopt the accretionary tail scenario discussed in Morbidelli et al. (2018). In other words, we assume that the "late heavy bombardment" did not happen (Cartwright et al., 2022; Hartmann, 2019; Zellner, 2017), and that the impact flux on Earth was monotonically decreasing throughout the Hadean eon. Figure 6.1b shows n_m, our assumed lunar impact history taken from Morbidelli et al. (2018) (red line in their Figure 5). We use the parameterization $n_m = 10^{ae^{bt}+c}$, where a, b, and c are fit parameters given in Figure 6.1b.

Extrapolating the lunar impact history to Earth requires correcting for Earth's greater gravitational attraction. Assuming that the approach velocity of impactors far from the Earth and Moon was on average 18 km/s (Morbidelli et al., 2018), then Earth should receive $s_0 = 1.36$ times more impacts per surface area than the Moon. Therefore, the number of impacts on Earth is

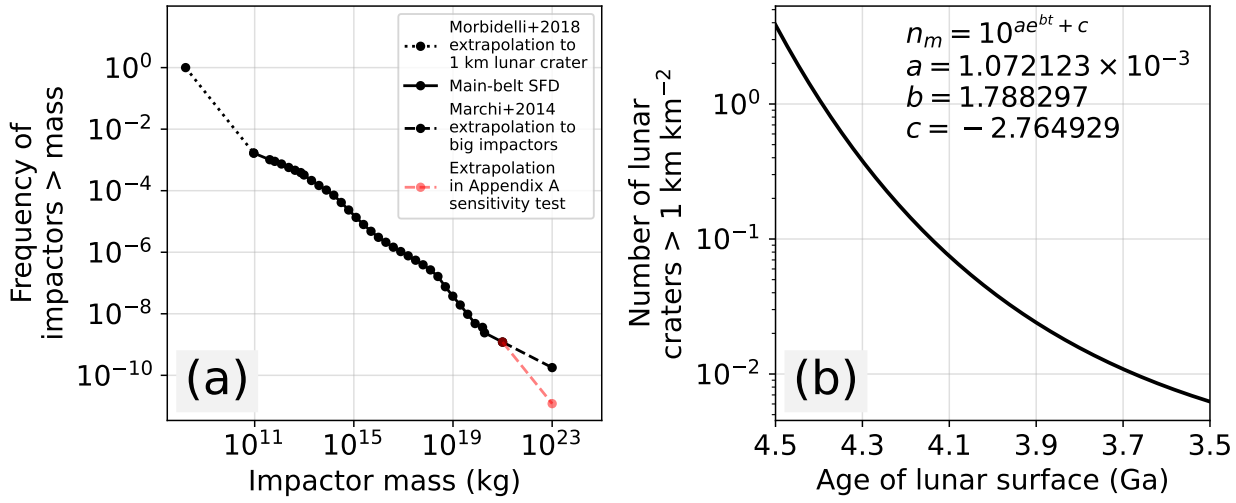

Figure 6.1: Our assumed (a) size-frequency distribution of impactors and (b) lunar cratering record. Most of the size-frequency distribution is identical to the main-belt asteroids (Extended Data Figure 1 in Marchi et al., 2014). We extrapolate to objects $\lesssim 10^{11}$ kg using the observed frequency ratio of > 1 km and > 20 km lunar craters following Morbidelli et al. (2018), and, in the main text, log-log extrapolate to asteroids $\gtrsim 10^{21}$ kg following Marchi et al. (2014). In Chapter Appendix 6.6.1 we also consider the red dashed extrapolation to $\gtrsim 10^{21}$ kg impacts. The lunar cratering record is the red line in Figure 5 of Morbidelli et al. (2018).

$$N_0 = A_\oplus s_0 n_m = A_\oplus s_0 10^{ae^{bt}+c} \tag{6.2}$$

Equation (6.2) also accounts for Earth's surface area ($A_\oplus$), making N_0 the number of impacts on Earth since age t that would cause a crater > 1 km on the moon. As discussed previously, Morbidelli et al. (2018) use crater scaling relations to show that a 1 km lunar crater corresponds to a 50 m object with mass $m_0 = 1.64 \times 10^8$ kg.

The time derivative of N_0 gives the flux, F_0:

$$F_0(t) = \frac{dN_0}{dt} \tag{6.3}$$

The average number of impacts on Earth between time t_1 and t_2 with mass greater than m is then

$$\begin{aligned} N(m, t_1, t_2) &= \int_{t_1}^{t_2} f(t, m) dt \\ &= S_0(m) \int_{t_1}^{t_2} \frac{dN_0}{dt} dt \\ &= S_0(m) A_\oplus s_0 \left(10^{ae^{bt_2}+c} - 10^{ae^{bt_1}+c} \right) \end{aligned} \tag{6.4}$$

To simulate impact histories, we consider a grid of $s \sim 200$ impactor masses between 10^{12} and 10^{23} kg, and a grid of ~ 60 times between 4.5 and 3.5 Ga. Indexes j and i indicate the mass and time grid cells respectively, while, for example, $j - \frac{1}{2}$ and $j + \frac{1}{2}$ indicate the edges of the grid cell. We can compute the expected number of impacts within a mass and time grid cell with the following

$$\overline{N}_{ij} = N(m_{j-\frac{1}{2}}, t_{i-\frac{1}{2}}, t_{i+\frac{1}{2}}) - N(m_{j+\frac{1}{2}}, t_{i-\frac{1}{2}}, t_{i+\frac{1}{2}}) \tag{6.5}$$

Next, we sample a Poisson distribution for each $\overline{N}_{ij}$, giving a stochastic number of impacts in each mass and time grid cell which constitutes an impact history. By modeling impacts

as a Poisson process, we are assuming that each impact does not change the probability of the next one (i.e., impacts are independent). Performing this sampling thousands of times captures many of the possible impact histories. We only keep impact histories that accrete a total mass of 2×10^{22} to 6×10^{22} kg because this is approximately the mass implied by the HSEs in Earth's mantle, assuming that HSEs were delivered by late accretion. This range of masses is based on Day and Walker (2015) who used mantle HSEs to suggest that the Earth was impacted by $\sim 3 \times 10^{22}$ to 4.8×10^{22} kg of material, but we choose a wider range of masses because HSEs could have been lost to Earth's core or to space during impacts (Marchi et al., 2018).

Our final step is to assign impact velocities to each collision in the many sampled impact histories. Figure 6.5 in the Chapter Appendix shows Earth's impact velocity distribution. We created this distribution using the JPL database of close approaches to Earth by small bodies (Park and Chamberlin, 2023), considering all close-approach asteroids within 0.05 AU to Earth. The database gives the approach velocity of each asteroid far from Earth, so we compute the impact velocity by accounting for Earth's gravitational potential energy. Here, we are assuming that the impact velocity distribution for small bodies (e.g. < 10 km) is identical to the velocity distribution for bigger asteroids (e.g. $> 10km$). This may not be the case because small bodies are more strongly influenced by processes like the Yarkovsky effect (Bottke Jr et al., 2006), where an asteroid's orbit is altered by anisotropic thermal emission.

The final collection of sampled impact histories can then be used to compute impact statistics that are relevant to the timing and likelihood of the origin of life.

6.3 Results

Figure 6.2 illustrates three of the 5000 impact histories computed with our Monte-Carlo approach (Section 6.2). In Figure 6.2a, a Moneta-sized impact occurs at ~ 4.43 Ga delivering nearly all of Earth's mantle HSEs. The impact should also reduce the Hadean atmosphere creating conditions favorable for prebiotic chemistry. However, in this case, Moneta is not a

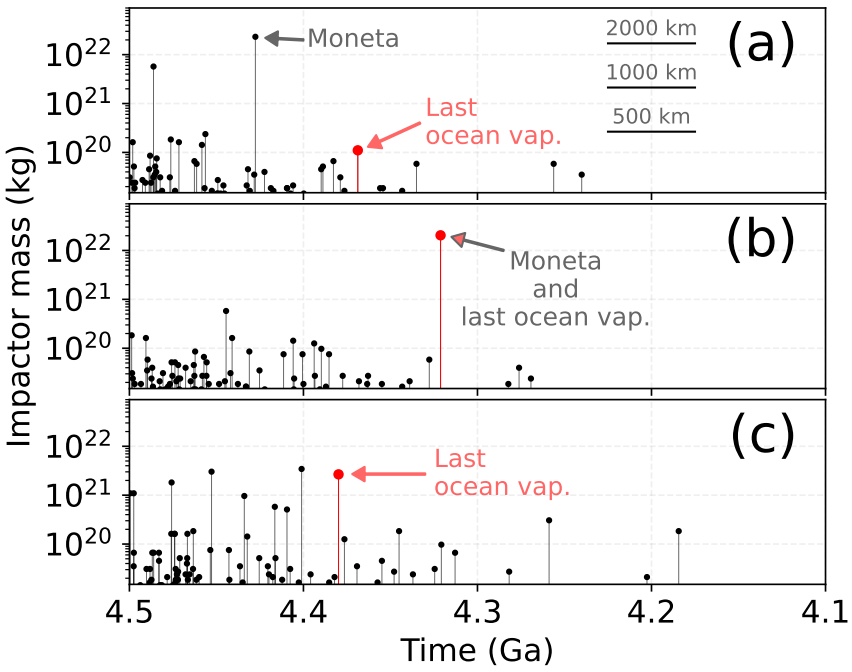

Figure 6.2: Three simulated impact histories of the 5000 derived from our Monte-Carlo approach (Section 6.2). Each vertical line indicates an impact of a mass shown by the y-axis. The red lines indicate the last impact to vaporize the ocean assuming 10% of an impacts kinetic energy heats the ocean. (a) gives conversions between impact mass and diameter for 500, 1000 and 2000 km asteroids.

life-starting impact because Moneta is followed by an ocean-vaporizing collision at ~ 4.37 Ga which we assume destroys any existing biosphere. Based on smoothed-particle hydrodynamics impact simulations, we nominally assume that 10% of an impact's kinetic energy goes into vaporizing the ocean (Chapter Appendix 6.6.2, Citron and Stewart, 2022). Vaporizing the ocean requires 5×10^{27} J, so a $> 5 \times 10^{28}$ J impact should deliver sufficient energy under our assumptions. Chapter Appendix 6.6.2 considers alternative criteria for ocean-vaporization. In Figure 6.2a, the last ocean-vaporizing impact is only $\sim 10^{20}$ kg (360 km) but has a large impact velocity of 32 km/s giving it 5.12×10^{28} J of kinetic energy.

Moneta also occurs in the Figure 6.2b impact realization. In this scenario, any life created in the wake of Moneta will not be subsequently impact-exterminated because Moneta is the last impact to vaporize the ocean.

Figure 6.2c shows an impact history where Moneta does not occur. Instead, Earth's mantle HSEs are delivered by multiple 10^{21} to 4×10^{21} kg collisions. Whether this bombardment history would cause biopoiesis depends on the required minimum impact mass to produce significant origin-of-life nitriles (e.g. HCN and HCCCN). Chapter 5 uses photochemical models of post-impact atmospheres to show that, optimistically, an impact $> 4 \times 10^{20}$ kg should give rise to an atmosphere that makes significant HCN and HCCCN. Under this optimistic requirement, the last ocean-vaporizing impact in Figure 6.2c could successfully start life and occurs at 4.38 Ga with mass 3×10^{21} kg. However, with pessimistic modeling assumptions, Chapter 5 finds that a $> 5 \times 10^{21}$ kg impactor is instead required for substantial nitrile delivery to the surface. In this alternative scenario, an origin of life never occurs in Figure 6.2c because there is no impactor larger than 5×10^{21} kg.

As illustrated in Figure 6.2, a life-starting impact does not occur in every simulated impact history. In our impact-driven model for the origin of life, biopoiesis requires (1) an impact of sufficient mass to make prebiotic nitriles and (2) the lack of a later ocean-vaporizing collision that destroys the biosphere without rekindling it. Figure 6.3 shows the probability of both conditions occurring as a function of the minimum impact mass that produces prebiotic molecules. For example, consider the Chapter 5 optimistic minimum mass of 4×10^{20} kg

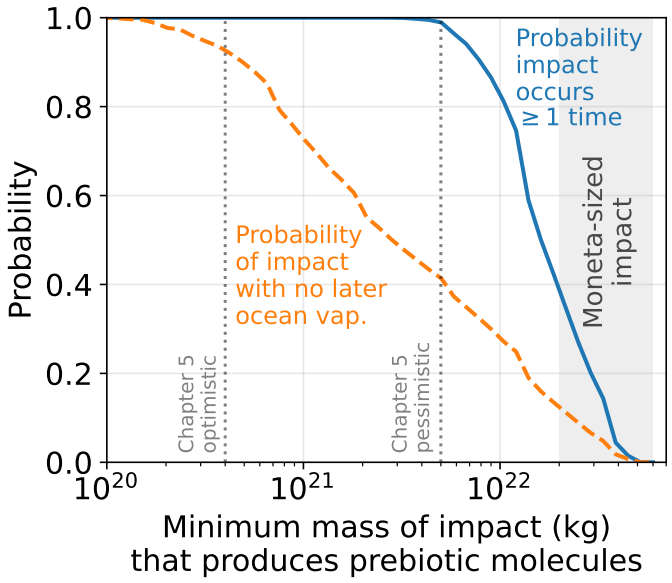

Figure 6.3: The probability of an impact that causes favorable conditions for an origin of life on Earth. The blue solid line is the probability of an impact occurring at least once. The orange dashed line is the probability of an impact without a subsequent ocean-vaporizing collision. Probabilities are shown as a function of the minimum impact mass to produce significant prebiotic molecules (e.g. HCN). Two plausible minimum masses are the Chapter 5 optimistic and pessimistic scenarios indicated with vertical dotted lines. The shaded region between 2×10^{22} and 6×10^{22} kg are Moneta-sized impacts because they deliver most all of Earth's mantle HSEs. There is a 92% chance of an impact creating favorable origin of life conditions in the Chapter 5 optimistic case, and a 41% chance in the pessimistic case.

indicated in Figure 6.3. All simulated impact histories have at least one impact bigger than 4×10^{20} kg (blue line in Figure 6.3 is 1.0 at the given mass). However, the probability of the origin of life in this scenario is 92%, because 8% of the time the last 4×10^{20} kg collision is followed by a smaller ocean-vaporizing impact that perhaps sterilizes the planet (orange dashed line in Figure 6.3 with 0.92 at 4×10^{20} kg). An origin of life is less probable if we consider the Chapter 5 pessimistic minimum mass ($> 5 \times 10^{21}$ kg) to produce significant origin-of-life nitriles. A $> 5 \times 10^{21}$ kg impact without later ocean vaporization occurs 41% of the time. A life-starting impact was therefore relatively likely on the early Earth, and was strongly favored (92% probability) under optimistic assumptions.

To estimate the most likely timing for the origin of life, we consider both the optimistic and pessimistic criteria of Chapter 5. Figure 6.4a is the optimistic case, showing the timing (Figure 6.4a (i)) and mass (Figure 6.4a (ii)) of the last $> 4 \times 10^{20}$ kg impactor for the 92% of impact histories that do not experience later ocean vaporization. The median timing of a life-starting impact is 4.34 Ga with 95% uncertainty between 3.89 and 4.46 Ga. The large uncertainty mostly stems from the stochastic, Poisson nature of asteroid bombardment. The probability distribution for the mass of the life-starting impact peaks at 4×10^{20} kg and decreases with increasing mass because of the size-frequency distribution of asteroids (Figure 6.1a). There is only a 10% chance that the impactor is Moneta-sized (i.e., between 2×10^{22} and 6×10^{22} kg).

The timing of an origin of life impact is qualitatively unchanged when instead adopting the Chapter 5 pessimistic case, which requires a $> 5 \times 10^{21}$ kg impact without later ocean vaporization (Figure 6.4b). In this scenario, the median timing for life's origin is 4.36 Ga with a 95% confidence interval spanning 3.94 to 4.49 Ga (Figure 6.4b (i)). Under these assumptions, the life-starting impact is Moneta-sized 31% of the time (Figure 6.4b (ii)), which is more probable compared to "optimistic" case (Figure 6.4a (ii)).

In this model for biopoiesis, life would probably start approximately within 10s of millions of years after a life-starting impact because this is the maximum duration of the H_2- and CH_4- rich atmosphere that makes nitriles like HCN (Chapter 5). We ignore the $<$ 10s million

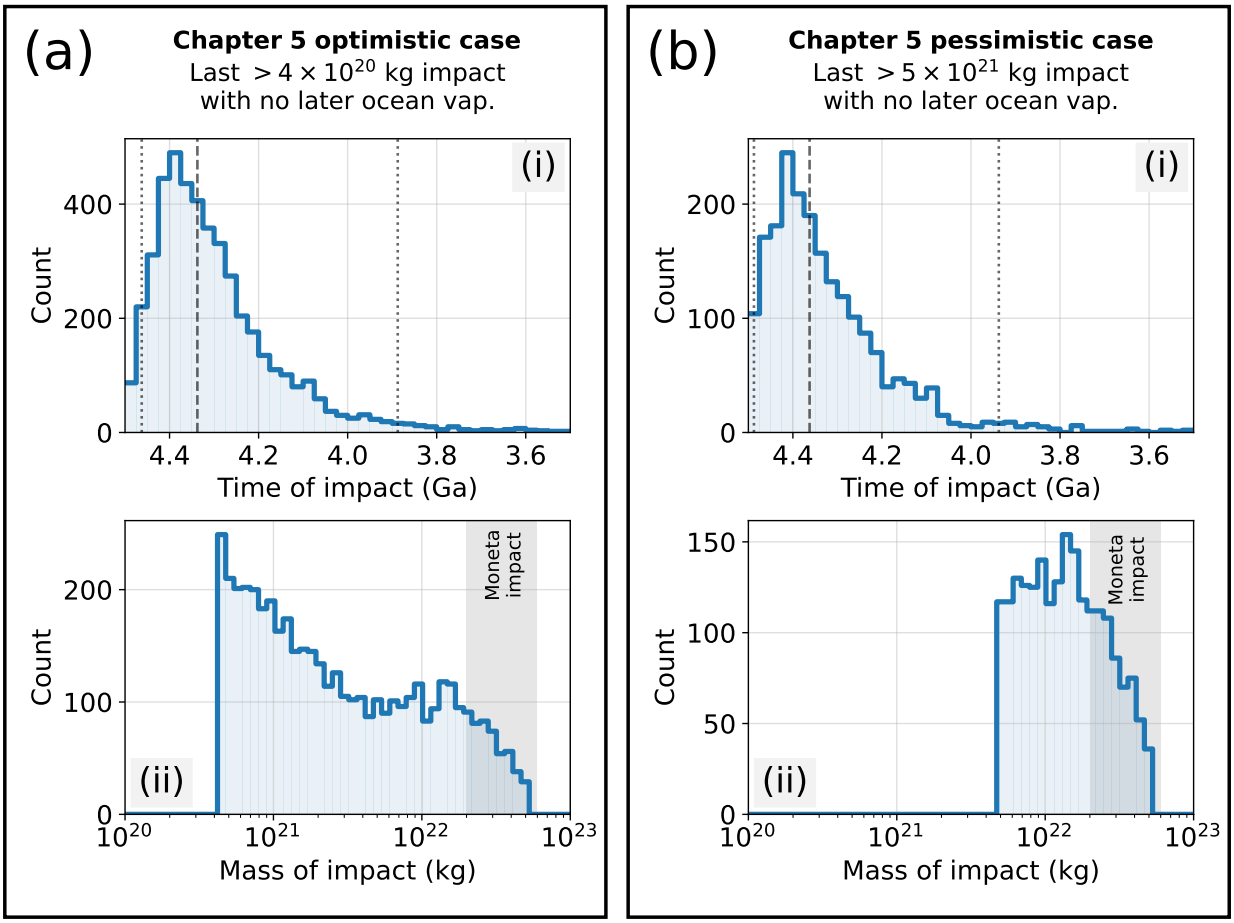

Figure 6.4: The timing and mass of a life-starting impact on the early Earth. (a) considers an optimistic minimum impact mass needed to generate the molecules for an RNA origin of life and (b) examines a pessimistic minimum impact mass Chapter 5. In either (a) or (b), panels (i) and (ii) show probability distributions for the timing and mass, respectively, of the last impact the produces prebiotic molecules which does not have a later ocean-vaporizing collision. The vertical dashed lines on (a) i and (b) i plot are median values, and the vertical dotted lines are the 95% confidence intervals. In an impact-driven origin of life, biopoiesis most likely occurred at 4.34 Ga (95% CI: 3.89 to 4.46 Ga) assuming panel (a) and at 4.36 Ga (95% CI: 3.94 to 4.49 Ga) assuming panel (b).

year span between an impact and life's origin because it is small compared to our $\sim$ 500 million-year uncertainty for the timing of a life-starting impact.

6.4 Discussion

Our estimated timing for biopoiesis is compatible with the earliest well-accepted geologic evidence of life in the form of stromatolites in the 3.5 Ga Pilbara block of western Australia (Walter et al., 1980; Buick et al., 1981; Van Kranendonk et al., 2018). Older geologic evidence of life exists, such as a $>$ 3.7 Ga black shale metamorphosed to graphite with negative δ^{13}C characteristic of biology (Rosing, 1999; Ohtomo et al., 2014). Also, Bell et al. (2015) discovered graphite inclusions in a 4.1 Ga zircon grain with ^{13}C depletions compatible with biological activity, but this is a tentative biosignature because there are abiotic mechanisms for making isotopically light carbon (Javaux, 2019). If the Bell et al. (2015) finding is indeed a sign of life, then it would be generally compatible with our estimated timing in Figure 6.4, because we find that there is only a $\sim$ 10% chance of life starting after 4.1 Ga.

Furthermore, Hadean zircons provide some constraint on Earth's impact history which we do not explicitly account for in our calculations. The oldest zircons are from Jack Hills, Australia, with U-Pb dates as old as $\sim$ 4.38 Ga (Valley et al., 2014). Benner et al. (2020) argued that a Moneta-scale impact ($\sim 2 \times 10^{22}$ kg) could not have occurred after this date, because such a collision would heat the crust enough to potentially reset all U-Pb chronometers. Benner et al. (2020) makes this claim based on Abramov et al. (2013), who used models of impact ejecta coupled to simulations of radiogenic Pb-loss in zircons to investigate chronometers resetting during the hypothesized "late-heavy bombardment". However, Abramov et al. (2013) considers impacts much smaller than Moneta (e.g. $< 10^{21}$ kg), and does not clearly establish a minimum impactor mass that would reset all zircon chronometers globally. Given this ambiguity, our simulations do not use zircon chronometers as a constraint on Earth's impact history.

Even if an impact failed to reset a zircon chronometer, the shock wave produced by an asteroid collision may create micro- to nano-structural features in zircons that could be

preserved over billions of years (Reimink et al., 2023). Therefore, the presence or absence of shocked Hadean zircons in the geologic record may provide some constraint on Earth's impact history. For example, Reimink et al. (2023) estimated the probability of preserved zircons with shock features assuming Earth experienced a "late-heavy bombardment" at 3.9 Ga. In this scenario, they find that shocked zircons were likely preserved yet find none in a collection of 4.02 Ga zircons from the Acasta Gneiss Complex. Overall, the absence of preserved shocked zircons suggests that a "late-heavy bombardment" did not occur at 3.9 Ga. Our Monte-Carlo models of Earth's impact history do not use zircon shock features as a constraint. A better model would incorporate this information.

It is temping to extrapolate our results beyond the early Earth to exoplanets, but we must do so with caution because planets orbiting different stars may have bombardment histories unlike the Hadean. Planets in the habitable zone of a late M-type star during the stellar main-sequence phase were interior to the habitable zone for several hundred million years during the super luminous pre-main-sequence phase (Luger and Barnes, 2015). Lichtenberg and Clement (2022) use N-body simulations to show that, for planets hosted by late M-dwarfs, large asteroid impacts are not useful for prebiotic chemistry because big impacts most likely occur within 100 million years of planet formation during the stellar pre-main-sequence when the planet is outside of the habitable zone. The pre-main-sequence phase is not an issue for an impact-induced origin of life on planets orbiting sun-like stars because the phase only lasts ~ 3 Myrs, while large asteroid impacts occur for 100s Myrs (Lichtenberg and Clement, 2022). Therefore, our result that a life-starting impact was likely on the early Earth (92% chance in an optimistic case) might be best extrapolated to habitable zone exoplanets orbiting sun-like stars.

A caveat to our results is that ocean-vaporization by an impact is likely a complicated function of impact mass, velocity, and incident angle, which we do not account for (Chapter Appendix 6.6.2). Throughout Section 6.3 we have assumed that 10% of an impactor's kinetic energy heats the planetary surface ($f_{\rm E,vap} = 0.1$), leading to a required $> 5 \times 10^{28}$ J collision to vaporize an ocean. Figure 6.8 in the Chapter Appendix uses simulations of impacts from

Citron and Stewart (2022) to show that $f_{\mathrm{E,vap}} = 0.1$ is a reasonable assumption, but that values between 2.5% and 25% are also possible and that $f_{\mathrm{E,vap}}$ likely also depends on impact angle.

To determine the sensitivity of our results to $f_{\mathrm{E,vap}}$, we recomputed the likelihood and timing of an impact that starts life in Chapter Appendix 6.6.2 using $f_{\mathrm{E,vap}} = 0.025$ and $f_{\mathrm{E,vap}} = 0.25$. We find that the probability of a life-starting impact is somewhat sensitive to $f_{\mathrm{E,vap}}$, while the timing does not depend strongly on $f_{\mathrm{E,vap}}$. Overall, this uncertainty does not change our qualitative conclusion that an origin of life impact on the early Earth was not a fluke. Even in our worst-case scenario (i.e., Chapter 5 pessimistic case with $f_{\mathrm{E,vap}} = 0.25$) a life-starting impact occurs in 20% of impact realizations (Figure 6.9 in the Chapter Appendix). Additionally, uncertainty in $f_{\mathrm{E,vap}}$ does not change our general conclusion that the most likely timing for the origin of life was ~ 4.35 Ga, with 95% uncertainty spanning the Hadean eon (Figure 6.10 in the Chapter Appendix). However, a more complete understanding of $f_{\mathrm{E,vap}}$ as a function of impact angle and other similar parameters may change this result.

An additional related caveat is that our calculations assume that an impact that vaporizes the ocean also sterilizes the planet, but this may not be the case because microbes might have survived in the deep subsurface (Sleep et al., 1989; Grimm and Marchi, 2018). If ocean-vaporization does not destroy the biosphere, then our results would favor an origin of life earlier than we predict in Figure 6.4, and a life-starting impact would also be more probable than we have estimated (Figure 6.3).

6.5 Conclusions

We use Monte-Carlo simulations of Earth's impact history to determine the most likely timing for the origin of life that requires early ribonucleobase synthesis. We use the results of Chapter 5, which finds that significant origin of life precursor molecules, such as HCN, are produced in the Hadean atmosphere after a $> 4 \times 10^{20}$ kg impact in an optimistic case, and after a $> 5 \times 10^{21}$ kg impact in a pessimistic scenario. We consider both possibilities,

and assume such impacts can cause life's origin so long as they are not followed by a smaller ocean-vaporizing collision that sterilizes the planet.

For either the optimistic or pessimistic cases, we find that the most likely timing for an origin of life impactor is ~ 4.35 Ga with a 95% uncertainty spanning the entire Hadean eon (approximately 4.45 to 3.9 Ga). The large uncertainty is caused by the intrinsic stochastic nature of impacts. These results suggest that the Benner et al. (2020) proposed timing of the origin of life, at 4.36 ± 0.1 Ga, is too narrow. Furthermore, the mass of the life-starting impactor is most likely (69% to 90% probability) smaller than the Moneta impactor (Figure 6.4) proposed by Benner et al. (2020), because the size frequency distribution of asteroids prefers more frequent smaller impactors.

Our simulations of Earth's impact history do not always result in a bombardment favorable for an origin of life. There are some impact histories where a collision of sufficient mass to produce prebiotic molecules does not occur, or alternatively, does occur but primitive life is subsequently destroyed by an ocean-vaporizing impact that does not rekindle the biosphere. With our nominal assumptions, a life-starting impact occurs 92% or 41% of the time when we assume a $> 4 \times 10^{20}$ kg or $> 5 \times 10^{21}$ kg impact without later ocean-vaporization is required to start life, respectively. In our worst-case scenario, which assumes that impacts can more easily vaporize the ocean, a $> 5 \times 10^{21}$ kg impact without subsequent planet sterilization occurs in 20% of simulated impact histories (Figure 6.9 in the Chapter Appendix).

If life began after an impact that generated a reducing atmosphere, then this work suggests that origin of life on Earth was fairly likely (at least a 20% chance) and was indeed strongly favored (92% chance) under optimistic assumptions. Given that rocky planets form from accretionary impacts, our work supports an optimistic outlook for life on exoplanets orbiting sun-like stars and future searches for biosignatures.

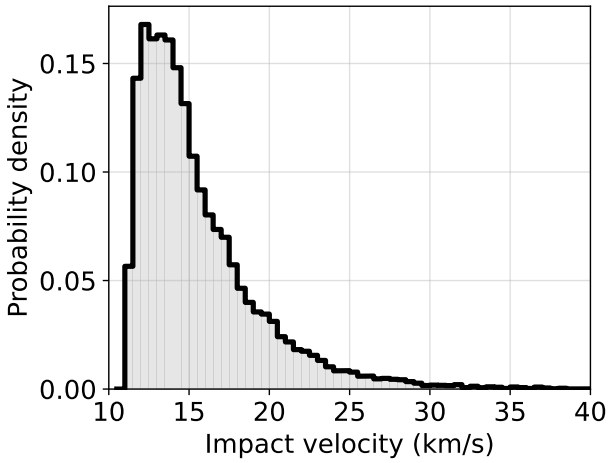

Figure 6.5: Our assumed probability distribution for the velocity of impacts derived from modern observations of asteroid close approaches (Park and Chamberlin, 2023).

6.6 Chapter Appendix

6.6.1 Size-frequency distribution sensitivity test

We assume that the size-frequency distribution of objects that struck the early Earth is similar to the main-belt asteroids. A problem with this approach is that the main-belt asteroids only contain objects up to $\sim$ 1000 km diameter, yet the early Earth is expected to have experience impacts larger than this (Marchi et al., 2014). Therefore, we must extrapolate the size-frequency distribution above $\sim$ 1000 km to larger objects. Throughout the main text we use the same extrapolation as Marchi et al. (2014) (the black dashed line in Figure 6.1), who extends the size-frequency distribution with a log-log slope of $d(\ln S_0)/d(\ln m) = -0.415$.

To test the sensitivity of our results to this chosen extrapolation, we re-did our Monte-Carlo analysis using a log-log slope of $d(\ln S_0)/d(\ln m) = -1$ (the red dashed line in Figure 6.1) for impactors bigger than $\sim$ 1000 km diameter. Figures 6.6 and 6.7 show how our results change when adopting this alternative extrapolation. Overall, our results are qualitatively unchanged for the different extrapolation slope ($d(\ln S_0)/d(\ln m)$).

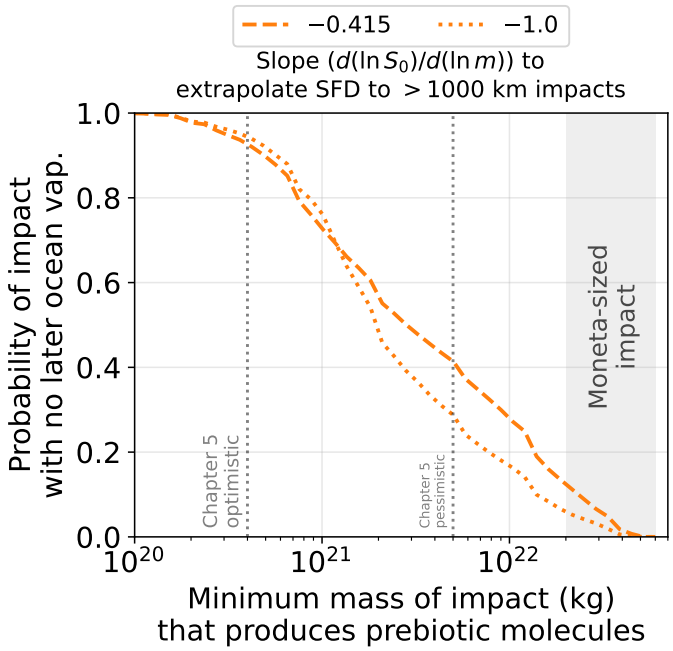

Figure 6.6: Similar to Figure 6.3, except we consider different extrapolations of the size-frequency distribution (SFD) for impactors larger than 1000 km diameter. The line labeled $d(\ln S_0)/d(\ln m) = -0.415$ is the black dashed extrapolation in Figure 6.1a. The $d(\ln S_0)/d(\ln m) = -1.0$ case is shown by the red dashed extrapolation in Figure 6.1a.

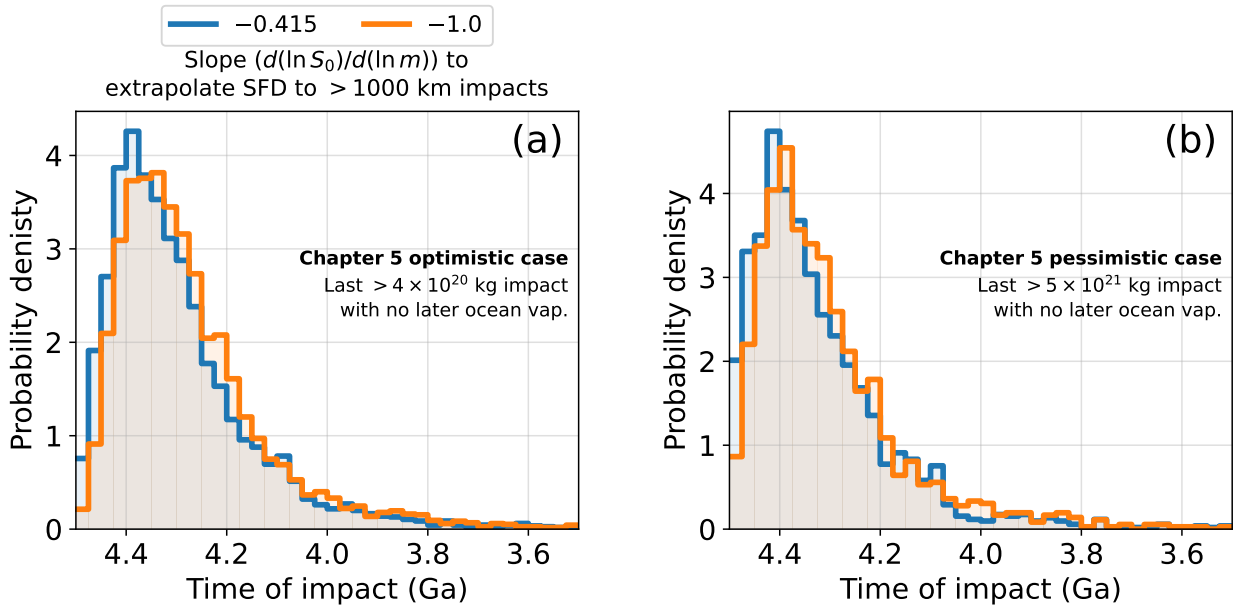

Figure 6.7: Similar to Figure 6.4, except we consider different extrapolations of the size-frequency distribution (SFD) for impactors larger than 1000 km diameter. The line labeled $d(\ln S_0)/d(\ln m) = -0.415$ is the black dashed extrapolation in Figure 6.1a. The $d(\ln S_0)/d(\ln m) = -1.0$ case is shown by the red dashed extrapolation in Figure 6.1a.

6.6.2 Impact energy required for ocean vaporization

Recently, Citron and Stewart (2022) performed smoothed-particle hydrodynamics impact simulations over a range of impact angles, masses and velocities to estimate the impact properties that can vaporize an ocean. Figure 6.8a shows their simulation results for the change in the atmosphere's and ocean's internal energy ($\Delta \mathrm{IE}_{\mathrm{atmo}}$) as a function of impact kinetic energy ($\mathrm{E}_{\mathrm{imp}}$), along with log-log extrapolations for each impact angle. Figure 6.8 gives the same information, but the y-axis is instead the fraction of the impactor's energy that heats the atmosphere and ocean over the course of their simulations. For the most probable incident impact angle of 45° about $\sim 10\%$ of the impactors kinetic energy heats the atmosphere ($f_{\mathrm{E,vap}} = 0.1$), so we nominally adopt this value in the main text to determine which collisions vaporize the ocean.

Energy delivery to the atmosphere/ocean appears to depend on impact angle, mass and velocity (Figure 6.8). Additionally, all of the Citron and Stewart (2022) simulations are far more massive than the minimum threshold for ocean-vaporization, so we must rely on extrapolations. Therefore, our assumption of a constant $f_{\mathrm{E,vap}} = 0.1$ is an over-simplification. To remedy this shortcoming, we considered building a parameterization for $f_{\mathrm{E,vap}}$ that depends on multiple impact properties (e.g., impact angle) using the Citron and Stewart (2022) simulation results, but this was unsuccessful because their calculations do not consider a wide enough parameter space.

The evaluate the sensitivity of our results to an assumed constant $f_{\mathrm{E,vap}} = 0.1$, we recomputed the likelihood and timing of a life-starting impact using $f_{\mathrm{E,vap}} = 0.025$ and $f_{\mathrm{E,vap}} = 0.25$ (Figure 6.9 and 6.10). We chose these values because they are reasonable lower and upper bounds based on the Citron and Stewart (2022) simulations (Figure 6.8b). The probability of an impact that produces substantial prebiotic molecules without later ocean vaporization decreases with increasing $f_{\mathrm{E,vap}}$ (Figure 6.9). For example, for $f_{\mathrm{E,vap}} = 0.1$, the probability of a $> 4 \times 10^{20}$ kg impact (Chapter 5 optimistic case) without subsequent ocean vaporization is 92%. For $f_{\mathrm{E,vap}} = 0.025$ and $f_{\mathrm{E,vap}} = 0.25$ the probabilities are instead 99.9%

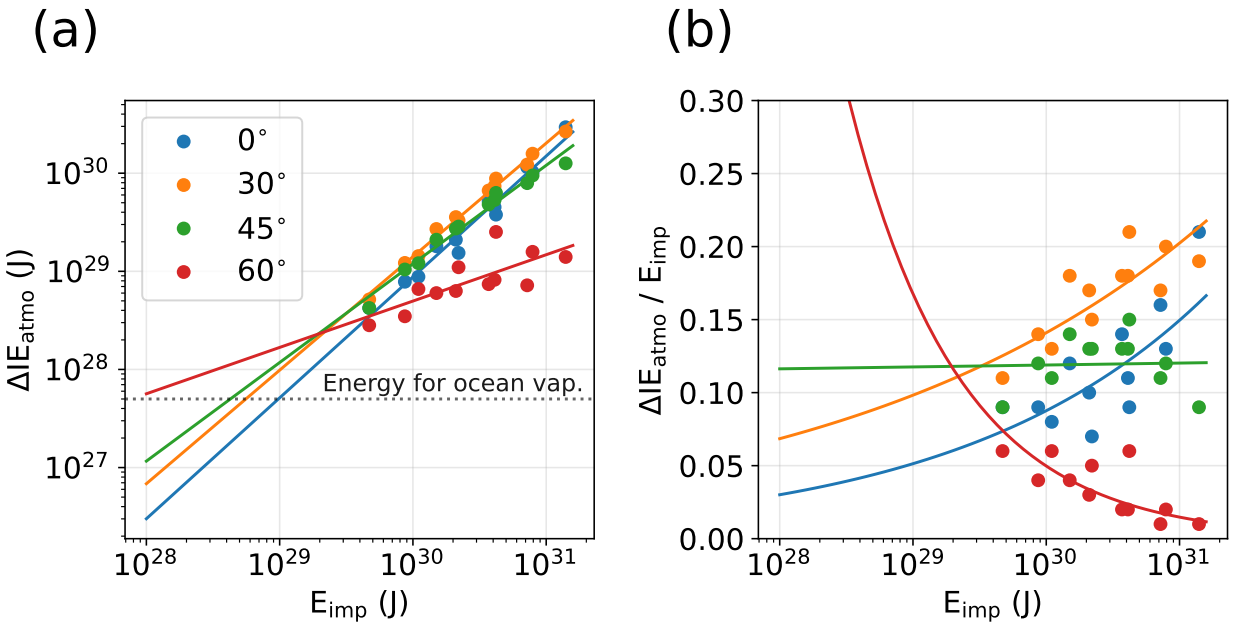

Figure 6.8: Citron and Stewart (2022) smoothed-particle hydrodynamics simulations that show how much impactor kinetic energy heats the atmosphere and ocean. Different colors indicated various incident impact angles. (a) shows the simulated change in internal energy of the atmosphere and ocean as a function of the impactor energy, with linear log-log extrapolations for each impact angle. The dotted horizontal line at 5×10^{27} J indicates the energy needed to vaporize an ocean (Sleep et al., 1989). (b) contains the same information as (a), except the y-axis is the fraction of impactor energy that heats the atmosphere and ocean.

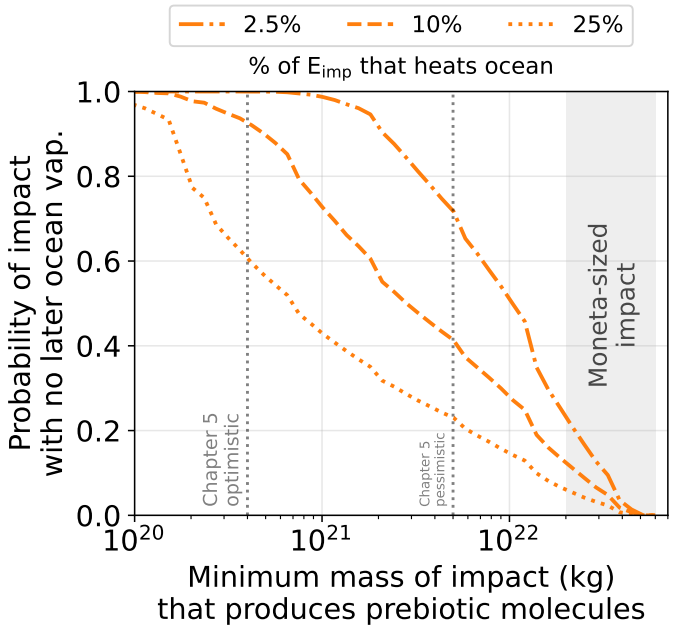

Figure 6.9: Similar to Figure 6.3, except we consider different values for the fraction of impactor energy that heats the ocean.

and 60%, respectively.

Figure 6.10 shows the timing of the last impact to make conditions favorable for biopoiesis that does not experience subsequent ocean vaporization for $f_{\mathrm{E,vap}}$ values of 0.025, 0.1 (nominal value), and 0.25. As in the main text, we consider the Chapter 5 optimistic (Figure 6.10a) and pessimistic (Figure 6.10b) minimum impactor masses to produce significant prebiotic molecules. In Figure 6.10a, the timing of the last life-starting impact is relatively insensitive to $f_{\mathrm{E,vap}}$. In the Chapter 5 pessimistic case (Figure 6.10b), an origin of life is preferred later in the Hadean for larger values of $f_{\mathrm{E,vap}}$.

Overall, uncertainty in the impact properties required to vaporize the ocean has a small effect on our qualitative conclusions. Regardless of $f_{\mathrm{E,vap}}$, the origin of life on Earth from an impact does not appear to be a fluke (Figure 6.9) and biopoiesis is preferred early in the Hadean with uncertainty spanning the entire eon (Figure 6.10). However, it is conceivable that a more complete understanding $f_{\mathrm{E,vap}}$ as a function of impact angle and other impact

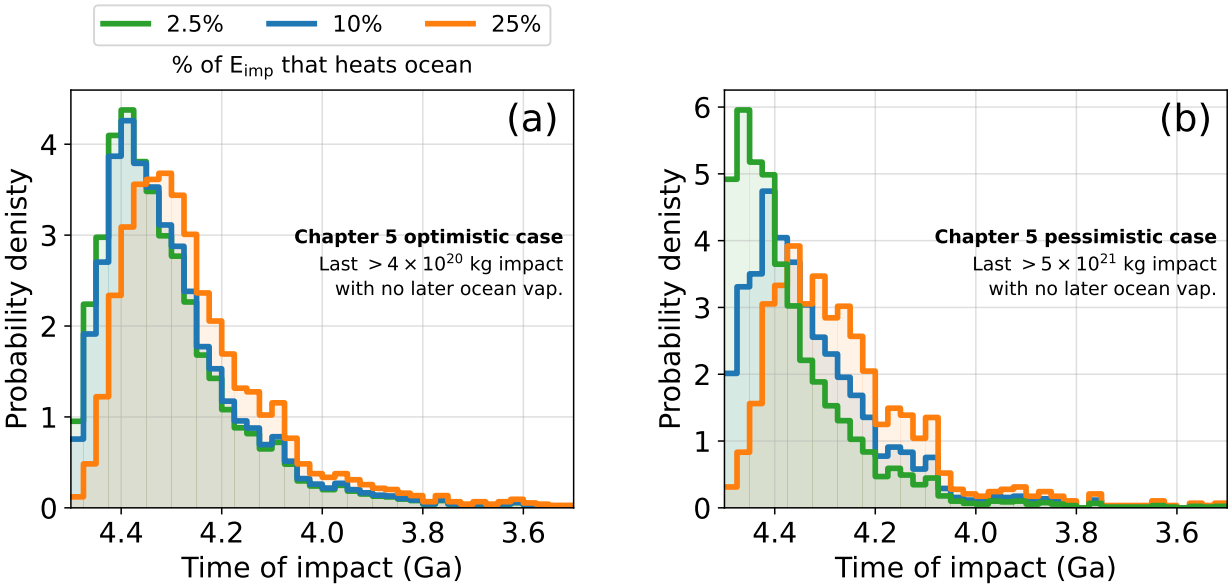

Figure 6.10: Similar to Figure 6.4, except we consider different values for the fraction of impactor energy that heats the ocean.

parameters could change these results.

Chapter 7

CONCLUSIONS

"The purpose of a storyteller is not to tell you how to think, but to give you questions to think upon." - Brandon Sanderson

Chapters 2 through 4 study how life impacted the early Earth's atmosphere to inform the search for life on exoplanets. Chapter 2 computes the change in Earth's atmosphere-ocean chemical disequilibrium when life emerged. I find that the prebiotic Earth had a relatively big disequilibrium due to the coexistence of water vapor, CO, H_2 and CO_2. This atmospheric free energy was produced by volcanism. When life emerged, it consumed much of the free energy in the prebiotic atmosphere, replacing it with a smaller disequilibrium between biogenic waste gases: CO_2, CH_4, N_2 and liquid water. My finding that life destroyed much of the atmospheric free energy on prebiotic Earth contrasts the traditional view, proposed by Lovelock (1965), that big disequilibrium should be generally associated with life. The early Earth suggests a more subtle relationship between life and atmospheric free energy.

I suggest that the disequilibrium-life relationship can be understood by considering the "edibility" of the disequilibrium in terms of reaction activation energy. Life consumed the prebiotic disequilibrium between H_2 and CO_2 or CO and H_2O because the reactions combining these species had relatively small activation energy barriers that could be overcome by enzymes. In contrast, the free energy in Earth's atmosphere and ocean since the origin of life had big activation energy barriers that were insurmountable by biological catalysis. In other words, the prebiotic disequilibrium was "edible" and the disequilibrium present since biopoiesis was not. On this basis, I argue that big "edible" disequilibrium (e.g., the coexistence of volcanic H_2 and CO_2 or CO and H_2O) should be considered an anti-biosignature in exoplanet atmospheres. Life on an inhabited planet would consume this free lunch.

Life's presence or absence on an exoplanet cannot be definitively deduced by mere detections of "edible" or "inedible" chemical disequilibrium. We must also consider the surface fluxes of biogenic gases, and whether they might be mimicked by abiotic processes. This reality motivated Chapter 3, which considers the surface fluxes of methane required to sustain the CH_4-CO_2 disequilibrium biosignature characteristic of the Archean Earth, and whether these fluxes might be imitated by magmatic volcanic outgassing on an exoplanet. Over a wide parameter space, my model of volcanic outgassing suggests that big methane fluxes comparable to biological fluxes are unlikely. In the rare circumstances where volcanic methane appears

possible in our model, volcanoes also produce large amounts of carbon monoxide. Therefore, a genuine CH_4-CO_2 biosignature should most likely coincide with the lack of atmospheric CO.

Chapter 4 investigates atmospheric O_2, Earth's most renowned sign of life, during the Great Oxidation Event around 2.4 billion years ago. I use a novel time-dependent photochemical model to show that O_2 is unstable for concentrations between 10^{-8} to 10^{-4} mixing ratio. Natural perturbations to the atmosphere (e.g. volcanic eruptions, or changes in climate) drive this instability because they can cause O_2 between 10^{-8} and 10^{-4} mixing ratio to change by ~ 4 orders of magnitude. My modeling results provide a physical explanation for geologic evidence of O_2 oscillations preserved in the geologic record (Poulton et al., 2021). Furthermore, the possibility of unstable O_2 requires that oxygen was bigger than 10^{-4} mixing ratio in the mid-Proterozoic eon. If O_2 concentrations were lower (e.g. 10^{-5} mixing ratio), then the natural perturbations to Earth would cause O_2 to occasionally drop below 10^{-7} mixing ratio, which would be incompatible with the geologic record of sulfur isotopes. My new constraint on Proterozoic O_2 ($> 10^{-4}$ mixing ratio) has implications for the detectability of the Proterozoic biosphere if it were to manifest on an exoplanet.

The likelihood of finding life on exoplanets is inextricably linked to the likelihood of the emergence of life. This fact motivates Part II of this thesis, which attempts to understand the atmospheric composition and climate on the Hadean Earth when life first began. I focus on the RNA-world hypothesis for the origin of life, which requires nitriles (e.g. HCN and HCCCN) to abiotically synthesize the first molecules capable of encoding genetic information. In Chapter 5, I use atmospheric chemistry and climate models to show that massive asteroid impacts could create H_2- and CH_4-rich atmospheres that would photochemically produce HCN and HCCCN. Nitrile production is most efficient for impactor masses larger than 5×10^{20} to 4×10^{21} kg (570 to 1330 km diameter). Smaller impacts generate about four orders of magnitude less HCN and fail to produce HCCCN. The minimum impact mass to cause big prebiotic molecule production ($> 5 \times 10^{20}$ vs. $> 4 \times 10^{21}$ kg) depends on a variety of assumptions, including whether nickel-catalyzed methane production occurs in the post-

impact environment, and how effectively an impactor can reduce the Hadean atmosphere.

My models suggest that photochemically generated nitriles would dissolve in rain droplets or otherwise be incorporated in aerosols that would fall into waterbodies on land. At this point, origin of life chemistry would have some of the required ingredients, but perhaps an unfavorable climate. With the caveat of uncertain planetary albedo from clouds, the reducing atmospheres that make nitriles would have > 360 K surface temperatures because of a strong H_2-H_2 collision-induced absorption greenhouse effect. Such warm temperatures could be a problem for the longevity of RNA and its precursors. As a solution, I suggest that prebiotic molecules are stockpiled and preserved in salts until the H_2-rich atmosphere escapes to space. After H_2 escapes, the climate would be temperate. In this cooler climate, stockpiled nitriles could then be released into waterbodies on land, providing an ideal setting for prebiotic chemistry.

The scenario in the previous paragraph is a hypothesis with only some support in the literature. This idea should be tested by further modeling and experiments, including work that determines the efficiency of preserving cyanides in minerals and salts in warm post-impact conditions.

The final chapter of this thesis considers the following thought experiment: Suppose life began in the wake of a post-impact reducing atmosphere. Given our understanding for what is needed to produce a post-impact highly reducing atmosphere from Chapter 5 and our understanding of Earth's impact history, when was the most likely timing of life's emergence on the early Earth? Furthermore, do all possible stochastic impact realizations result in biopoiesis, or do a significant fraction fail to make origin of life conditions favorable?

Chapter 6 attempts to answer these questions using Monte-Carlo simulations of Earth's impact history. Based on Chapter 5, I assume the minimum impact mass to generate significant prebiotic nitriles and an origin of life is $> 5 \times 10^{20}$ kg in an optimistic case and $> 4 \times 10^{21}$ kg in a pessimistic scenario. For either assumption, I find that the last life-starting impact is generally favored early in the Hadean eon (~ 4.35 Ga), however the 95% uncertainty is big and spans about 4.45 to 3.9 Ga. Only a fraction of my simulated impact histories result

in an origin of life. In some cases, an impact of sufficient mass to make prebiotic molecules does not occur, or alternatively does occur, but is followed by an impact that vaporizes the ocean, which I assume sterilizes the planet. In an optimistic case, life begins in $\sim 90\%$ of stochastic impact realizations. In my most pessimistic case, life's emergence still has a 20% chance of success. If this thought experiment has merit, then these results bode well for life on rocky exoplanets given that they all formed from accretionary impacts.

BIBLIOGRAPHY

Oleg Abramov, David A Kring, and Stephen J Mojzsis. The impact environment of the hadean earth. *Geochemistry*, 73(3):227–248, 2013.

Panagiotis S Adam, Guillaume Borrel, and Simonetta Gribaldo. Evolutionary history of carbon monoxide dehydrogenase/acetyl-coa synthase, one of the oldest enzymatic complexes. *Proceedings of the National Academy of Sciences*, 115(6):E1166–E1173, 2018.

A Adriani, BM Dinelli, M Lopez-Puertas, M Garcia-Comas, ML Moriconi, and B Funke. Vertical profiles of hcn in titan's atmosphere from non-lte emission at 3 microns by cassini/vims observations. *Icarus*, 214:584–595, 2011.

CM OD Alexander, R Bowden, ML Fogel, KT Howard, CDK Herd, and LR Nittler. The provenances of asteroids, and their contributions to the volatile inventories of the terrestrial planets. *Science*, 337(6095):721–723, 2012.

David S Amundsen, Pascal Tremblin, James Manners, Isabelle Baraffe, and Nathan J Mayne. Treatment of overlapping gaseous absorption with the correlated-k method in hot jupiter and brown dwarf atmosphere models. *Astronomy & Astrophysics*, 598:A97, 2017.

K Andersen and KT Shanmugam. Energetics of biological nitrogen fixation: determination of the ratio of formation of h2 to nh4+ catalysed by nitrogenase of klebsiella pneumoniae in vivo. *Microbiology*, 103(1):107–122, 1977.

Kyle R Anderson and Michael P Poland. Abundant carbon in the mantle beneath hawaii. *Nature Geoscience*, 10(9):704–708, 2017. ISSN 1752-0908.

Max Appl. Ammonia: Priciples & industrial practice. 1999.

P Ardia, Marc M Hirschmann, AC Withers, and BD Stanley. Solubility of ch4 in a synthetic basaltic melt, with applications to atmosphere–magma ocean–core partitioning of volatiles and to the evolution of the martian atmosphere. *Geochimica et Cosmochimica Acta*, 114: 52–71, 2013. ISSN 0016-7037.

Katherine Armstrong, Daniel J Frost, Catherine A McCammon, David C Rubie, and Tiziana Boffa Ballaran. Deep magma ocean formation set the oxidation state of earth's mantle. *Science*, 365(6456):903–906, 2019. ISSN 0036-8075.

Giada Arney, Shawn D Domagal-Goldman, Victoria S Meadows, Eric T Wolf, Edward Schwieterman, Benjamin Charnay, Mark Claire, Eric Hébrard, and Melissa G Trainer. The pale orange dot: the spectrum and habitability of hazy archean earth. *Astrobiology*, 16(11): 873–899, 2016.

Sonja Aulbach and Vincenzo Stagno. Evidence for a reducing archean ambient mantle and its effects on the carbon cycle. *Geology*, 44(9):751–754, 2016.

Guillaume Avice, Bernard Marty, Raymond Burgess, A Hofmann, Pascal Philippot, Kevin Zahnle, and David Zakharov. Evolution of atmospheric xenon and other noble gases inferred from archean to paleoproterozoic rocks. *Geochimica et Cosmochimica Acta*, 232: 82–100, 2018.

Jeffrey L Bada and Jun Korenaga. Exposed areas above sea level on earth¿ 3.5 gyr ago: Implications for prebiotic and primitive biotic chemistry. *Life*, 8(4):55, 2018.

Jeffrey L Bada and Antonio Lazcano. Some like it hot, but not the first biomolecules. *Science*, 296(5575):1982–1983, 2002.

Peter M Banks and Gaston Kockarts. *Aeronomy*. Elsevier, 2013.

Joanna K Barstow and Patrick GJ Irwin. Habitable worlds with jwst: transit spectroscopy of the trappist-1 system? *Monthly Notices of the Royal Astronomical Society: Letters*, 461 (1):L92–L96, 2016.

Sidney Becker, Jonas Feldmann, Stefan Wiedemann, Hidenori Okamura, Christina Schneider, Katharina Iwan, Antony Crisp, Martin Rossa, Tynchtyk Amatov, and Thomas Carell. Unified prebiotically plausible synthesis of pyrimidine and purine rna ribonucleotides. *Science*, 366(6461):76–82, 2019.

Stefan Behnel, Robert Bradshaw, Craig Citro, Lisandro Dalcin, Dag Sverre Seljebotn, and Kurt Smith. Cython: The best of both worlds. *Computing in Science & Engineering*, 13 (2):31–39, 2010.

Elizabeth A Bell, Patrick Boehnke, T Mark Harrison, and Wendy L Mao. Potentially biogenic carbon preserved in a 4.1 billion-year-old zircon. *Proceedings of the National Academy of Sciences*, 112(47):14518–14521, 2015.

Steven A Benner, Elizabeth A Bell, Elisa Biondi, Ramon Brasser, Thomas Carell, Hyo-Joong Kim, Stephen J Mojzsis, Arthur Omran, Matthew A Pasek, and Dustin Trail. When did life likely emerge on earth in an rna-first process? *ChemSystemsChem*, 2019. ISSN 2570-4206.

Steven A Benner, Elizabeth A Bell, Elisa Biondi, Ramon Brasser, Thomas Carell, Hyo-Joong Kim, Stephen J Mojzsis, Arthur Omran, Matthew A Pasek, and Dustin Trail. When did life likely emerge on earth in an rna-first process? *ChemSystemsChem*, 2(2):e1900035, 2020.

William F Bottke, Richard J Walker, James MD Day, David Nesvorny, and Linda Elkins-Tanton. Stochastic late accretion to earth, the moon, and mars. *science*, 330(6010): 1527–1530, 2010.

William F Bottke Jr, David Vokrouhlickỳ, David P Rubincam, and David Nesvornỳ. The yarkovsky and yorp effects: Implications for asteroid dynamics. *Annu. Rev. Earth Planet. Sci.*, 34:157–191, 2006.

Scott E Bryan, Ingrid Ukstins Peate, David W Peate, Stephen Self, Dougal A Jerram, Michael R Mawby, JS Goonie Marsh, and Jodie A Miller. The largest volcanic eruptions on earth. *Earth-Science Reviews*, 102(3-4):207–229, 2010.

Roger Buick, JSR Dunlop, and DI Groves. Stromatolite recognition in ancient rocks: an appraisal of irregularly laminated structures in an early archaean chert-barite unit from north pole, western australia. *Alcheringa*, 5(3):161–181, 1981.

Alexander Burcat and Branko Ruscic. Third millenium ideal gas and condensed phase thermochemical database for combustion (with update from active thermochemical tables). Technical report, Argonne National Lab.(ANL), Argonne, IL (United States), 2005.

Christopher J Burke, Jessie L Christiansen, F Mullally, Shawn Seader, Daniel Huber, Jason F Rowe, Jeffrey L Coughlin, Susan E Thompson, Joseph Catanzarite, Bruce D Clarke, et al. Terrestrial planet occurrence rates for the kepler gk dwarf sample. *The Astrophysical Journal*, 809(1):8, 2015.

RC Burns. The nitrogenase system from azotobacter activation energy and divalent cation requirement. *Biochimica et Biophysica Acta (BBA)-Enzymology*, 171(2):253–259, 1969.

Josep G Canadell, Pedro MS Monteiro, Marcos H Costa, L Cotrim da Cunha, Peter M Cox, AV Eliseev, Stephanie Henson, Masao Ishii, Samuel Jaccard, Charles Koven, et al. Global carbon and other biogeochemical cycles and feedbacks. *Climate change*, 2021.

Don E Canfield, Minik T Rosing, and Christian Bjerrum. Early anaerobic metabolisms. *Philosophical Transactions of the Royal Society B: Biological Sciences*, 361(1474):1819–1836, 2006.

Donald E Canfield, Kirsten S Habicht, and BO Thamdrup. The archean sulfur cycle and the early history of atmospheric oxygen. *Science*, 288(5466):658–661, 2000. ISSN 0036-8075.

JA Cartwright, KV Hodges, and M Wadhwa. Evidence against a late heavy bombardment event on vesta. *Earth and Planetary Science Letters*, 590:117576, 2022.

David C Catling and James F Kasting. *Atmospheric evolution on inhabited and lifeless worlds*. Cambridge University Press, 2017.

David C Catling and Kevin J Zahnle. The archean atmosphere. *Science Advances*, 6(9): eaax1420, 2020. ISSN 2375-2548.

David C Catling, Kevin J Zahnle, and Christopher P McKay. Biogenic methane, hydrogen escape, and the irreversible oxidation of early earth. *Science*, 293(5531):839–843, 2001. ISSN 0036-8075.

David C Catling, Christopher R Glein, Kevin J Zahnle, and Christopher P McKay. Why O_2 is required by complex life on habitable planets and the concept of planetary" oxygenation time". *Astrobiology*, 5(3):415–438, 2005. ISSN 1531-1074.

David C. Catling, Joshua Krissansen-Totton, Nancy Y. Kiang, David Crisp, Tyler D. Robinson, Shiladitya DasSarma, Andrew J. Rushby, Anthony Del Genio, William Bains, and Shawn Domagal-Goldman. Exoplanet biosignatures: A framework for their assessment. *Astrobiology*, 18(6):709–738, 2018. doi: 10.1089/ast.2017.1737.

DC Catling, MW Claire, and KJ Zahnle. Anaerobic methanotrophy and the rise of atmospheric oxygen. *Philosophical Transactions of the Royal Society A: Mathematical, Physical and Engineering Sciences*, 365(1856):1867–1888, 2007. ISSN 1364-503X.

Thomas R Cech. The rna worlds in context. *Cold Spring Harbor perspectives in biology*, 4 (7):a006742, 2012.

Kaitlin Cerrillo. *On The Habitability Of An Impacted Young Earth: The effects of a post-impact, reducing atmosphere on Hadean Earth's habitability*. PhD thesis, 2022.

WL Chameides and James CG Walker. Rates of fixation by lightning of carbon and nitrogen in possible primitive atmospheres. *Origins of life*, 11(4):291–302, 1981.

WL Chameides, DH Stedman, RR Dickerson, DW Rusch, and RJ Cicerone. No x production in lightning. *Journal of Atmospheric Sciences*, 34(1):143–149, 1977.

Sydney Chapman and Thomas George Cowling. *The mathematical theory of non-uniform gases: an account of the kinetic theory of viscosity, thermal conduction and diffusion in gases*. Cambridge university press, 1990.

Robert I Citron and Sarah T Stewart. Large impacts onto the early earth: Planetary sterilization and iron delivery. *The Planetary Science Journal*, 3(5):116, 2022.

Mark W Claire, David C Catling, and Kevin J Zahnle. Biogeochemical modelling of the rise in atmospheric oxygen. *Geobiology*, 4(4):239–269, 2006. ISSN 1472-4677.

Mark W Claire, John Sheets, Martin Cohen, Ignasi Ribas, Victoria S Meadows, and David C Catling. The evolution of solar flux from 0.1 nm to 160 μm: quantitative estimates for planetary studies. *The Astrophysical Journal*, 757(1):95, 2012.

Mark W Claire, James F Kasting, Shawn D Domagal-Goldman, Eva E Stüeken, Roger Buick, and Victoria S Meadows. Modeling the signature of sulfur mass-independent fractionation produced in the archean atmosphere. *Geochimica et Cosmochimica Acta*, 141:365–380, 2014.

GJ Cooke, DR Marsh, C Walsh, B Black, and J-F Lamarque. A revised lower estimate of ozone columns during earth's oxygenated history. *Royal Society open science*, 9(1):211165, 2022.

Joy A Crisp. Rates of magma emplacement and volcanic output. *Journal of Volcanology and Geothermal Research*, 20(3-4):177–211, 1984. ISSN 0377-0273.

Sean A Crowe, Guillaume Paris, Sergei Katsev, CarriAyne Jones, Sang-Tae Kim, Aubrey L Zerkle, Sulung Nomosatryo, David A Fowle, Jess F Adkins, Alex L Sessions, et al. Sulfate was a trace constituent of archean seawater. *Science*, 346(6210):735–739, 2014.

Jun Cui, RV Yelle, Véronique Vuitton, JH Waite Jr, WT Kasprzak, DA Gell, HB Niemann, ICF Müller-Wodarg, N Borggren, GG Fletcher, et al. Analysis of titan's neutral upper atmosphere from cassini ion neutral mass spectrometer measurements. *Icarus*, 200(2): 581–615, 2009.

Søren Dahl, E Törnqvist, and IJJOC Chorkendorff. Dissociative adsorption of N_2 on ru(0001): a surface reaction totally dominated by steps. *Journal of Catalysis*, 192(2): 381–390, 2000.

James MD Day and Richard J Walker. Highly siderophile element depletion in the moon. *Earth and Planetary Science Letters*, 423:114–124, 2015.

Massimo Di Giulio. On the rna world: evidence in favor of an early ribonucleopeptide world. *Journal of molecular evolution*, 45:571–578, 1997.

Graham Dixon-Lewis. Computer modeling of combustion reactions in flowing systems with transport. *Combustion chemistry*, pages 21–125, 1984.

Shawn D Domagal-Goldman, Antígona Segura, Mark W Claire, Tyler D Robinson, and Victoria S Meadows. Abiotic ozone and oxygen in atmospheres similar to prebiotic earth. *The Astrophysical Journal*, 792(2):90, 2014. ISSN 0004-637X.

Alexandra E Doyle, Edward D Young, Beth Klein, Ben Zuckerman, and Hilke E Schlichting. Oxygen fugacities of extrasolar rocks: Evidence for an earth-like geochemistry of exoplanets. *Science*, 366(6463):356–359, 2019. ISSN 0036-8075.

DH Ehhalt, LE Heidt, RH Lueb, and W Pollock. The vertical distribution of trace gases in the stratosphere. *Pure and Applied Geophysics*, 113(1):389–402, 1975.

David Ehrenreich, Vincent Bourrier, Peter J Wheatley, Alain Lecavelier Des Etangs, Guillaume Hébrard, Stéphane Udry, Xavier Bonfils, Xavier Delfosse, Jean-Michel Désert, David K Sing, et al. A giant comet-like cloud of hydrogen escaping the warm neptune-mass exoplanet gj 436b. *Nature*, 522(7557):459–461, 2015.

Giuseppe Etiope and Barbara Sherwood Lollar. Abiotic methane on earth. *Reviews of Geophysics*, 51(2):276–299, 2013.

James Farquhar, Huiming Bao, and Mark Thiemens. Atmospheric influence of earth's earliest sulfur cycle. *Science*, 289(5480):756–758, 2000.

Thomas J Fauchez, Martin Turbet, Geronimo L Villanueva, Eric T Wolf, Giada Arney, Ravi K Kopparapu, Andrew Lincowski, Avi Mandell, Julien de Wit, and Daria Pidhorodetska. Impact of clouds and hazes on the simulated jwst transmission spectra of habitable zone planets in the trappist-1 system. *The Astrophysical Journal*, 887(2):194, 2019. ISSN 0004-637X.

J Fiebig, Andri Stefansson, A Ricci, F Tassi, F Viveiros, S Silva, TM Lopez, C Schreiber, S Hofmann, BW Mountain, et al. Abiogenesis not required to explain the origin of volcanic-hydrothermal hydrocarbons. 2019.

D Fischer, B Peterson, J Bean, et al. The luvoir mission concept study final report. 2019.

Woodward W Fischer, James Hemp, and Jena E Johnson. Evolution of oxygenic photosynthesis. *Annual Review of Earth and Planetary Sciences*, 44:647–683, 2016.

Bevan M French. Some geological implications of equilibrium between graphite and a c-h-o gas phase at high temperatures and pressures. *Reviews of Geophysics*, 4(2):223–253, 1966. ISSN 8755-1209.

Yuka Fujii, Daniel Angerhausen, Russell Deitrick, Shawn Domagal-Goldman, John Lee Grenfell, Yasunori Hori, Stephen R Kane, Enric Pallé, Heike Rauer, Nicholas Siegler, et al. Exoplanet biosignatures: observational prospects. *Astrobiology*, 18(6):739–778, 2018.

Yoshihiro Furukawa, Hiromoto Nakazawa, Toshimori Sekine, and Takeshi Kakegawa. Formation of ultrafine particles from impact-generated supercritical water. *Earth and Planetary Science Letters*, 258(3-4):543–549, 2007.

Fabrice Gaillard and Bruno Scaillet. A theoretical framework for volcanic degassing chemistry in a comparative planetology perspective and implications for planetary atmospheres. *Earth and Planetary Science Letters*, 403:307–316, 2014.

S Gaudi et al. Habex: Habitable exoplanet observatory final report. 2019.

H Genda, R Brasser, and SJ Mojzsis. The terrestrial late veneer from core disruption of a lunar-sized impactor. *Earth and Planetary Science Letters*, 480:25–32, 2017.

Walter Gilbert. Origin of life: The rna world. *Nature*, 319(6055):618, 1986. ISSN 1476-4687.

Colin Goldblatt and Kevin J Zahnle. Clouds and the faint young sun paradox. *Climate of the Past*, 7(1):203–220, 2011.

Colin Goldblatt, Timothy M Lenton, and Andrew J Watson. Bistability of atmospheric oxygen and the great oxidation. *Nature*, 443(7112):683–686, 2006. ISSN 1476-4687.

Aaron D Goldman and Betul Kacar. Cofactors are remnants of life's origin and early evolution. *Journal of Molecular Evolution*, 89(3):127–133, 2021.

Helge M. Gonnermann and Michael Manga. *Dynamics of magma ascent in the volcanic conduit*, pages 55–84. Cambridge University Press, Cambridge, 2013. ISBN 9781139021562. doi: DOI:10.1017/CBO9781139021562.004. URL `https://www.cambridge.org/core/books/modeling-volcanic-processes/dynamics-of-magma-ascent-in-the-volcanic-conduit/8B8F375FB8709B62A6C917BEE97C0007`.

David G. Goodwin, Harry K. Moffat, Ingmar Schoegl, Raymond L. Speth, and Bryan W. Weber. Cantera: An object-oriented software toolkit for chemical kinetics, thermodynamics, and transport processes. 2022. doi: 10.5281/zenodo.6387882. Version 2.6.0.

Iouli E Gordon, Laurence S Rothman, Christian Hill, Roman V Kochanov, Y Tan, Peter F Bernath, Manfred Birk, V Boudon, Alain Campargue, KV Chance, et al. The hitran2016

molecular spectroscopic database. *Journal of Quantitative Spectroscopy and Radiative Transfer*, 203:3–69, 2017.

RJ Graham, Tim Lichtenberg, Ryan Boukrouche, and Raymond T Pierrehumbert. A multi-species pseudoadiabat for simulating condensable-rich exoplanet atmospheres. *The Planetary Science Journal*, 2(5):207, 2021.

Bethan S Gregory, Mark W Claire, and Sarah Rugheimer. Photochemical modelling of atmospheric oxygen levels confirms two stable states. *Earth and Planetary Science Letters*, 561:116818, 2021. ISSN 0012-821X.

John Lee Grenfell, Jean-Mathias Grießmeier, Beate Patzer, Heike Rauer, Antigona Segura, Anja Stadelmann, Barbara Stracke, Ruth Titz, and Philip Von Paris. Biomarker response to galactic cosmic ray-induced no x and the methane greenhouse effect in the atmosphere of an earth-like planet orbiting an m dwarf star. *Astrobiology*, 7(1):208–221, 2007. ISSN 1531-1074.

John Lee Grenfell, Stefanie Gebauer, P v Paris, Mareike Godolt, and Heike Rauer. Sensitivity of biosignatures on earth-like planets orbiting in the habitable zone of cool m-dwarf stars to varying stellar uv radiation and surface biomass emissions. *Planetary and Space Science*, 98:66–76, 2014. ISSN 0032-0633.

R. E. Grimm and S. Marchi. Direct thermal effects of the hadean bombardment did not limit early subsurface habitability. *Earth and Planetary Science Letters*, 485:1–8, 2018. ISSN 0012821X. doi: 10.1016/j.epsl.2017.12.043. URL `https://doi.org/10.1016/j.epsl.2017.12.043`.

Simon L Grimm, Matej Malik, Daniel Kitzmann, Andrea Guzmán-Mesa, H Jens Hoeijmakers, Chloe Fisher, João M Mendonça, Sergey N Yurchenko, Jonathan Tennyson, Fabien Alesina, et al. Helios-k 2.0 opacity calculator and open-source opacity database for exoplanetary atmospheres. *The Astrophysical Journal Supplement Series*, 253(1):30, 2021.

Ashley P Gumsley, Kevin R Chamberlain, Wouter Bleeker, Ulf Söderlund, Michiel O de Kock, Emilie R Larsson, and Andrey Bekker. Timing and tempo of the great oxidation event. *Proceedings of the National Academy of Sciences*, 114(8):1811–1816, 2017. ISSN 0027-8424.

Vincent P Gutschick. *Microbes and engineering aspects*. Springer-Verlag, 1982.

Andrés Guzmán-Marmolejo, Antígona Segura, and Elva Escobar-Briones. Abiotic production of methane in terrestrial planets. *Astrobiology*, 13(6):550–559, 2013. ISSN 1531-1074.

RV Hageman and RH Burris. Current topics in bioenergetics. 1980.

Ernst Hairer and Gerhard Wanner. *Solving ordinary differential equations II*, volume 375. Springer Berlin Heidelberg, 1996.

Alex N Halliday and Robin M Canup. The accretion of planet earth. *Nature Reviews Earth & Environment*, 4(1):19–35, 2023.

R_ WF Hardy, Richard D Holsten, EK Jackson, and RC1086994 Burns. The acetylene-ethylene assay for N_2 fixation: laboratory and field evaluation. *Plant physiology*, 43(8): 1185–1207, 1968.

Robert J Hargreaves, Iouli E Gordon, Michael Rey, Andrei V Nikitin, Vladimir G Tyuterev, Roman V Kochanov, and Laurence S Rothman. An accurate, extensive, and practical line list of methane for the hitemp database. *The Astrophysical Journal Supplement Series*, 247(2):55, 2020.

CE Harman, EW Schwieterman, James C Schottelkotte, and JF Kasting. Abiotic O_2 levels on planets around f, g, k, and m stars: possible false positives for life? *The Astrophysical Journal*, 812(2):137, 2015.

William K Hartmann. History of the terminal cataclysm paradigm: Epistemology of a planetary bombardment that never (?) happened. *Geosciences*, 9(7):285, 2019.

D Hauglustaine, C Heinze, E Holland, D Jacob, U Lohmann, S Ramachandran, PL Da Silva Dias, SC Wofsy, and X Zhang. Couplings between changes in the climate system and biogeochemistry. *Climate change*, 2007.

Alan C Hindmarsh, Peter N Brown, Keith E Grant, Steven L Lee, Radu Serban, Dan E Shumaker, and Carol S Woodward. Sundials: Suite of nonlinear and differential/algebraic equation solvers. *ACM Transactions on Mathematical Software (TOMS)*, 31(3):363–396, 2005. ISSN 0098-3500.

Marc M Hirschmann and Anthony C Withers. Ventilation of co2 from a reduced mantle and consequences for the early martian greenhouse. *Earth and Planetary Science Letters*, 270 (1-2):147–155, 2008. ISSN 0012-821X.

Marc M Hirschmann, AC Withers, P Ardia, and NT Foley. Solubility of molecular hydrogen in silicate melts and consequences for volatile evolution of terrestrial planets. *Earth and Planetary Science Letters*, 345:38–48, 2012. ISSN 0012-821X.

Heinrich D Holland. *The chemical evolution of the atmosphere and oceans*. Princeton University Press, 1984. ISBN 0691023816.

Heinrich D Holland. Volcanic gases, black smokers, and the great oxidation event. *Geochimica et Cosmochimica Acta*, 66(21):3811–3826, 2002.

Peter O Hopcroft, Paul J Valdes, and Jed O Kaplan. Bayesian analysis of the glacial-interglacial methane increase constrained by stable isotopes and earth system modeling. *Geophysical research letters*, 45(8):3653–3663, 2018. ISSN 0094-8276.

Sarah M Hörst. Titan's atmosphere and climate. *Journal of Geophysical Research: Planets*, 122(3):432–482, 2017.

Herbert E Huppert, R Stephen J Sparks, J Stewart Turner, and Nicholas T Arndt. Emplacement and cooling of komatiite lavas. *Nature*, 309(5963):19–22, 1984. ISSN 1476-4687.

Giada Iacono-Marziano, Yann Morizet, Emmanuel Le Trong, and Fabrice Gaillard. New experimental data and semi-empirical parameterization of h2o–co2 solubility in mafic melts. *Geochimica et Cosmochimica Acta*, 97:1–23, 2012. ISSN 0016-7037.

Jonathan P Itcovitz, Auriol SP Rae, Robert I Citron, Sarah T Stewart, Catriona A Sinclair, Paul B Rimmer, and Oliver Shorttle. Reduced atmospheres of post-impact worlds: The early earth. *The Planetary Science Journal*, 3(5):115, 2022.

Gareth Izon, Aubrey L Zerkle, Kenneth H Williford, James Farquhar, Simon W Poulton, and Mark W Claire. Biological regulation of atmospheric chemistry en route to planetary oxygenation. *Proceedings of the National Academy of Sciences*, 114(13):E2571–E2579, 2017.

Gareth Izon, Genming Luo, Benjamin T Uveges, Nicolas Beukes, Kouki Kitajima, Shuhei Ono, John W Valley, Xingyu Ma, and Roger E Summons. Bulk and grain-scale minor sulfur isotope data reveal complexities in the dynamics of earth's oxygenation. *Proceedings of the National Academy of Sciences*, 119(13):e2025606119, 2022.

Emmanuelle J Javaux. Challenges in evidencing the earliest traces of life. *Nature*, 572(7770): 451–460, 2019.

Aleisha C Johnson, Chadlin M Ostrander, Stephen J Romaniello, Christopher T Reinhard, Allison T Greaney, Timothy W Lyons, and Ariel D Anbar. Reconciling evidence of oxidative weathering and atmospheric anoxia on archean earth. *Science Advances*, 7(40): eabj0108, 2021. ISSN 2375-2548.

Benjamin W Johnson and Boswell A Wing. Limited archaean continental emergence reflected in an early archaean 18o-enriched ocean. *Nature Geoscience*, 13(3):243–248, 2020.

James W Johnson, Eric H Oelkers, and Harold C Helgeson. Supcrt92: A software package for calculating the standard molal thermodynamic properties of minerals, gases, aqueous

species, and reactions from 1 to 5000 bar and 0 to 1000 c. *Computers & Geosciences*, 18 (7):899–947, 1992.

Gerald F Joyce and Jack W Szostak. Protocells and rna self-replication. *Cold Spring Harbor Perspectives in Biology*, 10(9):a034801, 2018. ISSN 1943-0264.

Shintaro Kadoya, Joshua Krissansen-Totton, and David C Catling. Probable cold and alkaline surface environment of the hadean earth caused by impact ejecta weathering. *Geochemistry, Geophysics, Geosystems*, 21(1):e2019GC008734, 2020.

Tijs Karman, Iouli E Gordon, Ad van Der Avoird, Yury I Baranov, Christian Boulet, Brian J Drouin, Gerrit C Groenenboom, Magnus Gustafsson, Jean-Michel Hartmann, Robert L Kurucz, et al. Update of the hitran collision-induced absorption section. *Icarus*, 328: 160–175, 2019.

James F Kasting and David Catling. Evolution of a habitable planet. *Annual Review of Astronomy and Astrophysics*, 41(1):429–463, 2003. ISSN 0066-4146.

James F Kasting, Kevin J Zahnle, and James CG Walker. Photochemistry of methane in the earth's early atmosphere. *Precambrian Research*, 20(2-4):121–148, 1983.

James F Kasting, David H Eggler, and Stuart P Raeburn. Mantle redox evolution and the oxidation state of the archean atmosphere. *The Journal of Geology*, 101(2):245–257, 1993.

JF Kasting and TM Donahue. The evolution of atmospheric ozone. *Journal of Geophysical Research: Oceans*, 85(C6):3255–3263, 1980. ISSN 0148-0227.

JJ Keady and DP Kilcrease. Radiation. In *Allen's Astrophysical Quantities*, pages 95–120. Springer, 2002.

Anthony D Keefe and Stanley L Miller. Was ferrocyanide a prebiotic reagent? *Origins of Life and Evolution of the Biosphere*, 26:111–129, 1996.

P Kharecha, J Kasting, and J Siefert. A coupled atmosphere-ecosystem model of the early archean earth. *Geobiology*, 3(2):53–76, 2005. ISSN 1472-4677.

Caitlin Elizabeth King. *Diversity and activity of aerobic thermophilic carbon monoxide-oxidizing bacteria on Kilauea Volcano, Hawaii*. Louisiana State University and Agricultural & Mechanical College, 2013.

Michael A Kipp, Joshua Krissansen-Totton, and David C Catling. High organic burial efficiency is required to explain mass balance in earth's early carbon cycle. *Global Biogeochemical Cycles*, 35(2), 2021.

Ravi Kumar Kopparapu, Ramses Ramirez, James F Kasting, Vincent Eymet, Tyler D Robinson, Suvrath Mahadevan, Ryan C Terrien, Shawn Domagal-Goldman, Victoria Meadows, and Rohit Deshpande. Habitable zones around main-sequence stars: new estimates. *The Astrophysical Journal*, 765(2):131, 2013. ISSN 0004-637X.

Jun Korenaga. Scaling of stagnant-lid convection with arrhenius rheology and the effects of mantle melting. *Geophysical Journal International*, 179(1):154–170, 2009.

Jun Korenaga. Was there land on the early earth? *Life*, 11(11):1142, 2021.

Richard G Kraus, Seth Root, Raymond W Lemke, Sarah T Stewart, Stein B Jacobsen, and Thomas R Mattsson. Impact vaporization of planetesimal cores in the late stages of planet formation. *Nature Geoscience*, 8(4):269–272, 2015.

Alexander J Krause, Benjamin JW Mills, Shuang Zhang, Noah J Planavsky, Timothy M Lenton, and Simon W Poulton. Stepwise oxygenation of the paleozoic atmosphere. *Nature Communications*, 9(1):4081, 2018.

Monika E Kress and Christopher P McKay. Formation of methane in comet impacts: implications for earth, mars, and titan. *Icarus*, 168(2):475–483, 2004.

Victor C Kress and Ian SE Carmichael. The compressibility of silicate liquids containing fe 2 o 3 and the effect of composition, temperature, oxygen fugacity and pressure on their redox states. *Contributions to Mineralogy and Petrology*, 108:82–92, 1991.

Joshua Krissansen-Totton, David S Bergsman, and David C Catling. On detecting biospheres from chemical thermodynamic disequilibrium in planetary atmospheres. *Astrobiology*, 16 (1):39–67, 2016.

Joshua Krissansen-Totton, Giada N Arney, and David C Catling. Constraining the climate and ocean ph of the early earth with a geological carbon cycle model. *Proceedings of the National Academy of Sciences*, 115(16):4105–4110, 2018a.

Joshua Krissansen-Totton, Ryan Garland, Patrick Irwin, and David C Catling. Detectability of biosignatures in anoxic atmospheres with the james webb space telescope: A trappist-1e case study. *The Astronomical Journal*, 156(3):114, 2018b.

Joshua Krissansen-Totton, Stephanie Olson, and David C Catling. Disequilibrium biosignatures over earth history and implications for detecting exoplanet life. *Science advances*, 4 (1):eaao5747, 2018c.

Joshua Krissansen-Totton, Jonathan J Fortney, Francis Nimmo, and Nicholas Wogan. Oxygen false positives on habitable zone planets around sun-like stars. *AGU Advances*, 2(2): e2020AV000294, 2021a.

Joshua Krissansen-Totton, Michael A Kipp, and David C Catling. Carbon cycle inverse modeling suggests large changes in fractional organic burial are consistent with the carbon isotope record and may have contributed to the rise of oxygen. *Geobiology*, 19(4):342–363, 2021b.

Florian Kurzweil, Mark Claire, Christophe Thomazo, Marc Peters, Mark Hannington, and Harald Strauss. Atmospheric sulfur rearrangement 2.7 billion years ago: Evidence for oxygenic photosynthesis. *Earth and Planetary Science Letters*, 366:17–26, 2013.

Thomas A Laakso and Daniel P Schrag. A small marine biosphere in the proterozoic. *Geobiology*, 17(2):161–171, 2019.

PP Lavvas, A Coustenis, and IM Vardavas. Coupling photochemistry with haze formation in titan's atmosphere, part i: Model description. *Planetary and Space Science*, 56(1):27–66, 2008a.

PP Lavvas, Athéna Coustenis, and IM Vardavas. Coupling photochemistry with haze formation in titan's atmosphere, part ii: Results and validation with cassini/huygens data. *Planetary and Space Science*, 56(1):67–99, 2008b.

Marion Le Voyer, Erik H Hauri, Elizabeth Cottrell, Katherine A Kelley, Vincent JM Salters, Charles H Langmuir, David R Hilton, Peter H Barry, and Evelyn Füri. Carbon fluxes and primary magma co2 contents along the global mid-ocean ridge system. *Geochemistry, Geophysics, Geosystems*, 20(3):1387–1424, 2019. ISSN 1525-2027.

AN LeCheminant and LM Heaman. Mackenzie igneous events, canada: Middle proterozoic hotspot magmatism associated with ocean opening. *Earth and Planetary Science Letters*, 96(1-2):38–48, 1989.

Jérémy Leconte, Franck Selsis, Franck Hersant, and Tristan Guillot. Condensation-inhibited convection in hydrogen-rich atmospheres-stability against double-diffusive processes and thermal profiles for jupiter, saturn, uranus, and neptune. *Astronomy & Astrophysics*, 598: A98, 2017.

Christophe Lécuyer, Philippe Gillet, and François Robert. The hydrogen isotope composition of seawater and the global water cycle. *Chemical Geology*, 145(3-4):249–261, 1998.

Owen R Lehmer, David C Catling, Mary N Parenteau, and Tori M Hoehler. The productivity of oxygenic photosynthesis around cool, m dwarf stars. *The Astrophysical Journal*, 859 (2):171, 2018. ISSN 0004-637X.

Randall J LeVeque et al. *Finite volume methods for hyperbolic problems*, volume 31. Cambridge university press, 2002.

John S Lewis. Asteroid resources. *Space resources materials: National Aeronautics and Space Administration Special Publication*, 509:59–77, 1992.

Gang Li, Iouli E Gordon, Laurence S Rothman, Yan Tan, Shui-Ming Hu, Samir Kassi, Alain Campargue, and Emile S Medvedev. Rovibrational line lists for nine isotopologues of the co molecule in the x1σ+ ground electronic state. *The Astrophysical Journal Supplement Series*, 216(1):15, 2015.

Zheng-Xue Anser Li and Cin-Ty Aeolus Lee. The constancy of upper mantle fo2 through time inferred from v/sc ratios in basalts. *Earth and Planetary Science Letters*, 228(3-4): 483–493, 2004. ISSN 0012-821X.

Tim Lichtenberg and Matthew S Clement. Reduced late bombardment on rocky exoplanets around m dwarfs. *The Astrophysical Journal Letters*, 938(1):L3, 2022.

Philippa Liggins, Oliver Shorttle, and Paul B Rimmer. Can volcanism build hydrogen-rich early atmospheres? *arXiv preprint arXiv:2007.12037*, 2020.

Andrew P Lincowski, Victoria S Meadows, David Crisp, Tyler D Robinson, Rodrigo Luger, Jacob Lustig-Yaeger, and Giada N Arney. Evolved climates and observational discriminants for the trappist-1 planetary system. *The Astrophysical Journal*, 867(1):76, 2018. ISSN 0004-637X.

P.J. Linstrom and W.G. Mallard. Nist chemistry webbook, nist standard reference database number 69, 1998. URL `https://doi.org/10.18434/T4D303`. Accessed on June 14, 2023.

Peter S Liss and PG Slater. Flux of gases across the air-sea interface. *Nature*, 247(5438): 181–184, 1974.

Torbjørn Ljones. Nitrogen fixation and bioenergetics: the role of atp in nitrogenase catalysis. *FEBS letters*, 98(1):1–8, 1979.

JC Loison, Eric Hébrard, M Dobrijevic, KM Hickson, F Caralp, V Hue, G Gronoff, Olivia Venot, and Y Bénilan. The neutral photochemistry of nitriles, amines and imines in the atmosphere of titan. *Icarus*, 247:218–247, 2015.

Mercedes Lopez-Morales, Sagi Ben-Ami, Gonzalo Gonzalez-Abad, Juliana Garcia-Mejia, Jeremy Dietrich, and Andrew Szentgyorgyi. Optimizing ground-based observations of o2 in earth analogs. *The Astronomical Journal*, 158(1):24, 2019.

James E Lovelock. A physical basis for life detection experiments. *Nature*, 207:568–570, 1965.

James Ephraim Lovelock. Thermodynamics and the recognition of alien biospheres. *Proceedings of the Royal Society of London. Series B. Biological Sciences*, 189(1095):167–181, 1975.

Rodrigo Luger and Rory Barnes. Extreme water loss and abiotic o2 buildup on planets throughout the habitable zones of m dwarfs. *Astrobiology*, 15(2):119–143, 2015. ISSN 1531-1074.

Jacob Lustig-Yaeger, Victoria S Meadows, and Andrew P Lincowski. The detectability and characterization of the trappist-1 exoplanet atmospheres with jwst. *The Astronomical Journal*, 158(1):27, 2019. ISSN 1538-3881.

Timothy W Lyons, Christopher T Reinhard, and Noah J Planavsky. The rise of oxygen in earth's early ocean and atmosphere. *Nature*, 506(7488):307, 2014. ISSN 1476-4687.

S Marchi, WF Bottke, LT Elkins-Tanton, M Bierhaus, K Wuennemann, A Morbidelli, and DA Kring. Widespread mixing and burial of earth's hadean crust by asteroid impacts. *Nature*, 511(7511):578–582, 2014. ISSN 1476-4687.

S Marchi, RM Canup, and RJ Walker. Heterogeneous delivery of silicate and metal to the earth by large planetesimals. *Nature geoscience*, 11(1):77–81, 2018.

A Marten, T Hidayat, Y Biraud, and R Moreno. New millimeter heterodyne observations of titan: Vertical distributions of nitriles hcn, hc3n, ch3cn, and the isotopic ratio 15n/14n in its atmosphere. *Icarus*, 158(2):532–544, 2002.

ST Massie and DM Hunten. Stratospheric eddy diffusion coefficients from tracer data. *Journal of Geophysical Research: Oceans*, 86(C10):9859–9868, 1981.

Dan McKenzie. Speculations on the generation and movement of komatiites. *Journal of Petrology*, 2020.

Victoria S Meadows. Reflections on o2 as a biosignature in exoplanetary atmospheres. *Astrobiology*, 17(10):1022–1052, 2017.

Victoria S Meadows and David Crisp. Ground-based near-infrared observations of the venus nightside: The thermal structure and water abundance near the surface. *Journal of Geophysical Research: Planets*, 101(E2):4595–4622, 1996.

Victoria S Meadows, Christopher T Reinhard, Giada N Arney, Mary N Parenteau, Edward W Schwieterman, Shawn D Domagal-Goldman, Andrew P Lincowski, Karl R Stapelfeldt, Heike Rauer, Shiladitya DasSarma, et al. Exoplanet biosignatures: understanding oxygen as a biosignature in the context of its environment. *Astrobiology*, 18(6):630–662, 2018.

NR Meyer, AL Zerkle, and DA Fike. Sulphur cycling in a neoarchaean microbial mat. *Geobiology*, 15(3):353–365, 2017.

Stephen R Meyers and Alberto Malinverno. Proterozoic milankovitch cycles and the history of the solar system. *Proceedings of the National Academy of Sciences*, 115(25):6363–6368, 2018.

Stanley L Miller and Harold C Urey. Organic compound synthesis on the primitive earth. *Science*, 130(3370):245–251, 1959. ISSN 0036-8075.

Shin Miyakawa, H James Cleaves, and Stanley L Miller. The cold origin of life: A. implications based on the hydrolytic stabilities of hydrogen cyanide and formamide. *Origins of Life and Evolution of the Biosphere*, 32(3):195–208, 2002.

Yoshinori Miyazaki and Jun Korenaga. A wet heterogeneous mantle creates a habitable world in the hadean. *Nature*, 603(7899):86–90, 2022.

P Mollière, JP Wardenier, R Van Boekel, Th Henning, K Molaverdikhani, and IAG Snellen. petitradtrans-a python radiative transfer package for exoplanet characterization and retrieval. *Astronomy & Astrophysics*, 627:A67, 2019.

Alessandro Morbidelli, D Nesvorny, Vera Laurenz, S Marchi, David C Rubie, Linda Elkins-Tanton, M Wieczorek, and Steven Jacobson. The timeline of the lunar bombardment: Revisited. *Icarus*, 305:262–276, 2018.

Yves Moussallam, Clive Oppenheimer, and Bruno Scaillet. On the relationship between oxidation state and temperature of volcanic gas emissions. *Earth and Planetary Science Letters*, 520:260–267, 2019. ISSN 0012-821X.

Felix Muller, Luis Escobar, Felix Xu, Ewa Wegrzyn, Milda Nainyte, Tynchtyk Amatov, Chun-Yin Chan, Alexander Pichler, and Thomas Carell. A prebiotically plausible scenario of an rna–peptide world. *Nature*, 605(7909):279–284, 2022.

A Mundl-Petermeier, RJ Walker, RA Fischer, V Lekic, MG Jackson, and MD Kurz. Anomalous 182w in high 3he/4he ocean island basalts: Fingerprints of earth's core? *Geochimica et Cosmochimica Acta*, 271:194–211, 2020.

William F Murphy. The rayleigh depolarization ratio and rotational raman spectrum of water vapor and the polarizability components for the water molecule. *The Journal of Chemical Physics*, 67(12):5877–5882, 1977.

Lee T Murray. Lightning no x and impacts on air quality. *Current Pollution Reports*, 2: 115–133, 2016.

Catherine D Neish, Arpad Somogyi, and Mark A Smith. Titan's primordial soup: formation of amino acids via low-temperature hydrolysis of tholins. *Astrobiology*, 10(3):337–347, 2010.

Robert W Nicklas, Igor S Puchtel, Richard D Ash, Philip M Piccoli, Eero Hanski, Euan G Nisbet, Pedro Waterton, D Graham Pearson, and Ariel D Anbar. Secular mantle oxidation across the archean-proterozoic boundary: Evidence from v partitioning in komatiites and picrites. *Geochimica et Cosmochimica Acta*, 250:49–75, 2019.

Yoko Ohtomo, Takeshi Kakegawa, Akizumi Ishida, Toshiro Nagase, and Minik T Rosing. Evidence for biogenic graphite in early archaean isua metasedimentary rocks. *Nature Geoscience*, 7(1):25–28, 2014.

Hidenori Okamura, Antony Crisp, Sarah Hübner, Sidney Becker, Petra Rovó, and Thomas Carell. Proto-urea-rna (wöhler rna) containing unusually stable urea nucleosides. *Angewandte Chemie International Edition*, 58(51):18691–18696, 2019.

Stephanie L Olson, Christopher T Reinhard, and Timothy W Lyons. Limited role for methane in the mid-proterozoic greenhouse. *Proceedings of the National Academy of Sciences*, 113(41):11447–11452, 2016. ISSN 0027-8424.

Hugh SC O'Neill. Quartz-fayalite-iron and quartz-fayalite-magnetite equilibria and the free energy of formation of fayalite (fe 2 sio 4) and magnetite (fe 3 o 4). *American Mineralogist*, 72(1-2):67–75, 1987. ISSN 1945-3027.

Clive Oppenheimer, Bruno Scaillet, Andrew Woods, A Jeff Sutton, Tamar Elias, and Yves Moussallam. Influence of eruptive style on volcanic gas emission chemistry and temperature. *Nature Geoscience*, 11(9):678–681, 2018. ISSN 1752-0908.

G Ortenzi, L Noack, F Sohl, CM Guimond, JL Grenfell, C Dorn, JM Schmidt, S Vulpius, N Katyal, and D Kitzmann. Mantle redox state drives outgassing chemistry and atmospheric composition of rocky planets. *Scientific reports*, 10(1):1–14, 2020. ISSN 2045-2322.

Tobias Owen. The search for early forms of life in other planetary systems: future possibilities afforded by spectroscopic techniques. *Strategies for the Search for Life in the Universe: A Joint Session of Commissions 16, 40, and 44, Held in Montreal, Canada, During the IAU General Assembly, 15 and 16 August, 1979*, pages 177–185, 1980.

Ryan Park and Alan Chamberlin. Jpl small-body close-approach database, 2023. URL `https://ssd-api.jpl.nasa.gov/doc/cad.html`.

Bhavesh H Patel, Claudia Percivalle, Dougal J Ritson, Colm D Duffy, and John D Sutherland. Common origins of rna, protein and lipid precursors in a cyanosulfidic protometabolism. *Nature Chemistry*, 7(4):301–307, 2015.

AA Pavlov and JF Kasting. Mass-independent fractionation of sulfur isotopes in archean sediments: strong evidence for an anoxic archean atmosphere. *Astrobiology*, 2(1):27–41, 2002. ISSN 1531-1074.

Alexander A Pavlov, Lisa L Brown, and James F Kasting. Uv shielding of nh3 and o2 by organic hazes in the archean atmosphere. *Journal of Geophysical Research: Planets*, 106 (E10):23267–23287, 2001.

Ben KD Pearce, Karan Molaverdikhani, Ralph E Pudritz, Thomas Henning, and Kaitlin E Cerrillo. Toward rna life on early earth: From atmospheric hcn to biomolecule production in warm little ponds. *The Astrophysical Journal*, 932(1):9, 2022.

Rudolf Penndorf. Tables of the refractive index for standard air and the rayleigh scattering coefficient for the spectral region between 0.2 and 20.0 μ and their application to atmospheric optics. *Journal of the Optical Society of America*, 47(2):176–182, 1957.

Laurette Piani, Yves Marrocchi, Thomas Rigaudier, Lionel G Vacher, Dorian Thomassin, and Bernard Marty. Earth's water may have been inherited from material similar to enstatite chondrite meteorites. *Science*, 369(6507):1110–1113, 2020.

Noah J Planavsky, Dan Asael, Axel Hofmann, Christopher T Reinhard, Stefan V Lalonde, Andrew Knudsen, Xiangli Wang, Frantz Ossa Ossa, Ernesto Pecoits, Albertus JB Smith, et al. Evidence for oxygenic photosynthesis half a billion years before the great oxidation event. *Nature Geoscience*, 7(4):283–286, 2014a.

Noah J Planavsky, Christopher T Reinhard, Xiangli Wang, Danielle Thomson, Peter McGoldrick, Robert H Rainbird, Thomas Johnson, Woodward W Fischer, and Timothy W Lyons. Low mid-proterozoic atmospheric oxygen levels and the delayed rise of animals. *science*, 346(6209):635–638, 2014b.

Ulrich Platt. The origin of nitrous and nitric acid in the atmosphere. In *Chemistry of multiphase atmospheric systems*, pages 299–319. Springer, 1986.

O Poch, P Coll, Arnaud Buch, SI Ramírez, and F Raulin. Production yields of organics of astrobiological interest from h2o–nh3 hydrolysis of titan's tholins. *Planetary and Space Science*, 61(1):114–123, 2012.

Simon W Poulton, Andrey Bekker, Vivien M Cumming, Aubrey L Zerkle, Donald E Canfield, and David T Johnston. A 200-million-year delay in permanent atmospheric oxygenation. *Nature*, 592(7853):232–236, 2021. ISSN 1476-4687.

Matthew W Powner, Béatrice Gerland, and John D Sutherland. Synthesis of activated pyrimidine ribonucleotides in prebiotically plausible conditions. *Nature*, 459(7244):239–242, 2009.

Sukrit Ranjan and Dimitar D Sasselov. Constraints on the early terrestrial surface uv environment relevant to prebiotic chemistry. *Astrobiology*, 17(3):169–204, 2017.

Sukrit Ranjan, Edward W Schwieterman, Chester Harman, Alexander Fateev, Clara Sousa-Silva, Sara Seager, and Renyu Hu. Photochemistry of anoxic abiotic habitable planet atmospheres: Impact of new h $_2$ o cross-sections. *arXiv preprint arXiv:2004.04185*, 2020.

Birger Rasmussen, Andrey Bekker, and Ian R Fletcher. Correlation of paleoproterozoic glaciations based on U–Pb zircon ages for tuff beds in the transvaal and huronian supergroups. *Earth and Planetary Science Letters*, 382:173–180, 2013. ISSN 0012-821X.

Eoghan P Reeves and Jens Fiebig. Abiotic synthesis of methane and organic compounds in earth's lithosphere. *Elements: An International Magazine of Mineralogy, Geochemistry, and Petrology*, 16(1):25–31, 2020. ISSN 1811-5217.

Jesse Reimink, Carolyn Crow, Desmond Moser, Benjamin Jacobsen, Ann Bauer, and Thomas Chacko. Quantifying the effect of late bombardment on terrestrial zircons. *Earth and Planetary Science Letters*, 604:118007, 2023.

Christopher T Reinhard, Stephanie L Olson, Edward W Schwieterman, and Timothy W Lyons. False negatives for remote life detection on ocean-bearing planets: lessons from the early earth. *Astrobiology*, 17(4):287–297, 2017.

Paul B Rimmer and Sarah Rugheimer. Hydrogen cyanide in nitrogen-rich atmospheres of rocky exoplanets. *Icarus*, 329:124–131, 2019.

Paul B Rimmer and Oliver Shorttle. Origin of life's building blocks in carbon-and nitrogen-rich surface hydrothermal vents. *Life*, 9(1):12, 2019.

Dougal J Ritson, Claudio Battilocchio, Steven V Ley, and John D Sutherland. Mimicking the surface and prebiotic chemistry of early earth using flow chemistry. *Nature communications*, 9(1):1–10, 2018. ISSN 2041-1723.

Dougal J Ritson, Mikolaj W Poplawski, Andrew D Bond, and John D Sutherland. Azoles as auxiliaries and intermediates in prebiotic nucleoside synthesis. *Journal of the American Chemical Society*, 144(42):19447–19455, 2022.

Juan Carlos Rosas and Jun Korenaga. Rapid crustal growth and efficient crustal recycling in the early earth: Implications for hadean and archean geodynamics. *Earth and Planetary Science Letters*, 494:42–49, 2018.

Minik T Rosing. 13c-depleted carbon microparticles in¿ 3700-ma sea-floor sedimentary rocks from west greenland. *Science*, 283(5402):674–676, 1999.

Laurence S Rothman, IE Gordon, RJ Barber, H Dothe, Robert R Gamache, A Goldman, VI Perevalov, SA Tashkun, and J Tennyson. Hitemp, the high-temperature molecular spectroscopic database. *Journal of Quantitative Spectroscopy and Radiative Transfer*, 111 (15):2139–2150, 2010.

David C Rubie, Vera Laurenz, Seth A Jacobson, Alessandro Morbidelli, Herbert Palme, Antje K Vogel, and Daniel J Frost. Highly siderophile elements were stripped from earth's mantle by iron sulfide segregation. *Science*, 353(6304):1141–1144, 2016.

S Rugheimer, L Kaltenegger, A Segura, J Linsky, and S Mohanty. Effect of uv radiation on the spectral fingerprints of earth-like planets orbiting m stars. *The Astrophysical Journal*, 809(1):57, 2015. ISSN 0004-637X.

Sarah Rugheimer and Lisa Kaltenegger. Spectra of earth-like planets through geological evolution around fgkm stars. *The Astrophysical Journal*, 854(1):19, 2018. ISSN 0004-637X.

Carl Sagan and Christopher Chyba. The early faint sun paradox: Organic shielding of ultraviolet-labile greenhouse gases. *Science*, 276(5316):1217–1221, 1997.

Carl Sagan, W Reid Thompson, Robert Carlson, Donald Gurnett, and Charles Hord. A search for life on earth from the galileo spacecraft. *Nature*, 365(6448):715–721, 1993.

Robert A Sanchez, James P Ferbis, and Leslie E Orgel. Studies in prebiodc synthesis: Ii. synthesis of purine precursors and amino acids from aqueous hydrogen cyanide. *Journal of Molecular Biology*, 30(2):223–253, 1967.

Dimitar D Sasselov, John P Grotzinger, and John D Sutherland. The origin of life as a planetary phenomenon. *Science Advances*, 6(6):eaax3419, 2020. ISSN 2375-2548.

Boris Sauterey, Benjamin Charnay, Antonin Affholder, Stéphane Mazevet, and Régis Ferrière. Co-evolution of primitive methane-cycling ecosystems and early earth's atmosphere and climate. *Nature Communications*, 11(1):1–12, 2020. ISSN 2041-1723.

Laura Schaefer and Bruce Fegley Jr. Chemistry of atmospheres formed during accretion of the earth and other terrestrial planets. *Icarus*, 208(1):438–448, 2010. ISSN 0019-1035.

KF Scheidegger. Temperatures and compositions of magmas ascending along mid-ocean ridges. *Journal of geophysical research*, 78(17):3340–3355, 1973. ISSN 0148-0227.

Trent L Schindler and James F Kasting. Synthetic spectra of simulated terrestrial atmospheres containing possible biomarker gases. *Icarus*, 145(1):262–271, 2000. ISSN 0019-1035.

Daniel Schmider, Lubow Maier, and Olaf Deutschmann. Reaction kinetics of CO and CO_2 methanation over nickel. *Industrial & Engineering Chemistry Research*, 60(16):5792–5805, 2021.

Peter Schönheit, Wolfgang Buckel, and William F Martin. On the origin of heterotrophy. *Trends in microbiology*, 24(1):12–25, 2016.

Edward W Schwieterman, Christopher T Reinhard, Stephanie L Olson, Kazumi Ozaki, Chester E Harman, Peng K Hong, and Timothy W Lyons. Rethinking co antibiosignatures in the search for life beyond the solar system. *The Astrophysical Journal*, 874(1): 9, 2019.

Antígona Segura, James F Kasting, Victoria Meadows, Martin Cohen, John Scalo, David Crisp, Rebecca AH Butler, and Giovanna Tinetti. Biosignatures from earth-like planets around m dwarfs. *Astrobiology*, 5(6):706–725, 2005.

Antígona Segura, Kara Krelove, James F Kasting, Darrell Sommerlatt, Victoria Meadows, David Crisp, Martin Cohen, and Eli Mlawer. Ozone concentrations and ultraviolet fluxes on earth-like planets around other stars. *Astrobiology*, 3(4):689–708, 2003. ISSN 1531-1074.

J.H. Seinfeld, P.D.C.J.H. Seinfeld, and S.N. Pandis. *Atmospheric Chemistry and Physics: From Air Pollution to Climate Change*. Wiley-Interscience publication. Wiley, 2006. ISBN 9780471178156.

Stephen Self, Millard F Coffin, Michael R Rampino, and John A Wolff. Large igneous provinces and flood basalt volcanism. In *The Encyclopedia of Volcanoes*, pages 441–455. Elsevier, 2015.

DE Shemansky. Co2 extinction coefficient 1700–3000 å. *The Journal of Chemical Physics*, 56(4):1582–1587, 1972.

Steven F Sholes, Joshua Krissansen-Totton, and David C Catling. A maximum subsurface biomass on mars from untapped free energy: CO and H_2 as potential antibiosignatures. *Astrobiology*, 19(5):655–668, 2019.

E Simoncini, N Virgo, and Axel Kleidon. Quantifying drivers of chemical disequilibrium: theory and application to methane in the earth's atmosphere. *Earth System Dynamics*, 4 (2):317–331, 2013.

Norman H Sleep. Asteroid bombardment and the core of theia as possible sources for the earth's late veneer component. *Geochemistry, Geophysics, Geosystems*, 17(7):2623–2642, 2016.

Norman H Sleep and Kevin Zahnle. Carbon dioxide cycling and implications for climate on ancient earth. *Journal of Geophysical Research: Planets*, 106(E1):1373–1399, 2001.

Norman H Sleep, Kevin J Zahnle, James F Kasting, and Harold J Morowitz. Annihilation of ecosystems by large asteroid impacts on the early earth. *Nature*, 342(6246):139–142, 1989.

Hilton A Smith and John C Posey. The separation of hydrogen and deuterium by the reaction of iron with steam. *Journal of the American Chemical Society*, 79(6):1310–1313, 1957.

Megan L Smith, Mark W Claire, David C Catling, and Kevin J Zahnle. The formation of sulfate, nitrate and perchlorate salts in the martian atmosphere. *Icarus*, 231:51–64, 2014.

IAG Snellen, RJ De Kok, R Le Poole, Matteo Brogi, and Jayne Birkby. Finding extraterrestrial life using ground-based high-dispersion spectroscopy. *The Astrophysical Journal*, 764(2):182, 2013.

Sanjoy M Som, David C Catling, Jelte P Harnmeijer, Peter M Polivka, and Roger Buick. Air density 2.7 billion years ago limited to less than twice modern levels by fossil raindrop imprints. *Nature*, 484(7394):359–362, 2012.

Renato Spahni, Jérôme Chappellaz, Thomas F Stocker, Laetitia Loulergue, Gregor Hausammann, Kenji Kawamura, Jacqueline Flückiger, Jakob Schwander, Dominique Raynaud, and Valérie Masson-Delmotte. Atmospheric methane and nitrous oxide of the late pleistocene from antarctic ice cores. *Science*, 310(5752):1317–1321, 2005. ISSN 0036-8075.

CC Stamper, E Melekhova, JD Blundy, RJ Arculus, MCS Humphreys, and RA Brooker. Oxidised phase relations of a primitive basalt from grenada, lesser antilles. *Contributions to Mineralogy and Petrology*, 167(1):954, 2014. ISSN 0010-7999.

Roscoe Stribling and Stanley L Miller. Energy yields for hydrogen cyanide and formaldehyde syntheses: the hcn and amino acid concentrations in the primitive ocean. *Origins of Life and Evolution of the Biosphere*, 17(3):261–273, 1987.

Darrell F Strobel, Sushil K Atreya, Bruno Bézard, Francesca Ferri, F Michael Flasar, Marcello Fulchignoni, Emmanuel Lellouch, and Ingo Müller-Wodarg. *Atmospheric structure and composition*, pages 235–257. Springer, 2009.

John D Sutherland. The origin of life—out of the blue. *Angewandte Chemie International Edition*, 55(1):104–121, 2016. ISSN 1433-7851.

Robert B Symonds. *Volcanic-gas studies: Methods, results, and applications, in Volatiles in magma*, volume 30, pages 1–66. 1994.

Eiichi Takahashi. Melting of a dry peridotite klb-1 up to 14 gpa: Implications on the origin of peridotitic upper mantle. *Journal of Geophysical Research: Solid Earth*, 91(B9):9367–9382, 1986.

Maggie A Thompson, Joshua Krissansen-Totton, Nicholas Wogan, Myriam Telus, and Jonathan J Fortney. The case and context for atmospheric methane as an exoplanet biosignature. *Proceedings of the National Academy of Sciences*, 119(14):e2117933119, 2022.

Feng Tian, JF Kasting, and K Zahnle. Revisiting hcn formation in earth's early atmosphere. *Earth and Planetary Science Letters*, 308(3-4):417–423, 2011. ISSN 0012-821X.

Feng Tian, Kevin France, Jeffrey L Linsky, Pablo JD Mauas, and Mariela C Vieytes. High stellar fuv/nuv ratio and oxygen contents in the atmospheres of potentially habitable planets. *Earth and Planetary Science Letters*, 385:22–27, 2014. ISSN 0012-821X.

Zoe R Todd and Karin I Öberg. Cometary delivery of hydrogen cyanide to the early earth. *Astrobiology*, 20(9):1109–1120, 2020.

Zoe R Todd, Gabriella G Lozano, Corinna L Kufner, Dimitar D Sasselov, and David C Catling. Ferrocyanide survival under near ultraviolet (300–400 nm) irradiation on early earth. *Geochimica et Cosmochimica Acta*, 335:1–10, 2022.

Jonathan D Toner and David C Catling. Alkaline lake settings for concentrated prebiotic cyanide and the origin of life. *Geochimica et Cosmochimica Acta*, 260:124–132, 2019.

Owen B Toon, CP McKay, TP Ackerman, and K Santhanam. Rapid calculation of radiative heating rates and photodissociation rates in inhomogeneous multiple scattering atmospheres. *Journal of Geophysical Research: Atmospheres*, 94(D13):16287–16301, 1989.

Melissa G Trainer, Alexander A Pavlov, H Langley DeWitt, Jose L Jimenez, Christopher P McKay, Owen B Toon, and Margaret A Tolbert. Organic haze on titan and the early earth. *Proceedings of the National Academy of Sciences*, 103(48):18035–18042, 2006.

Benjamin M Tutolo, William E Seyfried, and Nicholas J Tosca. A seawater throttle on h2 production in precambrian serpentinizing systems. *Proceedings of the National Academy of Sciences*, 117(26):14756–14763, 2020. ISSN 0027-8424.

Harold C Urey. On the early chemical history of the earth and the origin of life. *Proceedings of the National Academy of Sciences*, 38(4):351–363, 1952.

John W Valley, Aaron J Cavosie, Takayuki Ushikubo, David A Reinhard, Daniel F Lawrence, David J Larson, Peter H Clifton, Thomas F Kelly, Simon A Wilde, Desmond E Moser, et al. Hadean age for a post-magma-ocean zircon confirmed by atom-probe tomography. *Nature Geoscience*, 7(3):219–223, 2014.

MJ Van Kranendonk, T Djokic, G Poole, S Tadbiri, L Steller, and R Baumgartner. Depositional setting of the fossiliferous, c. 3480 ma dresser formation, pilbara craton: A review. *Earth's Oldest Rocks, 2nd ed.; Van Kranendonk, MJ, Bennett, VC, Hoffmann, JE, Eds*, pages 985–1006, 2018.

IM Vardavas and J˘ H Carver. Solar and terrestrial parameterizations for radiative-convective models. *Planetary and Space Science*, 32(10):1307–1325, 1984.

V Vuitton, RV Yelle, and VG Anicich. The nitrogen chemistry of titan's upper atmosphere revealed. *The Astrophysical Journal*, 647(2):L175, 2006.

Paul J Wallace. Volatiles in subduction zone magmas: concentrations and fluxes based on melt inclusion and volcanic gas data. *Journal of volcanology and Geothermal Research*, 140(1-3):217–240, 2005. ISSN 0377-0273.

Paul J Wallace, Terry Plank, Marie Edmonds, and Erik H Hauri. *Volatiles in magmas*, pages 163–183. Elsevier, 2015.

MR Walter, R Buick, and JSR Dunlop. Stromatolites 3,400–3,500 myr old from the north pole area, western australia. *Nature*, 284:443–445, 1980.

Changle Wang, Maxwell A Lechte, Christopher T Reinhard, Dan Asael, Devon B Cole, Galen P Halverson, Susannah M Porter, Nir Galili, Itay Halevy, Robert H Rainbird, et al. Strong evidence for a weakly oxygenated ocean–atmosphere system during the proterozoic. *Proceedings of the National Academy of Sciences*, 119(6):e2116101119, 2022.

Lewis M Ward, Birger Rasmussen, and Woodward W Fischer. Primary productivity was limited by electron donors prior to the advent of oxygenic photosynthesis. *Journal of Geophysical Research: Biogeosciences*, 124(2):211–226, 2019.

Matthew R Warke, Tommaso Di Rocco, Aubrey L Zerkle, Aivo Lepland, Anthony R Prave, Adam P Martin, Yuichiro Ueno, Daniel J Condon, and Mark W Claire. The great oxidation event preceded a paleoproterozoic "snowball earth". *Proceedings of the National Academy of Sciences*, 117(24):13314–13320, 2020. ISSN 0027-8424.

Diane T Wetzel, Malcolm J Rutherford, Steven D Jacobsen, Erik H Hauri, and Alberto E Saal. Degassing of reduced carbon from planetary basalts. *Proceedings of the National Academy of Sciences*, 110(20):8010–8013, 2013. ISSN 0027-8424.

Frank M White and Joseph Majdalani. *Viscous fluid flow*, volume 3. McGraw-Hill New York, 2006.

Harold B White. Coenzymes as fossils of an earlier metabolic state. *Journal of molecular evolution*, 7:101–104, 1976.

Nicholas Wogan, Joshua Krissansen-Totton, and David C Catling. Abundant atmospheric methane from volcanism on terrestrial planets is unlikely and strengthens the case for methane as a biosignature. *The Planetary Science Journal*, 1(3):58, 2020a.

Nicholas Wogan, Joshua Krissansen-Totton, and David C Catling. Abundant atmospheric methane from volcanism on terrestrial planets is unlikely and strengthens the case for methane as a biosignature. *The Planetary Science Journal*, 1(3):58, 2020b.

Nicholas F Wogan and David C Catling. When is chemical disequilibrium in earth-like planetary atmospheres a biosignature versus an anti-biosignature? disequilibria from dead to living worlds. *The Astrophysical Journal*, 892(2):127, 2020.

Nicholas F Wogan, David C Catling, Kevin J Zahnle, and Mark W Claire. Rapid timescale for an oxic transition during the great oxidation event and the instability of low atmospheric O_2. *Proceedings of the National Academy of Sciences*, 119(37):e2205618119, 2022.

Eric T Wolf, Ravi Kopparapu, Jacob Haqq-Misra, and Thomas J Fauchez. Exocam: A 3D climate model for exoplanet atmospheres. *The Planetary Science Journal*, 3(1):7, 2022.

ET Wolf and OB Toon. Fractal organic hazes provided an ultraviolet shield for early earth. *Science*, 328(5983):1266–1268, 2010.

Joanna M Wolfe and Gregory P Fournier. Horizontal gene transfer constrains the timing of methanogen evolution. *Nature ecology & evolution*, 2(5):897–903, 2018.

Richard Wolfenden. Degrees of difficulty of water-consuming reactions in the absence of enzymes. *Chemical reviews*, 106(8):3379–3396, 2006.

DAVID R Wones and M CHARLES Gilbert. The fayalite-magnetite-quartz assemblage between 600 and 800 c. *American Journal of Science*, 267:480–488, 1969.

Robin Wordsworth and Raymond Pierrehumbert. Abiotic oxygen-dominated atmospheres on terrestrial habitable zone planets. *The Astrophysical Journal Letters*, 785(2):L20, 2014. ISSN 2041-8205.

Robin Wordsworth, Yulia Kalugina, Sergei Lokshtanov, Andrei Vigasin, Bethany Ehlmann,

James Head, Cecilia Sanders, and Huize Wang. Transient reducing greenhouse warming on early mars. *Geophysical Research Letters*, 44(2):665–671, 2017.

Fabian Wunderlich, Markus Scheucher, Mareike Godolt, John Lee Grenfell, Franz Schreier, P Christian Schneider, David J Wilson, Alejandro Sánchez López, Manuel López Puertas, and Heike Rauer. Distinguishing between wet and dry atmospheres of trappist-1 e and f. *arXiv preprint arXiv:2006.11349*, 2020.

Huixiang Xie, Yong Zhang, Karine Lemarchand, and Patrick Poulin. Microbial carbon monoxide uptake in the st. lawrence estuarine system. *Marine Ecology Progress Series*, 389:17–29, 2009.

Mahipal Yadav, Ravi Kumar, and Ramanarayanan Krishnamurthy. Chemistry of abiotic nucleotide synthesis. *Chemical reviews*, 120(11):4766–4805, 2020.

K Zahnle, M Claire, and D Catling. The loss of mass-independent fractionation in sulfur due to a palaeoproterozoic collapse of atmospheric methane. *Geobiology*, 4(4):271–283, 2006.

K Zahnle, Mark S Marley, Caroline V Morley, and Julianne I Moses. Photolytic hazes in the atmosphere of 51 eri b. *The Astrophysical Journal*, 824(2):137, 2016.

Kevin Zahnle, Robert M Haberle, David C Catling, and James F Kasting. Photochemical instability of the ancient martian atmosphere. *Journal of Geophysical Research: Planets*, 113(E11), 2008.

Kevin J Zahnle. Photochemistry of methane and the formation of hydrocyanic acid (hcn) in the earth's early atmosphere. *Journal of Geophysical Research: Atmospheres*, 91(D2): 2819–2834, 1986.

Kevin J Zahnle and Mark S Marley. Methane, carbon monoxide, and ammonia in brown dwarfs and self-luminous giant planets. *The Astrophysical Journal*, 797(1):41, 2014. ISSN 0004-637X.

Kevin J Zahnle, Marko Gacesa, and David C Catling. Strange messenger: A new history of hydrogen on earth, as told by xenon. *Geochimica et Cosmochimica Acta*, 244:56–85, 2019.

Kevin J Zahnle, Roxana Lupu, David C Catling, and Nick Wogan. Creation and evolution of impact-generated reduced atmospheres of early earth. *The Planetary Science Journal*, 1(1):11, 2020. ISSN 2632-3338.

Nicolle EB Zellner. Cataclysm no more: new views on the timing and delivery of lunar impactors. *Origins of Life and Evolution of Biospheres*, 47:261–280, 2017.

Shuichang Zhang, Xiaomei Wang, Emma U Hammarlund, Huajian Wang, M Mafalda Costa, Christian J Bjerrum, James N Connelly, Baomin Zhang, Lizeng Bian, and Donald E Canfield. Orbital forcing of climate 1.4 billion years ago. *Proceedings of the National Academy of Sciences*, 112(12):E1406–E1413, 2015.

Mingyu Zhao, Christopher T Reinhard, and Noah Planavsky. Terrestrial methane fluxes and proterozoic climate. *Geology*, 46(2):139–142, 2018. ISSN 0091-7613.

Appendix A

PHOTOCHEMICAL MODELING EQUATIONS

Most work in this thesis leverages 1-D photochemical models to help understand the composition of the early Earth atmosphere. Several chapters contain brief descriptions of the equations governing photochemical models (e.g., Sections 4.2 and 5.6.3), but no description is complete and not all assumptions are explicit. The purpose of this Appendix is to provide a full derivation of the governing equations, from a simple statement of the conservation of mass all the way to a finite volume discretization that can be implemented in a computer program.

A.1 The Photochemical Equation

We begin our derivation of the governing photochemical equations with a statement of the the conservation of molecules. Such statements of conservation are often called *continuity equations*.

$$\frac{\partial n_i}{\partial t} + \boldsymbol{\nabla} \cdot \boldsymbol{\Phi_i} = \sigma_i \tag{A.1}$$

Here, n_i is the number density of molecule i in molecules cm^{-3}, t is time in seconds, $\boldsymbol{\nabla}$ is the gradient operator ($\boldsymbol{\nabla} \equiv [\frac{\partial}{\partial x}, \frac{\partial}{\partial y}, \frac{\partial}{\partial z}]$), $\boldsymbol{\Phi_i}$ is a vector of the flux of n_i in molecules cm^{-2} s^{-1} ($\boldsymbol{\Phi_i} = [\Phi_{i,x}, \Phi_{i,y}, \Phi_{i,z}]$), and σ_i is the source or sink of molecule i in molecules cm^{-3} s^{-1}. Table A.1 describes all other variables. Equation (A.1) states that a molecule's concentration changes over time at a point in space because of the molecules entering or leaving the space (i.e. $\boldsymbol{\nabla} \cdot \boldsymbol{\Phi_i}$), and the production or destruction of molecules (i.e. σ_i).

A one-dimensional atmospheric model assumes that species concentrations only changes in the vertical z direction, and is homogeneous in the horizontal directions ($n_i(x, y, z, t) = n_i(z, t)$). Therefore,

$$\boldsymbol{\nabla} \cdot \boldsymbol{\Phi_i} = \frac{\partial \Phi_{i,z}}{\partial z} \tag{A.2}$$

From here, onward, we will drop the z subscript to reduce clutter ($\Phi_{i,z} = \Phi_i$). The flux of gases ($\Phi_{i,\text{gas}}$) is determined by eddy and molecular diffusion, and the flux of particles

($\Phi_{i,\text{particle}}$) is given by eddy diffusion and the rate particles fall through the atmosphere.

$$\Phi_{i,\text{gas}} = \Phi_{i,\text{eddy}} + \Phi_{i,\text{molecular}} \tag{A.3}$$

$$\Phi_{i,\text{particle}} = \Phi_{i,\text{eddy}} + \Phi_{i,\text{fall}} \tag{A.4}$$

Here, $\Phi_{i,\text{eddy}}$, $\Phi_{i,\text{molecular}}$ and $\Phi_{i,\text{fall}}$ are approximated by

$$\Phi_{i,\text{eddy}} = -Kn\frac{\partial}{\partial z}\left(\frac{n_i}{n}\right) \tag{A.5}$$

$$\Phi_{i,\text{molecular}} = -n_i D_i \left(\frac{n}{n_i}\frac{\partial}{\partial z}\left(\frac{n_i}{n}\right) - \frac{1}{H_a} + \frac{1}{H_i} + \frac{\alpha_{Ti}}{T}\frac{\partial T}{\partial z}\right) \tag{A.6}$$

$$\Phi_{i,\text{fall}} = -w_i n_i \tag{A.7}$$

We derive Equation (A.6) in Section A.6 starting with the general binary diffusion equation. Equation (A.6) assumes the atmosphere is an ideal gas at hydrostatic equilibrium, and that the diffusing gas is a minor atmospheric constituent. In Equation (A.7), w_i is the fall velocity of a particle, which can be estimated with Stokes' law (Section A.7).

We assume that the sources and sinks of molecule or particle i are chemical reactions, rainout in droplets of liquid, the effects of lightning, and condensation or evaporation:

$$\sigma_i = P_i - L_i - R_{i,\text{ rainout}} + Q_{i,\text{ lightning}} + C_{i,\text{ cond}} \tag{A.8}$$

Here, P_i is chemical production and L_i is chemical loss. Substituting Equations (A.2) and (A.8) into Equation (A.1) gives a simplified continuity equation:

$$\frac{\partial n_i}{\partial t} = -\frac{\partial}{\partial z}\Phi_i + P_i - L_i - R_{i,\text{ rainout}} + Q_{i,\text{ lightning}} + C_{i,\text{ cond}} \tag{A.9}$$

The 1-D continuity equation (Equation (A.9)) and corresponding fluxes (Equations (A.3) - (A.7)) are a system of partial differential equations (PDEs) describing how the number

density (n_i) of each chemical species i changes of altitude and time. This system assumes the atmosphere is one-dimensional, and uses an approximation of molecular diffusion (Equation (A.6)).

A.2 The assumption of time-constant total number density

Most photochemical models solve a simplified version of Equation (A.9) which assumes that the total number density does not change over time ($\partial n/\partial t \approx 0$). This approach is perfectly valid for steady-state photochemical calculations, and is also reasonable for atmospheric transitions which maintain approximately constant surface pressure and atmospheric temperature. However, $\partial n/\partial t \neq 0$ when an evolution involves large changes in atmospheric mass and temperature such as, for example, the evolution of the atmosphere during a runaway greenhouse.

Models that take $\partial n/\partial t \approx 0$, assume a time-constant temperature prescribed through the whole atmospheric column. The surface pressure is also a free parameter, and pressures above the surface are computed using the hydrostatic equation. The time-constant total number density throughout the atmosphere is determined by the ideal gas law ($n = \frac{P}{kT}$).

In order to guarantee that all mixing ratios in the atmosphere sum to 1 (or equivalently $\sum_i n_i = n$), models prescribe a background filler gas with a mixing ratio $f_{\text{background}} = 1 - \sum_i f_i$. N_2, CO_2 or H_2 are common choices for the background gas, depending on the atmosphere under investigation. By definition, the background gas is not conserved.

The constant number density assumption is not necessary. In Chapter 5, I built a photochemical model that directly solves Equation (A.9), and assumes no background filler gas. This was useful in Chapter 5 because I was evolving atmospheres that changed from being H_2-dominated to N_2-dominated. Section 5.6.3 briefly derives the fundamental model equations for directly solving Equation (A.9). The rest of this appendix considers a model assuming time-constant number density, because this is a more common method to simulate 1-D photochemistry.

Below, we rework Equation (A.9) with the assumption of constant number density. This

process involves considering the evolution of mixing ratios (f_i) instead of number densities (n_i). The ideal gas law and Dalton's law gives a relation between f_i and n_i (Chapter 1 in Catling and Kasting (2017)):

$$n_i = f_i n \tag{A.10}$$

Differentiating Equation (A.10) with respect to time yields

$$\frac{\partial n_i}{\partial t} = f_i \frac{\partial n}{\partial t} + n \frac{\partial f_i}{\partial t} \tag{A.11}$$

Applying the assumption of constant number density ($\partial n / \partial t = 0$) gives

$$\frac{\partial n_i}{\partial t} = n \frac{\partial f_i}{\partial t} \tag{A.12}$$

We can substitute Equation (A.12) into (A.9) and rearrange to produce a simplified version of the continuity equation,

$$\frac{\partial f_i}{\partial t} = -\frac{1}{n}\frac{\partial}{\partial z}\Phi_i + \frac{P_i}{n} - \frac{L_i}{n} - \frac{R_{i,\text{ rainout}}}{n} + \frac{Q_{i,\text{ lightning}}}{n} + \frac{C_{i,\text{ cond}}}{n} \tag{A.13}$$

We can re-write $\Phi_{i,\text{gas}}$ and $\Phi_{i,\text{particle}}$ (Equation (A.3) and Equation (A.4)) in terms of mixing ratios instead of number densities using Equation (A.10). After substitution, and rearrangement we are left with

$$\Phi_{i,\text{gas}} = -\left(K + D_i\right) n \frac{\partial f_i}{\partial z} - \gamma_i n f_i \tag{A.14}$$

Where γ_i is given by

$$\gamma_i = D_i \left(\frac{1}{H_i} - \frac{1}{H_a} + \frac{\alpha_{\text{Ti}}}{T}\frac{\partial T}{\partial z} \right) \tag{A.15}$$

The flux of particles in terms of mixing ratios is

$$\Phi_{i,\text{particle}} = -Kn\frac{\partial f_i}{\partial z} - w_i n f_i \tag{A.16}$$

Equations (A.13), (A.14) and (A.16) are a new, simplified version of the continuity equation, describing how the volume mixing ratio of gases and particles evolve over time and altitude. These equations have the following assumptions

- The atmosphere is one-dimensional
- The ideal gas law.
- Hydrostatic equilibrium
- Time-constant total number density ($\partial n/\partial t \approx 0$) and time-constant temperature and pressure.
- A background filler gas (e.g. N_2 for modern Earth)
- The molecular diffusion terms in Equation (A.14) assumes the atmosphere is in hydrostatic equilibrium and that gas i is a minor constituent diffusing through a more abundant background.

The assumption of constant number density made above has at least one very important consequence: certain boundary conditions, diffusion coefficients, and source terms (e.g. chemistry) can violate the constant number density assumption by an amount that causes Equation (A.13) to yield nonphysical mixing ratios.

One example is an atmosphere with an extremely large surface flux of a gas into a thin atmosphere. In this case, in reality, the atmosphere would grow in mass and become thicker. But, Equation (A.13) does not allow the atmosphere to become thicker. Instead, the mixing ratio of the gas being fluxed into the atmosphere might increase to a value larger than 1, which is not a sensible value for a mixing ratio.

Chemical reactions can also cause nonphysical mixing ratios when using Equation (A.13). Suppose an atmosphere contains 0.6 mixing ratio H_2 with and N_2 background. Also, suppose that the atmosphere is very hot so that the disproportionation reaction, $H_2 \rightarrow H+H$, proceeds rapidly and to near completion. Assuming Equation (A.13), the resulting evolution would produce a H mixing ratio of 1.2, which again, is an invalid mixing ratio.

A.3 Finite volume discretization of the model equations

We use the finite volume method to discretize Equation (A.13) allowing an approximate numerical solution. The finite volume method divides the spatial domain (z) into grid cells, or finite volumes, in order to approximate the cell-averaged value of the mixing ratio of a species, f_i. Approximations to the cell-averaged value of f_i are modified over time by considering the flux of molecules through the edges of the cells, and the sources and sinks of molecules within the cell. The main advantage of this approach is that the approximation conserves molecules, which is not always the case for other PDE discretization methods. Molecule conservation is valuable for understanding whether a model run has reached steady-state, or interrogating the redox fluxes into and out of an atmosphere. Below, we describe the application of the finite-volume method to Equation (A.13). For an in-depth understanding of the finite-volume method, see LeVeque et al. (2002).

Consider an atmosphere that has been vertically divided into m grid-cell (i.e. finite volumes) of thickness Δz^j. The superscript j refers to a grid cell (j does not refer to a power), where $j = l$ is the lowest altitude grid-cell $j = m$ highest grid-cell. z^j is the altitude at the center of grid-cell j, such that the upper and lower edges of the cell are given by $z^{j+1/2} = z^j + \frac{\Delta z^j}{2}$ and $z^{j-1/2} = z^j - \frac{\Delta z^j}{2}$, respectfully.

Consider a single grid cell between altitudes $z = z^{j-1/2}$ and $z = z^{j+1/2}$. First, we can re-arrange Equation (A.13) to produce the following

$$\frac{\partial n_i}{\partial t} = -\frac{\partial \Phi_i}{\partial z} + \sigma_i \tag{A.17}$$

Integrating Equation (A.17) from the bottom to the top of the grid cell gives

$$\frac{\partial}{\partial t}\int_{z^{j-1/2}}^{z^{j+1/2}} n_i dz = -(\Phi_i(z^{j+1/2}) - \Phi_i(z^{j-1/2})) + \int_{z^{j-1/2}}^{z^{j+1/2}} \sigma_i dz \tag{A.18}$$

The average value of n_i and σ_i between $z^{j-1/2}$ and $z^{j+1/2}$ are given by the integrals

$$\overline{n_i}^j = \frac{1}{\Delta z^j}\int_{z^{j-1/2}}^{z^{j+1/2}} n_i dz \tag{A.19}$$

$$\overline{\sigma_i}^j = \frac{1}{\Delta z^j}\int_{z^{j-1/2}}^{z^{j+1/2}} \sigma_i dz \tag{A.20}$$

Substituting the above expressions into Equation (A.18) yields

$$\frac{\partial}{\partial t}\overline{n_i}^j(t) = -\frac{\Phi_i(z^{j+1/2},t) - \Phi_i(z^{j-1/2},t)}{\Delta z^j} + \overline{\sigma_i}^j(t) \tag{A.21}$$

Equation (A.21) states that the average number density of species i in the j atmospheric layer ($\overline{n_i}^j$) changes over time because of the fluxes at the edges of the layer (e.g. $\Phi_i(z^{j+1/2},t)$), and the average production or loss of the species in the layer ($\overline{\sigma_i}^j$). The above formula is exact for $\overline{n_i}^j(t)$. However, we now make the following assumptions:

1. $\overline{n_i}^j(t)$, $\overline{\sigma_i}^j(t)$, $\Phi_i(z^{j+1/2},t)$, $\Phi_i(z^{j-1/2},t)$ are constant over small segments of time, Δt.
2. $\overline{n_i}^j \approx \overline{f_i}^j \overline{n}^j$
3. We can approximate $\Phi_i(z^{j+1/2},t)$, $\Phi_i(z^{j-1/2},t)$, and $\overline{\sigma_i}^j(t)$ in terms of cell-averaged quantities, such as $\overline{f_i}^j$ and $\overline{f_i}^{j+1}$

We denote the approximate quantities in the following way

$$f_i^j \approx \overline{f_i}^j \qquad \Phi_i^{j+1/2} \approx \Phi_i(z^{j+1/2},t)$$

$$n^j \approx \overline{n}^j \qquad \Phi_i^{j-1/2} \approx \Phi_i(z^{j-1/2},t)$$

$$\sigma_i^j \approx \overline{\sigma_i}^j(t)$$

Re-writing Equation (A.21), substituting in the approximate quantities gives

$$\frac{\partial f_i^j}{\partial t} = -\frac{1}{n^j}\frac{\Phi_i^{j+1/2} - \Phi_i^{j-1/2}}{\Delta z^j} + \frac{\sigma_i^j}{n^j} \tag{A.22}$$

We now must derive expressions for the gas and particle fluxes at grid-cell edges that are accurate and stable for our problem.

A.3.1 Gases

In the equation for gas flux (Equation (A.14)), the first term is diffusive and the second term is advective. For most all plausible diffusion coefficients and advection velocities the diffusion term dominates, therefore, it is suitable to use a centered finite volume scheme (Equation 4.10 in LeVeque et al. (2002)):

$$\Phi_{i,\mathrm{gas}}^{j+1/2} = -(K + D_i)^{j+1/2} n^{j+1/2} \left(\frac{\partial f_i}{\partial z}\right)^{j+1/2} - (\gamma_i n)^{j+1/2} f_i^{j+1/2} \tag{A.23}$$

A centered finite volume approximation gives

$$\left(\frac{\partial f_i}{\partial z}\right)^{j+1/2} \approx \frac{f_i^{j+1} - f_i^j}{\Delta z^{j+1/2}}$$

Where $\Delta z^{j+1/2} = \frac{1}{2}\Delta z^j + \frac{1}{2}\Delta z^{j+1}$. Also, $f_i^{j+1/2}$ can be estimated by linearly interpolating between the two adjacent cells.

$$f_i^{j+1/2} \approx \frac{\Delta z^j f_i^{j+1} + \Delta z^{j+1} f_i^j}{\Delta z^{j+1} + \Delta z^j}$$

Therefore,

$$\Phi_{i,\mathrm{gas}}^{j+1/2} = -(K + D_i)^{j+1/2} n^{j+1/2} \frac{f_i^{j+1} - f_i^j}{\Delta z^{j+1/2}} - (\gamma_i n)^{j+1/2} \frac{\Delta z^j f_i^{j+1} + \Delta z^{j+1} f_i^j}{\Delta z^{j+1} + \Delta z^j} \tag{A.24}$$

Using an similar procedure, $\Phi_{i,\mathrm{gas}}^{j-1/2}$ is given by

$$\Phi_{i,\text{gas}}^{j-1/2} = -(K + D_i)^{j-1/2} n^{j-1/2} \frac{f_i^j - f_i^{j-1}}{\Delta z^{j-1/2}} - (\gamma_i n)^{j-1/2} \frac{\Delta z^{j-1} f_i^j + \Delta z^j f_i^{j-1}}{\Delta z^j + \Delta z^{j-1}} \tag{A.25}$$

Substituting Equations (A.24) and (A.25) into Equation (A.22) and re-arranging gives an equation of the form

$$\begin{aligned} \frac{\partial f_i^j}{\partial t} &= (A_i^{j,\text{upper}} + B_i^{j,\text{upper}}) f_i^{j+1} \\ &+ (A_i^{j,\text{center}} + B_i^{j,\text{center}}) f_i^j \\ &+ (A_i^{j,\text{lower}} + B_i^{j,\text{lower}}) f_i^{j-1} \\ &+ \frac{\sigma_i^j}{n^j} \end{aligned} \tag{A.26}$$

The A coefficients for gases correspond to the diffusive approximations to the cell-edge fluxes:

$$\begin{aligned} A_{i,\text{gas}}^{j,\text{upper}} &= A_{i,\text{gas}}^{j,1} \\ A_{i,\text{gas}}^{j,\text{center}} &= -A_{i,\text{gas}}^{j,1} - A_{i,\text{gas}}^{j,2} \\ A_{i,\text{gas}}^{j,\text{lower}} &= A_{i,\text{gas}}^{j,2} \end{aligned} \qquad \begin{aligned} A_{i,\text{gas}}^{j,1} &= \frac{(K + D_i)^{j+1/2} n^{j+1/2}}{n^j \Delta z^j \Delta z^{j+1/2}} \\ A_{i,\text{gas}}^{j,2} &= \frac{(K + D_i)^{j-1/2} n^{j-1/2}}{n^j \Delta z^j \Delta z^{j-1/2}} \end{aligned}$$

The B coefficients for gases correspond to the advection approximations to the cell-edge fluxes:

$$\begin{aligned} B_{i,\text{gas}}^{j,\text{upper}} &= B_{i,\text{gas}}^{j,1} \\ B_{i,\text{gas}}^{j,\text{center}} &= B_{i,\text{gas}}^{j,2} + B_{i,\text{gas}}^{j,3} \\ B_{i,\text{gas}}^{j,\text{lower}} &= B_{i,\text{gas}}^{j,4} \end{aligned} \qquad \begin{aligned} B_{i,\text{gas}}^{j,1} &= \frac{(\gamma_i n)^{j+1/2}}{n^j \Delta z^j} \frac{\Delta z^j}{\Delta z^{j+1} + \Delta z^j} \\ B_{i,\text{gas}}^{j,2} &= \frac{(\gamma_i n)^{j+1/2}}{n^j \Delta z^j} \frac{\Delta z^{j+1}}{\Delta z^{j+1} + \Delta z^j} \\ B_{i,\text{gas}}^{j,3} &= -\frac{(\gamma_i n)^{j-1/2}}{n^j \Delta z^j} \frac{\Delta z^{j-1}}{\Delta z^j + \Delta z^{j-1}} \\ B_{i,\text{gas}}^{j,4} &= -\frac{(\gamma_i n)^{j-1/2}}{n^j \Delta z^j} \frac{\Delta z^j}{\Delta z^j + \Delta z^{j-1}} \end{aligned}$$

The lower boundary condition is the flux through the lower edge of the lowest-altitude cell,

$\Phi_i^{l-1/2} = \Phi_i^{\text{lower}}$. Similarly, the upper boundary condition is the flux through through the top edge of the highest-altitude cell, $\Phi_i^{m+1/2} = \Phi_i^{\text{upper}}$. It follows from Equation (A.22) that

$$\frac{\partial f_i^l}{\partial t} = -\frac{1}{n^l}\frac{\Phi_i^{\text{l}+1/2} - \Phi_i^{\text{lower}}}{\Delta z^l} + \frac{\sigma_i^l}{n^l} \tag{A.27}$$

$$\frac{\partial f_i^m}{\partial t} = -\frac{1}{n^m}\frac{\Phi_i^{\text{upper}} - \Phi_i^{m-1/2}}{\Delta z^m} + \frac{\sigma_i^m}{n^m} \tag{A.28}$$

Plugging in Equation (A.24) and (A.25) into Equation (A.27) and (A.28) gives the following general expression for the rate mixing ratios change at the boundaries

$$\begin{aligned}
\frac{\partial f_i^l}{\partial t} &= (A_i^{l,\text{upper}} + B_i^{l,\text{upper}}) f_i^{l+1} \\
&+ (A_i^{l,\text{center}} + B_i^{l,\text{center}}) f_i^l \\
&+ \frac{\Phi_i^{\text{lower}}}{n^l \Delta z^l} \\
&+ \frac{\sigma_i^l}{n^l}
\end{aligned}
\qquad
\begin{aligned}
\frac{\partial f_i^m}{\partial t} &= (A_i^{m,\text{center}} + B_i^{m,\text{center}}) f_i^m \\
&+ (A_i^{m,\text{lower}} + B_i^{m,\text{lower}}) f_i^{m-1} \\
&- \frac{\Phi_i^{\text{upper}}}{n^m \Delta z^m} \\
&+ \frac{\sigma_i^m}{n^m}
\end{aligned}
\tag{A.29}$$

For gases, the A and B coefficients for the lower boundary are

$$A_{i,\text{gas}}^{l,\text{upper}} = A_{i,\text{gas}}^{l,1} \qquad B_{i,\text{gas}}^{l,\text{upper}} = B_{i,\text{gas}}^{l,1}$$

$$A_{i,\text{gas}}^{l,\text{center}} = -A_{i,\text{gas}}^{l,1} \qquad B_{i,\text{gas}}^{j,\text{center}} = B_{i,\text{gas}}^{l,2}$$

and the upper boundary,

$$A_{i,\text{gas}}^{m,\text{center}} = -A_{i,\text{gas}}^{m,2} \qquad B_{i,\text{gas}}^{m,\text{center}} = B_{i,\text{gas}}^{m,3}$$

$$A_{i,\text{gas}}^{m,\text{lower}} = A_{i,\text{gas}}^{m,2} \qquad B_{i,\text{gas}}^{m,\text{lower}} = B_{i,\text{gas}}^{m,4}$$

A.3.2 Particles

The equation for particle flux (Equation (A.14)), contains an advection term representing the falling of particles. This advection can be much stronger than the eddy diffusion term, especially high in the atmosphere. Therefore, for stability, we use a first-order upwind scheme

for particle advection and a centered scheme for diffusion. A centered approximation is not stable for advection-dominated transport (Chapter 4 in LeVeque et al. (2002)). We can split the particle flux (Equation (A.16)) into diffusive and advection components,

$$\begin{aligned}\Phi_{i,\text{particle}} &= \Phi_{i,\text{diff}} + \Phi_{i,\text{advec}} \\ \Phi_{i,\text{diff}} &= -Kn\frac{\partial f_i}{\partial z} \\ \Phi_{i,\text{advec}} &= -w_i n f_i\end{aligned}$$

Therefore, we can write Equation (A.22) as

$$\frac{\partial f^j_{i\in\text{particle}}}{\partial t} = -\frac{1}{n^j}\frac{\Phi^{j+1/2}_{i,\text{diff}} - \Phi^{j-1/2}_{i,\text{diff}}}{\Delta z^j} - \frac{1}{n^j}\frac{\Phi^{j+1/2}_{i,\text{advec}} - \Phi^{j-1/2}_{i,\text{advec}}}{\Delta z^j} + \frac{\sigma^j_i}{n^j} \tag{A.30}$$

Applying a centered scheme to the diffusive fluxes follows the procedure shown in Section A.3.1. To apply a first-order upwind scheme, we first recognize that if particle are falling, then information is traveling from up to down in the model. Therefore, an upwind scheme approximates advective fluxes with a forward difference

$$\frac{\Phi^{j+1/2}_{i,\text{advec}} - \Phi^{j-1/2}_{i,\text{advec}}}{\Delta z^j} \approx \frac{\Phi^{j+1}_{i,\text{advec}} - \Phi^{j}_{i,\text{advec}}}{\Delta z^j} = \frac{(-w_i n f_i)^{j+1} - (-w_i n f_i)^{j}}{\Delta z^j} \tag{A.31}$$

Applying a centered scheme to diffusion and an upwind scheme to advection, and rearranging, gives the A and B coefficients for Equation (A.26) for particles:

$$\begin{aligned}A^{j,\text{upper}}_{i,\text{particle}} &= A^{j,1}_{i,\text{particle}} \\ A^{j,\text{center}}_{i,\text{particle}} &= -A^{j,1}_{i,\text{particle}} - A^{j,2}_{i,\text{particle}} \\ A^{j,\text{lower}}_{i,\text{particle}} &= A^{j,2}_{i,\text{particle}}\end{aligned} \qquad \begin{aligned}A^{j,1}_{i,\text{particle}} &= \frac{K^{j+1/2}n^{j+1/2}}{n^j\Delta z^j\Delta z^{j+1/2}} \\ A^{j,2}_{i,\text{particle}} &= \frac{K^{j-1/2}n^{j-1/2}}{n^j\Delta z^j\Delta z^{j-1/2}}\end{aligned}$$

$$B^{j,\text{upper}}_{i,\text{particle}} = B^{j,1}_{i,\text{particle}} \qquad B^{j,1}_{i,\text{particle}} = \frac{w^{j+1}n^{j+1}}{n^j \Delta z^j}$$
$$B^{j,\text{center}}_{i,\text{particle}} = B^{j,2}_{i,\text{particle}} \qquad B^{j,2}_{i,\text{particle}} = -\frac{w^j}{\Delta z^j}$$
$$B^{j,\text{lower}}_{i,\text{particle}} = 0$$

Following the same procedure as we did in Section A.3.1, we can write the A and B coefficients for Equation (A.29) for particles at the lower boundary:

$$A^{l,\text{upper}}_{i,\text{particle}} = A^{l,1}_{i,\text{particle}} \qquad B^{l,\text{upper}}_{i,\text{particle}} = B^{l,1}_{i,\text{particle}}$$
$$A^{l,\text{center}}_{i,\text{particle}} = -A^{l,1}_{i,\text{particle}} \qquad B^{l,\text{center}}_{i,\text{particle}} = 0$$

and the upper boundary,

$$A^{m,\text{center}}_{i,\text{particle}} = -A^{m,2}_{i,\text{particle}} \qquad B^{m,\text{center}}_{i,\text{particle}} = B^{m,2}_{i,\text{particle}}$$
$$A^{m,\text{lower}}_{i,\text{particle}} = A^{m,2}_{i,\text{particle}} \qquad B^{m,\text{lower}}_{i,\text{particle}} = 0$$

A.3.3 Summary

Equations (A.26) and (A.29) are a system of ordinary differential equations (ODEs) which are a finite volume approximation of our original system of PDEs (Equation (A.13)). The number of ODEs is the number evolving species (gases + particles) multiplied by the number of atmospheric grid-cells. For example, with 100 species and 200 vertical layers then there are 20,000 ODEs.

A.4 Source terms

Recall the source term, σ^j_i, which is a combination of chemical reactions, rainout in droplets of liquid, the impact of lightning, condensation, and other similar processes. This appendix does not contain a complete explanation for how to model these effects. Instead, for a description of how to model chemical reactions see Sections 3.1.2 in Catling and Kasting (2017). Also, Appendix B.8 in Catling and Kasting (2017) describes how to account for photolysis, rainout and lightning.

A.5 Solving the system of ordinary differential equations

Given initial conditions, boundary conditions, a description of the source terms (e.g. chemical reactions), and values for various free parameters (e.g. K), we can evolve Equations (A.26) and (A.29) forward in time using an ordinary differential equation solver. However, chemical kinetics ODEs are extremely stiff, meaning that some dependent variables (i.e. mixing ratios) change much more quickly than others. Stiff equations require highly stable, implicit integration methods. For a complete description of stiff equations and implicit integration methods see Hairer and Wanner (1996).

We argue that it is best to use an implicit ODE integration method developed by an expert, rather than a home-brewed algorithm. Applied mathematicians have spent their whole careers thinking hard about how to create the most stable and accurate integrators. One good option for chemical kinetics problems is the CVODE BDF method (BDF stands for backward differential formula) which has been optimized by experts at Laurence Livermore National Laboratory for decades (Hindmarsh et al., 2005).

Using an existing implicit integration method like CVODE BDF for photochemical calculations requires the user code a function for Equations (A.26) and (A.29). Furthermore, implicit integrators also require a function for the Jacobian of Equations (A.26) and (A.29). For details on how to form a Jacobian from Equations (A.26) and (A.29) see Appendix B.3 in Catling and Kasting (2017).

A.6 Molecular Diffusion

The general molecular diffusion equation giving the relative diffusion velocity of gas i with respect to gas j in one dimension is (Equation 15.1 in Banks and Kockarts (2013), or Equation 14.1, 1 in Chapman and Cowling (1990))

$$v_i - v_j = -D_{ij}\left(\frac{n^2}{n_i n_j}\frac{\partial}{\partial z}\left(\frac{n_i}{n}\right) + \frac{\mu_j - \mu_i}{\overline{\mu}}\frac{1}{P}\frac{\partial P}{\partial z} + \frac{\alpha_{Ti}}{T}\frac{\partial T}{\partial z} - \frac{\mu_i \mu_j}{\overline{\mu} N_a k T}(a_i - a_j)\right) \tag{A.32}$$

Here, a_1 and a_2 are external accelerations of each molecule from, for example, a magnetic or electric field if the molecule is an ion. We assume neutral molecules such that $a_i = a_j = 0$. We also assume that the atmosphere is an ideal gas and is in hydrostatic equilibrium:

$$\frac{\partial P}{\partial z} = -g\rho = \frac{-gP\overline{\mu}}{N_a kT} \tag{A.33}$$

$$\frac{1}{P}\frac{\partial P}{\partial z} = \frac{-g\overline{\mu}}{N_a kT} = \frac{-1}{H_a} \tag{A.34}$$

Substitution of $a_i = a_j = 0$ and Equation (A.34) into Equation (A.32) gives

$$v_i - v_j = -D_{ij}\left(\frac{n^2}{n_i n_j}\frac{\partial}{\partial z}\left(\frac{n_i}{n}\right) - \frac{\mu_j - \mu_i}{\overline{\mu}}\frac{1}{H_a} + \frac{\alpha_{Ti}}{T}\frac{\partial T}{\partial z}\right) \tag{A.35}$$

We make the further approximation that gas i is small abundance compared to gas j which we take to be a stationary background gas ($v_j = 0$, $n_j = n$, $\mu_j = \overline{\mu}$). This gives the flux of molecular diffusion used in our photochemical model

$$\Phi_i^{\text{molecular}} = n_i v_i = -n_i D_i\left(\frac{n}{n_i}\frac{\partial}{\partial z}\left(\frac{n_i}{n}\right) - \frac{1}{H_a} + \frac{1}{H_i} + \frac{\alpha_{Ti}}{T}\frac{\partial T}{\partial z}\right) \tag{A.36}$$

Also, we estimate the molecular diffusion coefficient with the formula (Equation 15.29 in Banks and Kockarts (2013))

$$D_i = \frac{b_i}{n} = \frac{1.52 \times 10^{18}}{n}\sqrt{\left(\frac{1}{\mu_i} + \frac{1}{\overline{\mu}}\right)T} \tag{A.37}$$

Note, this equation is also in Catling and Kasting (2017) (Equation B.4), but it contains a typo, omitting a power of 0.5 for the $\left(\frac{1}{\mu_i} + \frac{1}{\overline{\mu}}\right)$ term.

A.7 Particle Fall Velocity

The particle fall velocity (w_i) is given by stokes law with a slip correction factor ($C_{c,i}$) (Equation 9.42 in Seinfeld et al. (2006)).

$$w_i = \frac{2}{9}\frac{(\rho_i - \rho)r_i^2}{\eta}C_{c,i} \tag{A.38}$$

We approximate the dynamic viscosity of air (η) with the following empirical relation from Equation 1-36 and Table 1-2 in White and Majdalani (2006). This expression is for modern Earth air.

$$\eta = 1.716 \times 10^{-4}\left(\frac{T}{273}\right)^{3/2}\left(\frac{384}{T+111}\right) \tag{A.39}$$

The slip correction factor ($C_{c,i}$), is given by Equation 9.34 in Seinfeld et al. (2006).

$$C_{c,i} = 1 + \frac{\lambda}{r_i}\left(-1.257 + 0.4\exp\left(\frac{1.1r_i}{\lambda}\right)\right) \tag{A.40}$$

Here, λ is the mean free path, which comes from the kinetic theory of gases (Equation 9.6 in Seinfeld et al. (2006))

$$\lambda = \frac{2\eta}{n}\sqrt{\frac{\pi N_a}{8kT\overline{\mu}}} \tag{A.41}$$

Table A.1: Variables for this Appendix

Variable	Definition	Units
f_i	Mixing ratio of species i	dimensionless
n_i	Number density of species i	molecules cm^{-3}
z	Altitude	cm
t	Time	seconds
n	Total number density	molecules cm^{-3}
P_i	Total chemical production of species i	molecules cm^{-3} s^{-1}
L_i	Total chemical loss of species i	molecules cm^{-3} s^{-1}
$R_{\text{i, rainout}}$	Production and loss of species i from rainout	molecules cm^{-3} s^{-1}
$Q_{\text{i, lightning}}$	Production and loss of species i from lightning	molecules cm^{-3} s^{-1}
Φ_i	Vertical flux of species i	molecules cm^{-2} s^{-1}
K	Eddy diffusion coefficient	cm^2 s^{-1}
D_i	Molecular diffusion coefficient	cm^2 s^{-1}
H_i	$= N_a kT/\mu_i g$, The scale heights of species i	cm
H_a	$= N_a kT/\overline{\mu} g$, The average scale height.	cm
N_a	Avogadro's number	molecules mol^{-1}
k	Boltzmann's constant	erg K^{-1}
μ	Molar mass. $\overline{\mu}$ is mean molar mass of the atmosphere, and μ_i is the molar mass of species i	g mol^{-1}
g	Gravitational acceleration	cm s^{-2}
α_{Ti}	Thermal diffusion coefficient of species i. We neglect this term ($\alpha_{\text{Ti}} = 0$)	dimensionless
T	Temperature	K
w_i	Fall velocity of a particle	cm s^{-1}
η	Dynamic viscosity of air. Equation (A.39).	dynes s cm^{-2}

Appendix B

CURRICULUM VITAE

Nicholas Wogan

Department of Earth and Space Science/Astrobiology Program

University of Washington, Seattle, WA

Email: wogan@uw.edu

Website: `https://nicholaswogan.github.io/`

GitHub: `https://github.com/Nicholaswogan`

Date generated: August 25, 2023

Education

2017 - Present Ph.D Graduate Student, Dual-title Earth and Space Science and Astrobiology, University of Washington, Seattle, WA.

2012 - 2016 B.S., Physics major, University of Oregon Honors College.

Professional Experience

2017 - Present Research Assistant, Planetary Science and Astrobiology, University of Washington, Seattle, WA. Advisor: David Catling.

2016 - 2017 Research Assistant, Geophysics, University of Oregon, Eugene, OR. Supervisor: Eugene Humphreys.

2014 - 2015 Undergraduate Research Assistant, Geophysics, University of Oregon, Eugene, OR. Supervisor: Dean Livelybrooks.

2014 Undergraduate Teaching Assistant, Introductory Physics, University of Oregon, Eugene, OR. Supervisor: Ben McMorran.

Awards and Honors

2023 The David A. Johnston Award for Research Excellence, Earth and Space Science Department, University of Washington.

2023 NASA Postdoctoral Program fellowship recipient

2023 Award for best graphic in presentation, Earth and Space Science Gala, University of Washington.

2017 Top Scholar Award, Earth and Space Science Department, University of Washington.

2016 Undergraduate Research Award, Physics department, University of Oregon.

2016 Undergraduate Honors Thesis: Passed with Distinction, University of Oregon Honors college.

2012 Presidential Scholarship Recipient, University of Oregon.

Teaching Experience

2019 Teaching Assistant: Intro. Astrobiology (ASTBIO 115; Winter), University of Washington.

2018 Teaching Assistant: Intro. Geology (ESS 101; Winter), University of Washington.

2014 Undergraduate Teaching Assistant: Intro. Physics (PHYS 251), University of Oregon.

Recent Outreach

2022 Astronomy on Tap presentation at Bickerson Brewhouse, Seattle, WA.

2022 "Rockin' Out" volunteer. Rockin' Out is a K-12 volunteer-based outreach program at the Department of Earth and Space Sciences at the University of Washington.

2021 - 2022 Mentoring Maanit Goel, a high school student in Seattle, WA.

Peer-Reviewed Publications

In-Prep

2023 **Nicholas Wogan**, David Catling, Kevin Zahnle (2023). Timing and Likelihood of the origin of life derived from post-impact highly reducing atmospheres. In-prep.

Submitted

2023 Zoe Todd, **Nicholas Wogan**, David Catling (2023). Environmental influences on the formation of ferrocyanide and implications for prebiotic chemistry. Submitted to *ACS Earth and Space Chemistry*.

Accepted

2023 **Nicholas Wogan**, David Catling, Kevin Zahnle, Roxana Lupu (2023). Origin of life molecules in the atmosphere after big impacts on the early Earth. Accepted to the *Planetary Science Journal*.

Published

2023 Zachary Cohen, Zoe Todd, **Nicholas Wogan**, Roy Black, Sarah Keller, David Catling (2023). Plausible sources of membrane-forming fatty acids on the early Earth: a review of the literature and an estimation of amounts. *ACS Earth and Space Chemistry*. DOI:10.1021/acsearthspacechem.2c00168.

2022 **Nicholas Wogan**, David Catling, Kevin Zahnle, and Mark Claire (2022). Rapid timescale for an oxic transition during the Great Oxidation Event and the instability of low atmospheric O_2. *Proceedings of the National Academy of Sciences*. DOI:10.1073/pnas.2205618119.

2022 Maggie Thompson, Joshua Krissansen-Totton, **Nicholas Wogan**, Myriam Telus, and
Jonathan Fortney (2022). The case and context for atmospheric methane as an exoplanet biosignature. *Proceedings of the National Academy of Sciences*. DOI:10.1073/pnas.2117933119.

2021 Joshua Krissansen-Totton, Max Galloway, **Nicholas Wogan**, Jasmeet Dhaliwal, and
Jonathan Fortney (2021). Waterworlds probably do not experience magmatic outgassing. *The Astrophysical Journal*. DOI:10.3847/1538-4357/abf560.

2021 Joshua Krissansen-Totton, Jonathan Fortney, Francis Nimmo, and **Nicholas Wogan**. Oxygen false positives on habitable zone planets around Sun-like stars. *AGU Advances*. DOI:10.1029/2020AV000294.

2020 **Nicholas Wogan**, Joshua Krissansen-Totton and David Catling. Abundant atmospheric methane from volcanism on terrestrial planets is unlikely and strengthens the case for methane as a biosignature. *The Astrophysical Journal*. DOI:10.3847/PSJ/abb99e.

2020 Kevin Zahnle, Roxana Lupu, David Catling, and **Nicholas Wogan**. Creation and evolution of impact-generated reduced atmospheres of early Earth. *The Planetary Science Journal*. DOI:10.3847/PSJ/ab7e2c.

2020 **Nicholas Wogan** and David Catling. When is chemical disequilibrium in

Earth-like planetary atmospheres a biosignature versus an anti-biosignature? Disequilibria from dead to living worlds. *The Astrophysical Journal*. DOI: 10.3847/1538-4357/ab7b81.

Selected Conference Presentations

Invited

2022 **Nicholas Wogan**, David Catling, Kevin Zahnle, and Mark Claire. Rapid timescale for an oxic transition during the Great Oxidation Event and the instability of low atmospheric O_2. NASA Goddard Exoplanets Seminar.

2020 **Nicholas Wogan** and David Catling. Atmospheric synthesis of prebiotic molecules on the Hadean Earth. Prebiotic Chemistry and Early Earth Environments Consortium (PCE3), remote conference.

Contributed

2023 **Nicholas Wogan**, David Catling, Kevin Zahnle, and Mark Claire. Rapid timescale for an oxic transition during the Great Oxidation Event and the instability of low atmospheric O_2. Greenbank Astrobiology conference.

2022 **Nicholas Wogan**, David Catling and Kevin Zahnle. Atmospheric nitriles for the origin of life from the atmosphere after large asteroid impacts on the Hadean Earth. Latsis Conference, Zurich, Switzerland.

2022 **Nicholas Wogan**, David Catling and Kevin Zahnle. Origin of life chemistry in the atmosphere after large impacts on the early Earth. Astrobiology Science Conference, Atlanta, GA.

2021 **Nicholas Wogan**, David Catling and Kevin Zahnle. Molecules for the origin of life from impact-generated atmospheres on early Earth. Simons Foundation Collaboration on the Origin of Life Annual meeting, remote conference.

2021 **Nicholas Wogan**, David Catling and Kevin Zahnle. Molecules for the origin of life from impact-generated atmospheres on early Earth. Goldschmidt, remote conference.

2019 **Nicholas Wogan** and David Catling. When is chemical disequilibrium in Earth-like planetary atmospheres a biosignature versus an anti-biosignature? Investigating disequilibria from prebiotic to post-biotic worlds. American Geophysical Union Fall Meeting, San Francisco, CA.

Open Source Software

- photochem: `https://github.com/Nicholaswogan/photochem`. A one-dimensional photochemical-climate model.
- clima: `https://github.com/Nicholaswogan/clima`. A one-dimensional radiative transfer code and suite of climate models.
- numbalsoda: `https://github.com/Nicholaswogan/numbalsoda`. A high-performance ordinary differential equation solver for Python.
- NumbaMinpack: `https://github.com/Nicholaswogan/NumbaMinpack`. High-performance non-linear root solving for Python.
- fortran-yaml-c: `https://github.com/Nicholaswogan/fortran-yaml-c`. A YAML parser and emitter for Fortran.